Structure-function analyses of ion channels involved in glutamatergic signaling

By

Caleigh Mariko Azumaya

Dissertation

Submitted to the Faculty of the
Graduate School of Vanderbilt University
in partial fulfillment of the requirements
for the degree of

DOCTOR OF PHILOSOPHY
in
Molecular Physiology and Biophysics

January 31, 2019
Nashville, Tennessee

Approved:

Roger J. Colbran Ph.D.

Danny G. Winder, Ph.D.

C. David Weaver, Ph.D.

Eric Delpire, Ph.D.

ACKNOWLEDGEMENTS

I would like to acknowledge the funding that made this thesis work and my graduate career possible. The work presented in this thesis was funded by the NIH (R01HD061543), the Vanderbilt University Trans-Institutional Program, and other internal funding to Terunaga Nakagawa, R21MH102546 to TN and C David Weaver, R01GM125629 and the American Heart Association (15SDG25700146) to Julio Cordero-Morales, and the Molecular Biophysics Training Grant (to CMA) from the NIH (T32GM008320) to Walter Chazin.

All high throughput screening experiments were performed in the Vanderbilt High-throughput Screening Core Facility which is an institutionally supported core with assistance provided by Corbin Whitwell. The Vanderbilt Discovery Library was distributed by the Vanderbilt High-throughput Screening Core Facility. EM data collections on the FEI Polara and FEI TF20 were conducted at the Center for Structural Biology's Molecular Cryo-EM facility at Vanderbilt University. We thank Dr. Scott Collier and Dr. Elad Binshtein for their support at the facility. We thank Dr. James Fitzpatrick and Michael Rau for providing access and facilitating data collection using the Titan Krios at the Washington University School of Medicine in St. Louis. CryoEM reconstructions were conducted using the CPU and GPU resources of ACCRE at Vanderbilt University and we used the DORS storage system supported by the NIH (S10RR031634 to Jarrod Smith). We acknowledge the use of SBGrid supported software. For AMPAR work, we thank Kwangho Kim at the Vanderbilt Chemical Synthesis Core for synthesizing NBQX and Elena Zaika for assistance on cell culture and cell line development. For our TRPC work, we thank Dr. Valeria Vásquez for experimental advice and critically reading the manuscript, Dr. Efren Maldonado and Dr. Erkan Karakas for advice during model construction, Dr. Alejandro Mata for TRPC3 patch-clamp recordings, Dr. Silvio Panettieri and Dr. George John for synthesis of GSK-1702934A, Dr. Jonathan Jaggar for providing the hTRPC3 clone, and members of the Cordero-Vásquez and Nakagawa laboratories for technical assistance.

I would like to thank my committee members, Roger Colbran, Danny Winder, David Weaver, and Eric Delpire, for their great assistance during my committee meetings and coming to the many talks that I gave over the course of my career. I appreciate their support relating to my scientific work and my career development. Roger was especially available to me to discuss my future career plans even though he was really too busy to be doing this kind of consulting while also running the department. I would also like to thank Melanie Ohi, who left my committee when she moved to Michigan, for her unrelenting support and advocacy for me from the moment she was my IMPACT leader first year in graduate school to when I received the postdoc offer that I wanted the most. The staff support that I received from Scott, Elad, Mariena, and Emily while working in the cryoEM and HTS cores at Vanderbilt was rivaled only by their personal support of my work and personal well-being while in graduate school.

I would like to thank my labmates, particularly Elena and Aichu Kamalova, who have been here with me the longest. But also, Natalie Shanks who guided me through a few early decisions even though she left the lab before I joined, and Natalie Hawken who was an inspiringly productive undergraduate. I will always appreciate Teru for being a mentor that I can always look to for inspiration in both scientific thought and in work ethic. I have never wavered in the knowledge that he has been just as invested in my work and productivity as I have during my PhD. I would like to thank him for his support in finding a postdoc to continue working in cryoEM and I am especially glad for the lessons he taught me during the difficult paper turn arounds that we had in my last year in the lab.

I would like to thank my previous mentors, Jochen, Leigh, and Linda for their support in my scientific pursuits before I arrived at Vanderbilt. Also, thank you to my friends from before graduate school who stuck around even when I was holed up and not responsive for days. Thank you for coming to visit me in Nashville multiple times (or even every year, Ashley Williamson) and special thanks to Katie Martin, Jennifer Huffman, Elise James, Ashley, Bonnie Pascal, Marilyn

Harvey, and Katie Davis for coming to celebrate my defense. I cannot tell you how important that was and how overwhelming supported I felt. Also, a big thank you to Emily Ale who spent many hours texting back and forth while I was on the scope all night and she was working night shifts and to Katie Martin, who started a podcast with me as a way to keep in touch even more than we already did (please look up the Science Scholars Podcast if you're reading this).

I would like to thank the friends that I made in graduate school, especially Meredith Frazier, Kim Alexander, Stephanie Lotridge-Moore, Diana Contreras, Diane Saunders, Stephanie Carnes, and Juan Gnecco, who slogged through this experience with me and my friends that moved to Nashville from Virginia overtime. I'm extremely grateful to have had such a strong supporter in Ian Williams while we were in graduate school. When everything seemed to be going wrong you were there to give some perspective while I stopped crying. Thank you to my friends that I made outside of school during my time at Vanderbilt, special shout-out to Ela Joshi, Liz Petruzziello, and Kristen Ivory, that kept me from only speaking about science for 6 years straight.

I would like to thank my family for their scientifically inclined genes and also their undeniable support, even when they weren't 100% sure what I was doing. And finally, I would like to thank both of my parents who shaped me into a baby scientist straight out of the womb and gave me every available resource to be successful in science and in life. I would never have had the educational foundation that has allowed me to reach this point in my life if you had not supported me in every was possible. Thank you for being both good scientific role models as well as good people that I aspire to be more like every day.

TABLE OF CONTENTS

LIST OF TABLES

LIST OF FIGURES

COMMON ABBREVIATIONS

ER	endoplasmic reticulum
AMPAR	α-amino-3-hydroxy-5-methyl-4-isoxazolepropionic acid receptor
TRPC	canonical transient receptor potential
IP_3R	inositol 1,4,5-triphosphate receptor
NMR	nuclear magnetic resonance
NTD	N-terminal domain
cryoEM	cryogenic electron microscopy
AQP-0	aquaporin-0
TM	transmembrane
TMD	transmembrane domain
MSP	membrane scaffold protein
OmpX	outer membrane protein X
DLPC	1,2-dilauroyl-sn-glycero-3-phosphocholine
POPC	1-palmitoyl-2-oleoyl-sn-glycero-3-phosphocholine
mol%	molar percentage
PE	phosphatidylethanolamine
cytb5	cytochrome b5
CYP	cytochrome p450
TRPV	vanillin transient receptor potential
PI	phosphoinositide
RyR	ryanodine receptor
K_d	dissociation constant
CHAPS	3-((3-cholamidopropyl) dimethylammonio)-1-propanesulfonate
CNS	central nervous system
AP	auxiliary protein
iGluR	ionotropic glutamate receptor
LTP	long-term potentiation
LTD	long-term depression
KO	knockout
LBD	ligand binding domain
CTD	C-terminal domain
DDM	n-dodecyl--D-maltoside
FW	fluorowillardiine
TARP	transmembrane AMPAR auxiliary protein
stg	stargazin
CNIH	cornichon homolog
GPCR	G protein coupled receptor
SNP	single nucleotide polymorphisms
GSG1L	germline specific gene 1 like
M1-4	transmembrane helix 1-4
NAM	negative allosteric modulator
CTZ	cyclothiazide
PAM	positive allosteric modulator
FDA	food and drug administration
TRP	transient receptor potential
TRPM	melastatin TRP
TRPA	ankyrin TRP
TRPML	mucolipin TRP
TRPP	polycystic TRP

S1-S5	membrane spanning helices 1-6
CPD	cytoplasmic domain
DAG	diacylglycerol
CaM	calmodulin
LHD	linker helical domain
OAG	1-oleoyl-2-acetyl-sn-glycerol
GDN	glyco-diosgenin
PLC	phospholipase C
CaMKII	Ca^{2+}/calmodulin-dependent protein kinase II
FSGS	focal segmental glomerulosclerosis
HEK	human embryonic kidney
mGluR	metabotropic glutamate receptor
CIRB	CaM/IP3receptor-binding
DED	direct electron detector
DQE	detective quantum efficiency
MTF	modulation transfer function
SNR	signal to noise ratio
RELION	regularized likelihood optimization
cisTEM	computational imaging system for transmission electron microscopy
cryoSPARC	cryo-EM single particle ab initio reconstruction and classification
FSC	Fourier shell correlation
GPU	graphics processing unit
GO	graphene oxide
DOX	doxycycline
IRES	internal ribosome entry site
MBP	maltose binding protein
TEV	tobacco etch virus
HRP	horseradish peroxidase
HTS	high throughput screening
KA	kynurenic acid
Hyg	hygromycin
G418	geneticin
NBQX	2,3-dioxo-6-nitro-1,2,3,4-tetrahydrobenzo[*f*]quinoxaline-7-sulfonamide
TB	terrific broth
IPTG	isopropyl β-D-1-thiogalactopyranoside
NaCl	sodium chloride
NaPhos	sodium phosphate
BME	β-mercaptoethanol
FPLC	fast protein liquid chromatography
PMSF	phenylmethane sulfonyl fluoride
Tris	Tris(hydroxymethyl)aminomethane
HEPES	2-[4-(2-hydroxyethyl)piperazin-1-yl]ethanesulfonic acid
VDL	Vanderbilt discovery library
VSD	voltage-sensitive dye
DMEM	Dulbecco's Modified Eagle's medium
FBS	fetal bovine serum
O/N	overnight
HBSS	Hank’s balanced salt solution
FDSS	Functional Drug Screening System
CMPD	compound
GLU	glutamate

VHL	vehicle
CRC	concentration response curve
KCl	potassium chloride
$MgCl_2$	magnesium chloride
$CaCl_2$	calcium chloride
%max	percent maximum
NaF	sodium fluoride
EGTA	ethylene glycol-bis(β-aminoethyl ether)-N,N,N′,N′-tetraacetic acid
CsOH	cesium hydroxide
NaOH	sodium hydroxide
PenStrep	penicillin-streptomycin
WT	wild type
DMSO	dimethyl sulfoxide
Sf9	Spodoptera frugiperda
TCEP	tris(2-carboxyethyl)phosphine
LBC	ligand binding core
Tni	*Trichoplusia ni*
EDTA	ethylenediaminetetraacetic acid
LMNG	lauryl maltose neopentyl glycol
n	stoichiometry
CCD	charge coupled device
SPIDER	system for processing image data from electron microscopy and related fields
RCT	random conical tilt
PCR	polymerase chain reaction
Cu	copper
Au	gold
WUCCI	Washington University in St. Louis Center for Cellular Imaging
Cs	spherical aberration
ACCRE	Advanced Computing Center for Research and Education
CTF	contrast transfer function
NCS	non-crystallographic symmetry
PDB	protein database
EMDB	electron microscopy database
DW	dose weighting
AP2	adaptor protein 2
PICK1	protein interacting with C kinase 1
MAGUK	membrane-associated guanylate kinases
GRIP	glutamate receptor interacting protein
NSF	N-ethylmaleimide-sensitive factor
PSD	postsynaptic density
EC50	half maximal effective concentration
IC50	half maximal inhibitory concentration
AUC	area under the curve
SDS-PAGE	sodium dodecyl sulfate polyacrylamide gel electrophoresis
AR	ankyrin repeat
ARD	ankyrin repeat domain
PMAL-C8	Poly(Maleic Anhydride-alt-1-Decene) substituted with 3-(Dimethylamino)
HH	horizontal helix
VH	vertical helix
RMSD	root mean square deviation
PTEN	phosphatase and tensin homolog

ITC	isothermal calorimetry
CLD	center linker domain
ARM	Armadillo solenoid domain
JD	juxtamembrane domain
β-TF	β-trefoil domains
SPA	single particle analysis
cryoET	cryogenic electron tomography
FIB	focused ion beam
microED	microcrystal electron diffraction
TEM	transmission electron microscope

CHAPTER 1: INTRODUCTION

AMPAR, TRPC, and IP_3R involvement in glutamatergic signaling

Glutamatergic neurotransmission is a mechanism by which an action potential is propagated from one neuron to the next. When an electrical signal reaches the presynaptic bouton of an excitatory synapse, this depolarization triggers release of glutamate, a neurotransmitter, into the synaptic cleft. Glutamate can then bind to a variety of receptors, which results in various downstream effects. In this dissertation, we focus on one class of ionotropic glutamate receptors (iGluR), an ion channel that sits downstream of the metabotropic glutamate receptors (mGluR), and a receptor that sits in the endoplasmic reticulum (ER) and modulates ion channel function at the neuronal membrane. The iGluR that our work focuses on is the AMPA receptor (AMPAR), whose specific function and importance will be discussed in the next section. Generally, iGluRs immediately gate to allow positively charged ions to flow into the cell, causing fast depolarization of the postsynaptic neuron. This makes up the bulk of excitatory post-synaptic currents (EPSCs), but these receptors desensitize quickly. The canonical transient receptor potential (TRPC) channels are involved in the slow component of EPSCs. Glutamate binds to mGluR1, triggering the $G_{\alpha q}$ protein to activate phospholipase C, which results in the generation of diacylglycerol (DAG). DAG can then bind to TRPC channels, which gate to allow positively charged ions, including calcium into the neuron. This creates the inward EPSC and calcium ions can act as second messengers in downstream signaling pathways. TRPC channels can be modulated by a variety of factors. Binding of inositol 1,4,5-triphosphate receptors (IP_3R) to the TRPC channel increases channel activity. While this binding site has been mapped using biochemical techniques, further information about the arrangement of the two proteins can be inferred from the structures determined in this dissertation.

Structure and function of ionotropic glutamate receptors

Memory formation and mood regulation are important in defining and improving every individual's life. AMPAR-based changes in synaptic morphology and connectivity often underlie central nervous system (CNS) dysregulation that leads to mood and psychological disorders[41,42]. Alterations in AMPAR levels and functionality have been implicated in many cognitive diseases, including Alzheimer's[43,44], depression[45,46], bipolar and other mood disorders[47,48], and Parkinson's[47]. Depression and opiate dependence are debilitating CNS conditions for which treatment is often ineffective; a deeper understanding of AMPAR interactions could lead to new therapeutic options for both of these afflictions[49]. Cognitive disorders often rob those affected of their autonomy, decrease overall quality of life, and cost the United States billions of dollars in healthcare expenses. A better understanding of the *in vivo* function of AMPARs and how they are regulated by auxiliary proteins (APs) is necessary to better characterize effective treatments and to discover and improve small molecule modulators.

AMPA receptor function

Glutamatergic neurotransmission is one of the main forms of communication utilized in the CNS. These fast, chemical signals are transduced across the membrane of the postsynaptic neuron by iGluRs that act as ligand-gated cation channels (**Figure 1-2**). AMPARs are a subtype of iGluR characterized by fast activation, deactivation, and desensitization[51]. They mediate the majority of fast excitatory neurotransmission in the CNS, and their activity plays a key role in synaptic strength and plasticity both through differential trafficking[52] and variations in gating kinetics[51]. AMPAR dynamics are integral to synaptic plasticity[53], in the form of long-term potentiation (LTP) and long-term depression (LTD), which are accepted cellular correlates of memory storage and learning[54]. AMPAR-mediated changes in key physiological processes, such as LTP, have been extensively studied *in*

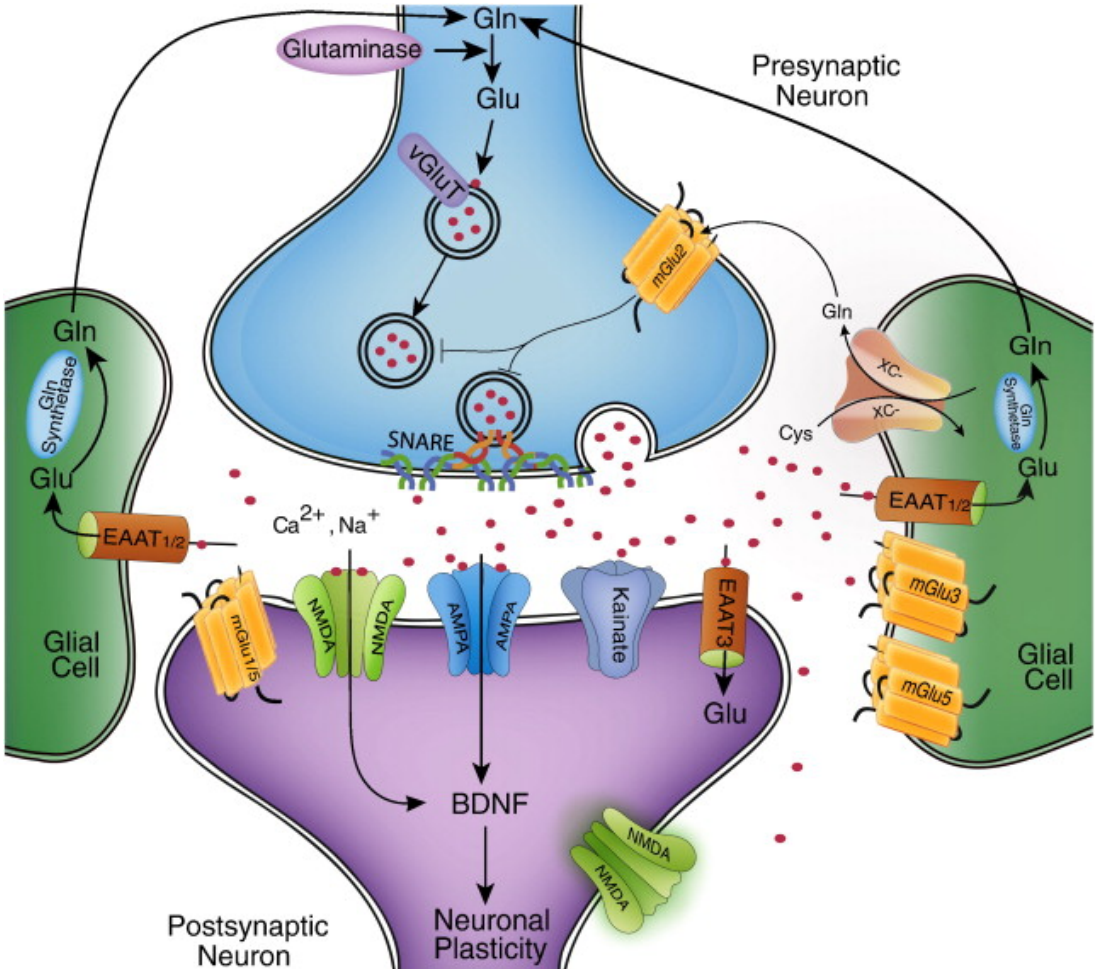

Figure 1-1. Schematic of glutamatergic neurotransmission.
Many components are involved in glutamatergic neurotransmission. AMPARs sit in the postsynaptic density (PSD) along with other iGluRs. These receptors bind glutamate when it is released from the presynaptic bouton and immediately gate to allow positively charged ions to flow in and depolarize the postsynaptic neuron. The presence of glutamate in the synapse is managed by glutamate transporters that move glutamate into neighboring glial cells. Metabotropic glutamate receptors, NMDARs, and kainate receptors also bind glutamate and promote long term synaptic plasticity. Image from Niciu, MJ, et al, 2012[50].

vivo. AMPARs are homo or heterotetramers composed of up to two different of four homologous subunits, GluA1-GluA4. GluA1 knockout (KO) mice lack LTP[55], which was also demonstrated to be accompanied by hyperactivity and deficiencies in short term spatial working memory[56]. These KO mice can be contrasted with GluA2/GluA3 KO mice that show decreased synaptic transmission, but still undergo LTP and LTD[57], and GluA2 KO mice that demonstrate increased LTP and behavioral abnormalities[58,59]. The core tetramer subunits are composed of an NTD, ligand binding (LBD), TMD, and C-terminal (CTD) domain. These homo and heterotetramers are sufficient for ligand-induced ion flow[60,61], but there are many levels of functional modulation by subunit assembly[62], alternative splicing[63], RNA editing at the Q/R site in the pore helix, with glutamine (Q) allowing calcium permeability and higher peak amplitude[64,65], phosphorylation[66], and APs[67–76]. All of these lead to great diversity within in the AMPAR family.

AMPA receptor structure

The full-length tetramer of AMPARs has been studied extensively at using a variety of structural techniques. In 2009, the first snapshot of the AMPAR was presented. The receptor was engineered to reduce flexibility between the LBD and NTD, locked in a closed state with the inhibitor ZK200775, and crystallized in the detergent n-dodecyl-β-D-maltoside (DDM)[17] (**Figure 1-3A**). This study was followed up by multiple papers that were able to leverage both crystallography and the increasing resolution available with the development of cryoEM to study the receptor in complex with agonists, glutamate, fluorowillardiine (FW), and quisqualate, as well as desensitization blockers, LY451646 and (R,R)-2b, and even a naturally occurring toxin, con-ikot-ikot[18,19,22] (**Figure 1-3B**). These ligands induce a drastic rearrangement of the LBDs and NTDs. Upon application of agonist, the receptor undergoes fast activation and desensitization, seen in its structure as the NTD dimers moving apart and down towards the LBD layer. Additionally, the LBD dimers rotate counterclockwise through their upper (D1) lobes to rupture their 2-fold symmetry with the lower (D2) lobes separating. With this opening and rotation, they instead rupture their D1-D1 interface in a desensitized state and separate into four distinct densities[19]. The majority of structural studies have been carried out with homotetramers of the GluA2 subunit because of its robust expression in mammalian cells, but the full-length structure of the GluA2/GluA3 heterotetramer has also been solved[77] (**Figure 1-3C**). This brought into focus two main organizations of the receptor, the Y-shape that was first visualized in the inactive crystal structure and an O-shaped conformation that is more compact at the N-terminal domains and along the axis perpendicular to the plasma membrane. This conformation more closely resembles structures of the N-methyl-D-aspartate receptor (NMDAR)[78,79] (**Figure 1-3D**).

AMPAR auxiliary proteins

AMPARs exist primarily in complex with transmembrane APs[67–76]. The *in vivo* importance of AMPAR APs has become clear from extensive electrophysiological, proteomic, and mutational analysis[80–83]. The highly divergent structures of APs parallel their broad spectrum of functional modulation of AMPARs[84–86] (**Figure 1-3E**). The prototypical AP, stargazin (TARP γ-2, stg), was discovered in the context of a spontaneous mutant stargazer mouse with severe ataxia and focal seizures[88]. Interestingly, deletion of stg led to a much more severe phenotype than losing any of the core AMPAR subunits. Many functional regions of the stg protein have been interrogated and structurally similar (TARPs γ-3, 4, 5, 7, 8 and GSG1L) and disparate (CNIHs, CKAMP44, synDIG, and sol-1) APs have been identified, but much remains to be learned about the molecular mechanism of modulation of these proteins on the AMPAR. For example, the stoichiometry between AMPAR and TARPs has been predicted to be 1:2[84,89], but structures have been solved with one, two, and four TARPs bound. It has also been proposed that TARP γ-8 and cornichon homolog 2 (CNIH2) binding is mutually exclusive[90] while TARP γ-8 and CKAMP44 binding is not[91], but most AP binding sites still need to be determined.

To focus in on one type of auxiliary subunit, CNIH2 and CNIH3 were discovered to associate

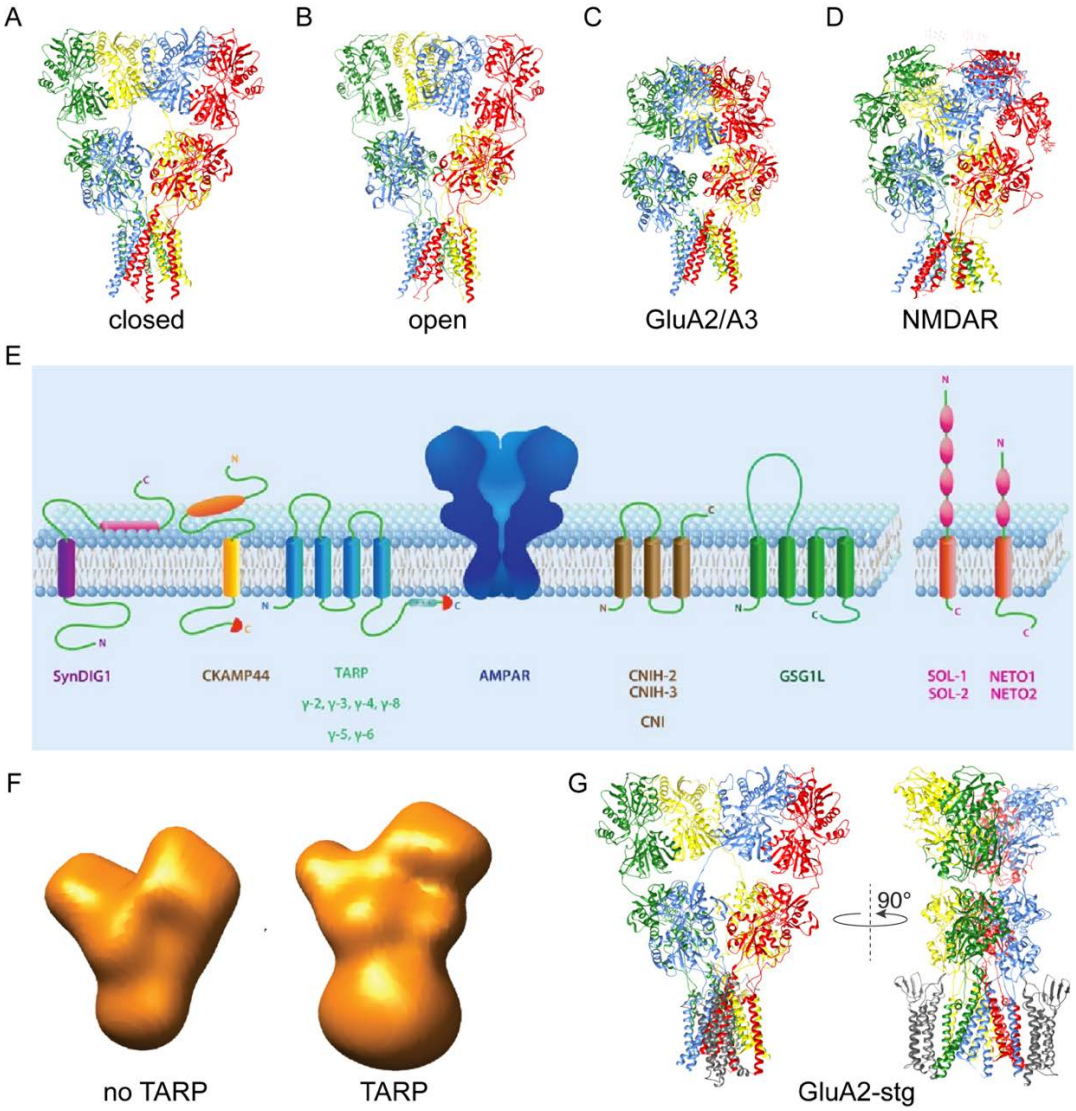

Figure 1-3. Structural characterization of the AMPAR and APs

The AMPAR tetramer has been extensively structurally characterized over the last ten years. Each of these structures have the four GluA subunits colored in red, blue, green, and yellow. **A.** The first high-resolution structure of the full-length GluA2 homotetramer was solved by crystallography in 2009 in an antagonist bound state (PDB:3KG2)[17]. **B.** After nearly a decade, a mostly open state of a GluA2 tetramer was trapped by applying glutamate and cyclothiazide to a GluA2-stg complex (PDB: 5WEO, the stg molecules have been removed for comparison)[16]. **C.** The GluA2/GluA3 heterotetramer revealed a novel organization of the extracellular domain that was more compact that the "Y-shaped" structures that had been seen previously (PDB:5IDE)[77]. **D.** The "O-shaped" structure of AMPAR heterotetramer looks most similar to the GluN1/GluN2B heterotetramer of the NMDA receptor that was solved using X-ray crystallography (PDB:4PE5)[78]. **E.** AMPAR auxiliary subunits are small transmembrane proteins that affect both trafficking of the receptor and its function at the neuronal surface. These proteins vary in topology and function, but all associate strongly with the AMPAR as assayed through biochemical and proteomic techniques. Image from Monyer and von Engelhardt, 2015[87]. **F.** AMPAR in complex with an AS was first visualized at low resolution in 2005[86]. **G.** Recently, higher resolution structures have been solved for the GluA2-stg (shown, PDB:5KUB) and GluA2-GSG1L complex that begin to elucidate the structural basis for the changes in gating kinetics these ASs cause[12,14].

with AMPAR *in vivo* through a proteomics screen of affinity purified AMPARs from rat brain[74]. They are highly expressed in the cortex and hippocampal formation, but are scarce in the striatum and absent in the cerebellar granule cells where stg is enriched[92]. CNIHs increase AMPAR conductance and decrease the rate of desensitization and deactivation even more than TARPs**.** CNIHs purify with AMPAR in similar ratios to stg and the other TARPs, indicating that they are likely integral to *in vivo* AMPAR function[74]. In humans, single nucleotide polymorphisms (SNPs) in the CNIH3 gene have been tied to increased risk of opioid dependence[49]. CNIHs are also interesting to study because while CNIH2/3 bind and modulate AMPARs, CNIH1/4 bind without altering AMPAR gating kinetics[93]. Understanding these differences could elucidate the differential effect of structurally similar APs. CNIH4 also reportedly interacts with G protein coupled receptors (GPCRs) in the early secretory system and coimmunoprecipitate with the COPII coat complex[94].

As discussed above many techniques have been utilized to describe the full length AMPAR structure and elucidate the mechanisms by which it activates and desensitizes[17,18,20–22]. *Nakagawa et al., 2005* presented the structure of a native AMPAR/TARP complex, purified from rat brain homogenate, at low resolution using negative stain cryoEM (**Figure 1-3F**)[86]. Very recently, recombinantly expressed protein complexes of AMPAR-stg and AMPAR-GSG1L have been solved to much higher resolution (**Figure 1-3G**), allowing us to visualize some of the interactions between AMPARs and their tetraspanin APs[12,14,15]. These structures show that the APs form four helix bundles that contact the M1 and M4 of the AMPAR with their third and fourth TM helices. The AMPAR-stg structure has been solved with one, two, and four APs bound and the AMPAR-GSG1L has been solved with one and two APs bound. The extracellular loops of stg and GSG1L are both spatially close to the D2 lobes of the AMPAR LBDs. While these regions of the cryoEM maps are lower resolution because of their inherent flexibility, there is a run of positively charged amino acids in the LBD that is adjacent to what is likely a negatively charged patch in the stg first extracellular loop. This suggests a mode of action for how stg could be slowing desensitization by stabilizing an open state of the receptor for longer. This would explain the retarded desensitization that is a hallmark of Type I TARP complexes[14,15]. Because the first loop of GSG1L is longer than that of stg it was not resolved in the published structure. When agonist was applied to AMPAR-GSG1L the rupture of LBD dimers in the desensitized state was seen, but the distance between dimers are slightly smaller because of a smaller turn of the subunits than for structures of the AMPAR without APs present. This could imply functional significance or that the receptor had already begun its transition back into an inactive state. They did not see the characteristic opening of the NTDs in the AMPAR-GSG1L complex when ligand was present[12]. GSG1L is known to be a negative regulator of the AMPAR, which may explain why the receptor is not revealing the drastic rearrangements seen without GSG1L. Understanding AMPAR interactions at a molecular level will allow us to better determine their mechanism of modulation and manipulate precise circuits within the CNS with small molecule inhibitors.

AMPAR modulators and their future as therapeutics

As discussed previously, AMPARs are critical for excitatory synaptic transmission and their impairment negatively impacts cognition, mood, and behavior. Being able to alter their function, or dysfunction, is integral to understanding the physiology of neurons and our ability to treat various neurological diseases[44,95,96]. Several AMPAR modulators have been identified and are used commonly as lab tools. Negative allosteric modulators (NAMs) such as GYKI 53655, pyridone perampanel, and quinazoline-4-one CP 465022 are AMPAR-specific antagonists. Mutational and structure studies show these compounds bind outside of the pore region of the molecule[97,98]. They slide into the interface at the extracellular extreme of M3, M4, and the pre-M1 helix, which tightens the top of the ion channel pore and their binding precludes the TMs from rearranging into an open state[98]. Cyclothiazide (CTZ), LY392098 and LY404187, and ampakines are positive allosteric modulators (PAMs) that work through a variety of mechanisms such as blocking desensitization or increasing agonist affinity[99–102]. Additionally, NAMs and PAMs targeting the channel forming subunits of AMPARs are being used and explored as therapeutics.

NAMs, such as perampanel[103,104], are approved by the FDA to attenuate seizures in epileptic patients. Although these compounds are effective, they can have severe side effects including dizziness and motor impairment[105]. Meanwhile PAMs, such as CX-516[41], have been shown to have anti-depressant effects in mouse models. Newer generations of these ampakine molecules, namely CX-717, have been studied further for treatment of attention deficit hyperactivity disorder (Eli Lilly), Alzheimer's[106], and opiate-induced respiratory depression[107].

APs show differential spatial and temporal expression patterns across the CNS[67,82]. Therefore, it is conceivable that specifically targeting AMPAR-AP complexes would enable a variety of targeted functional consequences, some of which may be useful for therapeutics. Selectively targeting specific AMPAR-AP complexes may enable us to determine if certain types of AMPAR-AP complexes are responsible for specific disease phenotypes. NAMs have been identified to target TARP γ-8 containing AMPARs[108–110]. The compound from Eli Lilly, LY3130481, was able to decrease ion flow through AMPARs associated with TARP γ-8 in both cellular assays and slice electrophysiology. When injected into mice it decreased seizure incidence at concentrations lower than perampanel and GYKI without causing the motor impairments associated with both of these compounds[110]. Mutational analysis of TARP γ-8 identified two key amino acids for LY3130481 binding, Val-117 and Gly-210, and upon further characterization it was determined that GluAX subunits are not necessary for LY313's binding to TARP γ-8[111]. Being able to target subpopulations of AMPARs will potentially decrease deleterious on-target effects of AMPAR agonists and antagonists that have derailed clinical studies in the past.

Transient receptor potential channels

The transient receptor potential (TRP) ion channels support calcium (Ca^{2+}) permeation in a variety of tissues, including, but not restricted to, those of the heart, brain, and kidney[112,113]. The 27 mammalian TRP channels are classified under six subfamilies, TRPC (canonical), TRPM (melastatins), TRPV (vanilloid), TRPA (ankyrin), TRPML (mucolipins), and TRPP (polycystins) based on primary structure similarity[113] (**Figure 1-4**). They are ubiquitously expressed throughout the body and involved in several physiological processes, including temperature detection, pain, neurotransmission, and vascular regulation[113,114]. The architectures of TRP channels have been extensively studied using cryoEM[112]. TRPV1 was one of the first high-resolution single particle cryoEM structures of a membrane protein to be determined by using direct electron detectors (DEDs) and advances in image analysis software[38]. Since this time the cryoEM field has exploded; with TRP channel structures being solved for members of all subfamilies. Detergents, nanodiscs, and amphipols have all been used successfully to determine structures of the full-length channels. The TMD forms the ion channel core of TRP channels and all subfamilies adopt the same general organization in this region of the protein. Each subunit consists of six membrane spanning segments, S1-S6, and a pore helix connecting to a re-entrant loop[38]. The pore forming helices (S5 and S6) adopt an inverted teepee structure similar to the architecture of potassium channels[117,118]. TRP channels share a unique common motif, the TRP box (EWKFAR), immediately adjacent to the ion channel gate. The N- and C-termini co-assemble into a cytoplasmic domain (CPD), which is the most variable substructure among the TRP receptor family members whose structures have been solved[38,119–129] (**Figure 1-4**). Even before the "resolution revolution" in cryoEM, there were four low resolution EM structures of full-length channels that hinted at the diversity of the CPD[130–133]. The observed structural diversity suggests that the CPD confers a subtype-specific function to the receptor, such as serving as an interface for protein-protein interactions and allosteric gating modulation.

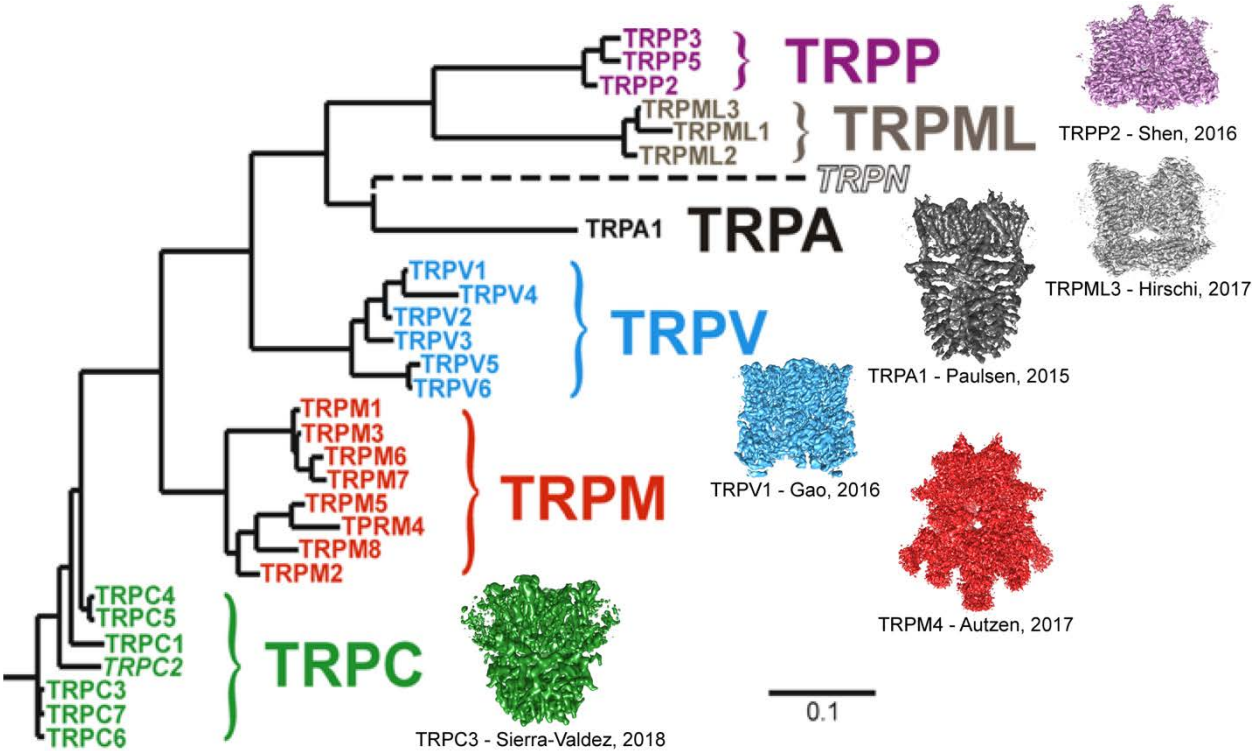

Figure 1-4. TRP channel phylogeny and representative structures.
TRP channels have been extensively studied structurally and functionally. These channels have similar organizations of their transmembrane helices but their cytoplasmic domains (CPDs) are highly variable. An evolutionary tree of the 27 mammalian TRP channels, TRPN is only found in *Drosophila melanogaster* and TRPC2 is a pseudogene, is presented with a representative structure from each subfamily to the right in the corresponding color. EMDB entries EMD-8354, EMD-8764, EMD-6267, EMD-8118, EMD-7132, EMD-7940. Evolutionary tree image adapted from Nilius, et. al. 2005[116].

TRPC subfamily

The TRPC ion channels consist of seven members, TRPC1-7. They are further divided into three groups based on sequence similarity and functional analyses: TRPC1/4/5 are activated by $G_{\alpha q}$-coupled receptors and receptor tyrosine kinases, whereas TRPC3/6/7 are activated directly by diacylglycerol (DAG). TRPC2 is a pseudogene[113]. TRPC6 is permeable to Ca^{2+} and sodium (Na^{+}) ions and DAG is sufficient to activate this channel[134]. Physiological gating occurs in synergy with the activation of a $G_{\alpha q}$/11-coupled receptor, such as the muscarinic receptors[135]. The currents elicited by TRPC channels depolarize the cell membrane to subsequently activate voltage-dependent ion channels, as well as secondary signaling triggered by Ca^{2+} ions[136]. TRPC3/6/7 gating is also influenced by glycosylation, phosphorylation, lipids (e.g., DAG, phosphatidylinositol (3,4,5)-trisphosphate (PIP_3)), and binding of other proteins such as calmodulin (CaM) and IP_3Rs[137–141]. A relevant feature of the TRPC subfamily is that its members can form homo- and heterotetramers[142,143]; hence TRPC physiological and biophysical properties might be broader in heteromultimeric assemblies[144]. A TRPC subunit consists of an N-terminus formed by four ankyrin repeats (Ars), the linker helical domain (LHD, helices 1-9), and the pre-S1 elbow. The N-terminus is followed by S1-S6 and a pore helix connecting to a re-entrant loop that forms the selectivity filter (the TMD). The TRP helix is immediately adjacent to S6, and the C-terminus consists of two α-helices connected by a short linker. Recently, a huge accumulation of structural information has been achieved for the subfamily of TRPC channels with the determination of the cryo-EM structures of TRPC4[125], the full-length[129] and CPD of TRPC6[120], and TRPC3[121,129,145]. The TRPC3 structure from Tang et al., was obtained using nanodiscs and was trapped in a closed state despite the presence of the DAG analog, 1-oleoyl-2-acetyl-sn-glycerol (OAG). The TRPC3 structures from Fan et al. and our group were obtained in detergents (digitonin and GDN) also in a closed state. Although, these structures shared overall topology, they diverge in the CPD spatial organization. Whether these differences are introduced by preparation methods or represent conformational variations that reflect physiologically relevant states remains to be determined, but we present function evidence of the allosteric effect the CPD can have on channel gating.

Clinical significance of the TRPC subfamily

Inherited mutations in TRP channels underlie numerous pathological conditions, such as peripheral neuropathies, heart failure, cardiac arrhythmia, and pulmonary hypertension[114]. In this dissertation, we have solved structures for TRPC6 and TRPC3. Biological processes regulated by TRPC6 include endothelial permeation in blood vessels, growth of neuronal processes, and glomerular filtration[113]. It has been reported that mechanical stretch can gate the TRPC6 receptor independent of phospholipase C (PLC) activation, which may underlie their involvement in hemodynamic regulation of blood vessels[146]. In the CNS, TRPC6 is expressed primarily in the hippocampal formation and, at lower levels, in the cortex. TRPC6 expression peaks during a critical period in mouse synaptogenesis, P7-P14[147], and channels were found to reside primarily in the postsynaptic density (PSD) of excitatory synapses based off of fluorescence and electron microscopy[148]. Overexpression in hippocampal neurons showed increased spine density and knockdown showed the opposite phenotype. At a behavioral level, hippocampus-based spatial memory improved slightly, shown by a decrease in escape latency from a Morris water maze, in transgenic animals with increased TRPC6 expression under control of the CaMKIIα promoter[148].

In contrast to TRPC6 in the CNS, TRPC6 expression in the kidney is highest during early development and drops off as animals mature[147]. Mutations in TRPC6 have been identified in patients with both adolescent and adult-onset focal segmental glomerulosclerosis (FSGS)[149–153]. FSGS patients usually present with proteinuria, hypertension, and approximately one fifth of people diagnosed with end stage renal disease have been diagnosed with FSGS[154]. Dysfunction in multiple cytoskeletal and structural proteins have been linked to FSGS[155,156], but mutations in TRPC6 affect channel gating and, in turn, calcium homeostasis. TRPC6 channels carrying

different FSGS mutations have been expressed in human embryonic kidney (HEK) cells and show varying gating phenotypes that span from gain- to loss-of-function[150,151,153]. Mutations that lead to a larger increase in channel current and Ca^{2+} influx present in a more severe phenotype, with FSGS manifesting earlier in life for these patients[150]. The mechanism of TRPC6 gating modulation by these mutations and its relation to disease is largely unknown. Locating and determining the structural impact of these disease-causing mutations in the channel is an important step towards solving this problem.

TRPC3 is expressed in the Purkinje cells and unipolar brush cells in the cerebellum[157,158]. It sits downstream of metabotropic glutamate receptor 1 (mGluR1) signaling[159] and regulates neuronal excitability in a circuit essential for behaviors related to motor learning and coordination. Indeed, a gain-of-function mutant in the TRPC3 S4−S5 linker region (T573A) causes abnormal Purkinje cell development and cerebellar ataxia (i.e., inability to coordinate balance, gait, extremities and eye movements) that facilitates backward ambulation in the *moonwalker* mouse[160,161]. Furthermore, TRPC3 expression was increased in mice with contextual fear memory deficits, suggesting a role for TRPC3 in regulating hippocampal neuron excitability associated with memory function[162]. In a proteomics study, TRPC3 was associated with 64 different proteins in rat brain homogenate. A majority of these proteins were classified as being often involved in regulation of gating or plasma membrane localization[163]. Notably, TRPC3 and TRPC6 contain a CaM/IP_3R-binding (CIRB) domain that binds both CaM and the IP_3R directly[137,140,141,164]. CaM binding inhibits the intrinsic activity of TRPC3 and the displacement of CaM by the IP_3R is proposed to increase channel activity[165]. PIP_3 has also been shown to displace CaM from TRPC6[137]. TRPC1 also interacts with the IP_3R, but this interaction has been shown to be Homer-dependent[166].

In other regions of the body, TRPC3 KO mice show decreased Ca^{2+} flux and store-operated channel Ca^{2+}-flux in pancreatic acinar cells. Subsequently, there are decreased Ca^{2+} oscillations, which prevent detrimental levels of cytosolic Ca^{2+}, inhibit digestive enzyme secretion, and the KOs develop less severe pancreatitis[167,168]. In cardiomyocytes and blood vessels, TRPC3 is an essential component of the cellular mechanisms by which vasoconstrictors regulate blood pressure[169,170]. Vasoconstrictors, such as angiotensin II, bind to PLC-coupled receptors, increasing the intracellular levels of DAG, which in turn activates TRPC3[134]. Upon activation, TRPC3 channels induce membrane depolarization and opening of L-type Ca^{2+} channels, increasing intracellular Ca^{2+} and promoting vasoconstriction[171]. Despite its relevance in the nervous, exocrine, and vascular systems, the TRPC3 gating mechanism remains elusive. Selective compounds for individual TRPC channels are sparse[172,173]; hence, it is expected that structural and mechanistic information will facilitate rational drug design; the outcome of which could sharpen pharmacological tools and development of new strategies to control neurological disorders and blood pressure.

Membrane proteins and the lipid membrane

Proteins can be classified broadly as soluble, peripheral membrane, or integral membrane proteins. Integral membrane proteins are embedded into and permanently associated with the membrane. These proteins are involved in all aspects of a cell or organism's life. Receptors sit in the plasma membrane (PM) and organelle membranes to function as signal transducers from one side of the membrane to the other. Transporters and channels traverse membranes in order to shuttle ions, small molecules, and even peptides that would not normally be membrane-permeable into new compartments. Membrane proteins are also important for cell-cell recognition, cell-cell interaction, and connecting membranes to the extracellular matrix or cytoskeleton. Finally, membrane proteins can be enzymatic assemblies involved in integral cellular functions[1]. In my work, I have focused on three different ion channels that function in the PM or the membrane of the endoplasmic reticulum (ER). Ion channels, as well as the many other membrane proteins are often targeted for therapeutic intervention because of their importance in a variety of basal

physiological processes and availability to the extracellular space. The viability of a drug target is generally assessed by it having a clear involvement in disease and the researcher being able to alter its function without affecting too many necessary biological processes. The protein must also be able to bind a small molecule in a specific and potent way. Over 50% of available therapeutics target membrane proteins[2–4], but studying their structure and function has always posed a sizable hurdle.

Lipid membranes and their binding to proteins

The lipid membrane is separated into an inner and outer leaflet, that are made up primarily of phospholipids. Polar or charged head groups of the lipids face aqueous solution and hydrophobic tails create a barrier between compartments. Lipid association can change the structure of certain proteins. α-synuclein has been studied using nuclear magnetic resonance (NMR) spectroscopy to show that when in solution, the entirety of the protein is unstructured. Upon binding to either small unilamellar vesicles or detergent micelles, the N-terminal domain (NTD) of the protein adopts a helical order than can be observed in both NMR and circular dichroism experiments. In this case, the presence of any type of lipid mimetic was sufficient to show ordering of the α-synuclein protein[5]. In cryogenic electron microscopy (cryoEM), lipids binding to proteins were visualized even before recent technological advances. A study of the purple membrane, indicated that bacteriorhodopsin and lipids are arranged in a highly ordered two-dimensional (2D) crystal lattice that can be imaged in a transmission electron microscope (TEM). Diffraction patterns of tilted and untilted samples were collected and analysis revealed nine α-helices of the protein and empty space in the middle that, using difference maps of wet and dry samples and binding assays, is implied to be filled with a lipid bilayer[6]. In 2005, 2D crystals of aquaporin-0 (AQP-0) in a lipid membrane were used to determine a structure at 1.9Å resolution. The group was able to resolve differing numbers of water molecules in different AQP-0 conformations as well as annular lipids that fit between tetramers[7]. Lipid composition in a membrane is variable and proteins can both prefer a specific chemical environment and/or shape of the membrane[8–10]. A native lipid environment is unique and difficult to replicate, but scientists have developed many types of membrane mimetics to study these proteins in a more controlled manner. Integral membrane proteins must often be purified and reconstituted in order to determine their structure. This method is also used to isolate specific proteins to study functionally. There are a variety of different lipid mimetics that have been developed over the years including detergents, liposomes. amphipols, nanodiscs, supported bilayers, and more (**Figure 1-1**).

Lipid membrane mimetics

Briefly, detergents are lipid mimetics that have a polar head group and a single nonpolar tail group that form aggregates called micelles. They surround the transmembrane (TM) regions of integral membrane proteins with their nonpolar tails to protect the membrane-inserted region of the protein from the hydrophilic solvent. A large variety of detergents have been used to stabilize membrane proteins for structural studies in the past. Notably, all ionotropic glutamate receptor (iGluR) structures have been determined from detergent-solubilized proteins[12–22]. Detergents are often used to stabilize proteins in crystallography because proteins are still able to form an ordered, crystalline lattice. Some membrane proteins are not stable in detergents and for these proteins the lipidic cubic phase was developed for crystallographic purposes[23]. Lipids, solvent, and proteins are combined and extruded using specific machinery so that a lipidic array is formed that supports membrane proteins in a structured, three-dimensional (3D) formation. These matrices are seeded and then grown by lateral diffusion of protein molecules into the membrane. This allows the proteins to be surrounded by a lipid bilayer, while keeping them in an ordered array[23,24]. This is a similar theory to 2D crystallography that was used to determine high

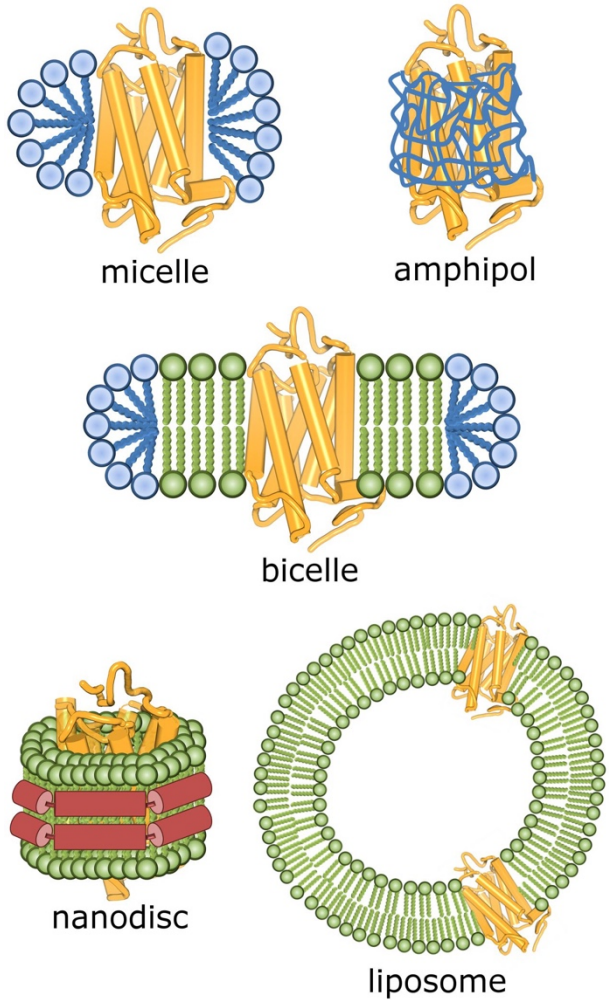

Figure 1-1. Lipid mimetics commonly used for reconstitution of membrane proteins. Detergents (micelles), mixtures of detergents and lipids (bicelles), amphipathic polymers (amphipols), and lipids (nanodiscs, liposomes) are some of the strategies that are employed to stabilize membrane proteins *in vitro*. Detergents and amphipols are represented in blue, lipids are in green, membrane scaffold protein are red cylinders. Image from Milic and Veprintsev, 2015[11].

resolution structures in cryoEM before the advent of current technology, discussed below in this introduction. Proteoliposomes have been an attractive way to study the function, and sometime structure, of proteins because one can control both the lipid environment of a purified protein and whether interacting partners are present in this *in vitro* system. Once reconstituted, the function of channels, receptors, and transporters can be assayed using the directionality of these liposomes to measure flux of ions or other indicators through the protein of interest[25].

Amphipols are polymers with a hydrophobic and a hydrophilic side that wrap themselves around the transmembrane domains (TMDs) of proteins in their chemically favored orientation[26]. A large benefit of amphipols over detergents is that samples in detergent will likely contain excess detergent that is over the critical micellar concentration, leading to contaminating detergent micelles that can disrupt crystal contacts and make cryoEM images more noisy[27]. Nanodiscs are small patches of lipid membrane that are spontaneously encircled by two copies of the amphipathic helix of membrane scaffold proteins (MSPs). This protein is a modified version of apolipoprotein-A1 and plasmids are commercially available for proteins of different helix length. Varying lengths of the MSP protein allow you to control the size of the nanodiscs you are preparing according to the surface area needed to embed your protein of interest. Some benefits of using nanodiscs are they are generally less viscous than proteoliposome preparations, they maintain stability of proteins for long periods of time, and you can choose a mixture of lipids that more closely mimics the native membrane as compared to detergents or amphipols[28–30]. Both amphipols and nanodiscs have successfully generated structures determined by cryoEM at high-resolution[31,32].

The effect of lipids on membrane protein structure and function

The choice of which lipid mimetic to use can be critical for both the observed structure and function of certain membrane proteins. Generally, proteins seem to be allowed more dynamicity in lipid bilayers than detergent micelles. Outer membrane protein X (OmpX) is a bacterial outer membrane protein that forms a β-barrel structure in the membrane. It was studied using NMR experiments to show that OmpX was folded into a β-barrel correctly in micelles, bicelles, and nanodiscs, but the transition in flexibility between the β-strands and loops that connect them is more apparent in lipids than in detergent and the relaxation rates indicate that being reconstituted in a detergent limits a protein's flexibility, which could affect both structure and function[33]. The M2 protein of the influenza A capsid is an example of how different lipids can affect the structure of a protein based off of the different thicknesses of the membrane and the head groups of the surrounding lipids. M2 assembles into a tetramer to form a proton channel to assist in viral assembly and budding. When studied in bilayers of different lipid mixtures, the arrangement of the pore region of the protein is altered. Using site-directed spin-label electron paramagnetic spectroscopy, it has been shown that M2 peptides embedded in thinner bilayers, formed by 1,2-dilauroyl-sn-glycero-3-phosphocholine (DLPC), show less spin coupling, indicating the spin labels are close to one another. The increase in spin coupling that is observed in thicker membranes made of 1-palmitoyl-2-oleoyl-sn-glycero-3-phosphocholine (POPC) indicates that the helices of the tetramer are changing their tilt with respect to one another and/or forming tighter interactions. The authors go on to refine their hypothesis from the TM helices "matching" the available hydrophobic span of the membrane to include impact of lateral pressure in the hydrophobic and hydrophilic regions. By adding in different molar percentages (mol%) of phosphatidylethanolamine (PE) to the lipid mixtures, they saw that adding up to 15 mol% showed increased spin coupling. The larger head group of PE increases lateral pressure on the M2 protein[34]. There is an abundance of PE in the membrane of influenza virions, which could indicate that the inclusion of PE in the lipid mimetic is integral to understanding the physiological organization of the M2 protein[35]. Lipids have also been shown to impact the interactions between proteins. Cytochrome P450s (CYPs) show a lower K_d for two different redox partners, cytochrome b5 (cytb5)[36] and cytochrome P450 oxidoreductase[37], in the presence of DPLC bilayers than in a

lipid free solution. In NMR experiments, chemical shifts indicating complex formation are visible for more residues in bicelles, than in micelles, than in a lipid-free mixture. This indicates that the presence of lipids facilitates the binding of cytb5 to CYP2B4 at the same interface.

Some examples of lipid effects from cryoEM studies are the structures that have been solved of TRPV1 and ryanodine receptors (RyRs). Structures have been solved of TRPV1 to near-atomic level in both amphipols and nanodiscs. The transmembrane region of TRPV1 was better resolved in the nanodisc-embedded sample, especially the side chains of amino acids that faced towards the lipid environment. At the high-resolution attained, they were able to determine specific phospholipid interactions with the protein and the double-knot toxin as well as a resolving a phosphoinositide (PI) bound in a known small molecule binding site. These findings were able to generate the hypothesis that temperature changes could cause these PIs to dissociate and gate the channel. This is an example of how understanding protein-lipid interactions can further inform the physiological functioning of membrane proteins[38,39]. For the RyR, a combination of ligands that was predicted to populate an open state captured a structure whose pore was not large enough for a hydrated calcium ion to pass through. Using ryanodine binding assays to measure the open probability of the channel in different lipid mimetics showed that the K_d of the RyR for ryanodine in detergent (CHAPS or Tween-20) is about five times higher than in a lipid membrane. There was also a decrease in K_d as more lipids were added to RyR solubilized in CHAPS. This means the lipid mimetic chosen will impact both the structure and open probability of the RyR with more lipids favoring higher open probability[40].

The resolution revolution of cryo-EM

The development of more advanced electron microscopes, detectors, and software has led to high-resolution structures being determined for previously inscrutable biological samples. Two notable areas of biology that are beginning to be impacted by cryoEM are membrane protein biology and drug discovery[174,175]. As discussed previously, the majority of drug targets are integral membrane proteins that integrate molecular information from a cell's environment and trigger downstream effects inside of cells. Membrane protein structures have been especially difficult to determine using crystallographic methods because of their relatively low expression levels, resistance to forming well-ordered crystals, and the need to keep their transmembrane helices packed in a physiologically relevant way surrounded by a lipid mimetic[174]. CryoEM is amenable for studying these proteins because proteins can be in solution until frozen and a much smaller amount of protein is needed. Lipid nanodisc technology, discussed above, has been used extensively in cryoEM[31,39,176–178]. As this technology becomes increasingly common, the effect of certain lipids on protein structure, and their functional consequences, will likely be open to study. While cryoEM is unlikely to replace crystallography in its ability to visualize small protein domains that form drug binding sites at atomic resolution, being able to see the entirety of the protein in the context of a lipid membrane is indispensable for developing allosteric modulators and understanding the underlying mechanisms of membrane protein function. Additionally, studies have concluded that proteins previously considered too small for structural determination by cryoEM, such as isocitrate dehydrogenase, lactate dehydrogenase, and glutamate dehydrogenase, can be determined to high-resolution[179]. This opens the door to studying small proteins with no symmetry that are popular drug targets. The resolution achievable in certain samples has been high enough to identify the orientation of small molecules in their binding sites[179–181] and even coordinated water molecules[182].

Historical perspective of cryoEM

In terms of hardware, the general architecture of the TEM was established in the early 1930's by Max Knoll and Ernst Ruska. This design was improved upon to increase the theoretical resolution limit by increasing the acceleration voltage, using a more consistent, brighter electron source (a field emission gun), developing more advanced lens systems to give a more coherent

electron beam, and building better vacuum systems[183]. In the early days of electron microscopy, the technique was primarily used by materials scientists. Near the midpoint of the 20th century, biologists were imaging thin sections of embedded biological tissue (**Figure 1-5A)**. There were multiple layers of difficulty to be addressed when moving to imaging purified proteins**.** Low dose methods were developed that allowed biological samples to be imaged with less radiation damage and many different techniques were developed to keep samples in a hydrated state within the vacuum column[184]. Electron crystallography was theorized early, but because only amplitudes can be calculated from diffraction patterns the phase problem that plagues crystallography still exists. DeRosier and Klug used the knowledge that refocusing the electron beam to generate 2D projections recovers this phase information and could be used to reconstruct biological samples in 3D[185]. Klug later won the 1982 Nobel Prize in Chemistry for his work on electron crystallography. The first attempts to develop the technology needed to freeze a thin layer of sample and insert it, pre-cooled, onto a cryostage were made on thin layers of crystallized catalase using the frozen hydrated method developed at Berkeley in the late 1970's (**Figure 1-5B**)[186]. Soon afterwards, Richard Henderson published electron crystallography structures at subnanometer resolution (**Figure 1-5C**)[187], Jacques Dubochet's lab developed the technology necessary for freezing samples in vitrified ice that we are still using today (**Figure 1-5D**)[188,189], and Joachim Frank published the first 3D reconstruction of a non-symmetrical particle in 1991(**Figure 1-5E**)[190]. These three men received the Nobel Prize in Chemistry in 2017 for their contributions to the field of modern electron microscopy.

Hardware advances

At this stage, electron microscopy was still referred to as "blobology" because of its limited resolution as compared to other commonly used structural biology techniques. In the past five years, the field has evolved rapidly because of advances in hardware and image processing software. In terms of hardware, resolution has been improved by the advent of the Titan Krios by Thermo Fisher and the JOEL 3200 by JOEL. Thermo Fisher introduced ConstantPower lenses that are less susceptible to thermal drift, a three lens condenser system that improves parallel sample illumination, an enclosure to dampen environmental perturbances, improved stage control, and an automated sample loader. These were all important developments, but the most important hardware that has been introduced are DEDs (**Figure 1-5F**).

DEDs were able to improve the detective quantum efficiency (DQE), which is compromised when electrons are not recorded with equal weight, and modulation transfer function (MTF)[195], which can be compromised by long range scattering internal to the detector, compared to charge coupled device detectors. This was accomplished by designing detectors that directly record electrons on a complementary metal oxide semiconductor detector with a smaller pixel size in dose-fractionation mode. These detectors are back thinned so that electrons that are back-scattered from the second silicon detector layer, which would normally contribute to noise in the micrograph, are minimized[196,197]. This increases the detector's DQE, but there is still room for improvement[198] (**Figure 1-6**). Dose-fractionation mode is also integral to improving attainable resolution. EM micrographs are lower contrast than hypothesized theoretically for multiple reasons, but one of them is there is inherent beam-induced motion. This motion originates from both a build-up of positive charge over time and radiolysis of the sample and the vitreous ice over time as the grid is exposed to the high energy electron beam[199,200]. It has been tracked using images of large virus particles that can be seen translating and rotating as exposure time increases[201]. Micrographs are recorded in this "movie-mode" where short frames are saved in a stack over a long exposure time. These frames can be aligned and motion-corrected in order to remove beam-induced motion to occurs over the course of collection. The movies can be dose-weighted so that the frames with the most information and the least radiation damage will be weighted more in the final averaged image. All of these features allow us to use higher electron

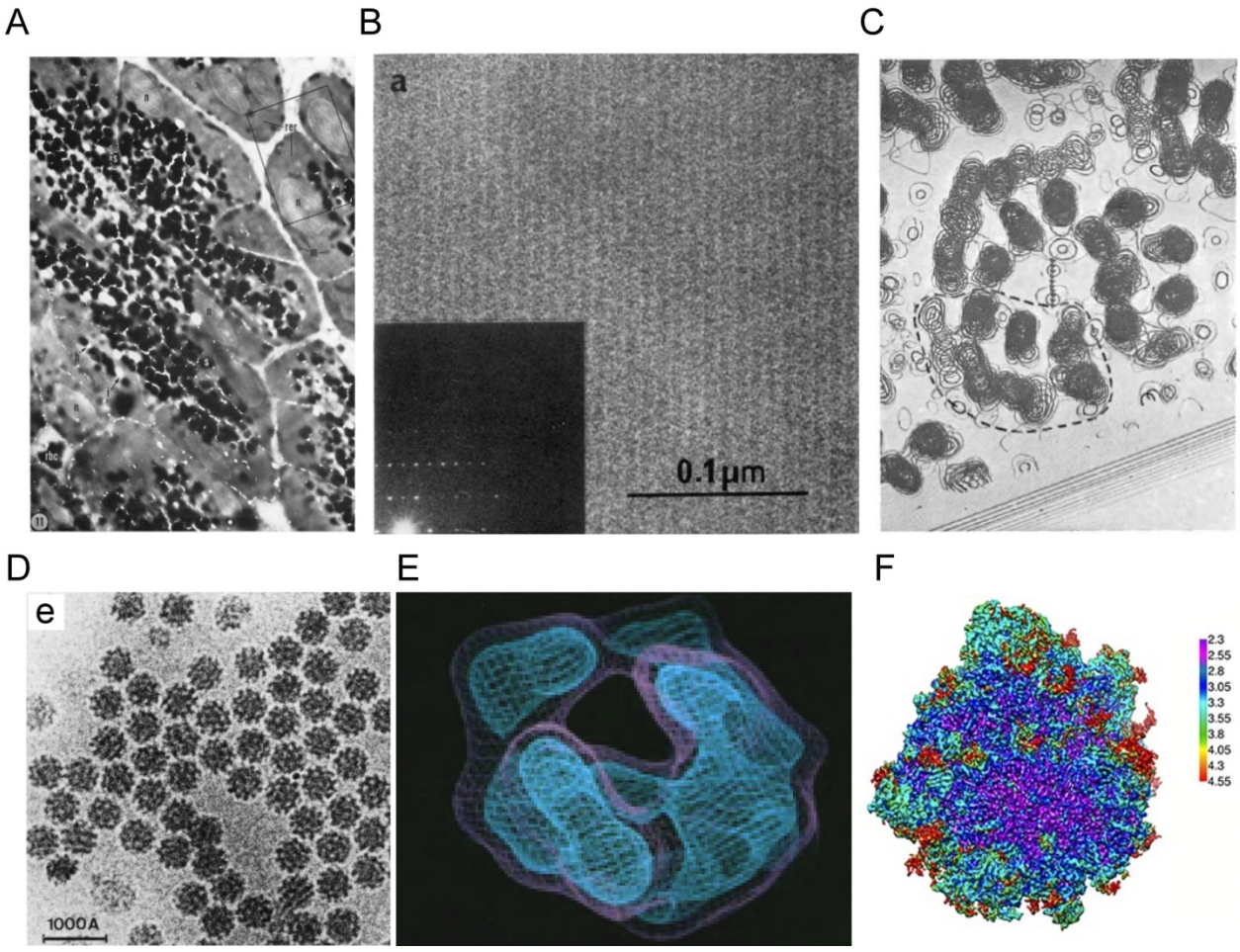

Figure 1-5. The evolution of samples imaged using cryoEM.
A. The first biological samples that were imaged using electron microscopy were thin sections of embedded tissue. **B.** Thin layers of catalase crystals were the next structures that were studied in a frozen hydrated state. **C.** Electron crystallography and **(D)** plunge-frozen samples were then used to determine protein structures, with the ability to reconstruct **(E)** particles that lack symmetry becoming possible in the early 1990's. **F.** The advent of DEDs and new image processing software have pushed the achievable resolution of cryoEM higher and higher. Images from Christensen, 1971[191]; Taylor, 1978[192]; Unwin and Henderson, 1975[6]; Adrian, et. al. 1984[193]; Frank, et. al. 1991[190]; Liu, et. al. 2017[194] from A to F.

dose and in turn increase the signal to noise ratio (SNR) in raw micrographs without the image blurring[202,203]. These alignment scripts will either align the entire image, smaller subsections of the image, or individual particles that have already been windowed[204].

Innovation in software and image processing

While DEDs are considered to be the advance that contributed the most to the resolution revolution, new image processing software packages have also contributed heavily. Possibly more important than their ability to increase resolution in final reconstructions, new image processing suites such as RELION[205], cisTEM[206], and cryoSPARC[207] have made it possible to sort out different complexes[208] and, in special cases, conformations[209] of proteins using new algorithms for 3D reconstruction and classification. In cryoEM samples, different projection images of the three dimensional particles are windowed out of the raw images and views that are similar are grouped and averaged into a 2D class average with higher SNR. These class averages can be generated in multiple ways, but the most successful technique seems to be using a maximum likelihood approach to classification[210,211]. The introduction of Bayesian statistics, by Scheres in 2010, to determine the most likely outcome based on prior knowledge and the available data marked a huge step forward in cryoEM data processing[205]. This allows the input parameters to be refined based on further analysis of the data. Implementation of the "gold-standard" Fourier shell correlation (FSC) determination, where data is separated into two independent halves to determine resolution, was employed to prevent overfitting that may occur in this approach. The inclusion of these statistics based-evaluation and tuning algorithms, along with the development of automatic image acquisition software[212], which is able to generate much larger input datasets, has increased the computation load associated with EM data analysis. Access to large computing clusters and data storage became necessary when these changes were implemented. GPU-based image processing software has increased the speed of analysis and decreased the computational demand of some programs[213], but these high quality GPU cards can also be economically prohibitive. Newer programs, namely cryoSPARC, have included stochastic gradient descent and branch-and-bound maximum likelihood optimization algorithms that are able to decrease computation load even further[207].

Importance of sample selection and preparation

While more flexible than other structural techniques, a biochemically-pure, well-packed, rigid protein above 500 kDa is still the ideal sample to image. Currently, even with recent advances, cryoEM can only determine atomic resolution structures for samples that are relatively ordered, stable, and homogenous. When individual particles are grouped and classified in 2D, flexible portions of the particle can be averaged out in a haze of density. These portions of the particle can be masked out in an attempt to increase resolution of the more rigid core, or the single class can be subclassified in an attempt to tease apart the different conformations present. Both of these techniques have advantages and disadvantages that need to be weighed against your final goal. While the particles are theoretically trapped in a native, hydrated state in the thin layer of vitrified ice, the stability of these proteins can be disrupted in multiple ways aside from damage during initial purification. The problem of proteins diffusing to and contacting the air-water interface in the time between botting of excess solvent and plunge-freezing has been well documented[184]. This is being addressed in variety of ways including decreasing the amount of time before plunging, implementing new self-wicking grids, and using carbon or graphene oxide (GO) support films[214–217]. The ability of programs to sort out different states and complexes of biological samples has allowed some *in silico* purification that would be nearly impossible and much more artificial to sort out biochemically[208], but large amounts of heterogeneity can still limit final resolution. The general abundance of a certain "type" of a particle also needs to be taken into account when determining how large of an initial data set needs to be collected.

In the work presented here, we used a Polara F30 and Titan Krios microscope that were

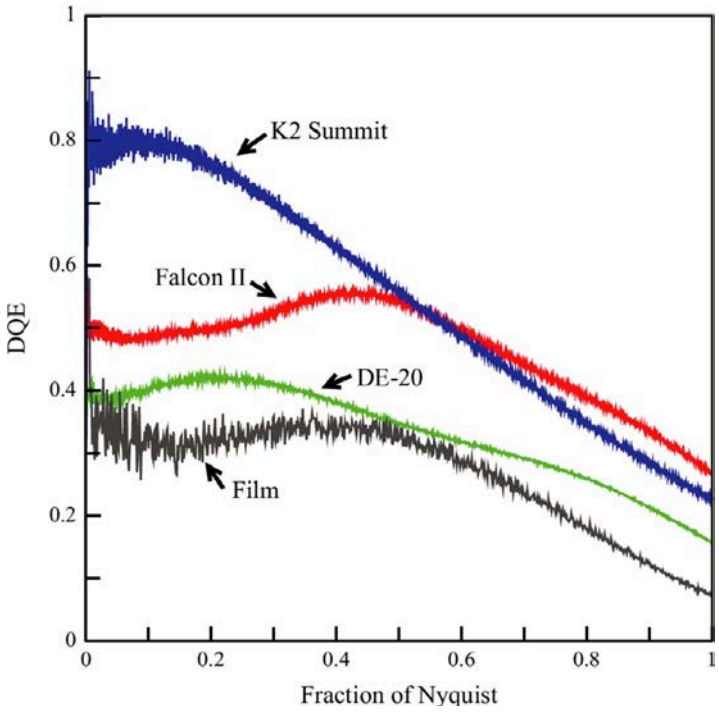

Figure 1-6. Improved detective quantum efficiency on direct electron detectors.
Three direct electron detectors were tested for their detective quantum efficiency in comparison to film. They perform much better at low resolution and continue to perform better even at the limit of resolution known as the Nyquist limit. Charge couple device detectors have better DQE at low resolution, but film had the higher DQE closer to the Nyquist limit. The detectors used in this thesis are all K2 Summit detectors. Image from McMullan, et al., 2014[198].

both outfitted with a K2 Summit direct electron detector. This equipment, along with improved image processing software, and good sample preparations allowed us to reach resolutions high enough to build atomic models, propose mechanisms of gating modulation, and visualize binding of annular lipids and permeant ions.

CryoEM structures presented in this dissertation

In this dissertation, we report a cryoEM structure of the TRPC6 CPD at an overall resolution of 3.8Å with its atomic model that was built *de novo*. This structure allowed us to map human disease mutations in three dimensional space and determine two mutational hotspots in the CPD. These sites surround points of contact between the N-terminal and C-terminal regions that are likely integral to allosteric channel gating modulation. We were able to resolve a domain swap that occurs at the intersection of horizontal and vertical helices in the C-terminus of TRPC6. This fold is also conserved in full-length and CPD structures of TRPC3.

Combining structural and functional approaches, our data show that the TRPC3 CPD is a stable module involved in allosteric gating. We present a 5.8Å structure of full-length TRPC3 in GDN detergent as well as a 4.0Å structure of the CPD in the same amphipol reconstitution as TRPC6. Functional characterization of mutants demonstrates that TRPC3 activity increases by shortening the loop connecting the TRP and horizontal helices; conversely elongating the loop has the opposite effect. These results support the C-terminal loop fine tuning the allosteric coupling between the cytoplasmic and transmembrane domains.

We were also able to obtain a structure of the IP_3R-3 receptor that allowed us to visualize annular lipids and permeant ions. IP_3Rs are ligand-gated Ca^{2+} release channels localized predominantly in the ER membrane of all cell types[218]. IP_3 generated by PLC upon G protein- or tyrosine kinase-coupled receptor activation binds to IP_3Rs and opens the channel leading to transfer of Ca^{2+} from the ER lumen to the cytoplasm[218]. Ca^{2+} released by IP_3Rs act as a universal messenger required to regulate diverse physiological processes including fertilization, muscle contraction, apoptosis, secretion, and synaptic plasticity[219,220]. Deregulation of the IP_3R results in pathological changes in Ca^{2+} signaling, leading to a broad spectrum of diseases including neurodegenerative, autoimmune, and metabolic diseases, as well as cancer[221]. Published structures in the unliganded (apo) and liganded states[222–231] provide a basis to develop mechanistic hypotheses on the channel gating. However, our structure visualizes a novel lipid density and allows us to model in previously uncharacterized parts of the protein.

Aims of dissertation

The aims of this Dissertation are separated into three parts:

Part 1: is to (a) determine a process for reconstitution of AMPARs into lipid nanodiscs and study their structure using electron microscopy and (b) develop a cell-based high-throughput assay to identify small molecule compounds that differentially modulate AMPA-AS complexes. I hypothesize that reconstituting receptors into a lipid environment will increase their inherent flexibility to better mimic their function *in vivo* and that this HTS screen will be useful for identifying lead compounds for further functional characterization and chemical optimization. This nanodisc preparation and HTS screen will allow us to identify and study AMPAR-AS specific compounds both structurally and functionally, teasing apart distinct sites of AMPAR action in the CNS.

Part 2: is to (a) determine a cryoEM structure of TRPC6 to determine where FSGS mutations are located in three dimensional space and (b) determine a cryoEM structure of TRPC3 and interrogate modulation of gating by the cytoplasmic domain. I postulate that cryoEM structures of homologous TRPC ion channels will allow building of *de novo* ion channel structures that indicate extensive interactions between their N- and C-termini form a cytoplasmic domain that influences channel gating. Knowledge of how to fine tune the opening and closing of TRPC channels will

lead to a better understand of their role in the slow component of the EPSC, especially in the Purkinje cell.

Part 3: is to determine a cryoEM structure of the type 3 IP_3R. I propose that solving a structure for the IP_3R in an unliganded state to high resolution will lead to a more thorough understanding of molecules associated with this channel, including lipids, permeant ions, and its interaction partner TRPC3.

CHAPTER II: MATERIALS AND METHODS

DNA constructs

The rat GluA2flip splice variant was used for all protein expression and high throughput screening experiments. A GluA2(Q) unedited DNA construct was cloned into pTREt-V_a. A FLAG tag was introduced before the C-terminus of the protein leaving the anti-GluA2 C-terminal epitope intact. pTREt-V_a was used to express this construct in HEK293 cells to create a parent cell line. The same procedure was used to create a GluA2(R) edited DNA construct in pTREt-V_a that doxycycline (DOX)-dependently expresses the protein. A 1D4-tag was added at the extreme C-terminus of mouse CNIH3 cDNA (Open Biosystems) separated from the protein with a NotI restriction site. CNIH3-1D4 was cloned into pTREt-V_b for expression and cloned into pTREt-V_a containing GluA2(Q)-FLAG for dual expression[232]. The same procedure was used to create rat GSG1L cDNA[233] with a C-terminal 1D4-tag separated from the protein with a NotI restriction site. Constitutively-expressed auxiliary subunits (stg and CNIH3) were cloned into a pBOSS-stg/CNIH3-IRES-mCherry plasmid and expressed in cells with DOX-dependent GluA2(R) expression in pTREt-V_a. Cell lines created can be found in **Table 2-1**.

A DNA construct containing 8xHis-maltose binding protein (MBP)-N-terminus truncated murine TRPC6 (94 amino acids) and putative glycosylation sites mutated (N472Q and N560Q)[234] was cloned into the pFastbac1 expression vector for protein expression. A DNA construct containing 8xHis-MBP-hTRPC3b with a conserved single-point mutation I395V was cloned into the pFastbac1 expression vector for protein expression. Recombinant baculovirus was obtained following the manufacturer's protocol (Bac-to-Bac expression system; Invitrogen). TRPC3 and WT and ΔTRPC6 constructs were cloned in pMO (a pcDNA3 modified vector) for transfection into HEK cells for recordings.

The gene encoding hIP_3R-3 (Accession: BC172406) was purchased from Dharmacon[235], subcloned (residues 5-2671) with C-terminal OneStrep tag into pFL vector, and incorporated into baculovirus using the Multibac expression system[236]. The gene encoding the hIP_3R-3 LBC (Met-4 to Asn-602) was subcloned into pAceBac1 vector with an N-terminal OneStrep tag followed by a TEV protease cleavage site and incorporated into baculovirus using the Multibac expression system[236].

Generating stable cell lines

The parental cell line for all stable cell lines was TetON human embryonic kidney 293 (HEK293) cells. To generate cell lines with DOX-inducible expression, 7.3 µg of the pTREt vector was co-transfected with 0.2 µg of a plasmid expressing a hygromycin resistance gene into TetON HEK293 cells using the calcium-phosphate method. Clones were selected by diluting the transfected cells at 1:40, 1:80, and 1:160 and growing for two weeks in selection media. The cell lines and their selection media are compiled in **Table 2-1**. Colonies that survived selection were plated and grown up. The cells were split and a portion of each were cultured in 12-well plates and induced with DOX for 24-hrs. Expression of the target protein was examined by Western blotting and immunocytochemistry using the antibodies in **Table 2-1** to asses protein expression. The GluA2flip(R) cell lines used in the high throughput screening cell assays constitutively express their auxiliary subunits. These cell lines were generated by transfecting DOX-inducible GluA2flip(R) cells with pBOSS-stg-IRES-mCherry or pBOSS-CNIH3-IRES-mCherry selecting for cells expressing these proteins using zeocin. See **Table 2-1** for details on plasmids, selection media, and antibodies used to verify protein expression.

Cell line	Parent cell	Plasmid	Selection Media	Antibodies	Used for:
TetON	HEK293		150 µg/ml G418	n/a	HTS
GluA2(R)	TetON	pTREt-Va	120 µg/ml hyg, 150 µg/ml G418	α-GluA2CT polyclonal antibody, HRP conjugated α-rabbit IgG (GE Healthcare, Cat#NA934V)	HTS
GluA2(R) stg	TetON	pTREt-Va and pBOSS	120 µg/ml hyg, 150 µg/ml G418, 100 µg/ml zeocin, 1 mM KA + 30 µM NBQX	α-GluA2CT and α-rabbit IgG	HTS
GluA2(R) CNIH3	TetON	pTREt-Va and pBOSS	120 µg/ml hyg, 150 µg/ml G418, 100 µg/ml zeocin, 1 mM KA + 30 µM NBQX	α-GluA2CT and α-rabbit IgG	HTS
GluA2(Q)	TetON	pTREt-Va	120 µg/ml hygromycin, 150 µg/ml G418	α-GluA2CT and α-rabbit IgG	HTS
GluA2(Q) stg	TetON	pTREt-Va dual expression	120 µg/ml hyg, 150 µg/ml G418, 1 mM KA + 30 µM NBQX	α-GluA2CT and α-rabbit IgG pan-TARP monoclonal antibody[86], HRP conjugated α-rabbit IgG	HTS
GluA2(Q) CNIH3	TetON	pTREt-Va dual expression	120 µg/ml hyg, 150 µg/ml G418, 1 mM KA + 30 µM NBQX	α-GluA2CT and α-rabbit IgG α-1D4 monoclonal antibody, HRP conjugated α-mouse IgG (GE Healthcare, Cat#NXA931)	HTS
GluA2(Q) GSG1L	TetON	pTREt-Va dual expression	120 µg/ml hyg, 150 µg/ml G418, 1 mM KA + 30 µM NBQX	α-GluA2CT and α-rabbit IgG α-1D4 and α-mouse IgG	HTS
GluA2(R)-FLAG	TetON	pTREt-Va	120 µg/ml hygromycin, 150 µg/ml G418	α-GluA2CT and α-rabbit IgG	EM

Table 2-1. Stable HEK293 cell lines and their selection media

These cells lines stably express the proteins indicated above. Selection media was used to isolate stable cell lines and as growth media. The antibodies were used in western blotting to assess protein expression in whole cell lysate. Stg and CNIH3 expressed in pBOSS vector expression was assessed through expression of mCherry. Hygromycin – hyg, G418 – neomycin, KA – kynurenic acid, stargazin – stg, CNIH3 – C3, HTS – high throughput screening.

Purification of TEV protease

TEV-S219V plasmid was expressed in BL21(DE3)CodonPlus-RIL strain *E. coli* in Terrific broth (TB) with ampicillin and chloramphenicol under IPTG induction and cells were pelleted at 3500 rpm for 115 min. An ion exchange MonoS column (GE Healthcare) was washed extensively with high salt buffer (20 mM sodium phosphate (NaPhos) pH7.0, 1 M NaCl, 10% glycerol) and equilibrated with low salt buffer (20 mM NaPhos pH7.0, 20 mM NaCl, 10% glycerol). 15 mL of cells were lysed in 75 mL resuspension buffer (40 mM NaPhos pH8, 400 mM NaCl, 20 mM imidazole, 5 mM β-mercaptoethanol) with sonication. Cell debris was pelleted at 50k rpm for 1 hr and lysate was run over 3 mL of Ni-NTA beads. Beads were washed with 15CV of resuspension buffer, 8CV wash buffer (resuspension buffer with 40 mM imidazole), and eluted with 7CV elution buffer (10 mM NaPhos pH 7.0, 40 mM NaCl, 300 mM imidazole, 10% glycerol). Elutions with highest protein concentration were diluted by two-fold with low salt buffer and injected 5 mL at a time onto the MonoS column on an FPLC. MonoS column was run for 20CV at 1 mL/min across a linear gradient to high salt buffer. Fractions with protein were pooled and a Bradford assay is run to determine protein concentration. 80% glycerol is added to 50% final concentration(1:1.3), and frozen in 1mL aliquots in liquid nitrogen to be stored at -80º. (Detailed protocol in **Appendix 1-1**)

Purification and cleavage of membrane scaffold protein (MSP2N2)

MSP2N2 plasmid was expressed in BL21 Rosetta *E. coli* in TB with kanamycin and chloramphenicol under IPTG induction. Cells were pelleted at 3500rpm for 15 min. 25 mL cells were resuspended in 60 mL 100 mM NaPhos pH7.6, 1 mM PMSF and lysed by sonication. 1% Triton-X was added and a second round of sonication was performed. Lysate was centrifuged at 20k rpm for 45 min and run over 9 mL Ni-NTA beads. Beads are washed with 225 mL buffer 1 (40 mM Tris pH8.0, 0.3 M NaCl, 1% Triton-X), 130 mL buffer 2 (40 mM Tris pH8.0, 0.3 M NaCl, 50 mM sodium cholate, 20 mM imidazole), 125 mL buffer 3 (40 mM Tris pH8.0, 0.3 M NaCl, 50 mM imidazole), and eluted in six 6 mL fractions with 40 mM Tris pH8.0, 0.3 M NaCl, 500 mM imidazole. The most concentrated elutions are dialyzed against 20 mM Tris pH7.4, 100 mM NaCl. Protein concentration is determined roughly with Bradford assay and cleaved with TEV protease in a 1:3 molar ratio diluted 2.5x in 20 mM NaPhos pH7.0, 50 mM NaCl, 1 mM DTT overnight at room temperature. The proteins are dialyzed against 20 mM Tris pH7.4, 100 mM NaCl. Imidazole is added to 40 mM and the sample is bound with 5 mL Ni-NTA for 1 hr at 4º. The flow-through is collected, 0.01% DDM is added, and dialyzed against 20 mM Tris pH7.4, 100 mM NaCl, 0.01% DDM, 0.25 mM EDTA. Protein is concentrated to ~3 mg/mL, aliquoted, frozen in liquid nitrogen, and stored at -80º. (Detailed protocol in **Appendix 1-2**)

Purification and reconstitution of GluA2 into MSP2N2 nanodiscs

Cell pellet was obtained from suspension culture of HEK cells expressing DOX-inducible GluA2-FLAG. Approximately 50 mL of cell pellet was resuspended in eight-volumes equivalent of solubilization buffer (20 mM HEPES pH7.4, 150 mM NaCl, 30 μM NBQX, 0.25% DDM), 0.1 mg/mL POPC, and protease inhibitors) and stirred at 4°C for 3 hours. Cell lysate was spun at 3500 rpm for 10 minutes followed by 45k rpm for 1 hr at 4°C. The supernatant was run over 3 mL FLAGM2 agarose beads (Sigma) and washed with wash buffer (0.1% DDM, 20 mM HEPES pH7.4, 150 mM NaCl, 30 μM NBQX). Complexes were eluted with 0.5 μg/ml FLAG peptide in wash buffer and concentrated to ~700 μL. The GluA2 tetramers were combined with POPC, or POPC and polar brain lipid extract (Avanti) in a 1:1 ratio, and MSP2N2 in a ratio determined for each batch of lipids dissolved and MSP purified (1:68,MSP:POPC; 1:75,MSP:brain lipid) and brought to 1.5 mL total volume with wash buffer. A negative control was set up with no MSP. The reaction was incubated on ice for 45 min, then 1.5g of biobeads were added and incubated on ice overnight. An additional 1 g of biobeads was added 24 hours after initial mixing and incubated on ice for an additional 24 hours. Reconstituted complexes were run over a PD-10 desalting column (GE

Healthcare) and eluted in gel filtration buffer (20 mM HEPES pH7.4, 150 mM NaCl). Nanodisc embedded receptors were run over a Superose 6 Increase column (GE Healthcare) with gel filtration buffer. Negative stain electron microscopy was performed to assess the homogeneity and purity of the final sample and sample was used without dilution on GO-coated cryoEM grids (see methods below). (Detailed protocol in **Appendix 1-3**)

Vanderbilt Discovery Library (VDL)

The Vanderbilt Discovery Collection is a library of 100,000 compounds that have been curated by the Vanderbilt Institute of Chemical Biology's High Throughput Screening facility for screening in biological systems to maximize lead potential and diversity (http://www.vanderbilt.edu/hts/services.html).

Voltage-sensitive dye (VSD) screening assay

Compound solutions were prepared as fresh aliquots by transferring 150 nl of selected compounds from VDL plates into Greiner 384-pp round-bottom plates using an Echo 555 (Labcyte) and diluted in 30 µl 1X FLIPR Blue VSD dye (Molecular Devices, cat #R8034) to 50 µM using a Combi liquid dispenser (Thermo). Greiner 384-pp round-bottom plates containing glutamate for the second add were dispensed by hand using a multi-channel pipet at 5X final concentration. A2R-stg cells were plated in 384-well BD PureCoat amine-coated plates (Corning Life Sciences) at 16k cells/well in DMEM medium supplemented with 10% heat-inactivated FBS and 100U/mL penicillin-streptomycin (PenStrep) antibiotic. NBQX, sodium butyrate, and DOX were added to the cells at 30 µM, 1 mM, and 8 µg/ml, respectively. Cells were incubated overnight (O/N) and washed 4 times in Hank's balanced salt solution (HBSS) containing 20 mM HEPES pH7.4, on an ELX405CW liquid aspirator and dispenser (BioTek). Buffer was left in the wells and an equal amount of 2X FLIPR dye solution was added and incubated on the cells at room temperature for 45 min. Fluorescence signal was collected at 1 Hz using Ex. 480±20 nm/Em. 540±40 nm on a Hamamatsu Functional Drug Screening System 6000 (FDSS). Baseline signal was collected for 10 seconds followed by addition of 10 µl of 5X compound for a final concentration of 10 µM. After 290 seconds, 12 µl of a 5X glutamate solution was added resulting in a concentration approximately 50% of the maximally effective glutamate concentration (EC_{50}).

Hits were selected from this initial screen using 4 different criteria, which we termed CMPDslope, CMPDmaxmin, GLUslope, and GLUmaxmin. CMPDslope was measured in a 10 sec window following the initial compound addition and CMPDmaxmin is the difference in the maximal and minimal fluorescence values found in the 100 sec window following compound addition. GLUslope is the fitted slope of the increase in fluorescence within 10 sec after adding glutamate. GLUmaxmin is the difference in the minimum and maximum value in fluorescence signal reached in the 100 sec window after adding glutamate. Compounds were classified as hits if they differed by 3 standard deviations of the mean for each criterion. Tier 1 hits were classified as those that hit in the GLUslope, GLUmaxmin, and CMPDmaxmin windows. Tier 2 hits were classified as compounds that hit in the GLUslope window and either the GLUmaxmin or CMPDmaxmin window. Tier 3 hits were classified as those that hit in only the GLUslope or the GLUmaxmin window. Tier 4 hits were classified as compounds that hit only in the CMPD window, CMPDslope or CMPDmaxmin. Hit selection was further narrowed using the criterion that their signal must return to near baseline values before entering the glutamate add window.

VSD concentration response curve (CRC) assay

This assay was carried out in the same way as the VSD screening assay except a 10-point concentration curve, from 40 µM to 10 nM, was plated in triplicate for each compound on a single 384-well plate. Data were summarized by plotting them as %max GLUslope against log [compound] that was fit to a four-parameter logistical model. %max GLUslope is defined as a normalized GLUslope expressed as a percentage of the mean maximum GLUslope, defined as

100, where background mean vehicle control (VHLslope) were subtracted from both values on a per plate basis. Thus, %max GLU slope = (GLUslope-mean VHLslope/mean maxGLUslope-mean VHLslope).

Calcium flux screening assays

Glutamate potency fold-shift assay

30 µM of each compound was pre-incubated with the cells for 120 secs and then an 11-point glutamate CRC from 4 mM to 10 pM was applied to the cells for 180 sec. 250 nl of selected compounds were plated from the reordered compound plates into Greiner 384-PP round-bottom plates using an Echo 555 (Labcyte) and diluted in 40 µl low calcium buffer (10 mM HEPES, pH 7.4, 140 mM NaCl, 5 mM KCl, 1 mM $MgCl_2$, 0.5 mM $CaCl_2$, and 10 mM glucose) to 2X final concentration using a Combi (Thermo). Greiner 384-pp round-bottom plates containing glutamate solutions were dispensed by hand using a multi-channel pipet at 5X final concentration. Cells were plated in 384-well BD PureCoat amine-coated plates (Greiner) at 10k cells/well in DMEM medium supplemented with 10% heat-inactivated FBS, 100U/mL PenStrep antibiotic, and 30 µM NBQX 40 hours before screening. Sodium butyrate and DOX were added to the cells at 1 mM and 5 µg/mL, respectively, 24 hours before screening. A2Q-stg cells were induced with 10 µg/mL DOX. Cells were incubated O/N and washed 4 times in low calcium buffer on an ELX405CW liquid aspirator and dispenser (BioTek). Buffer was left in the wells and an equal amount of 4.6 µM (2X) Fluo-8 (AAT Bioquest cat #21080) solution with 2.5 mM probenecid was added and incubated on the cells at room temperature for 40 minutes. Probenecid was added to block dye efflux from the cells[237]. Dye was washed off with low calcium buffer using the ELX405CW (BioTek) and plates were immediately inserted into the FDSS (Hamamatsu). Fluorescence signal was collected at 1 Hz using Ex. 480±20 nm/Em. 540±40 nm. Baseline signal was collected for 10 seconds followed by addition of 20 µl of 2X compound for a final concentration of 30 µM. After 290 seconds, 10 µl of a 5X glutamate solution in high calcium buffer (10 mM HEPES, pH 7.4, 140 mM NaCl, 5 mM KCl, 1 mM $MgCl_2$, 9 mM $CaCl_2$, and 10 mM glucose) was added for 180 seconds.

Calcium flux concentration response curves

The same FDDS addition protocol as above was used for a compound concentration range of 30 µM to 30 nM. These compound CRCs were applied to the cells 2 minutes before a 1mM glutamate stimulation. Additional replicate plates of compound followed by EC_{50} of glutamate were evaluated, both controlled with CTZ curves. Normalized FDSS traces were curve fit to CRCs using the initial GLUslope (GLUslope1) in a 3-6 sec window after glutamate application. CRCs were also plotted for the traces' area under the curve (AUC) in the GLUmaxmin window. Full CTZ and NBQX curves were used as reproducibility controls on each plate. Compounds were plotted as %max GLUslope against log [compound] and fit to a four-parameter logistical model as in the VSD.

Outside out patch recording with fast glutamate application

A2R-stg cells were plated on HNO_3 washed coverslips coated with 1:20000 poly-d-lysine (incubated for 20 min, washed with PBS 2x and media (DMEM supplemented with 10% FBS, 100U/mL PenStrep, geneticin (G418), zeocin, NBQX, and KA) for 2 hours. Cells were induced with 5 µg/mL DOX for 24 hours before recording. A2R cells were plated on 1:60000 poly-d-lysine for 2 hours and induced with 7.5 µg/mL DOX for 30 hours before recording. The cells were lifted from the coverslip after whole cell configuration was achieved and brought in front of the theta tubing. Ligand (1mM glutamate) was applied to the cells via theta tubing glass capillary mounted on a piezo actuator (P-830.30, Physik Instrumente) controlled by an LVPZT amplifier (E-505, Physik Instrumente), DAQ device (NI USB-6221, National Instruments), and LabView software (National Instruments). Recording was done using a single channel of a Multiclamp700B Amplifier (Axon Instruments) operated by pClamp10 software. Signals were digitized using Digidata1440A

(Axon Instruments) at a sampling rate of 50 kHz and low pass filtered at 2kHz. Borosilicate glass capillaries (O.D. 1.5 mm, I.D. 0.86 mm, Sutter) were pulled to manufacture electrodes with pipette resistances of 3.5-5 MΩ.

Internal solution was (in mM) 110 NaCl, 10 NaF, 5 EGTA, 0.5 $CaCl_2$, 1 $MgCl_2$, 10 Na_2ATP, 5 HEPES, adjusted to pH 7.3 with CsOH and 295 mOsm. External solution was (in mM) 145 NaCl, 2.5 KCl, 1.8 $CaCl_2$, 1 $MgCl_2$, 5 HEPES, 10 glucose, adjusted to pH 7.3 with NaOH and 301 mOsm. Standard solution without ligand was the external solution. The ligand solution contained 1mM glutamate in external solution, supplemented with 2mM glucose and 3mM NaCl to facilitate visualizing the interface of the two solutions and recording liquid junction potential after breaking the patch. The 10-90% rise time of liquid junction potential was around 300μs. VU0627849 was dissolved in external solution containing 1 mM glutamate to a final concentration of 40 μM. Tips of the tubing for each solution were positioned immediately before the opening of one compartment of the theta tubing. Drug-containing and drug-free glutamate solutions were switched using a manual valve located between the solution reservoir and theta glass tube. Solution speed was adjusted by the height of the reservoir using gravity.

Cell culture and whole cell electrophysiology

HEK293 cells were cultured in DMEM (Invitrogen), supplemented with 10% FBS and 1% PenStrep at 37°C and 5% CO_2. Transfections were performed in 6-well plates using Lipofectamin® 2000(Invitrogen) with Opti-MEM I reduced serum medium (Invitrogen). TRPC3 constructs cloned in pMO (a pcDNA3 modified vector) were used for transfection. WT TRPC6 and ΔTRPC6 cloned in pMO were used for transfection. For whole-cell recordings in HEK293 cells, the extracellular solution contained (in mM) 140 NaCl, 2.8 KCl, 1 $MgCl_2$, 2 $CaCl_2$, and 2 HEPES (pH 7.4). The pipette solution contained (in mM) 140 CsCl, 5 EGTA, and 10 HEPES (pH 7.2). Currents were recorded with an Axoclamp 200A amplifier (Molecular Devices) using a 1s ramp from -80 mV to 80 mV (for TRPC6) or -100 mV to 100 mV (for TRPC3). Pipettes were made of glass capillaries (Sutter Instruments) and fire-polished before use until a resistance between 2.8-4 MΩ was reached. Data was acquired with a sampling rate of 20 KHz and low-passed filtered (4 KHz) and analyzed off-line using Clampfit v10.4.2.0 (Molecular Devices). TRPC6 channel agonist OAG (Avanti Polar Lipids) in chloroform was dried under a gentle stream of N_2, dissolved in DMSO, sonicated for 20 min, and freshly dissolved in bath solution to the indicated concentration. TRPC3 channel agonist GSK-1702934A (GSK-170) and the antagonist GSK-417651A (GSK-417) from Focus Biomolecules were dissolved in DMSO and freshly dissolved in bath solution to the indicated concentration.

Mus musculus TRPC6 expression and purification (NP_038866.2)

Sf9 cells were infected with recombinant truncated TRPC6 baculovirus and harvested by centrifugation 72 hr after infection. Cell pellet from 0.8 L of culture was resuspended and lysed with a high-pressure homogenizer (Avestin) in a hypotonic buffer (36.5 mM sucrose, 50 mM Tris, 4 mM TCEP; pH 8) and supplemented with protease inhibitors (1 mM PMSF, 3 mg/ml aprotinin, 3 mg/ml leupeptin, and 1 mg/ml pepstatin). Cell debris was collected by low-speed centrifugation (8,000 *g* for 15 min). Membranes were collected by ultracentrifugation (100,000 *g* for 30 min at 4 °C) and solubilized in Buffer A (150 mM NaCl, 4 mM TCEP, 10 % Glycerol, 50 mM HEPES; pH 7.4) supplemented with protease inhibitors. Protein was extracted with 20 mM DDM (Anatrace) with gentle stirring for 2 h. The detergent-insoluble material was removed by centrifugation (150,000 *g* for 45 min), and the supernatant was incubated with amylose resin (New England Biolabs) with gentle stirring for 3 h. After loading onto the column and collecting the flow-through, the resin was washed with 10 column volumes of Buffer B (150 mM NaCl, 4 mM TCEP, 10 % Glycerol, 1 mM DDM, 50 mM HEPES; pH 7.4). Afterward, the protein was eluted with Buffer B supplemented with 20 mM maltose. The eluted protein was then mixed with PMAL-8 (Anatrace) at 1:3 (w/w) with gentle agitation for 2h at 4°C. Then, protein was digested with ProTEV Plus

protease (Promega) at 4°C overnight to remove the MBP tag. Cleaved protein was further purified by size exclusion chromatography on a Superose 6 10/300 GL column (GE Healthcare) pre-equilibrated with Buffer C (150 mM NaCl, 4 mM TCEP, 20 mM HEPES; pH 7.4). Peak fractions corresponding to the tetrameric channel were collected and concentrated to ~0.3 mg/ml for cryo-electron microscopy analysis.

Expression and purification of human TRPC3 (NP_003296.1)

Sf9 cells were infected with recombinant TRPC3 baculovirus and harvested by centrifugation 72 hr after infection. The cell pellet from 0.8 L of culture was resuspended and lysed with a high-pressure homogenizer (Avestin) in a hypotonic buffer (36.5 mM sucrose, 50 mM Tris, 4 mM TCEP; pH 8) and supplemented with protease inhibitors (1 mM PMSF, 3 mg/ml aprotinin, 3 mg/ml leupeptin, 1 mg/ml pepstatin). Cell debris was collected by low-speed centrifugation (8,000 g for 15 min at 4°C). Membranes were collected by ultracentrifugation (100,000 g for 30 min at 4°C). *For TRPC3 in GDN*: Membranes were solubilized in Buffer A1 (300 mM NaCl, 4 mM TCEP, 50 mM Tris; pH 8) supplemented with protease inhibitors. Protein was extracted with 1% digitonin (Millipore) with gentle stirring for 2 hr. The detergent-insoluble material was removed by centrifugation (150,000 g for 45 min at 4°C), and the supernatant was incubated with amylose resin (New England Biolabs) with gentle stirring for 3 hr. After loading onto the column and collecting the flow-through, the resin was washed with 10 column volumes of Buffer B1 (300 mM NaCl, 4 mM TCEP, 0.1% digitonin, 50 mM Tris; pH 8). Afterward, the protein was eluted with Buffer B1 supplemented with 20 mM maltose. The protein then was digested with ProTEV Plus protease (Promega) at 4°C overnight to remove the MBP tag. Cleaved protein was further purified by size exclusion chromatography on a Superose 6 10/300 GL column (GE Healthcare) pre-equilibrated with Buffer C1 (200 mM NaCl, 4 mM TCEP, 40 µM GDN, 50 mM Tris; pH 8). Peak fractions corresponding to the tetrameric channel were collected and concentrated to ~1.2 mg/ml for cryo-EM analysis. *For TRPC3 in PMAL-C8:* Membranes were solubilized in Buffer A2 (150 mM NaCl, 4 mM TCEP, 10% glycerol, 50 mM HEPES; pH 7.4) supplemented with protease inhibitors. Protein was extracted with 26 mM DDM (Anatrace) with gentle stirring for 2 h. The detergent-insoluble material was removed by centrifugation (150,000 g for 45 min at 4°C), and the supernatant was incubated with amylose resin (New England Biolabs) with gentle stirring for 3 h. After loading onto the column and collecting the flow-through, the resin was washed with 10 column volumes of Buffer B2 (150 mM NaCl, 4 mM TCEP, 10 % glycerol, 1 mM DDM, 0.1 mg/ml, 50 mM HEPES; pH 7.4). Afterward, the protein was eluted with Buffer B2 supplemented with 20 mM maltose. The eluted protein was then mixed with PMAL-C8 (Anatrace) at 1:3 (w/w) with gentle agitation for 2 hr at 4°C. The protein then was digested with ProTEV Plus protease (Promega) at 4°C overnight to remove the MBP tag. Cleaved protein was further purified by size exclusion chromatography on a Superose 6 10/300 GL column (GE Healthcare) pre-equilibrated with Buffer C2 (150 mM NaCl, 4 mM TCEP, 20 mM HEPES; pH 7.4). Peak fractions corresponding to the tetrameric channel were collected and concentrated to ~0.3 mg/ml for cryoEM analysis.

Expression and purification of human inositol 1,4,5-trisphosphate receptor type 3 ligand binding core (LBC)

The hIP_3R-3 LBC construct was expressed using the Tni (*Trichoplusia ni*)/Baculovirus system (DH10multibac). Tni (*Trichoplusia ni)* cells (2.5 x 10^6 cells/ml) grown in ESF921 medium (Expression Systems) were harvested by centrifugation (1952 x g, 20 min) 48 hours post infection. The cell pellet was resuspended in lysis buffer composed of 200 mM NaCl, 20 mM Tris-HCl pH 8.0, 10 % glycerol (v/v), 10 mM BME, and 1 mM PMSF. Cells were lysed using Avestin EmulsiFlex-C3 system (greater than 10,000 psi) and centrifuged at 40,000 rpm (Ti45 rotor) for 45 minutes. Supernatant was recovered and incubated with Strep-XT-Superflow resin (IBA Biotagnology) for 2 hours at 4°C. The resin was then washed with the wash buffer (200 mM NaCl, 20 mM Tris-HCl pH 8.0, 10% glycerol, and 10 mM BME) and the protein was eluted with the

elution buffer (200 mM NaCl, 50 mM Tris pH 8.2, 100 mM D-Biotin and 10 mM BME). The IP_3R-3 LBC was further purified by FPLC using Superdex 200 column (GE Healthcare) equilibrated with 200 mM NaCl, 20 mM Tris-HCl pH 8.0, 10% glycerol (v/v), and 0.5 mM TCEP. The fractions corresponding to the IP_3R-3 LBC were concentrated to 6 mg/ml.

Expression and purification of human inositol 1,4,5-trisphosphate receptor type 3

Sf9 cells (4 x 10^6 cells/mL) infected with the hIP_3R-3 baculovirus were harvested by centrifugation (4,000 g) 48 hours after infection. Cells resuspended in a lysis buffer of 200 mM NaCl, 40 mM Tris-HCl pH 8.0, 2 mM EDTA pH 8.0, 10 mM BME, 1 mM PMSF were lysed using Avastin EmulsiFlex-C3. The cell lysate was centrifuged at 6,000 g for 20 minutes and the membrane was pelleted by centrifugation at 40,000 rpm (Ti45 rotor) for 1 hour. Membrane pellets were resuspended and homogenized in ice-cold resuspension buffer (200 mM NaCl, 40 mM Tris-HCl pH 8.0, 2 mM EDTA pH 8.0, 10 mM BME), and solubilized using 0.5% Lauryl maltose neopentyl glycol (LMNG) and 0.1% GDN at membrane concentration of 100 mg/mL. After 4 hours of stirring, the insoluble material was separated by centrifugation at 40,000 rpm (Ti45 rotor) for 1 hour and the supernatant was passed through Strep-XT resin. The resin was washed with the wash buffer composed of 200 mM NaCl, 20 mM Tris-HCl pH 8.0, 1 mM EDTA, 10 mM BME, 0.005% LMNG, 0.005% GDN and the protein was eluted using the wash buffer supplemented with 100 mM D-Biotin (pH 8.2). Protein was further purified by size exclusion chromatography using Superose 6 (10/300 GL, GE Healthcare) equilibrated with 200 mM NaCl, 20 mM Tris-HCl pH 8.0, 1 mM EDTA pH 8.0, 2 mM TCEP, 0.005% LMNG, and 0.005% GDN. Fractions corresponding to hIP_3R-3 was concentrated to 2.3 mg/mL and used immediately for cryoEM imaging.

Isothermal titration calorimetry

Isothermal titration calorimetry experiments were conducted on a NanoITC instrument (TA Instruments) at 20°C. Molar ligand concentration in the syringe was at least 5 times that of protein in the sample cell. In experiments using IP_3 as the ligand, the IP_3R-3 LBC was dialyzed against 200 mM NaCl, 20 mM Tris-HCl pH 8.0, 10% (v/v) glycerol, 0.5 mM TCEP supplemented with 1 mM, 20 mM, 40 mM, or 100 mM EDTA, pH 8.0. In experiments using EDTA or BAPTA as the ligand, the hIP_3R-3 LBC construct was dialyzed against 200 mM NaCl, 20 mM Tris-HCl pH 8.0, 10% (v/v) glycerol, and 0.5 mM TCEP. Incremental titrations were performed with an initial baseline of 180s and injection intervals of 200s, stirring at 150 rpm. Titration data were analyzed in NanoAnalyze (TA Instruments) to generate a model and values for stoichiometry (n) and K_d.

Negative stain grid prep, data collection, and image processing

Four hundred mesh copper grids were coated with a thin layer of amyl acetate and subsequently with carbon (carbon evaporator model). Grids were glow discharged for 2 min at 25 mA (Quorom K100X). 4 µL of protein at 0.05 mg/mL was applied to each glow discharged grid and allowed to absorb for 30 seconds. Excess buffer was blotted on filter paper, washed twice in milliQ water, and negatively stained with 0.75% (w/v) uranyl formate[238]. Images were recorded on a 4k x 4k CCD camera using an FEI F20 transmission electron microscope operated at 200 kV. All images were taken at a nominal magnification of 50,000x in low dose mode at a defocus of -1.5 µm. Images were collected manually using Digital Micrograph or semi-automatically using SerialEM[212]. Manually collected images were processed using the SPIDER software package[239]. Images were converted to SPIDER format and particles were picked manually using the WEB display program. Images were rejected if they had a large amount of astigmatism or deviated by more than 0.1 µm from -1.5 µm defocus as determined by processing with CTFFIND3[240]. Once picked, the particles were windowed in 100 x 100 pixel boxes. 100 2D class averages were determined using eight iterations of multi-reference classification alignment. (see **Appendix 2-1** for step-by-step protocol) Images collected in SerialEM were processed using the RELION

software package[205]. Images were imported into RELION 2.1 and putative particles were identified by autopicking using templates generated from a small subset of manually picked particles. GluA2 particles extracted with a mask size of 256Å and box size of 256 x 256 pixels were run through 2-3 rounds of 10-iteration 2D classification to filter out any obvious contamination. The particles in selected class averages were re-extracted and re-centered using RELION. These selected particles were then subjected to 10 iterations of 2D classification. The same 2D classification protocol was used for TRPC and IP_3R-3 particles with mask sizes of 180Å and 260Å and box sizes of 256 x 256 pixels and 324 x 324 pixels, respectively.

Analysis of GluA2-nanodiscs in negative stain

AMPAR particles were sorted into three different 'Types' with their NTD dimers in a stacked, upright and touching, or splayed configuration. Each of the 100 class averages was manually assigned to Type 1, Type 2, or Type 3 conformation based on the orientation of their NTD dimers. The total number of particles in each 'Type' was determined by totaling all of the particles that were aligned in each class assigned to that conformation. Particles were sorted as 'unclassified' if their NTDs were not resolved in the class average. The percentage of particles in each type were the number of particles defined as that 'Type' divided by the total number of particles that were used in the final 2D alignment.

Random conical tilt (RCT) specimen preparation, data collection, and model generation

C-flat holey carbon 2/1 200 mesh grids were coated with thin carbon and sat to dry overnight. 4 µL of 0.05 mg/ml TRPC6 was applied to carbon-coated grids and allowed to absorb for 30 seconds. Excess buffer was blotted on filter paper, washed twice in milliQ water, and negatively stained with 0.75% (w/v) uranyl formate[238]. Images were recorded on a 4k x 4k CCD camera using an FEI F20 transmission electron microscope operated at 200 kV. Tilted images were taken at 28k magnification in low dose mode at 50° and a defocus of -1.8 µm. Paired, untilted images were taken at -1.5 µm defocus. Low resolution 3D models of TRPC6 in PMAL-8 were created using the SPIDER software package[239]. Micrographs were converted to SPIDER format and tilt pairs were manually picked using the WEB display program. The picked particles were windowed into 100 x 100 pixel boxes and bad particles were manually discarded from both the untilted and tilted data sets. 100 2D class averages were generated from the untilted particles using eight iterations of multi-reference classification alignment. Eight iterations of SPIDER backprojection were done to create initial models of TRPC6 in a "closed" and "open" conformation from two classes (class #55 and 83), respectively. Initial models were converted to mrc format with box and pixel size adjusted to match cryoEM data using EMAN2[241] (see **Appendix 2-2** for step-by-step protocol).

Cryo-EM grid preparation

Graphene oxide coated cryoEM grids

GO solution was prepared in PCR tubes by diluting graphene oxide (GrapheneSolutions-HighConcentration) in a 1:15 solution in milliQ water (5 µL GO, 70 µL H_2O). Solutions were centrifuged for 30 seconds in a UltraCruz mini centrifuge. 300 mesh Qualtifoil 1.2/1.3 gold grids were glow discharged for 60 sec at 40 mA in the air chamber of a GloQube (EMS). 3 µL of GO solution (without disturbing the precipitate) was applied to the carbon-coated side of the glow-discharged grids and allowed to incubate for one minute. GO was blotted from surface on filter paper with grid inverted. Two 20 µL water droplets were picked up on the coated side of the inverted grid, blotting on filter paper between. A final 20 µL water droplet was picked up on the non-coated side of the non-inverted grid and blotted on filter paper. Grids were allowed to dry at room temperature overnight before applying protein and plunging as stated below, with details in **Table 2-2**.

These conditions were determined after testing GO suspensions from different companies (GO from Sigma was diluted 1:10, GrapheneSolutions-GO was used undiluted, GrapheneSolutions-UltraHighConcentration was diluted 1:20) and determining the optimal concentration for grid coverage, particle contrast, and visible particle number. We tested two different batches of the GO from Sigma at 1:10 dilution, 1:7 dilution, and 1:5 dilution. 1:7 and 1:5 resulted in too much GO deposition on the grid. We also varied the time of glow discharging in the GloQube from 60, 75, 90sec. This variation did not have any observable effect on GO deposition or particle number.

Grid vitrification

All cryo-EM grids were prepared in the Vanderbilt cryoEM Facility. 200 or 400 mesh 2/1 C-flat grids were glow discharged for 2 min at 25 mA (Quorom K100X). GO coated grids were glow discharged for 30 sec at 25 mA. 2.0 µL of protein solution was applied to the carbon (or GO) side of the grid and blotting conditions are detailed in **Table 2-2**. All samples were incubated on the grid for 60 sec before blotting. Grids were plunged into liquid ethane using an FEI MarkIII or MarkIV Vitrobot.

Sample	Grid	Mesh/Hole	Vitrobot	Blot	Temp (°C)	Humidity
$TRPC3_{GDN}$ (1.2 mg/mL)	C-flat, holey carbon, Cu	200, 2/1	Mark III	7s, -3.5 µm	8	100%
$TRPC3_{PMAL}$ (0.3 mg/mL)	C-flat, holey carbon, Cu	400, 2/1	Mark III	8s, -3.5 µm	8	100%
$TRPC6_{PMAL}$ (0.3 mg/mL)	C-flat, holey carbon, Cu	200, 2/1	Mark III	8s, -3.5 µm	8	100%
IP3R-3 (2.3 mg/mL)	C-flat, holey carbon, Cu	200, 2/1	Mark IV	3s, force 1	8	100%
GluA2 nano (0.1 mg/mL)	Quantifoil, holey carbon, Au	300, 1.2/1.3	Mark IV	3-4s, force 10	8	100%

Table 2-2. Vitrobot conditions to prepare samples in vitrified ice
These are the final blotting conditions that were used to collect data in this thesis. Blot conditions include blot time and either blot offset (for the MarkIII) or blot force (MarkIV). Copper – Cu, Gold – Au,

When determining these blotting conditions, the blot offset was held constant on the MarkIII and blot time was varied to determine the best ice conditions, measured by the extent of Thon ring spread in raw micrographs determined in Gctf[242], particle number, and particle contrast. For the MarkIV, we changed both the blot time and blot force to determine the best parameters to use. We started plunging samples at a low blot force (2) and increasing blot time (up to 6 sec) similar to how we had previously optimized the MarkIII, but later moved to using a high blot force (~10 at 8ºC) and varying blot time slightly. This seems to give better control over the ice thickness and quality. The setting for the MarkIV humidifier to be “off during process” should be selected. It is important to note that blotting conditions will change for the MarkIII between seasons and there is a smaller, but appreciable, shift in the MarkIV, also. Slightly longer blot times are necessary in the summer.

Cryo-EM data collection

On Polara F30

The microscope was aligned for each data collection session as follows. First, a gain reference is recording on the K2 Summit Camera for linear and counted/super-resolution mode.

The C2 aperture is inserted and aligned and then gun tilt is adjusted to minimize exposure time in direct alignments. Gun shift is adjusted for all spot sizes in alignments. A cross-grating grid (Ted Pella) is inserted and correct eucentric height is set. The objective aperture is inserted and centered and focus is determined at high magnification using the detector. The beam pivot points are adjusted and rotation center set by eye. The detector is used again to correct any objective astigmatism and then find the correct coma alignments. Pivot points are checked once more and then the sample is inserted. Electron dose was calibrated using SerialEM on an empty part of the grid. Micrographs were collected in counted or super-resolution mode on a K2 Summit direct electron detector (Gatan) using a FEI Polara F30 microscope operated at 300 kV, at the Vanderbilt University cryo-EM Facility. Imaging conditions are detailed in **Table 2-3**. Images collected in super-resolution mode were binned by a factor of 2 before motion correction. Images collected in counted mode were not binned. Data were collected manually in Digital Micrograph and with automation using SerialEM in low-dose conditions.

On FEI Titan Krios

Micrographs were collected using an FEI Titan Krios microscope equipped with a Cs corrector at the Washington University in St. Louis Center for Cellular Imaging (WUCCI). Direct alignments, Cs corrector calibration, and energy filter tuning were performed by staff at the WUCCI. Images were recorded using a K2 Summit direct electron detector equipped with an energy filter (Gatan BioQuantum). Micrographs were collected in counting mode using EPU software-aided automation under low dose conditions. Imaging details are presented in **Table 2-3**.

Sample	Micro scope	Defocus (μm)	Mag.	Calibrated pixel size (Å/pixel)	Exp. (s)	Dose rate (e^-/pix/s)	Frame #
$TRPC3_{GDN}$	Polara	-1.8 - -4.8	31Kx	1.24699	8	12.5	40
$TRPC3_{PMAL}$	Krios	-1.2 - -3.0	105Kx	1.096	7.4	8	30
$TRPC6_{PMAL}$	Polara	-1.8 - -4.8	31Kx	1.24699	8	12.5	40
$TRPC6_{PMAL}$	Krios	-1.2 – 3.0	81Kx	1.41	9	11	47
IP_3R-3	Polara	-1.4 - -3.5	31Kx	1.24699	10	7.05	50
$GluA2_{brain\ lipid}$	Polara	-2.2 – -4.0	31Kx	1.24699	10	7.05	50
$GluA2_{brain\ lipid}$	Krios	-1.9 - -4.0	81Kx	1.41	11.1	12.25	37

Table 2-3. Imaging conditions for cryoEM data collection
These are the imaging conditions for collecting the data used to reconstruct structures presented in this thesis. The magnification specified is the nominal magnification on the microscope.

Cryo-EM image processing

Images were motion corrected by motioncor2[204] with a dose-weighting parameter specified in **Table 2-4**. For Polara F30 data, the image processing software Focus[243] was used for on-the-fly assessment of images being collected. Low image quality micrographs, such as micrographs with Thon ring spread to only 6.0Å, too much ice contamination, devitrification, defocus values outside the specified range, and astigmatism values of >500, were manually discarded. We followed an identical procedure for FEI Titan Krios dataset without the on-the-fly assessment, using dose-weighting parameters from **Table 2-4**, and a Cs aberration parameter of 0.001. Low quality micrographs were discarded upon manual inspection in RELION 2.1[205]. Motion correction[204] and Gctf[242] were run locally on a Nvidia GeForce GTX 750Ti or 1080Ti graphics card. Raw images were then loaded onto external hard drives (WD30EZRZ) for storage. Motion corrected images were stored on the DORS computing cluster managed by the Center for Structural Biology at Vanderbilt. Autopicking, 3D classification, and refinement were performed using the 1 of the 30 GPU nodes available at ACCRE. 2D classification was run on 5-15 nodes

of the 620 CPU nodes available at ACCRE. All cisTEM processes were run locally using 12 CPUs.

RELION 2.1

Dose-weighted, motion-corrected micrographs were imported into RELION 2.1 and contrast transfer function (CTF) was determined by Gctf[242]. Putative particles were identified by autopicking, using templates specified in *Table 1-4*. Particles were extracted with a mask size appropriate to the particle, box size of 256 x 256 pixels, and binned to 64 x 64 pixels to perform a fast, 25-iteration 2D classification to identify particles with the correct general architecture and filter out any clear contamination. The particles in selected class averages were re-extracted at full scale and re-centered using either RELION or a script from Terunaga Nakagawa (T.N.) (**Appendix 2-3**). These selected particles were subjected to 25 iterations of 2D classification. Averages with clearly resolved secondary structure were moved into 3D classification. Particle images were aligned and classified in 3D using an initial model and mask indicated in **Table 2-4**. 3D classification with symmetry imposed (C4 for TRPC and IP_3R data sets, was conducted and the best classes, as defined by the presence of resolved secondary structure in the ECD, TMD, and CPD from each batch was selected. The particles from these classes were pooled and subjected to 3D refinement, post-processing, and local resolution calculations in RELION 2.1, Post-processing was done by applying a B-factor (see **Table 2-4***)* that was calculated by RELION 2.1, based on Rosenthal and Henderson's method[244] and a mask defined in **Table 2-4**. Detailed statistics for each map and model are provided in **Tables 5-1, 6-1, 7-1**. The resolution of each map was estimated by the gold-standard FSC in RELION 2.1, using the FSC = 0.143 criteria. ACCRE submission scripts are in **Appendix 2-3**.

cisTEM

Refinement of the IP_3R-3 was also conducted using cisTEM[206]. The 117,711 particles used in the final RELION map were imported into cisTEM and autorefinement was run using the default settings with C4 symmetry. Parameters can be found in **Appendix 2-4**. The map generated in RELION was filtered to 30Å and used as an initial model for this refinement. The final average resolution at the "gold-standard" 0.143 cutoff was 3.98Å. This map was then sharpened in cisTEM with a B-factor of -160 to facilitate model building. Half-maps were generated using the 3D-generate module in cisTEM and output to generate a map with local resolution parameters imposed in RELION. Local resolution was also calculated in ResMap[245].

Model building, refinement, and validation

For all TRPC channel models, secondary structure was manually inserted using Coot[246]. From there, a polyalanine model was built manually, also in Coot. Subsequent amino acid assignment was performed for the CPDs by defining the densities of bulky residues in the structures solved in PMAL-8. A "hybrid" full-length TRPC3 atomic model was generated by combining the polyalanine model of the TMD with a full atom model of the CPD. Full-atom models for the tetrameric assemblies were generated using UCSF Chimera[247]. All models were optimized using Phenix's real-space refinement tool[248,249]. Validations of the final models were performed using MolProbity[250]. To prevent overfitting of the models into the density, refinement was run with strict geometric restraints on bond length bond angle, while non-crystallographic symmetry (NCS) was imposed. Real space refinement was iterated with manual adjustment in Coot to remove/minimize bond length, bond angle, rotamer, and Ramachandran outliers and keep model in the defined electron density (see **Appendix 2-5** for all modeling notes). Specifics for modeling can be found in individual *Experimental Procedures* sections.

Angle measurements

To estimate angles between helices, we create a 'pipes and planks' model using UCSF Chimera[247]. After exporting an image in the desired position, we used Fiji to obtain the angle

values by placing manually three points along the pair of helices. Angles were confirmed in Coot with an error of ±1º.

Data deposits

The EM density map and atomic coordinates were deposited to the PDB and EMDB under accession codes 6CV9 and EMD-7637, respectively. The EM density map and atomic coordinates for $TRPC3_{PMAL}$ were deposited to the PDB and EMDB under the accession codes 6D7L and EMD-7823. The EM density map and atomic coordinates for $TRPC3_{GDN}$ were deposited to the PDB and EMDB under accession codes 6DJR (polyalanine), 6DJS (hybrid), and EMD-7940. The EM density map and atomic coordinates for IP3R-3 were deposited to the PDB and EMDB under accession codes 6MA9, EMD-9052 (RELION map), and EMD-9051 (cisTEM map).

Protein	DW	Particle templates	2D mask (Å), box size (px)	Initial 3D model	3D Class Mask	Symm.	Refine Model	Refine Mask	Post Process Model	Post Process Mask	B-fact
$TRPC3_{GDN}$	2.5	TRPC6 averages	160, 256x256	TRPC6, EMDB: EMD-7637	threshold 0.00172, with a 5pix ext and 5pix soft edge	C4	3D class 2, job 191 @ 40Å	None	3D refine @ 10Å	threshold 0.0107 with a 4pix ext and 4pix soft edge	-179
$TRPC3_{PMAL}$	1.63	TRPC6 averages	160, 256x256	TRPC6, EMDB: EMD-7637	threshold 0.0205 with a 7pix ext and 7pix soft edge	C4	3D class 3, job 125 @ 20Å	threshold 0.0122 with a 5pix ext and 5 pix soft edge	3D refine @ 10Å	threshold 0.0107 with a 4pix ext and 4pix soft edge	-126
$TRPC6_{POLARA}$	2.5	Class averages obtained from 2000 manually picked particles	160, 256x256	Initial model from RCT class average #55 filtered at 60A	None	C4	3D class2, job 299 @ 30Å	threshold 0.0035 with a 3pix ext and 3pix soft edge	3D refine @ 15Å	threshold 0.0058 with a 6pix ext and 6pix soft edge	-133
$TRPC6_{KRIOS}$	1.56	TRPC6 averages	160, 256x256	$TRPC6_{POLARA}$ refinement filtered to 40A	threshold 0.003 with a 8pix ext and 4pix soft edge	C4	3D class 2, job 192 @ 30Å	threshold 0.0205 with a 7pix ext and 7pix soft edge	3D refine @ 10Å	threshold 0.0178 with a 5pix ext and 5pix soft edge	-126

IP_3R-3 (RELION)	1.4	Class averages obtained from 757 manually picked particles	280, 324x324	IP_3R type 1, EMDB: EMD-6369	None	C4	3D class 1, job 219 @ 40Å	threshold 0.0105 with 3pix ext and 3pix soft edge	3D refine @ 10Å	threshold 0.0113 with 4pix ext and 4pix soft edge	-166
IP_3R-3 (cisTEM)	1.4	No 2D	No 2D	No 3D classification	No 3D classification	C4	RELION refinement output, filtered to 20Å	None	3D refine @ 10Å	threshold 1.28 with 4pix ext and 4pix soft edge	-90
GluA2	1.4	Class averages obtained from 4486 manually picked particles	256, 324x324	N/A as of submission	N/A	N/A	N/A	N/A	N/A	N/A	N/A

Table 2-4. Imaging processing parameters for cryoEM data

Images were processed primarily in RELION, with the IP_3R-3 also being refined in cisTEM. The mask parameters were adjusted to achieve the highest resolution. All datasets were autopicked using templates. DW – dose weighting factor used for motion correction. Symmetry was imposed from 3D classification to postprocessing.

CHAPTER III: BIOCHEMICAL RECONSTITUTION AND NEGATIVE STAIN ANALYSIS OF IGLUR COMPLEXES IN LIPID NANODISCS

Aims

iGluRs are ligand-gated ion channels that play critical roles in synaptic transmission, synaptic plasticity, and structural maintenance of synapses. Their function and mechanism have been studied extensively by using methods in electrophysiology, molecular biology, genetics, biochemistry, cell biology, and behavioral analyses of animals. Despite a broad range of available experimental approaches, biophysical studies of iGluRs in the form of single particles have been difficult due to the lack of effective *in vitro* preparations in a near native state. Lipid nanodisc technology is a particularly attractive system for studying membrane proteins in isolation while maintaining the lipid bilayer environment. Reconstitution of detergent solubilized ion channels into lipid nanodiscs requires distinct conditions for each type of membrane protein. Here we apply lipid nanodisc technology to the AMPAR using both POPC and brain polar lipid extract. The receptors have unprecedented *in vitro* complex stability and retained previously reported domain architecture. The AMPAR complexes underwent characteristic glutamate-induced conformational changes. Based on these results, we suggest that stabilization of iGluRs into lipid nanodiscs is a viable approach, particularly advantageous for biophysical studies, such as structural investigation by cryoEM and electron paramagnetic resonance, single molecule fluorescent studies, and *in vitro* assay based drug discovery.

Results and Discussion

Reconstitution of AMPAR (GluA2) in lipid nanodiscs

To obtain recombinant AMPARs, we DOX-dependently expressed GluA2(R)-FLAG in TetON HEK cells (Clontech) and purified them in DDM detergent with FLAG affinity purification using established methods[251] **(Figure 3-1A)**. To enable large-scale culture the adherent cells were adapted to suspension culture in spinner flasks. The reconstitution of AMPAR was achieved by incubation of purified AMPAR, POPC lipids and the MSPD1E3, or POPC/brain lipids and MSP2N2, variants of MSP[29], in detergent followed by active removal of detergent by hydrophobic absorbents. The final product was biochemically pure, consisting of GluA2 and MSP in SDS-PAGE **(Figure 3-1B)**. The ratio of GluA2, POPC, and MSP was a critical parameter for successful reconstitution with minimal lipid vesicle contamination. The optimal ratio of POPC and MSP was therefore determined empirically for each preparation of MSP purified from *E. coli*, identifying the highest nanodisc yield and least void peak in gel filtration **(Figure 3-1C)** and visualizing of the contents of each fraction by negative stain EM. Specifically, a condition that maximizes absorbance in fraction 24 over the void volume (fraction 17) was identified in Superdex200 gel filtration and examined by EM to verify the nanodiscs were filled with lipid and did not accumulate uranium stain in the center. A leftward shift was seen in the peak elution above 1:70 that correlated well with full nanodiscs.

In the tetrameric assembly of AMPAR, two dimeric densities of NTDs and LBDs can be seen as each form dimers of dimers. The two NTD dimers **(Figure 3-1D, red)** clearly sit on top of the particle as a bulkier layer than the two LBD dimers **(Figure 3-1D, blue)** below. Within the dimeric NTDs, the boundary between each protomer can sometimes be resolved. The TMD **(Figure 3-1D, yellow)** is the transmembrane region that is composed of 16 TM helices, four from each GluA2 subunit, and the surrounding lipids and MSP of the lipid nanodisc. Negative stain EM showed that lipid nanodisc embedded GluA2 had a wider density at the bottom of the particle **(Figure 3-1E)** when compared to GluA2 prepared in DDM[93]**,** corresponding to the region of the AMPAR-TMD. The NTD and LBD were also clearly recognizable in the nanodisc embedded GluA2. Absence of irrelevant objects in the raw negative stain image further confirms that our preparation of GluA2 nanodiscs is pure. Furthermore, they were monodispersed and three distinct conformations of the NTD can be classified, which will be discussed later in relation to the effect of different ligands on the particles' distribution among these classes.

The same protocol was used to embed GluA2 homotetramers into lipid nanodiscs including a

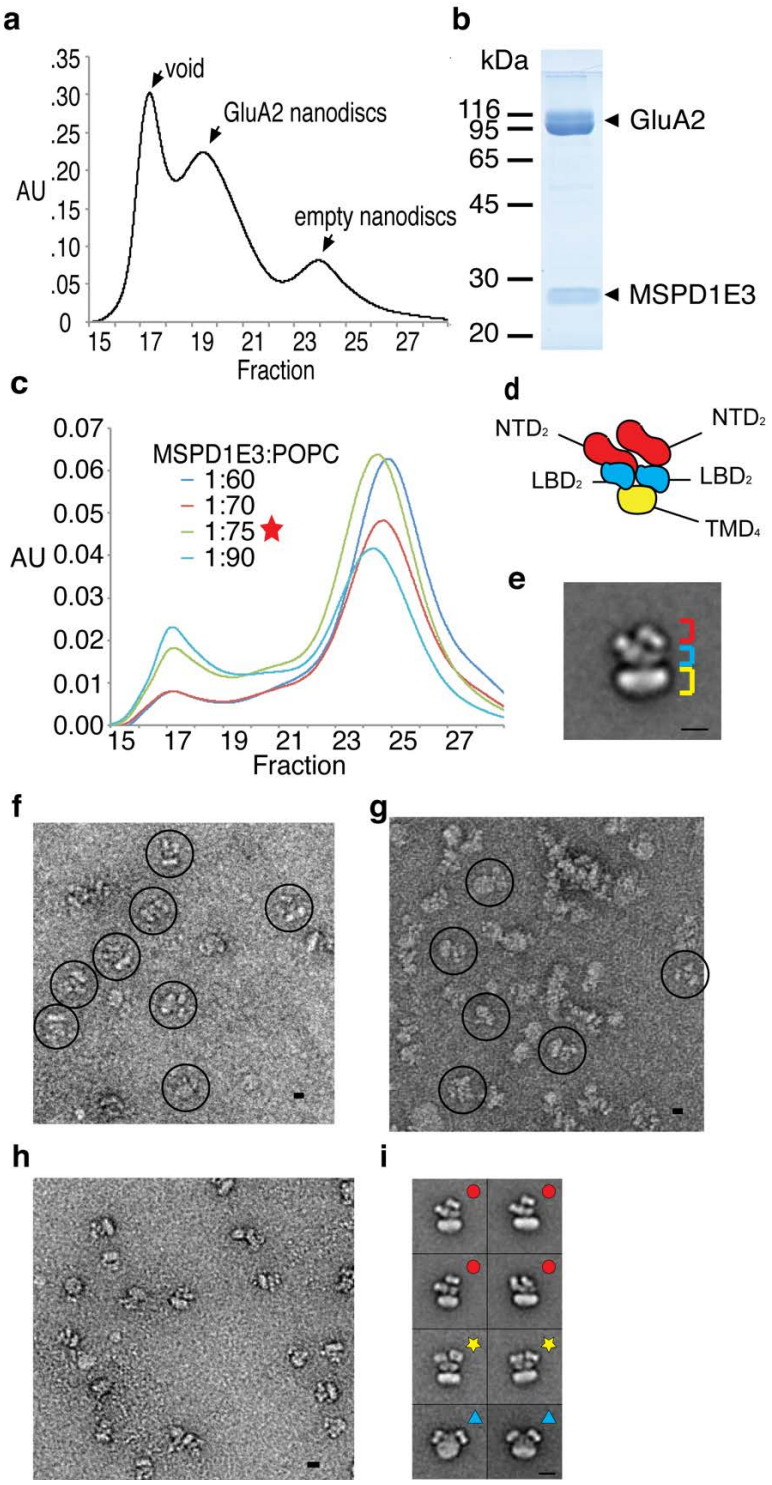

Figure 3-1. Reconstitution of GluA2 into lipid nanodiscs.
A. Superdex200 gel filtration chromatograph of GluA2(R) tetramers that have been anti-FLAG affinity purified and reconstituted into lipid nanodiscs. **B.** Coomassie brilliant blue (CBB) stained SDS-PAGE resolving fraction 19. Molecular weight marker (left), GluA2, and MSPD1E3 (MSP) are labeled. **C.** Superdex200 gel filtration chromatographs of empty nanodiscs, normalized to the peaks and overlaid, used to determine the optimal protein to lipid ratio to form full nanodiscs. See shift of peak to higher molecular weight between 1:70 and 1:75, without increasing the void peak (1:90). This experiment was performed for each batch of MSP or POPC and the ideal ratio in this case was 1:75 (star). **D.** Cartoon of the AMPAR tetramer as visualized using EM. NTD2, LBD2, and TMD4 indicate NTD dimer, LBD dimer, and TMD tetramer, respectively. **E.** Class average of GluA2 in lipid nanodisc. The NTD, LBD, and TMD

regions are identified in the same colors as panel D. **F.** Representative negative stain EM raw particle images of reconstituted GluA2-POPC with circles indicating intact, monodisperse particles. **G.** Negative stain EM raw particle image of reconstituted GluA2-brain lipid with circles indicating intact, monodisperse particles. **H.** Nanodiscs confer unprecedented stability to the complex. This micrograph was taken of a GluA2 nanodisc sample that had been prepared and stored at 4°C for one year. **I.** Example of the three different classifications of the receptor NTD dimers are shown, Type 1 – red circle, Type 2 – yellow star, Type 3 – blue triangle. All scale bars are 20 nm.

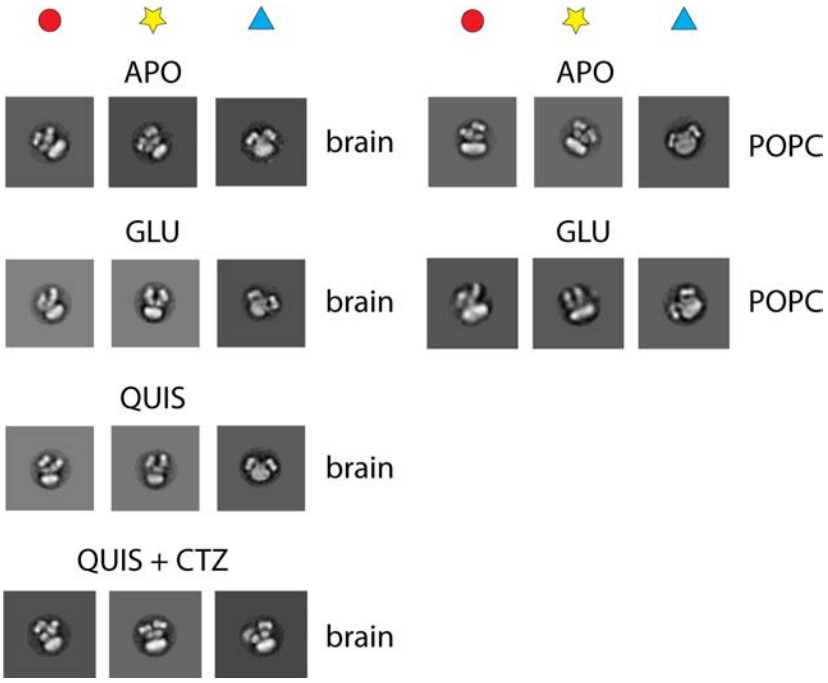

Figure 3-2. Negative stain class averages of receptors exposed to different ligands.
Type 1, 2, and 3 classifications of the receptor are shown for each sample. The ligand treatment is indicated above each set of class averages with the brain-lipid nanodiscs on the left and the POPC nanodiscs on the right.

mixture of polar brain lipid extract and POPC. In this preparation, we used MSP2N2 to ensure that the TM helices of GluA2 would not be contacting the MSP and were surrounded completely by lipids. The polar brain lipid extract and POPC were both dissolved in DDM detergent at 10 mg/mL and premixed before adding the FLAG-purified GluA2 and MSP. Both of nanodisc preparations were well resolved on negative stain grids (**Figure 3-1F and G**). After addition of ligands, we saw small difference in distributions across different NTD conformations. After embedding the GluA2 tetramer in lipid nanodiscs, the complex was stable in solution at 4°C for over a year without noticeable artifacts or degradation of the sample **(Figure 3-1H)**. This is in stark contrast to detergent micelle solubilized AMPAR which begin to dissociate from their tetrameric assembly in as little as 10 days. AMPARs that have been stored for a year also remain functional, as judged by their ability to separate their two NTD dimers in response to agonist application (data not shown).

Effect of agonists on the conformation of nanodisc embedded AMPARs

The lipid nanodisc embedded GluA2 undergoes conformational changes consistent with what was observed in detergents **(Figure 3-2**, **3-3**, and **Table 3-1).** Specifically, the two NTD dimers move apart from each other and toward the membrane plane when exposed to agonists relative to their original position in the unliganded state. Here, we classify the 2D averages generated through multireference alignment into three different groups. Particles are assigned as Type 1 **(Figure 3-1I**, red circle**)** if their two NTD dimers are stacked on top of one another and are generally diagonal to the plane of the lipid nanodisc. Type 2 particles **(Figure 3-1I**, yellow star**)** are characterized by two NTD dimers that sit vertically over the LBD dimers and are nearly touching, but with no overlap of each other. Type 2 classes have their two NTD dimers next to each other and not splayed apart. Type 3 particles **(Figure 3-1I**, blue triangle**)** are those with their two NTD dimers clearly and completely splayed apart. Often when the two NTD dimers are separated to the degree that classifies them as Type 3 the curvature of the nanodisc was enhanced and the LBDs were less resolved as individual densities.

Generally, agonists push the distribution of particles towards the Type 2 and 3 classes **(Figure 3-3**, **Table 3-1)**. The most drastic change in the distribution among conformations came from treatment with quisqualate and CTZ, a desensitization blocker[101] **(Figure 2-3**, **Table 3-1)**. Application of these two ligands has the lowest proportion of class Type 3. This data is our strongest indicator that Type 3 particles represent the desensitized state of the AMPAR. Based on the effects of different drugs, we propose that Type 1 and 2 classes represent a mixture of closed and open states that vary in subconductance state[252,253] and cannot be faithfully identified as one or the other at this resolution. Additionally, because Type 1 and 2 do not disappear in the presence of agonist, a small population within these Types also includes the conformations of desensitized, re-sensitized, and ligand-bound but channel-closed receptors. Because they are dominant in the presence of agonist and reduced by a desensitization blocker, Type 3 classes are desensitized AMPARs, characterized by an increased inter-NTD dimer distance[18,19]. Collectively, our data suggests that the lipid nanodisc embedded AMPAR particles undergo expected conformational changes in the presence of specific drugs and likely preserve their function. Interestingly, the proportion of receptors classified into a Type 3 conformation is lower in the glutamate sample of GluA2 in POPC alone compared to the brain lipid mixture (27% compared to 44%). This difference may indicate that the protein is more dynamic and able to enter a desensitized state faster in the presence of a more native polar brain lipid mixture. As discussed in the introduction, specific lipids can affect the function of receptors, and this increased effect of glutamate may indicate that lipids are binding to the TMD of the AMPAR and modulating its response to extracellular ligands.

Discussion

In this study, we have successfully applied lipid nanodisc technology to the AMPAR. Because they undergo conformational changes in response to agonists, our data suggests that the AMPAR remains responsive to agonists and allosteric modulators when embedded in nanodiscs. This advance drastically increases the stability of the functional complex, making it more feasible for use in structural biology and other biophysical experiments such as single molecule experiments of iGluRs[254–257] and *in vitro* drug screening.

To date, the AMPAR structure has been extensively studied in detergent micelles[17–19,21,22], but detergents can potentially introduce contacts that are not physiologically appropriate or destabilize

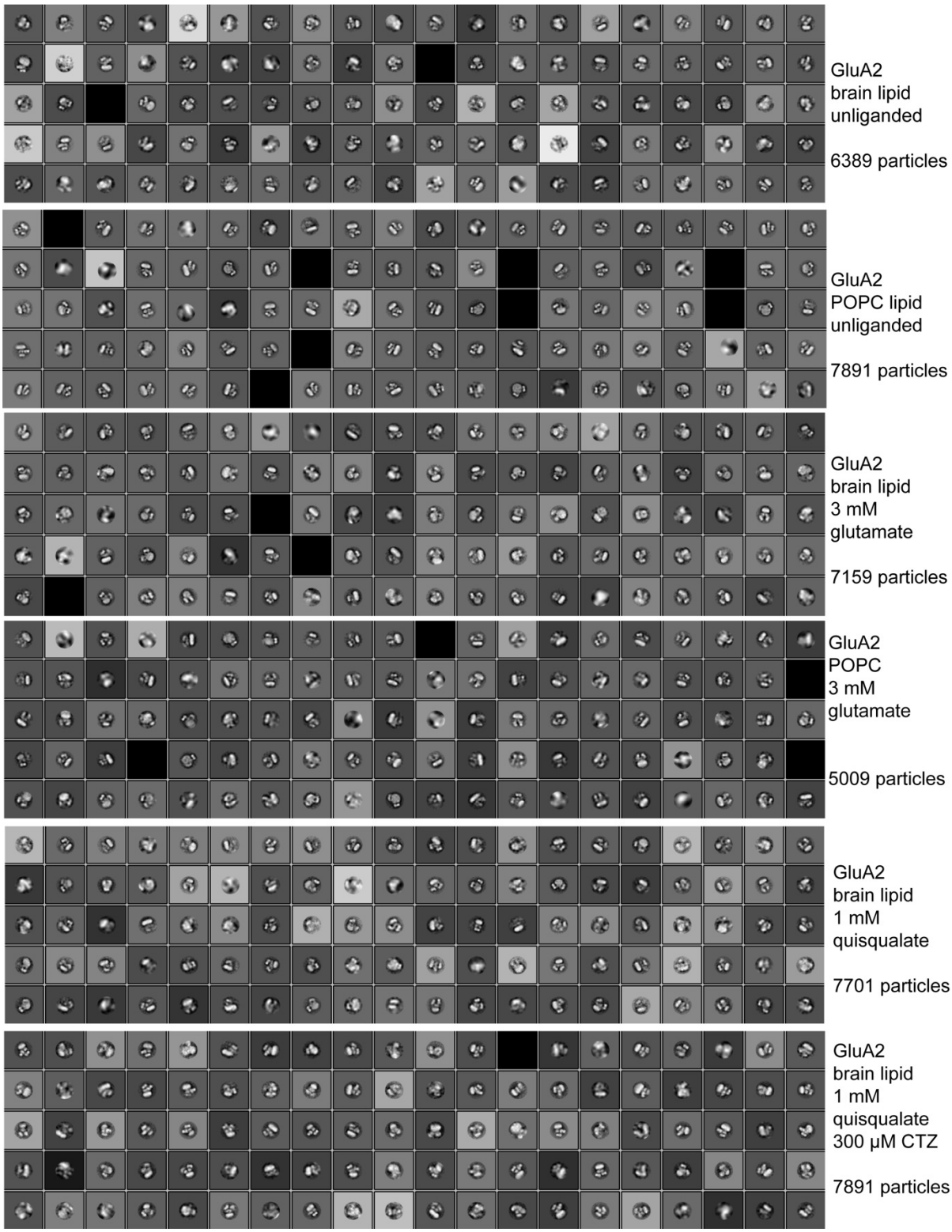

Figure 3-3. Negative stain class averages.
100 class averages that were calculated from each ligand group. Total number of particles in each data set is indicated on the right along with the ligand concentrations and the lipid environment in each sample.

Complex/Ligand	Type 1 ●	Type 2 ★	Type 3 ▲	Unclassified	# of Particles
GluA2-POPC Apo	58.3%	19.7%	12.0%	10.0%	7891
GluA2-POPC Glutamate	9.4%	40.4%	26.9%	23.3%	5009
GluA2-brain lipid Apo	43.3%	13.5%	19.8%	23.4%	6389
GluA2-brain lipid Glutamate	4.0%	31.5%	44.0%	20.5%	7159
GluA2-brain lipid Quisqualate	4.0%	24.9%	47.9%	23.2%	7701
GluA2-brain lipid Quisqualate + CTZ	52.4%	20.2%	11.0%	16.4%	7891

Table 3-1. Summary of ligand effects on GluA2 in different lipid environments.
Distribution of particles in Type 1, 2, or 3 conformation when various ligands are applied. Agonists are indicated in green and modulators (CTZ) are indicated in purple.

complexes that are intact in native membranes[258]. The RNA edited GluA2(R) isoform is unstable in detergent in the absence of the antagonist NBQX[83,86,259]. While detergent solubilized receptors have been able to give high resolution structures of the AMPAR previously, it is likely that this destabilizing effect precludes the AMPAR from sampling the entire conformational variability available to it in a native membrane environment. Furthermore, many membrane proteins demonstrate lipid binding or lipid-modified functions[260,261] and in fact, lipids are known to modulate iGluRs gating and trafficking[262,263]. In fact, negatively charged lipids have been shown to interact with the AMPAR auxiliary subunit stargazin and inhibit its binding to PSD-95[264], a model whose mechanism could be analyzed in detail using the controlled lipid environment of nanodisc-embedded AMPAR-AP complexes. Critical residues responsible for the action of noncompetitive modulators such as GYKI, CP-465,022, and (3-chlorophenyl)(6,7-dimethoxy-1-((4-methoxyphenoxy)methyl)-3,4-dihydroisoquinolin-2(1H)-yl)methanone (CIQ) were mapped to be in or near the TMD[97,98,265] and may also be affected by the absence or presence of certain lipids. The nanodisc preparation may be useful in investigating the role of functionally important posttranslational modifications, such as phosphorylation[266] and palmitoylation[267] of the iGluRs on receptor conformation. We studied the structural effects of ligand application at the low resolution that can be achieved by negative stain EM for the purposes of verifying iGluR functionality after incorporation into lipid nanodiscs. AMPAR nanodiscs showed similar NTD separation upon agonist application to that which has been seen previously in EM studies of AMPAR in detergent[18,86,232,259]. Mechanistic interpretation of the effect of NTD motion on gating, however, is controversial[268–270]. Even though we crudely classified particles into three conformational categories, differences could be already found for the effect of the same ligand on AMPAR in different lipid environments, indicating that a nanodisc-embedded AMPAR is important to study further.

Unlike liposome reconstitution that introduces receptors in regular and inverted orientations relative to the membrane curvature, nanodisc embedding exposes both the cytoplasmic and lumenal side of the receptor. The C-terminal domains of the AMPARs interact with a plethora of adaptor and scaffold proteins, such as AP-2[271], PICK1[272], MAGUK[233,273], GRIP/ABP[274,275], and NSF[276–278], that are critical for their trafficking regulation. It is thus likely that nanodisc-embedded iGluRs could serve as a platform to construct postsynaptic macromolecular assemblies for detailed mechanistic analyses. The structural investigation of complexes assembled *in vitro* may facilitate the molecular interpretation of cryo-electron tomography[279] and super-resolution light microscopy[280] data of the postsynaptic density (PSD).

What are the causes of unclassified particles (**Table 3-1**)? In single particle EM there is always a subpopulation of particles that were damaged during purification. However, those were characterized by the absence of sub-features, in our case easily discernable due to the high image contrast introduced by the negative stain and the lack of clearly defined NTD dimers and TMDs, and excluded from our analyses. The major causes of unclassifiable particles are the conformational variety and/or outliers that exist in the population. There are also cases where the negative stain is incomplete, reducing the image contrast and making the particles difficult for the algorithm to classify. Because of these unclassifiable particles, we can only compare robust changes in the distribution of particles among different conformations. Despite these parameters that need to be taken into account to interpret the results, negative stain EM has been used powerfully to study conformational changes of AMPARs and even other macromolecular complexes. The increased stability and flexibility of the receptors implied by changes identified by negative stain EM make nanodisc-embedded AMPAR an attractive candidate for cryoEM. We have begun to collect data on the receptor after optimizing GO grid coating and plunging conditions.

CHAPTER IV: SMALL MOLECULE MODULATORS OF AMPAR-AUXILIARY SUBUNIT COMPLEXES

This chapter is a paper published in *PLoS ONE* as "Screening for AMPA receptor auxiliary subunit specific modulators" Caleigh M. Azumaya, Emily L. Days, Paige N. Vinson, Shaun Stauffer, Gary Sulikowski, C. David Weaver, Terunaga Nakagawa.

Aims

AMPAR are ligand gated ion channels critical for synaptic transmission and plasticity. Their dysfunction is implicated in a variety of psychiatric and neurological diseases ranging from major depressive disorder to amyotrophic lateral sclerosis. Attempting to potentiate or depress AMPAR activity is an inherently difficult balancing act between effective treatments and debilitating side effects. A newly explored strategy to target subsets of AMPARs in the central nervous system is to identify compounds that affect specific AMPAR-AS complexes. This exploits diverse spatio-temporal expression patterns of known AMPAR ASs, providing means for designing brain region-selective compounds. We chose to screen for compounds that act on three auxiliary subunits that modulate AMPAR function differently. The auxiliary subunits studied in this screen are TARP γ-2 (stg), CNIH3, and GSG1L. They are expressed in different but partially overlapping neuronal populations in the CNS and provide an opportunity to identify chemical compounds that could serve as brain region-selective AMPAR modulators. Stg is concentrated in the cerebellar granule cells, CNIH3 is enriched in the hippocampus and cortex, and GSG1L is expressed in the striatum and cortex. Stg and CNIH3 are both positive regulators of AMPAR gating kinetics[67,74] and GSG1L suppresses AMPAR activity[281,282]. Here we report a high-throughput screening-based pipeline that can identify compounds that are selective for GluA2-CNIH3 and GluA2-stg complexes. These compounds will help us build upon the growing library of AMPAR-auxiliary subunit specific inhibitors, which have thus far all been targeted to TARP γ-8. To identify compounds that target the AMPAR-stg and AMPAR-CNIH3, specifically, we developed a high-throughput cellular assay using a VSD that shows an increase in fluorescence proportional to membrane depolarization. Identified hits were then filtered by a series of counter-screens to eliminate false positives and to determine specificity. Finally, a calcium flux assay using the calcium permeable isoform of GluA2, which is not RNA edited at the critical pore-lining amino acid[283], was performed to further characterize the hit compounds. These assays identified a NAM with higher potency on AMPAR complexes containing stargazin and CNIH3, a PAM that reproduces our VSD assay finding of auxiliary subunit dependent activity in electrophysiology, and a compound with PAM or NAM activity depending on which auxiliary subunits are present. These experiments have proven to be an effective way to identify candidate compounds as AMPAR auxiliary subunit specific PAMs and NAMs and could easily be applied to kainate receptor (KAR)-Neto1/2 and NMDAR-Neto1 complexes as well as non-iGluR-auxiliary subunit complexes worth investigating as therapeutic targets.

Results and Discussion

Cell lines for VSD assay

Cell based assays in combination with HTS were used to identify compounds that specifically target the AMPAR in complex with the TARP γ-8 auxiliary subunit[108,109]. Taking an analogous approach, we generated multiple cell lines as summarized in **Table 4-1** and developed a VSD based cellular assay compatible with HTS to screen ~39,000 compounds from the VDL. In detail, we first made HEK cell lines that constitutively expressed an auxiliary subunit and DOX dependently expressed the GluA2 subunit of the AMPAR. For these cells the flip splice isoform and pore RNA-edited (i.e. arginine (R) in the edited site) form of GluA2 was used, resulting in a CTZ-sensitive and calcium-impermeable channel. The constitutive expression of auxiliary subunits ensured an excess of auxiliary subunits to associate with mature AMPARs. The RNA-edited form of GluA2, with an arginine in the pore, naturally conducts less current than the unedited Q isoform of the channel, keeping these cell lines healthier during the assay. Nevertheless, while maintaining these lines, cells were cultured in 30 μM NBQX, an AMPAR antagonist, to decrease cell death due to excitotoxicity. A2R-GSG and A2R cells did not show any activity in the VSD

Cell Lines	Abbrev.	Description
TetON HEK cell	TetON	parental cell line
TetONGluA2flip(R) clone #4	A2R	DOX dependent A2R
TetONGluA2flip(R) clone #4 pBOSS-CNIH3 clone #3-3	A2R-C3	DOX dependent A2R, constitutive C3
TetONGluA2flip(R) clone #4 pBOSS-stg-IRES-mCherry clone #7	A2R-stg	DOX dependent A2R, constitutive C3
GluA2flip(Q)-FLAG + GSG1L-1D4 pTREt-Va TetON clone #20	A2Q-GSG	DOX dependent A2Q and GSG
GluA2flip(Q)-FLAG + CNIH3-1D4 pTREt-Va TetON clone #8	A2Q-C3	DOX dependent A2Q and C3
GluA2flip(Q)-FLAG pTREt-Va TetON clone #5	A2Q	DOX dependent A2Q
GluA2flip(Q)-FLAG-stargazin pTREt-Va TetON clone #13	A2Q-stg	DOX dependent A2Q and stg, tethered

Table 4-1. Summary of cell lines used for high throughput screening.
The stable HEK cell lines that were used for all screening in chapter 4, together with each assigned abbreviation and doxycycline (DOX) dependency of protein expression.

assay when exposed to glutamate (data not shown), consistent with negative modulatory function of GSG1L and low channel conductance of GluA2flip(R) variant[281,284].

A VSD assay screen

Our initial screening technique utilized a VSD whose fluorescence increases when the cell depolarizes. This allowed us to detect depolarization of HEK293 cell membranes when functional AMPAR complexes were present and gated by glutamate. After pre-incubation with the compounds diluted in VSD dye (**Figure 4-1Ai**), glutamate was added to the cells (**Figure 4-1Aii**), opening the AMPAR, and resulting in an increase in fluorescent signal. To analyze the results, we used 4 different parameters, which we termed CMPDslope, CMPDmaxmin, GLUslope, and GLUmaxmin, which are described in the methods section above (**Figure 4-1B**).

Compounds were classified as hits if a measurement varied by more than 3 standard deviations from the mean signal of an EC_{50} (3-4 μM) amount of glutamate (**Figure 4-1B(blue)**) within the test population of each 384-well plate. Hits were further categorized into Tier 1-4 as described in the methods (**Figure 4-1C**). The Z' was used to assess the reliability of the screen in a high-throughput format. Z' is the ratio of the difference in standard deviations of positive and negative controls over the difference in their means[285]. Values from 0.5-1 indicate that the response being measured is robust enough to be used as an HTS assay. Each glutamate plate contains a positive control (1 mM, maxGLU) and a negative control (30 μM, NBQX) to calculate the Z' score. An example of a hit compound is shown in Figure 1D (black traces), where a robust response was detected in A2R-stg cells (**Figure 4-1D1**) but not in A2R (**Figure 4-1D2**) or TetON (**Figure 4-1D3**) cells, which serve as counter-screens.

Responses to known AMPAR ligands in the VSD assay

Known AMPAR ligands were tested against A2R-stg and A2R-C3 cell lines using this method to validate our assay. We tested a partial agonist, FW, and two PAMs, CX-546 and CTZ[99,101,102]. FW showed

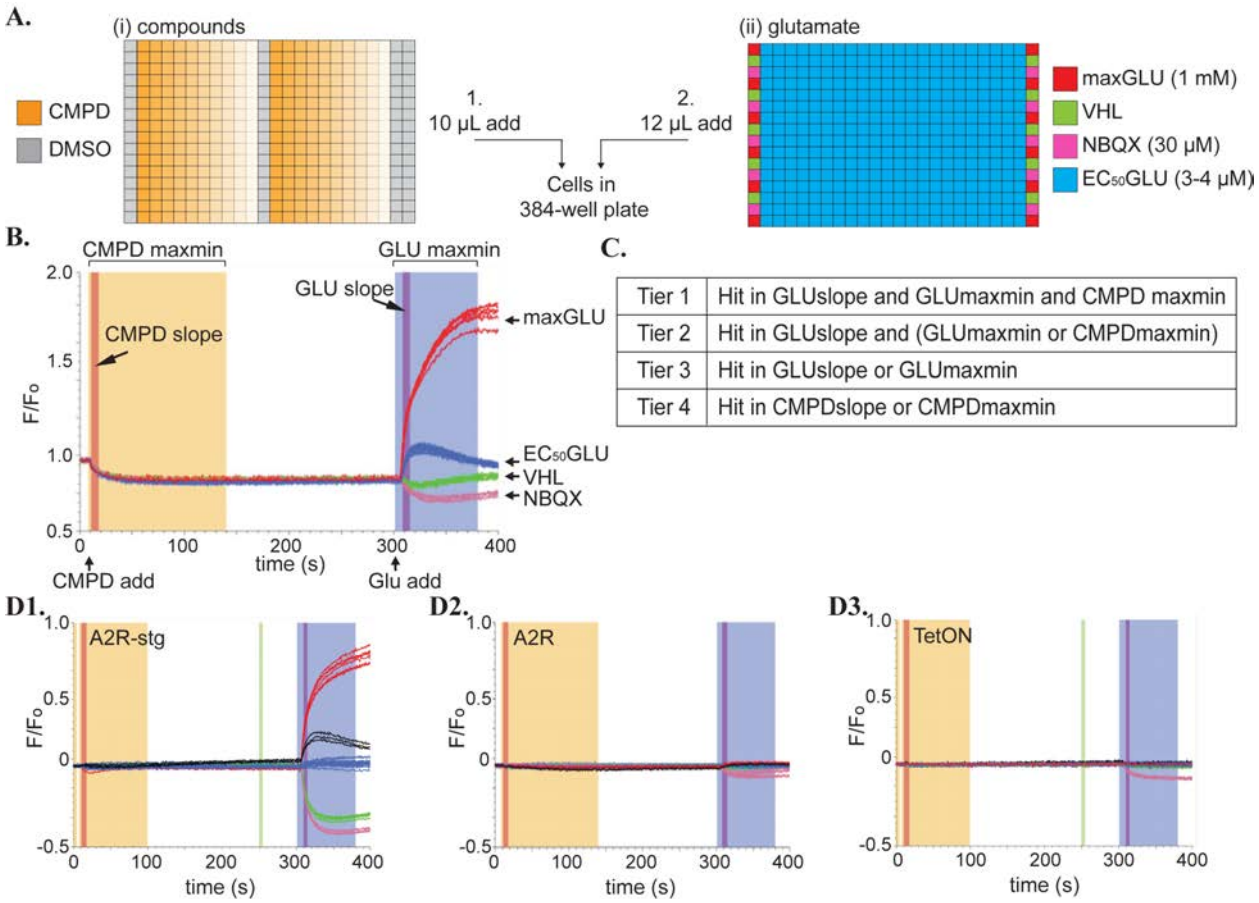

Figure 4-1. Configuration of VSD assays.

(A) Arrangement of wells in compound and glutamate plates added to cells by the FDSS. **(i)** Compounds (orange) are added at 10 µM concentration in initial screen and as a 40 µM – 10nM curve (decreasing color saturation) for CRC testing. **(ii)** Controls to determine a Z' for each plate line the edges of the glutamate plate. Positive control = 1mM glutamate (maxGLU, red), 1X FLIPR Blue dye vehicle (VHL, green), negative control = 30 µM NBQX (NBQX, pink). EC_{50} glutamate (3-4 µM) is added across the plate (EC_{50}GLU, blue) with columns 2 and 23 used as EC_{50}GLU controls with DMSO. DMSO control was moved to column 12, in CRC plates. **(B)** Normalized fluorescence data (ratio of the F/F_o) readout for the FDSS on a VSD experiment showing the compound and glutamate additions at 10 sec and 300 sec, respectively. Controls are shown in colors corresponding to their colors in the glutamate plate in A(ii). Different hit windows are shaded in dark orange (CMPDslope), light orange (CMPDmaxmin), purple (GLUslope), and violet (GLUmaxmin). **(C)** Definition of Tier 1-4 hits in our initial screen. Hits were determined as those compounds that deviated from the mean of the test population EC_{50}GLU by more than three standard deviations in the windows specified on a per plate basis. **(D)** Example of a compound (black trace) that hit on **(1)** A2R-stg cells but not on **(2)** A2R or **(3)** TetON cells. Controls are maxGLU (red), vehicle (green), 30 µM NBQX (pink), all normalized to EC_{50}GLU (blue).

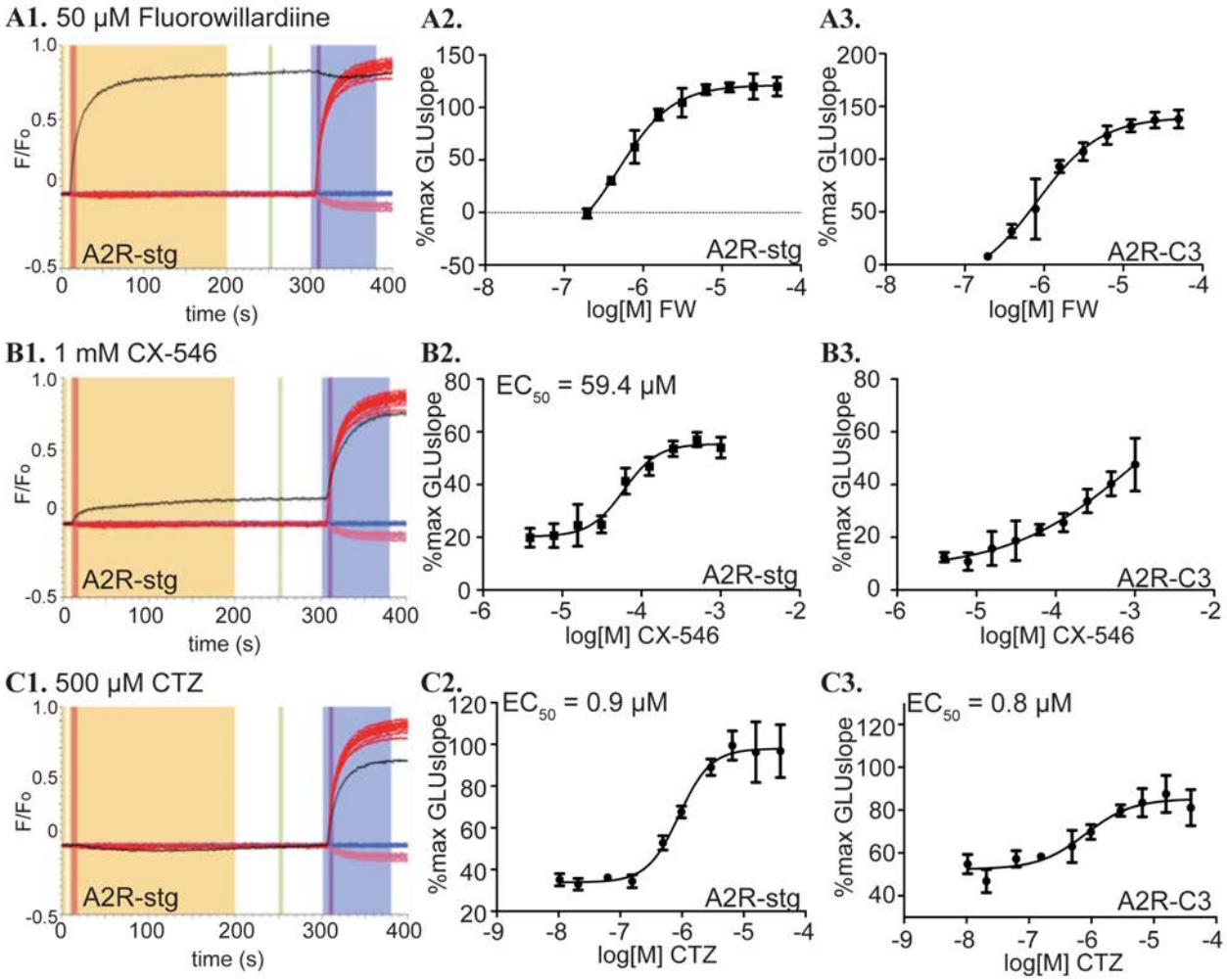

Figure 4-2. Behavior of established compounds in VSD assay.
(A1) Normalized fluorescence data for VSD assay on A2R-stg cells with 50 μM fluorowillardiine (black) with maxGLU (red) and NBQX (pink) controls, all normalized to EC_{50}GLU (blue). **(A2)** CRC curves for FW against A2-stg and (**A3)** A2-C3 cell lines calculated from the CMPDslope window. %max GLUslope = (CMPDslope - mean VHLslope)/(mean maxGLUslope - mean VHLslope) is further described in methods. (**B1)** Normalized fluorescence data for VSD assay on A2R-stg cells with 1 mM CX-546 (black) with maxGLU (red) and NBQX (pink) controls, all normalized to EC_{50}GLU (blue). **(B2)** CRC curves for CX-546 against A2R-stg and (**B3)** A2R-C3 cell lines calculated from the GLUslope window. %max GLUslope = (GLUslope - mean VHLslope)/(mean maxGLUslope - mean VHLslope) **(C1)** Normalized fluorescence data for VSD assay on A2R-stg cells with 500 μM cyclothiazide (CTZ, black) with maxGLU (red) and NBQX (pink), all normalized to EC_{50}GLU (blue). **(C2)** CRC curves for CTZ against A2-stg and **(C3)** A2-C3 cell lines calculated from the GLUslope window. Compound EC_{50} values that could be reliably calculated are in the top left corner of each graph.

a CMPDslope response comparable to the GLUslope response to glutamate alone as expected for a partial agonist (**Figure 4-2A1**, compare black FW and red glutamate traces). Due to an incomplete concentration response curve (CRC) (**Figure 4- 2A2-3**), we were unable to calculate a reliable EC_{50}. CX-546 is an ampakine PAM of AMPARs. In the absence of glutamate, there was a slight increase in fluorescence with CX-546 only at high concentrations (>250 μM) (**Figure 4-2B1**), which would be detected as a hit even with filtering criteria that we imposed in the actual screening. We found the EC_{50} for CX-546 on our A2R-stg cell line to be 59.4 μM. This is an order of magnitude more potent than the previously reported EC_{50} of 563 μM for GluA2-stg[286]. While an EC_{50} could not be accurately calculated for A2R-C3, CX-546 is over two orders of magnitude less potent than for A2R-stg (**Figure 4-2B2-3**). CTZ showed the least amount of activity in the compound only window (**Figure 4-2C1**), consistent with CTZ being a non-competitive allosteric modulator. The EC_{50}s of CTZ on A2R-stg and A2R-C3 cells were similar, 0.9 μM and 0.8 μM, respectively (**Figure 4-2C2-3**). These values were closer to published values of 2.2 μM on GluA2 alone[100] and 2 μM of GluA1-stargazin[287] than the EC_{50} value of CX-546. Responses to a known AMPAR partial agonist and PAMs demonstrate that our VSD assay can detect these drugs as hits.

Screening workflow

The screening workflow is summarized in Figure 4-3. Our primary screen tested 39,202 compounds against A2R-stg cells at a dose of 10 μM to detect changes in response compared to EC_{50} glutamate (**Figure 4-3 Box A**). From these, we pulled 187 Tier 1 hits, 325 Tier 2 hits, 1509 Tier 3 hits, and 3270 Tier 4 hits. Tier 3 and 4 hits were discarded if they didn't return to baseline before the addition of glutamate because their GLUslope values were difficult to compare to glutamate alone, reducing the numbers to be counter-screened to 628 and 44 in Tier 3 and Tier 4, respectively. These 1,184 compounds were subjected to counter-screens using duplicate wells of 10 μM compound to determine their activity against A2R and TetON cells (**Figure 4-1D**). Those compounds that showed activity would indicate auxiliary subunit and AMPAR independent effect in A2R and TetON cells, respectively, and were discarded. To determine their specificity for stargazin, these compounds were also screened against A2R-C3 cells. We kept compounds that were stargazin specific and that hit on both stargazin and CNIH3 (auxiliary subunit specific) (**Figure 4-3 Box B**). Collectively, these counter-screens reduced the number of GluA2-auxiliary subunit specific hits to 166 compounds. Full CRCs (see Experimental Procedures) were obtained against A2R-stg and A2R-C3 cell lines to determine if these compounds would fit to a dose response curve (**Figure 4-3 Box C**).

From these initial CRCs using the Vanderbilt Discovery Library plates, 77 PAMs, 10 NAMs, and 3 compounds with different effects on A2R-stg and A2R-C3 were identified. 39 PAMs were stargazin specific, 2 were CNIH3 specific, and 36 potentiated both cell lines. There were fewer NAMs identified, with only one stargazin specific NAM and 9 NAMs that hit both cell lines. 3 compounds showed opposite activity in the two cell lines (**Figure 4-3 Box D**). After discarding compounds with a large amount of activity in the compound only window at concentrations lower than 7.5 μM (**Figure 4-3 Box D**), 57 of these hits were supplied as dry samples from Life Chemicals to examine their reproducibility (**Figure 4-3 Box E**). When repeating CRCs with the new batch of samples, 48 of the 57 compounds were found to reproducibly show a curve fit in the range tested (n=2). The 57 reordered compounds were evaluated in the calcium flux assays for further testing as described below (**Figure 4-3 Box F**).

A calcium flux assay to further verify hits

GluA2(Q) cell lines were used in the calcium flux assays so that the AMPARs would be calcium-permeable. These assays have a more sensitive readout than the VSD assays described above. Fluo-8 based calcium flux assays were used as a final screen for the 57 ligands selected from the VSD assay and 28 of these showed PAM or NAM activity on A2Q-stg and/or A2Q-C3 cell lines that warranted performing full CRC experiments in all A2Q cell lines (**Figure 4-3 Box F**). For this purpose, we had created stable cell lines DOX dependently co-expressing GluA2flip(Q), the pore unedited, calcium-permeable isoform, and each auxiliary subunit (A2Q, A2Q-stg, A2Q-C3, A2Q-GSG; summarized in **Table 3-1**). To verify our assay, a compound CRC for CTZ was examined for each cell line, as described below, and gave EC_{50} values ranging from 0.4 to 1.9 μM, which were in good agreement with the known values

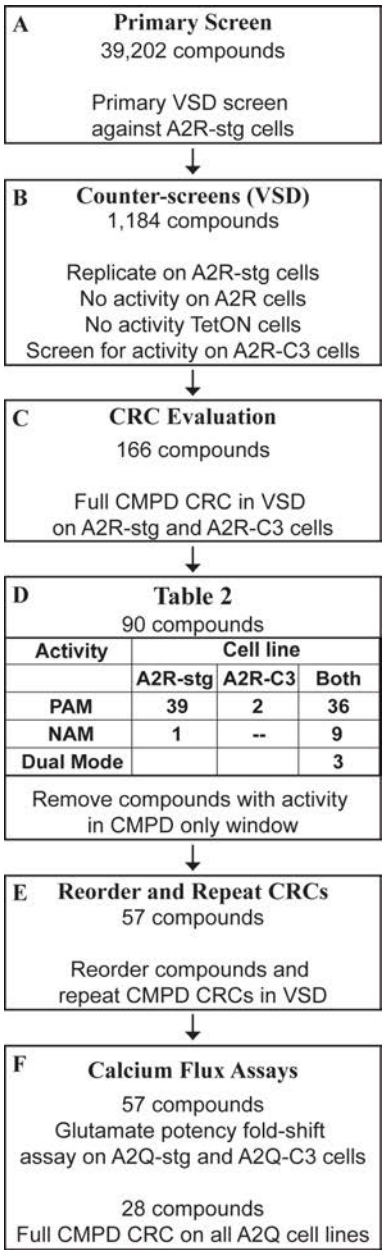

Figure 4-3. Workflow for identifying AMPAR-auxiliary subunit modulators.
(A) 39,202 compounds were initially screened using the VSD assay against A2R-stg cells. **(B)** 1,184 hits from (A) were counter-screened against A2R, TetON, and A2R-C3 cells. **(C)** 116 compounds were identified from counter-screening in (B) as being stargazin or auxiliary subunit specific (i.e. they did not hit on A2R or TetON cells). These were tested for full compound CRCs against A2R-stg and A2R-C3 cells using the VSD assay. These CRCs identified 90 hits that fit to sigmoidal dose response curves with potency under 10 μM. **(D) (Table 2)** We identified 39 stargazin specific PAMs, 2 CNIH3 specific PAMs, and 36 PAMs that had activity in both A2R-stg and A2R-C3 cells. We also found 1 stargazin specific NAM and 9 compounds with NAM activity on both cell lines. Three compounds gave opposite effects in the two cell lines. Hits were discarded for reorder if they showed activity in the compound only window. Hits with activity in the CMPD only windows were discarded. **(E)** 57 of the 90 compounds in (D) were re-screened with new batch samples as compound CRCs in the VSD assay. **(F)** 57 hits were tested in the glutamate potency fold-shift calcium flux assay and 28 were subjected to a full compound CRC calcium flux assay to study their effects using an orthogonal approach.

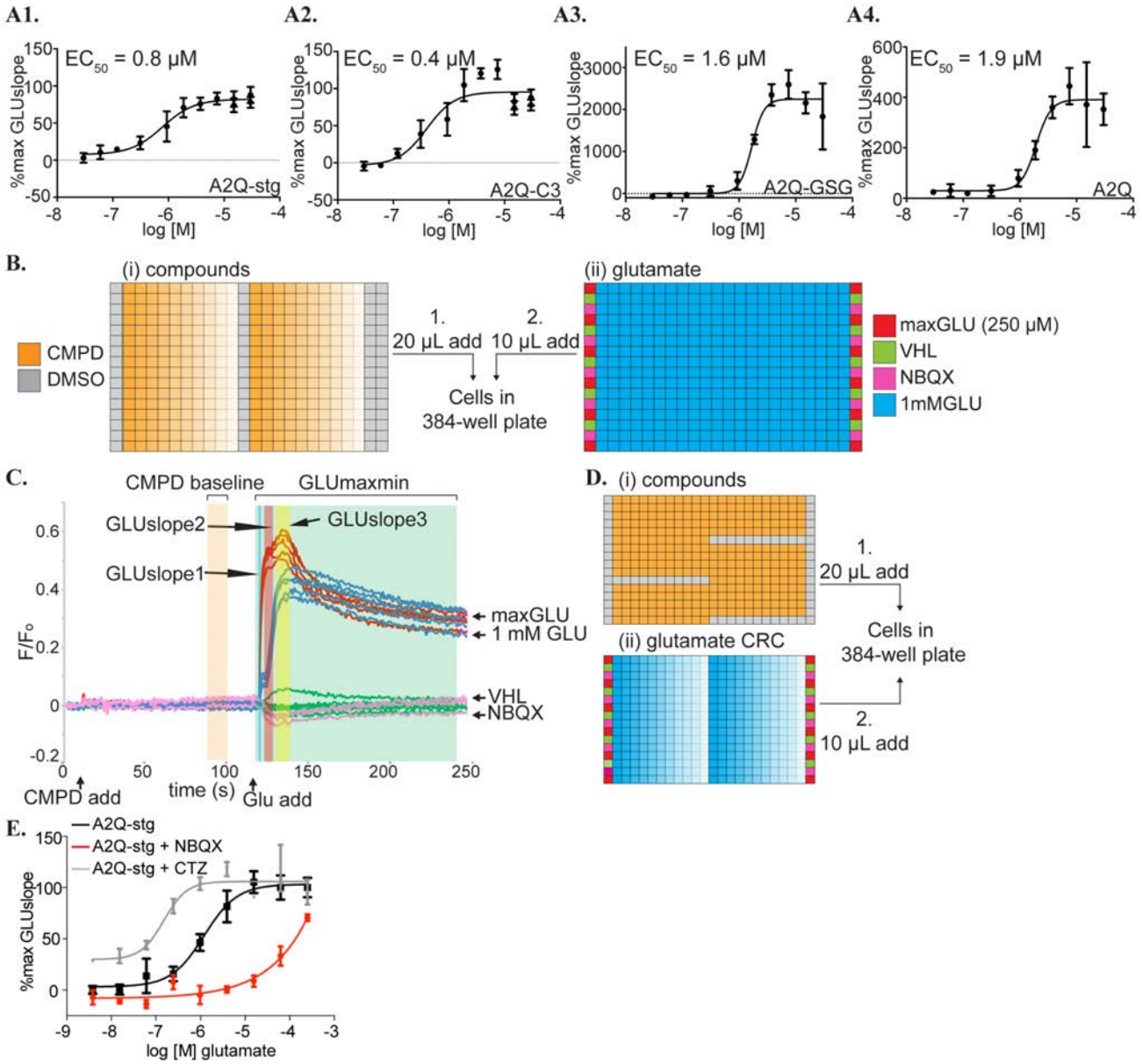

Figure 4-4. Controls and experimental setup for calcium flux assays.

(A) CRC curves for CTZ in the presence of 1 mM glutamate from **(1)** A2Q-stg, **(2)** A2Q-C3, **(3)** A2-GSG, **(4)** A2Q cell lines in the calcium flux assay. These CRCs are calculated from the GLUslope1 (t=122-125s) window. Calculated EC_{50} values are included in the top left of the graph. %max GLUslope = (GLUslope – mean VHLslope) / (mean maxGLUslope – mean VHLslope) as described in methods. **(B)** Compound and glutamate plates added to cells by the FDSS in our Fluo-8 calcium flux compound CRC assay. **(i)** Compounds (orange) are added as a 30 µM – 30 nM CRC (decreasing color saturation). **(ii)** Controls to determine a Z' for each plate line the edges of the glutamate plates. Positive control = 250 µM glutamate (maxGLU, red), high calcium buffer vehicle (VHL, green), and negative control = 30 µM NBQX (NBQX, pink). 1 mM glutamate is added across the plate (blue) with columns 12 and 23 used as a 1mM glutamate and DMSO control. **(C)** Vehicle subtracted, normalized fluorescence data readout for the FDSS on A2Q-stg cells in a calcium flux experiment showing the compound and glutamate applications at 10s and 120s, respectively. Controls are shown in colors corresponding to their colors in the glutamate plate in (D). Different hit windows are shaded in blue (GLUslope1, 122-125s), red (GLUslope2, 126-132s), yellow (GLUslope3, 140-150s), green (GLUmaxmin). The orange window is a reference baseline (CMPD baseline) prior to the glutamate addition used to determine if the compound shows activity in the absence of glutamate. **(D)** Compound and glutamate plates added to cells by the

FDSS in our Fluo-8-based glutamate potency fold-shift assay. **(i)** Compounds (orange) are first added at 30 μM with DMSO controls in columns 1,24, and also in K1-K12, F13-23, P13-23, overlapping with glutamate concentration curves for a per plate comparison to compound. **(ii)** Controls are loaded on the edge as in (Bii) and a glutamate CRC is loaded horizontally ranging from 4 mM to 10 pM (decreasing color saturation). **(E)** An example of the readout for our glutamate potency fold-shift assay. A rightward shift of the NBQX pretreated cells (red) as compared to glutamate alone (black) indicates NAM activity. The leftward shift of CTZ pretreated cells (grey) indicates PAM activity.

Compound	EC_{50}/IC_{50} VSD		EC_{50}/IC_{50} Ca^{2+} Sensing				Shift of Glutamate EC_{50}	
VU0612951	1.5 μM ±0.14	0.87 μM ±0.01				*7.5 μM ±0.20*	0.78	0.45
VU0627849	0.86 μM ±0.07	0.85 μM ±0.13	1.8 μM ±0.04	3.1 μM ±0.02	*24.9 μM ±0.09*	*14.1 μM ±0.22*	4.50	6.75
VU0539491	4.2 μM ±0.15	3.2 μM ±0.06	*9.4 μM ±0.21*				0.82	0.67
Cell line	**A2R-stg**	**A2R-C3**	**A2Q-stg**	**A2Q-C3**	**A2Q-GSG**	**A2Q**	**A2Q-stg**	**A2Q-C3**

Figure 4-5. Table of results from VSD and calcium flux assays.
EC_{50} or IC_{50} values determined by CRC fits from GLUslope. Boxes highlighted green indicate an EC_{50} or a positive trend, red indicate an IC_{50} or a negative trend. Estimated EC_{50} values are added in italics, but are estimated due to incomplete CRC curves or insufficient differences in %max GLUslope across the CRC. Glutamate potency fold-shift assays indicate how much fold-change occurred in the glutamate EC_{50} when cells were pretreated with 30 μM compound. Values greater than 2 indicate PAM activity and less than 1 indicate NAM activity.

(2.2 μM on GluA2 alone[100] and 2 μM on GluA1-stg[287] (**Figure 4-4A1-4**) and similar to those calculated from our VSD assay (**Figure 4-2C2-3**).

In brief, the compound CRC assay was conducted as follows (see methods for details). Cells were loaded with Fluo-8 and excess dye was washed out. After 120 secs of pre-incubation with compound at concentrations ranging from 30 μM to 30 nM (**Figure 4-4Bi**), 1 mM glutamate was added (**Figure 4-4Bii**). In the calcium assay, 250 μM was used as the maxGLU dose because the GLUslope1 values decreased at higher concentrations of glutamate, making it the dose with the maximal GLUslope1 response. This decrease in activity at high glutamate concentration has been seen in other publications[288,289]. We measured GLUslope in three consecutive time windows, referred to as GLUslope1-3, because three phases were clearly detectable (**Figure 4-4C**). The final CRC curves were calculated from GLUslope1, obtained from the first 3-6 sec window.

Prior to compound CRCs, we performed a glutamate potency fold-shift assay to determine how a maximal dose of compound would shift the EC_{50} of glutamate on A2Q-stg and A2Q-C3 cells. In this assay, a maximal dose (30 μM) of each compound (**Figure 4-4Di**) was incubated on cells for 120 secs and then a CRC for glutamate ranging from 4 mM to 10 pM was collected (**Figure 4-4Dii**). A rightward shift of the CRC for glutamate to a higher EC_{50} indicates NAM activity and a leftward shift to a lower EC_{50} indicates PAM activity (**Figure 4-4E**). 28 of the 57 compounds modified the activity, when compared to the glutamate EC_{50} or 1mM glutamate controls per plate. These compounds, considered active, were then evaluated as a CRC of the compounds in the calcium flux assay.

VU compound CRCs were collected against all A2Q containing cell lines using the same protocol as CTZ, described above (**Figure 4-4B**). The final compound CRC curves were calculated from GLUslope1. The area under the curve (AUC) in the GLUmaxmin window was used as an alternative measure to calculate the CRC because compounds sometimes deviated from the 1 mM glutamate trace in different GLUslope windows. The AUC measures the accumulation of calcium instead of gating and sometimes produced a CRC fit when GLUslope1 could not derive an EC_{50} value.

Description of candidate compounds

As described above, all compounds were subjected to a counter-screen against A2R and TetON cells. While this should, in theory, remove compounds with any activity on AMPAR without auxiliary subunits present, the increased sensitivity of the calcium flux assay revealed that some compounds did show NAM or PAM activity in A2Q cells. Our pipeline has led us to specify 3 compounds for further characterization (summarized in **Figure 4-5**) that exhibit the most robust difference in pharmacology between cell lines. In addition, these three compounds have attractive chemical structures and properties for further hit-to-lead exploration. Each of the three molecules identified bears a modular chemical structure with a central five-membered heterocyclic core structure - either a 1,3-triazole, isoxazole, or a 1,2,4-oxadiazole. The trisubstituted triazole containing a carbocyclic amide structure represented by VU0612951 displayed modest NAM activity (**Figure 4-6A**), whereas, the disubstituted isoxazole VU0627849 maintains robust potentiator activity (**Figure 4-6B**). Lastly, VU0539491, which contains a unique 1,1, disubstituted cyclic structure, also partially related to VU0612951 via the benzylic reverse-amide, shows mixed pharmacology (NAM and PAM) depending on the cell-type (**Figure 4-6C**).

Hit molecule VU0612951 was identified as a NAM in both A2R-stg and A2R-C3 cell lines in the VSD assay. In the raw VSD traces, NAM activity on A2R-stg was evident even at submicromolar concentrations, while on A2R-C3 cell line the NAM effect required concentrations higher than 1 μM (**Figure 4-7A**). The ~40% decreases in %max GLUslope across the CRC (**Figure 4-7B**) and right-shifts in the glutamate potency fold-shift assay (**Figure 4-5**) indicate strong NAM activity for stargazin and CNIH3 containing AMPAR complexes. The magnitude of effect on GLUslope for VU0612951 was low in the calcium flux assay and only evident at high concentrations (**Figure 4-7C**, 30 μM), making it difficult to reliably obtain CRCs. In fact, the CRCs calculated from GLUslope did not show a negative trend on any cell line except A2Q-stg (**Figure 4-7D).** We therefore used %max AUC instead of %max GLUslope to derive CRCs (**Figure 4-7E**), the results of which are consistent with VU0612951 as a NAM.

The most promising PAM discovered was VU0627849. The VSD raw data shows PAM activity on both A2R-stg and A2R-C3 complexes at concentrations as low as 2.5 μM (**Figure 4-8A**). These data fit well to CRCs calculated from the GLUslope (**Figure 4-8B**). This compound did not show any activity on A2R cells in our counter-screens (**Figure 4-3 Box B**). VU0627849 was also a PAM in all GluA2-

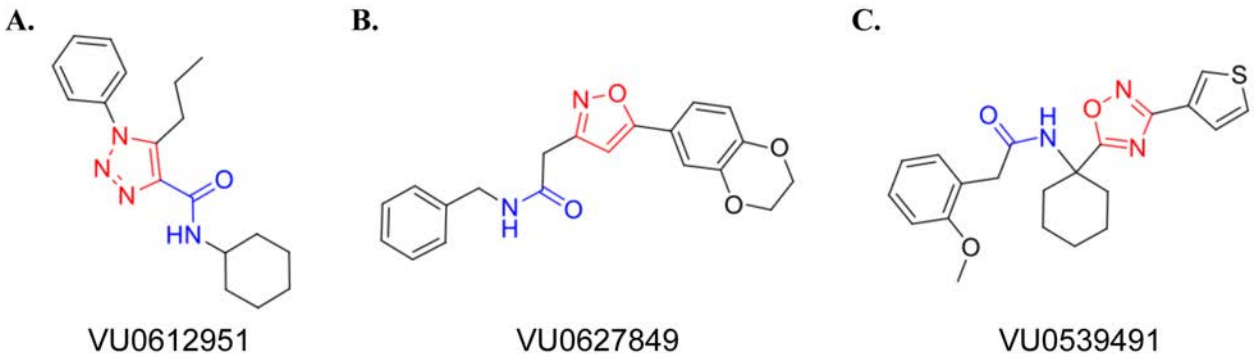

Figure 4-6. Chemical structures of our candidate hits.
(A) Structure of VU0612951 highlighting the 1,3-triazole group in red. **(B)** Structure of VU0627849 highlighting the isoxazole group in red. **(C)** Structure of VU0539491 highlighting the 1,2,4-oxadiazole group in red.

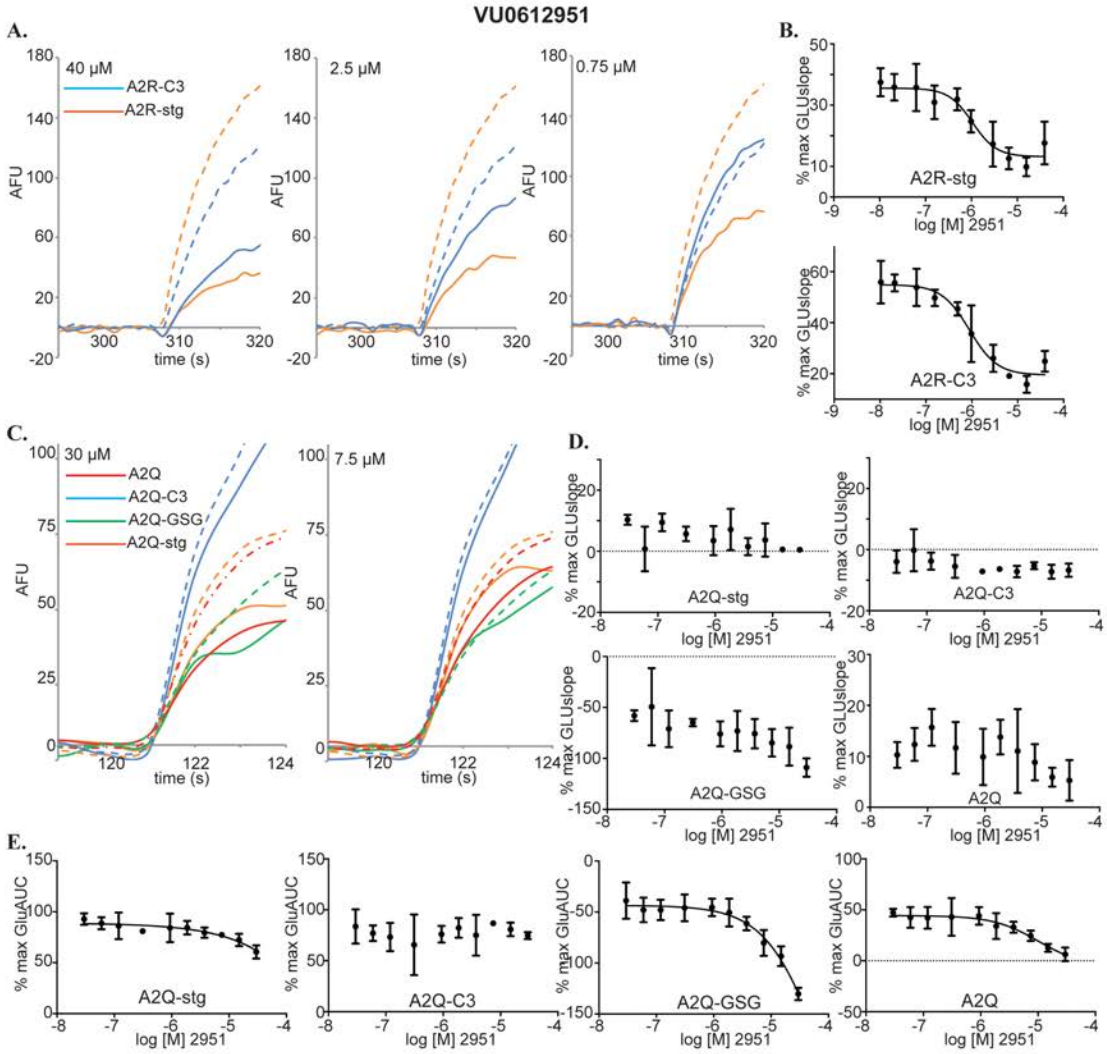

Figure 4-7. Characterization of VU0612951.
(A) Raw data for compound CRCs in the VSD assay. A2R-stg (orange) and A2R-C3 (blue). EC_{50}GLU traces are represented by dashed lines. Compound concentrations are indicated in the top left corner. **(B)** CRCs calculated from GLUslope in the VSD assay for A2R-stg and A2R-C3 cells. Error bars are standard deviations. **(C)** Raw data for compound CRCs in the calcium flux assay. A2Q (red), A2Q-stg (orange), A2Q-GSG (green), and A2Q-C3 (blue). Dashed lines are signal of 1mM glutamate without compound. **(D)** Compound CRCs in calcium flux assay for A2Q-stg, A2Q-C3, A2Q-GSG, and A2Q cell lines. These are derived from the GLUslope1 window. **(E)** Compound CRCs calculated from the AUC in the GLUmaxmin window of the calcium flux assay plotted as %max AUC in the GLUmaxmin window (see Fig 4C) vs. log [compound].

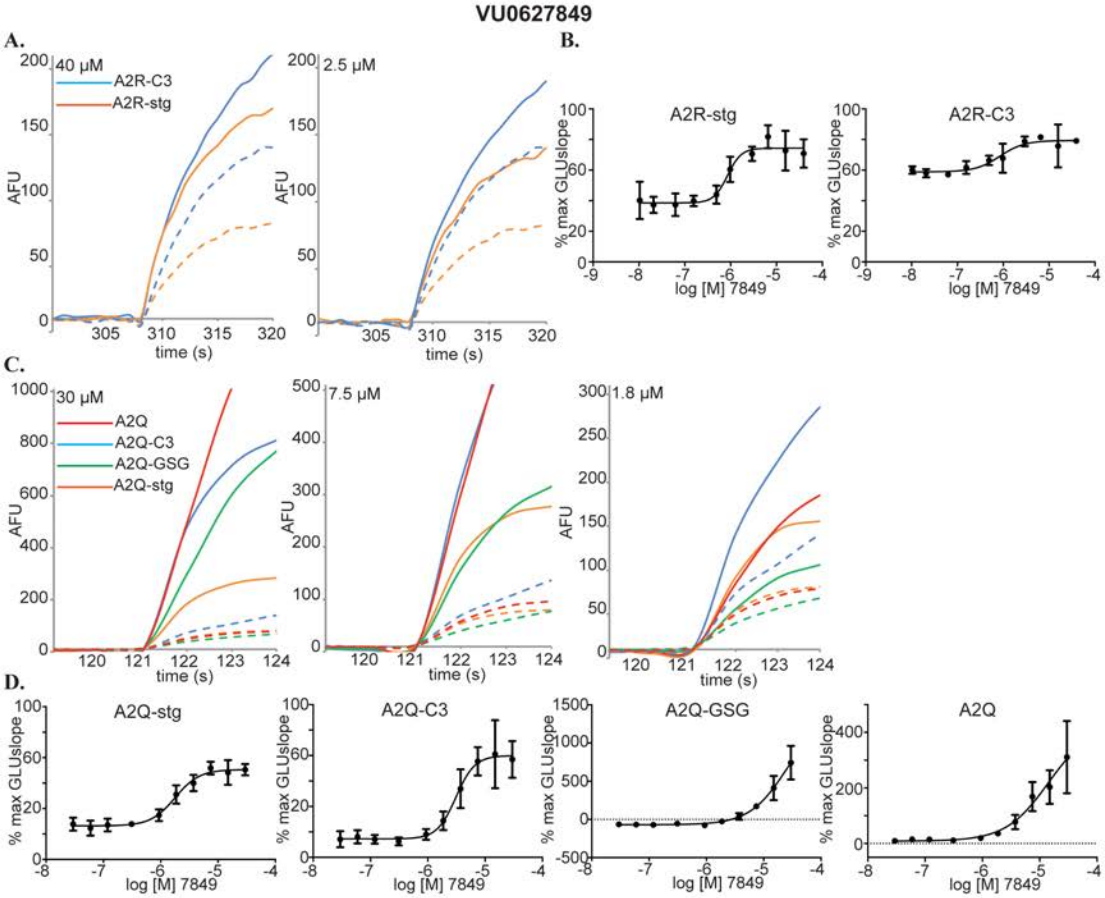

Figure 4-8. Characterization of VU0627849.
(A) Raw data for compound CRCs in the VSD assay. A2R-stg (orange) and A2R-C3 (blue). EC_{50}GLU traces are represented by dashed lines. Concentrations of compound are indicated in the top left corner. **(B)** CRCs calculated from GLUslope in the VSD assay for A2R-stg and A2R-C3. **(C)** Raw data for compound CRCs in the calcium flux assay. A2Q (red), A2Q-stg (orange), A2Q-GSG (green), and A2Q-C3 (blue). 1 mM glutamate traces are represented by dashed lines. **(D)** CRCs calculated from GLUslope1 in calcium flux assay for A2Q-stg, A2Q-C3, A2Q-GSG, and A2Q cell lines. Plotted as %max GLUslope vs. log [compound].

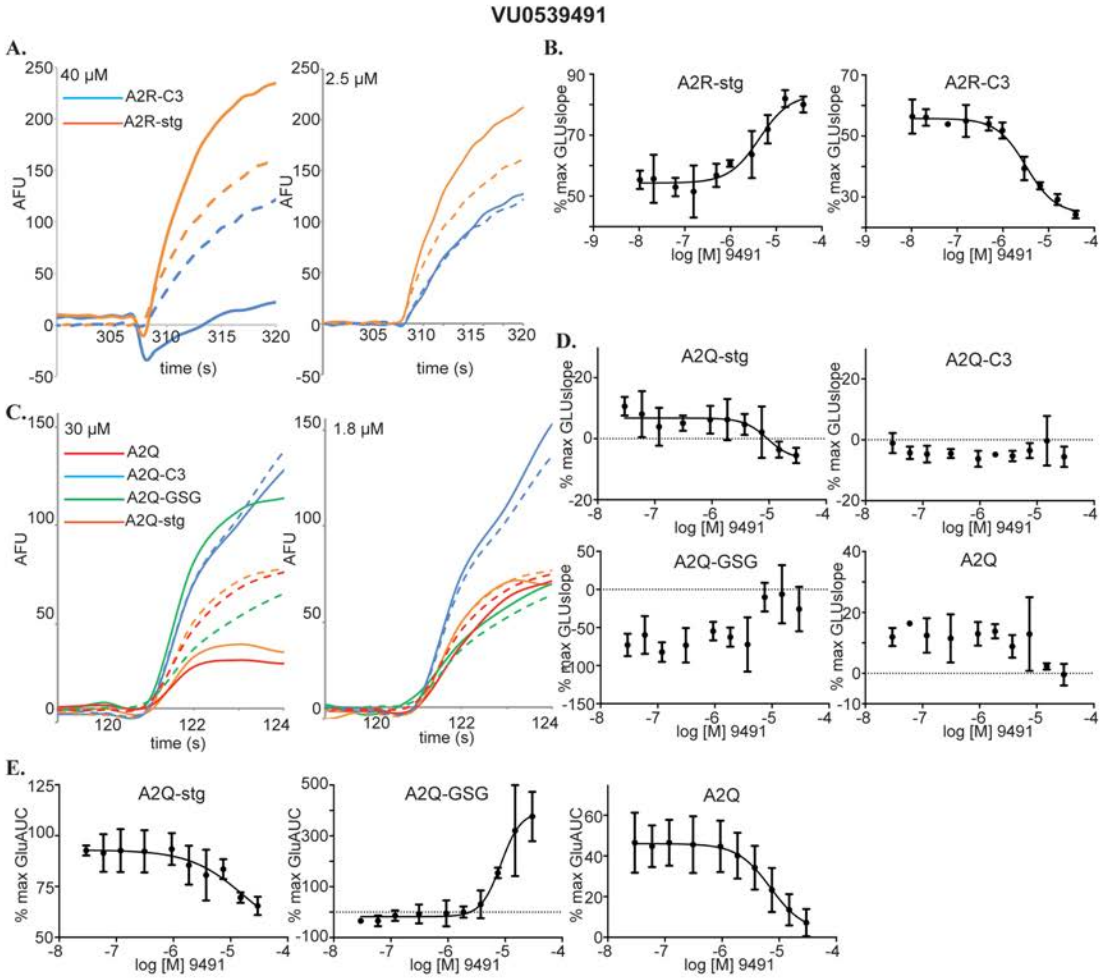

Figure 4-9. Characterization of VU0539491.
(A) Raw data for compound CRCs in the VSD assay. A2R-stg (orange) and A2R-C3 (blue). EC_{50}GLU traces are represented by dashed lines. Compound concentrations are indicated in the top left corner. **(B)** CRCs calculated from GLUslope in VSD assay for A2R-stg and A2R-C3. **(C)** Raw data for compound CRCs in the calcium flux assay. A2Q (red), A2Q-stg (orange), A2Q-GSG (green), and A2Q-C3 (blue). Traces obtained from applying 1 mM glutamate are represented by dashed lines. **(D)** Compound CRCs calculated from the GLUslope1 window in our calcium flux assay for A2Q-stg, A2Q-C3, A2Q-GSG, and A2Q cell lines. These show negative and positive trends but no curve fits. **(E)** Compound CRCs calculated from the AUC in the GLUmaxmin window of the calcium flux assay plotted as %max AUC vs. log [compound] as in (7E).

expressing cell lines in the calcium flux assay. VU627849 potentiated A2Q-stg cells the least compared to all others and its level of potentiation does not change between 7.5 and 30 μM (**Figure 4-8C**, solid orange). At these concentrations, the increases in response of A2Q-stg cells to VU0627849 were fixed to ~300 arbitrary fluorescence units (AFU), while in the other three cell lines the effects nearly doubled from 7.5 μM to 30 μM. (**Figure 4-8C**, compare solid lines between 30 and 7.5 μM). While the increase in GLUslope on A2Q-stg cells fits to a sigmoidal dose response curve, the positive change in %max GLUslope is only ~30% as compared to >80% for the other A2Q containing cell lines. (**Figure 4-8D**).

VU0627849 shows similar values to CTZ for increase in %max GLUslope across the CRC for A2Q-C3, A2Q-GSG, and A2Q cells. There was no appreciable difference in potency seen between cell lines for CTZ, but VU0627849 shows a lower EC_{50} for A2Q-C3 than A2Q-GSG or A2Q cells (**Figure 4-4A1-4** and **Figure 4-5**). Collectively, our data suggest that this compound acts as a PAM only on A2R when in complex with auxiliary subunits, but positively modulates A2Q regardless of the presence of auxiliary subunits. In fact, VU0627849 is least efficacious on the A2Q-stg cells when comparing all four complexes we tested.

VU0539491 was a particularly interesting compound identified by our VSD screen. It acted as a PAM on A2R-stg cells, but a NAM in A2R-C3 cells in the VSD assay (**Figure 4-9A** and **B**). While exhibiting a slight decrease in signal in the raw data from the calcium flux assay for A2Q-C3 cells (**Figure 4-9C**, 30 μM blue trace), it was clearly categorized as a NAM in the glutamate fold-shift assay (**Figure 4-5**). In addition, VU0539491 showed PAM activity in the A2Q-GSG cell line (**Figure 4-9C**, green trace), which appeared as a positive trend in the CRC calculated from GLUslope (**Figure 4-9D**, A2Q-GSG) and was corroborated by a more robust fit in the CRC calculated from the AUC (**Figure 4-9E**, A2Q-GSG). Slight NAM activity on A2Q and A2Q-stg cell lines can be seen in the highest dose (40 μM) of VU0539491 (**Figure 4-9C**, orange and red traces). As in the A2Q-GSG cells, the CRCs calculated from GLUslope showed negative trends for A2Q and A2Q-stg (**Figure 4-9D**, A2Q-stg and A2Q), but CRCs calculated from the AUC show more robust curve fits (**Figure 4-9E**, A2Q-stg and A2Q). The combination of these data indicates that VU0539491 acts as a slight NAM on A2R-C3 and A2Q, but a PAM on A2Q-GSG.

We have conducted a preliminary electrophysiological investigation of the compound VU0627849. Using a fast ligand application system, A2R and A2R-stg cells were stimulated with 1mM glutamate using a 100 ms pulse followed by a 50 ms interval and a second 20 ms pulse to evaluate recovery from desensitization (**Figure 4-10A** and **B**, red traces). In the presence of 40 μM VU0627849, we observed no change in peak amplitude but delayed increase in resensitization within 10 ms following initial activation and desensitization (**Figure 4-10B**, blue trace). In addition, an increased amplitude in the second pulse of glutamate was observed. These effects are drug specific because wash out of VU0627849 restored the original current (**Figure 4-10B**, black trace). We also see a small effect on A2R cells that was not seen in the VSD assay (**Figure 4-10A**, blue trace). VU0627849 acted as a PAM on A2R-stg cells, corroborating our HTS data from the VSD assay.

Discussion

High-throughput screening has been valuable in identifying TARP γ-8 subunit specific NAMs[108–111,290]. Given the structural and functional variety of AMPAR auxiliary subunits we predicted that there should be more compounds that are targeted against specific members of this family of complexes and chose to study those containing stargazin, CNIH3, and GSG1L. From a relatively small library of 39,000 compounds, our HTS workflow identified 3 compounds for further studies.

In the current study, we focus on the PAMs and NAMs that showed activity in the presence of glutamate. Our initial data already identified compounds that show activity in the absence of glutamate and there remains a possibility of identifying new agonists by choosing to study compounds that hit in the CMPDslope window, as seen when testing fluorowillardiine. Furthermore, the primary screening was conducted for only one third of the existing Vanderbilt Discovery Library. Collectively, our HTS workflow described here has potential to identify additional candidate compounds in the future.

An interesting byproduct of our study is the pharmacology of CX-546 on AMPARs in complex with different auxiliary subunits. CX-546, an ampakine PAM, shows more than an order of magnitude increase in potency on A2R-stg cells over A2R-C3 cells. In a previous report, CX-546 had different E_{max} values when applied to AMPAR with different TARPs, but the difference in CX-546 EC_{50} values for different Type I TARPs were all within the same order of magnitude[286]. While absolute potencies in our VSD assay may

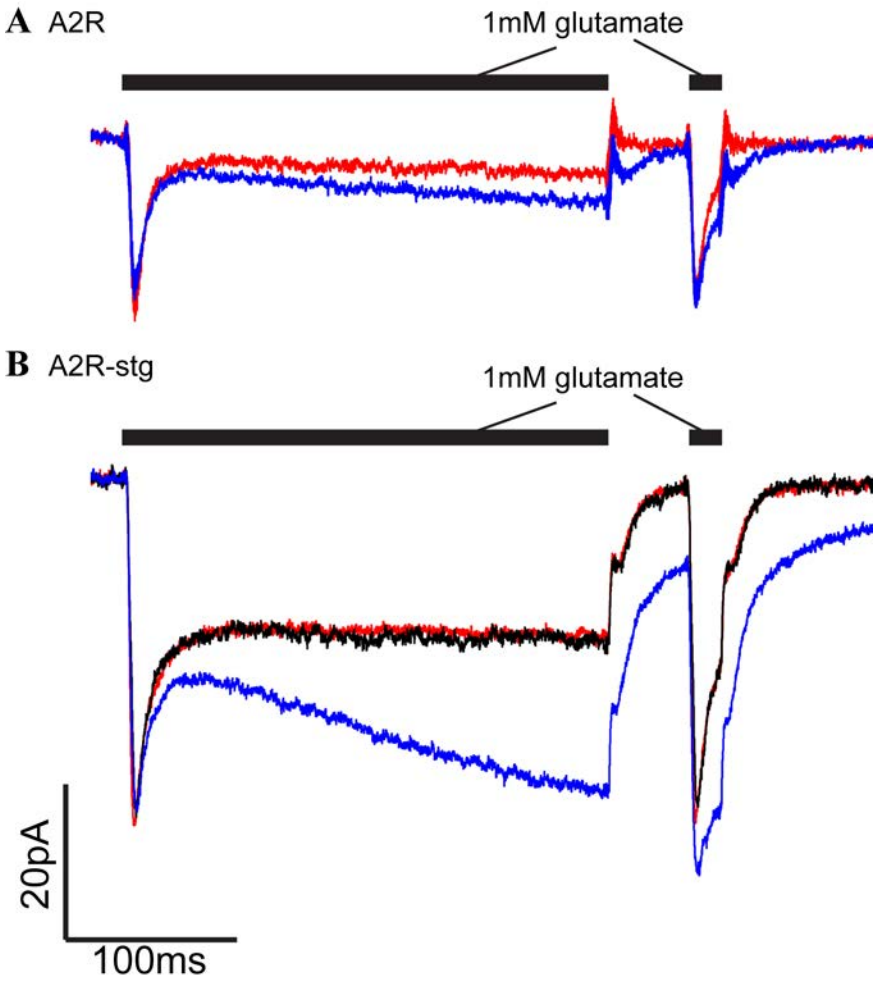

Figure 4-10. Electrophysiology recording for VU0627849.
(A) Whole-cell recordings of A2R cell line with (blue) and without (red) VU0627849 (40 μM). **(B)** Whole-cell recordings of A2R-stg cell line with (blue) and without (red) VU0627849 (40 μM). Recording after washout of drug is in black. In these experiments, glutamate (1 mM) is applied for 300 ms and 20 ms pulses with or without VU0627849.

not be reliable, we postulate that the relative difference in the potencies of CX-546 on the two complexes indicates unique pharmacology dependent on auxiliary subunits.

We identified 3 compounds for future characterization. We propose that VU0612951 is an indiscriminate NAM. While we were aiming to identify compounds with subunit specific effects, this compound has less standard deviation and a more robust response from A2R-stg cells than any others. The overall NAM profile of VU0612951 and its modular triazole core will make this an attractive template for further chemical modification to identify analogs with subunit specificity (**Figure 4-6A**). VU0627849 is an effective PAM that responds in the VSD and calcium flux assays similarly to CTZ, though they have dissimilar structures (**Figure 4-6B**). Unfortunately, it also hits multiple AMPAR complexes, but it has very little activity on A2R cells and seems to affect A2Q-stg cells less than the other A2Q cell lines in both calcium flux assays. VU0627849 could be used as a starting scaffold to determine if functional groups could be added to any of the rings to skew the activity more specifically toward a certain AMPAR-auxiliary subunit complex. VU0539491 gave conflicting results between the VSD and calcium flux assay. It appears to be a PAM in A2R-stg and NAM in A2R-C3 cell lines but acts as a NAM in the A2Q-stg and A2Q cell lines and as a PAM in A2Q-GSG (**Figure 4-6C**). VU0539491 showed similar potency in all cell lines, but the compound is most efficacious on A2R-stg cells, as a PAM, in the raw data at ~2 μM. The glutamate potency fold-shift assay also identified it as a NAM on A2Q-stg and A2Q-C3 cells (**Figure 4-5**). This compound will be interesting to study because it can act as a PAM or a NAM depending on which auxiliary subunit is present.

We acknowledge that full auxiliary subunit occupancy cannot be guaranteed with most of our cell lines and low auxiliary subunit occupancy of the AMPAR may have masked less robust candidate hits. Also, the potencies reported herein may not reflect the potency of these compounds on a fully occupied receptor. We do, however, use a tethered construct for the A2Q-stg cell line, guaranteeing a fully occupied receptor which shows the same response as A2R-stg cells for VU0612951 and VU0627849.

Further characterization using electrophysiology to validate selectivity and potency is necessary for these hits. Fluorescent signal based assays do not measure the fast kinetics of the AMPAR. Specifically, while a deviation in GLUslope and AUC are good indicators that the compounds are acting as PAMs or NAMs, we are not directly measuring gating, which occurs in several milliseconds. An initial investigation of the compound VU0627849 by fast ligand application electrophysiology recapitulated the results obtained from the VSD assay. Confirming the specificity of these compounds or further tailoring these scaffolds to make them specific may offer a whole new class of compounds for basic research and clinical use. Differential expression patterns for auxiliary subunits throughout the central nervous system seem to be a naturally designed way to specifically target AMPARs in certain regions of the brain or times of development.

Experimental Procedures

Cell lines were generated expressing GluA2flip(R), GluA2flip(R)-stargazin, GluA2flip(R)-CNIH3, GluA2flip(Q), GluA2flip(Q)-stargazin, GluA2flip(Q)-CNIH3, and GluA2flip(Q)-GSG1L complexes as detailed in *Materials and Methods* and **Table 2-1** and **Table 4-1**. Initial screening and hit selection were performed on 39,202 compounds using the VSD screening assay detailed in *Materials and Methods*. Hits were first counter-screened against A2R cells using the VSD assay and compounds that were found to be stargazin specific were further counter-screened against parental TetON HEK293 cells in the same way to see if their observed activity was due to receptors endogenous to HEK cells. Compounds that did not hit on either A2R or TetON cells were screened against A2R-C3 cells to determine whether they were stargazin or auxiliary subunit specific. *VSD concentration response curves (CRCs*): After the above counter-screens, compounds that remained positive were moved forward to collect complete CRCs for A2R-stg and A2R-C3 cell lines as described in *Materials and Methods.* Compounds with measurable potency under 10 μM that fit well to a CRC curve for either cell line were reordered as dry samples and another compound CRC in our VSD assay was run to verify that the EC_{50} results could be repeated. Compounds that were selected as hits using the VSD assay were subsequently screened against the calcium permeable A2Q-stg and A2Q-C3 cell lines in a glutamate potency fold-shift assay, detailed in *Materials and Methods* using the calcium sensing dye Fluo-8 (AAT Bioquest cat #21080). This assay is used to measure how pretreatment with compounds shifts the EC_{50} of glutamate on A2Q-stg and A2Q-C3 cells. For compounds that showed activity in the glutamate potency fold-shift assay, CRCs were run

against the calcium permeable A2Q-stg, A2Q-C3, A2Q-GSG1L, and A2Q cell lines. Outside-out patches were pulled from A2R and A2R-stg cell lines and subjected to fast glutamate application as detailed in *Materials and Methods*.

CHAPTER V: CRYO-EM STRUCTURE OF THE TRPC6 CYTOPLASMIC DOMAIN REVEALS MUTATION HOTSPOTS

This section is a paper published in *The Journal of Biological Chemistry* as "Cryo-EM structure of the cytoplasmic domain of murine transient receptor potential cation channel subfamily C member 6 (TRPC6)" Caleigh M Azumaya*, Francisco Sierra-Valdez*, Julio F. Cordero-Morales, and Terunaga Nakagawa.

Aims

The kidney maintains the internal milieu by regulating the retention and excretion of proteins, ions, and small molecules. The glomerular podocyte forms the slit diaphragm of the ultrafiltration filter, whose damage leads to progressive kidney failure and FSGS. The TRPC6 ion channel is expressed in the podocyte and mutations in its cytoplasmic domain cause FSGS in humans. *In vitro* evaluation of disease-causing mutations in TRPC6 has revealed that these genetic alterations result in abnormal ion channel gating. However, the mechanism whereby the cytoplasmic domain modulates TRPC6 function is largely unknown. Here we report a cryoEM structure of the cytoplasmic domain of murine TRPC6 at 3.8Å resolution. The cytoplasmic fold of TRPC6 is characterized by an inverted dome-like chamber pierced by four radial horizontal helices that converge into a vertical coiled-coil at the central axis. Unlike in other TRP channels, TRPC6 displays a unique domain swap that occurs at the junction of the horizontal helices and coiled-coil. Multiple FSGS mutations converge at the buried interface between the vertical coiled-coil and the ankyrin repeats, which form the dome, suggesting these regions are critical for allosteric gating modulation. This functionally critical interface is a potential target for drug design. Importantly, dysfunction in other family members leads to learning deficits (TRPC1/4/5) and ataxia (TRPC3). Our data provide a structural framework for the mechanistic investigation of the TRPC family.

Results and Discussion

Expression and purification of TRPC6

To determine the structure of the *Mus musculus* (m)TRPC6 cytoplasmic domain, we used a construct lacking the initial 94 residues at the N-terminus and the two glycosylation sites (N472Q and N560Q); referred to as TRPC6 hereafter (**Figure 5-1A**, top). This construct displays higher amounts of protein after purification than the wild type (WT) and recapitulates the lipid (OAG)-mediated activation observed in WT TRPC6 (**Figure 5-1A** and **B**). For expression and purification, we generated a baculovirus construct consisting of an 8xhistidine- MBP tag at the N-terminus of the TRPC6 sequence (**Figure 5-1A**; top). We expressed this construct in insect cells (Sf9), stably purified to homogeneity in DDM, transferred it to the amphipol PMAL-C8, and subsequently cleaved the MBP tag. Final size-exclusion chromatography resolved the TRPC6 as a single peak and to homogeneity as determined by SDS-PAGE gel (**Figure 5-1C**). Following this strategy, we obtained biochemical quantities of amphipol reconstituted detergent-free proteins for negative stain and cryo-electron microscopy analysis.

Structural heterogeneity in TRPC6 particles

The initial negative stain and cryoEM analysis of TRPC6 revealed an overall particle structure that consists of a combination of well-defined and flexible regions (**Figure 5-2**, **Figure 5-3A**). In the vitrified sample, the amphipol-embedded TRPC6 particles were monodisperse in the absence of detergent (**Figure 5-3B**). In the cryoEM class averages, substructures corresponding to α-helices were clearly detectable and views representing a four-fold symmetric architecture were observed within the well-defined region (**Figure 5-3C** and **5-5B**). In contrast, the flexible region was splayed apart at a variety of angles in the negative stain class averages (**Figure 5-4A**), while in the cryoEM class averages they were averaged out as diffuse densities (**Figure 5-3C** and **5-5B**). Attempts were made to identify a biochemical condition that would remove the structural heterogeneity, but this proved unsuccessful. To solve the cryoEM structure of the well-defined portion of the particle, while neglecting the heterogeneous remainder, we applied a mask to facilitate 3D classification in RELION2[205,213] so that only the well-structured region would be taken into account in our analysis (see Experimental Procedures).

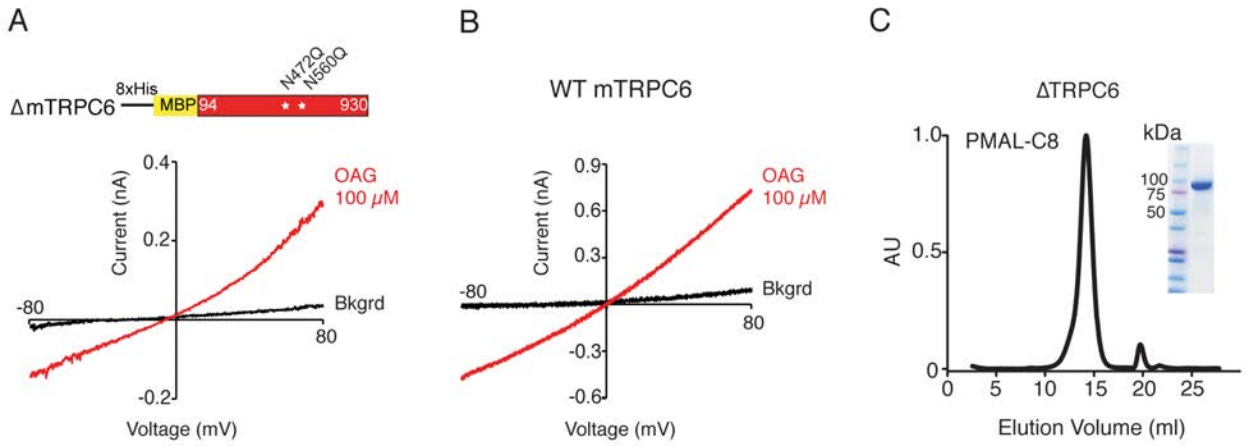

Figure 5-1. Functional and biochemical characterization of mTRPC6.
A and B. OAG-evoked currents of HEK293 cell-expressing Δ94TRPC6 (referred to as TRPC6 from here) and WT TRPC6, as determined by whole-cell patch-clamp recording. **C.** size-exclusion chromatography profile of PMAL-C8 TRPC6 protein. Inset, stained protein on the SDS-PAGE gel corresponds to the size of the purified channel monomers.

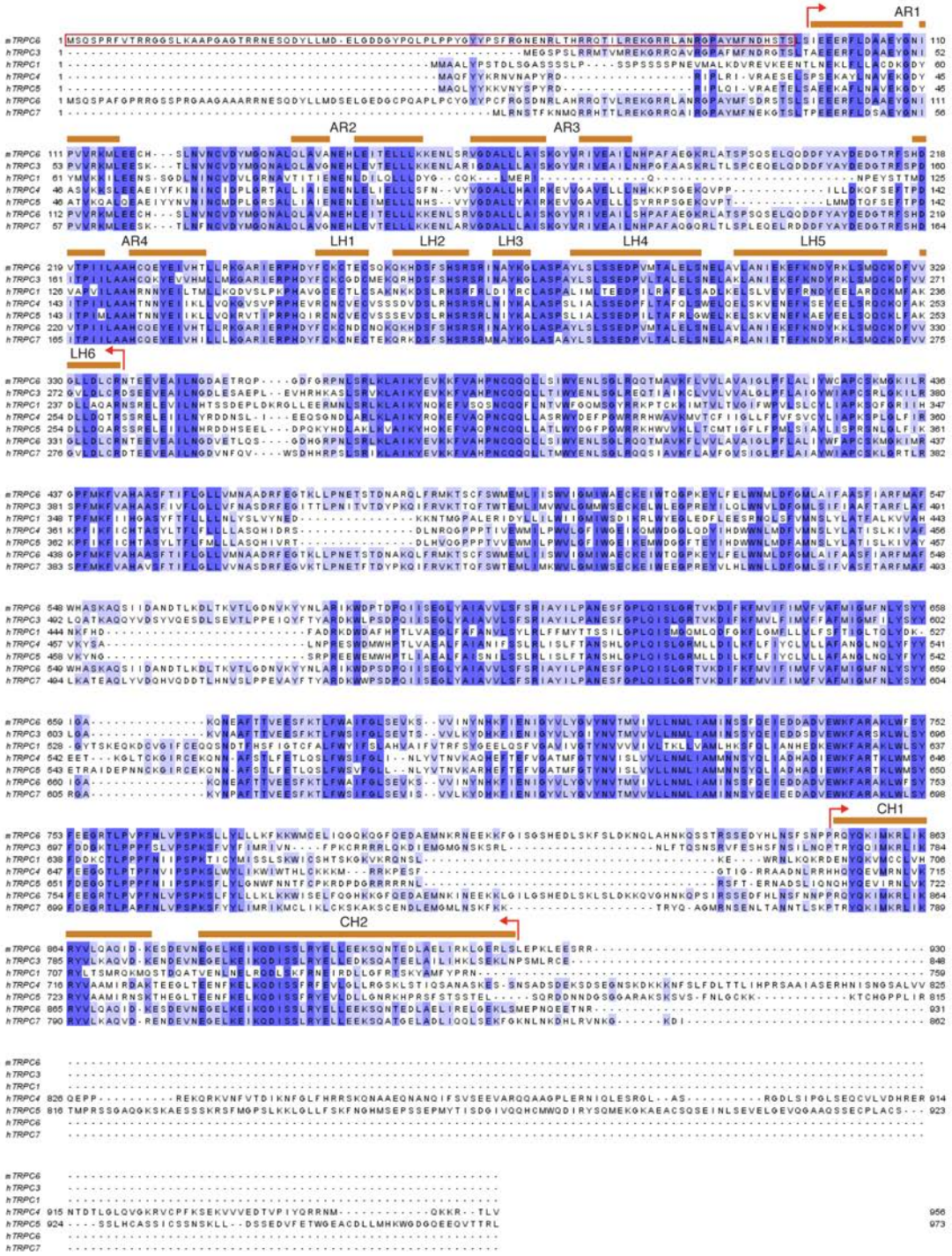

Figure 5-2. Sequence alignment of human TRPC and mouse TRPC6 channels
The sequences (hTRPC1/3/4/5/6/7 and mTRPC6) were aligned using the Clustal Omega program and colored using percentage of identity score in Jalview v2 (Waterhouse et al., 2009). Secondary structure assignments are based on the mouse TRPC6 structure. Red arrows indicate the cytoplasmic domains solved by cryoEM.

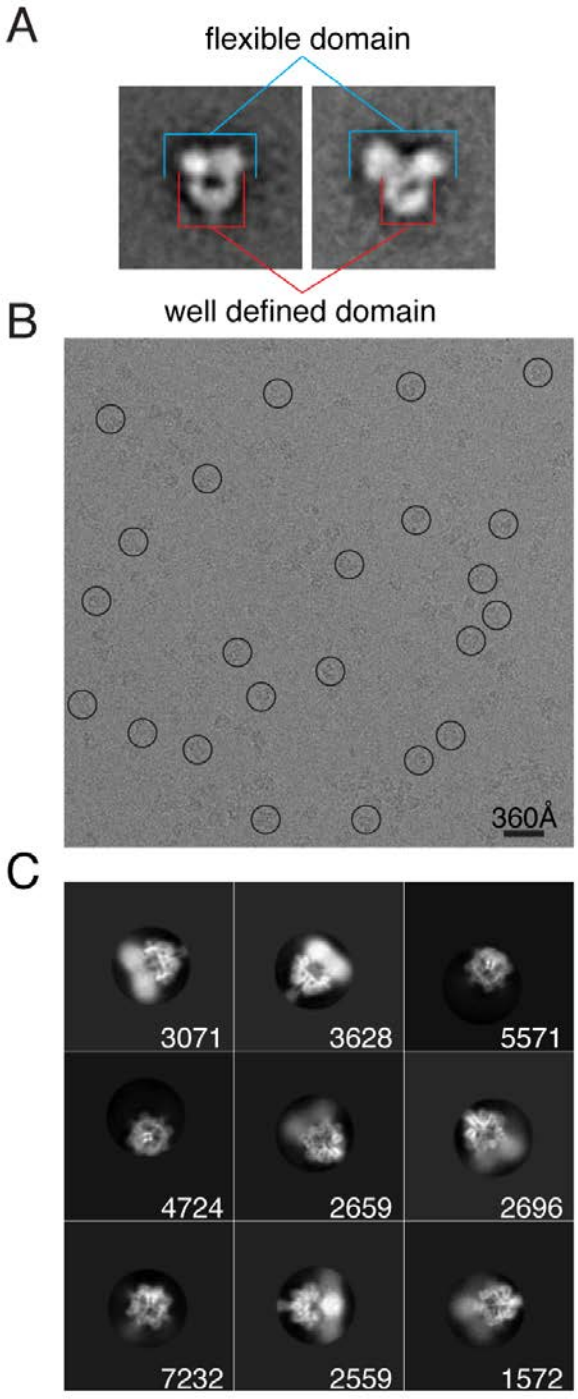

Figure 5-3. Projection structures of TRPC6.
A. Representative negative stain 2D class averages showing the flexible and well-defined domains of TRPC6. **B.** A representative raw micrograph of TRPC6 in vitrified ice recorded using a Titan Krios microscope. **C.** Representative 2D class averages of vitrified TRPC6 particles. The number of particles contained in each class is indicated in the bottom right corner.

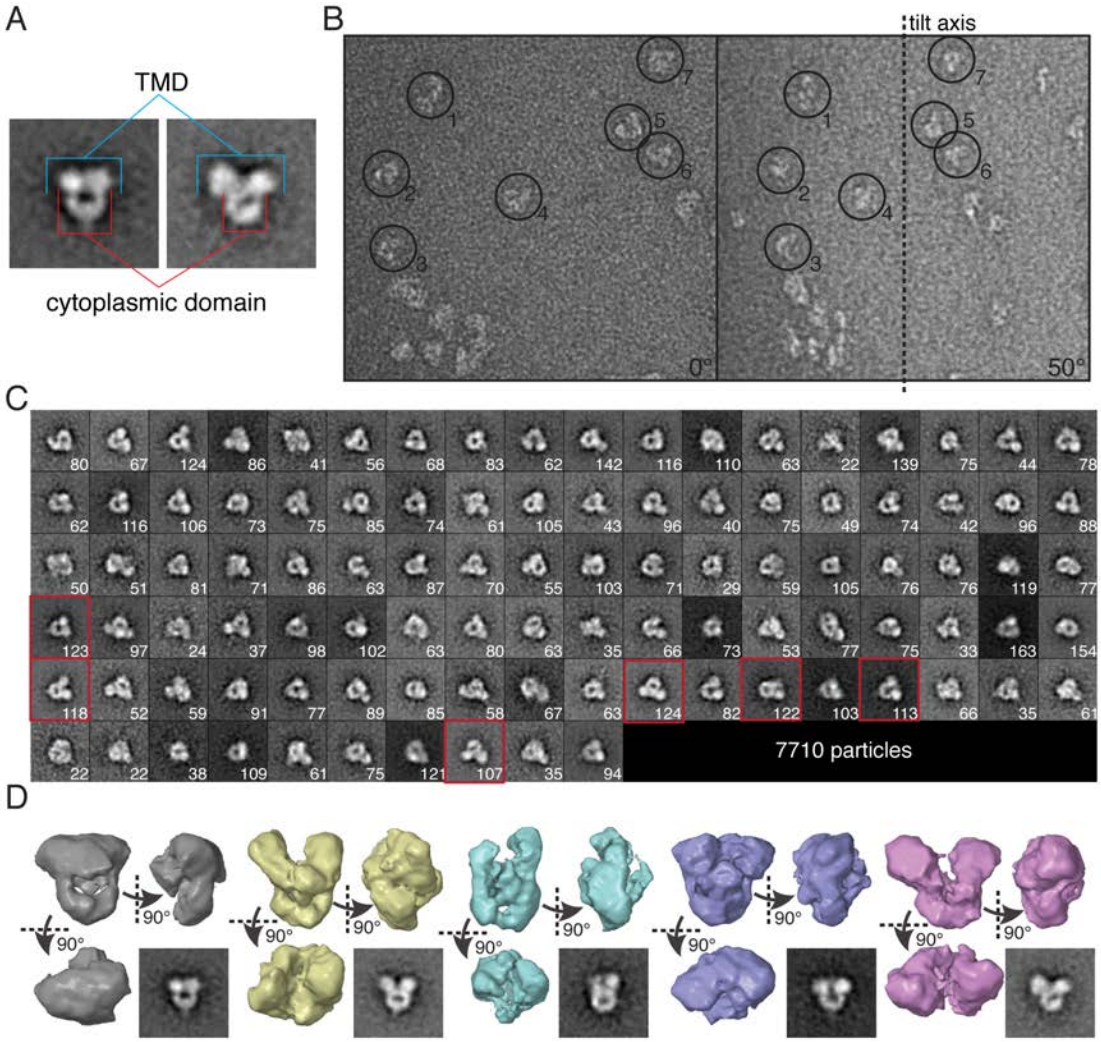

Figure 5-4. Negative stain and Random conical tilt analysis of TRPC6 in PMAL-8.
A. Representative negative stain class averages that show the intact, homogenous cytoplasmic domain (red) and the flexible TMD that are splayed apart at varying angles (cyan). **B.** Representative raw micrographs of untilted and tilted specimen taken in negative stain to generate an initial model of TRPC6 using random conical tilt. **C.** 100 class averages calculated from 7710 TRPC6 untiled particles. Averages that were used to derive initial models are boxed in red. **D.** 3D reconstructions viewed from three angles with the deriving class averages in the bottom right corner. The grey reconstruction (#55) was used as an initial model to align the unstained cryoEM data.

The structure of TRPC6 cytoplasmic domain

The primary structure of TRPC6 predicts that the N-terminal cytoplasmic segment consists of four ankyrin repeats (AR1-4) followed by the LHD comprising six additional α-helices connected by loops. In contrast, the C-terminal cytoplasmic segment is a shorter polypeptide and contains two long α-helices connected by a short linker, as shown in **Figure 5-6A** (also see **Figure 5-2**). The N-terminal and C-terminal portions of the polypeptides are known to fold into a cytoplasmic assembly in other TRP receptors[38,123,124,178,291,292].

The cryoEM density map clearly resolved individual polypeptides, the secondary structures, as well as the large side chains (**Figure 5-7**). At an overall resolution of 3.8Å (**Figure 5-6E**), we were able to build a *de novo* atomic model (statistics in **Table 5-1**). The global tetrameric architecture resembles a baseless wine glass (**Figure 5-6C** and **D**). More precisely, the structure adopted a 4-fold symmetric inverted dome-shape with a bundle of α-helices extending downward. The wall of the inverted dome was formed primarily from AR1-AR4, loops, and six additional α-helices, which correspond to the LHD, contributed by each subunit (**Figure 5-6B** and **Figure 5-8**). Hereafter, we refer to the individual helices in the LHD as LH1-6. Our results agree with secondary structure prediction, suggesting that the N-terminal cytoplasmic domain folds into AR1-4 and multiple α-helices (**Figure 5-2**). The structure in the EM density map lacked any characteristic transmembrane α-helices, and thus we concluded that the domain structure we solved is the cytoplasmic domain.

The cytoplasmic domain of TRPC6 is an independent module

Consistent with the majority of TRPC6 in PMAL adopting a splayed apart TMD, after 3D classification, the 3D map contained featureless density consisting mostly of noise around where the TMD would exist (**Figure 5-5** and **5-9**). This density disappears when the map is viewed at an optimal threshold that resolves the cytoplasmic domain. The transmembrane α-helices were completely unresolved, while the overall architecture of the cytoplasmic domain was well-defined, suggesting that the cytoplasmic domain forms a robust stable module even when the TMD fold is disordered. This observation is in agreement with the idea that the C-terminal coiled-coil domain of the TRP channel is critical for assembly[123,293,294]. The disordered TMD is unlikely to reflect a physiological state of the protein (see Discussion).

Organization of the loops and helices in the cytoplasmic domain

Extensive co-assembly of the N- and C-terminal domains is observed in this structure. In detail, the C-terminal cytoplasmic segment exits from the TMD, bends 90^{o} towards the central axis, and forms a horizontal helix (HH) running parallel to the membrane (**Figure 5-10A** and **Figure 5-8C**). As a result, in the tetrameric assembly, the HHs form a cross shape within a plane parallel to the membrane, in which the junction of the cross forms a right angle (**Figure 5-6B** and **5-10A**). The HH enters the inverted dome from the outside by penetrating through an opening formed between the AR domain and the LHD of the adjacent subunit. Each HH connects to a vertical helix (VH) after bending 90° near the central axis. These VHs assemble into a coiled-coil (**Figure 5-6C** and **5-6D**), which penetrates out of the inverted dome into the cytoplasm (**Figure 5-8C**).

Notably, subunit domain swaps occur when the four HHs merge near the central axis, characterized by a crossover of linkers that connect the HHs and VHs (**Figure 5-10A-C**). Immediately above these four crossover linkers, a density was found that appears to form a plug at the opening of the hollow coiled-coil tube (**Figure 5-10C**). The exact identity of the plug cannot be determined at the resolution of our map; however, an ion could be coordinated at this position. The plug density was only seen when the reconstruction was calculated from the Titan Krios dataset and was absent when calculated with the Polara dataset. The reason for the difference is unclear. Because the biochemical preparation method was identical and highly reproducible, we speculate that the difference may have emerged from contrasting electron dose applied to the specimen. We used 100e^{-}/Å^2 and 47e^{-}/Å^2 during data acquisition on the Polara and Titan Krios, respectively.

Other TRP channels such as TRPM4, TRPM8, and TRPA1 have a similar vertical coiled-coil domain but so far lack the C-terminal domain swap observed in TRPC6 (**Figure 5-10D**). Interestingly,

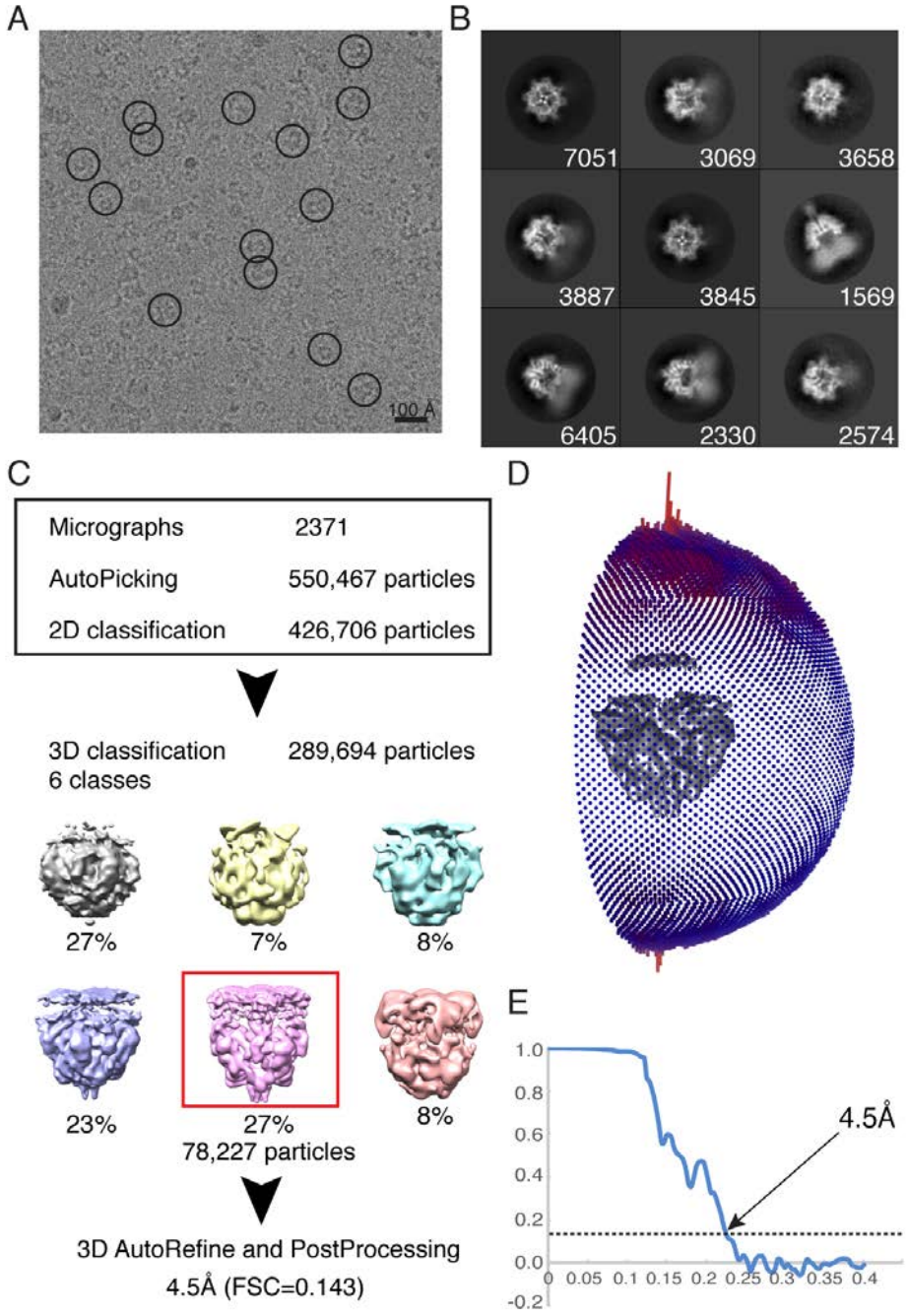

Figure 5-5. Polara data for TRPC6

A. Representative raw micrograph of the data collected on the FEI Polara. **B.** Representative 2D class averages. The particle number in each class is indicated in the bottom right corner. **C.** Flowchart of image processing, indicating the number of micrographs and particles in each step, culminating in a 4.5Å final structure. **D.** Angular distribution of the particles in the output of the final refinement. **E.** The FSC curve with a 0.143 cutoff line indicating a final resolution of 4.5Å.

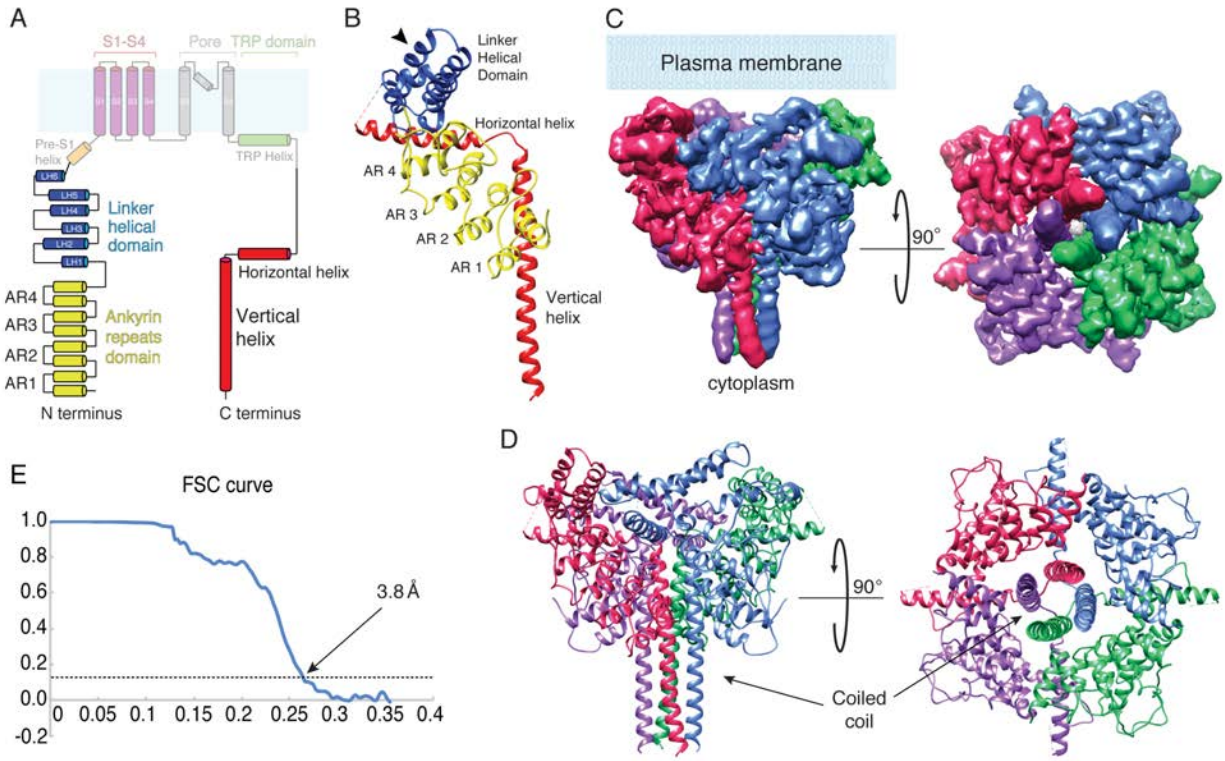

Figure 5-6. Cryo-EM structure and atomic model of TRPC6.
A. Secondary structure organization of TRPC6. **B.** The structure of a single subunit. The substructures are color-coded in the same way as in A. **C.** EM density map showing the tetrameric organization of the cytoplasmic domain. Each subunit is represented by different colors. The overall resolution is 3.8Å based on Fourier shell correlation_0.143, seen in E. **D.** Ribbon diagram of the atomic model generated from the EM density map. **E.** Fourier shell correlation (FSC) curve for the electron density map calculated from the Titan Krios data collected for TRPC6.

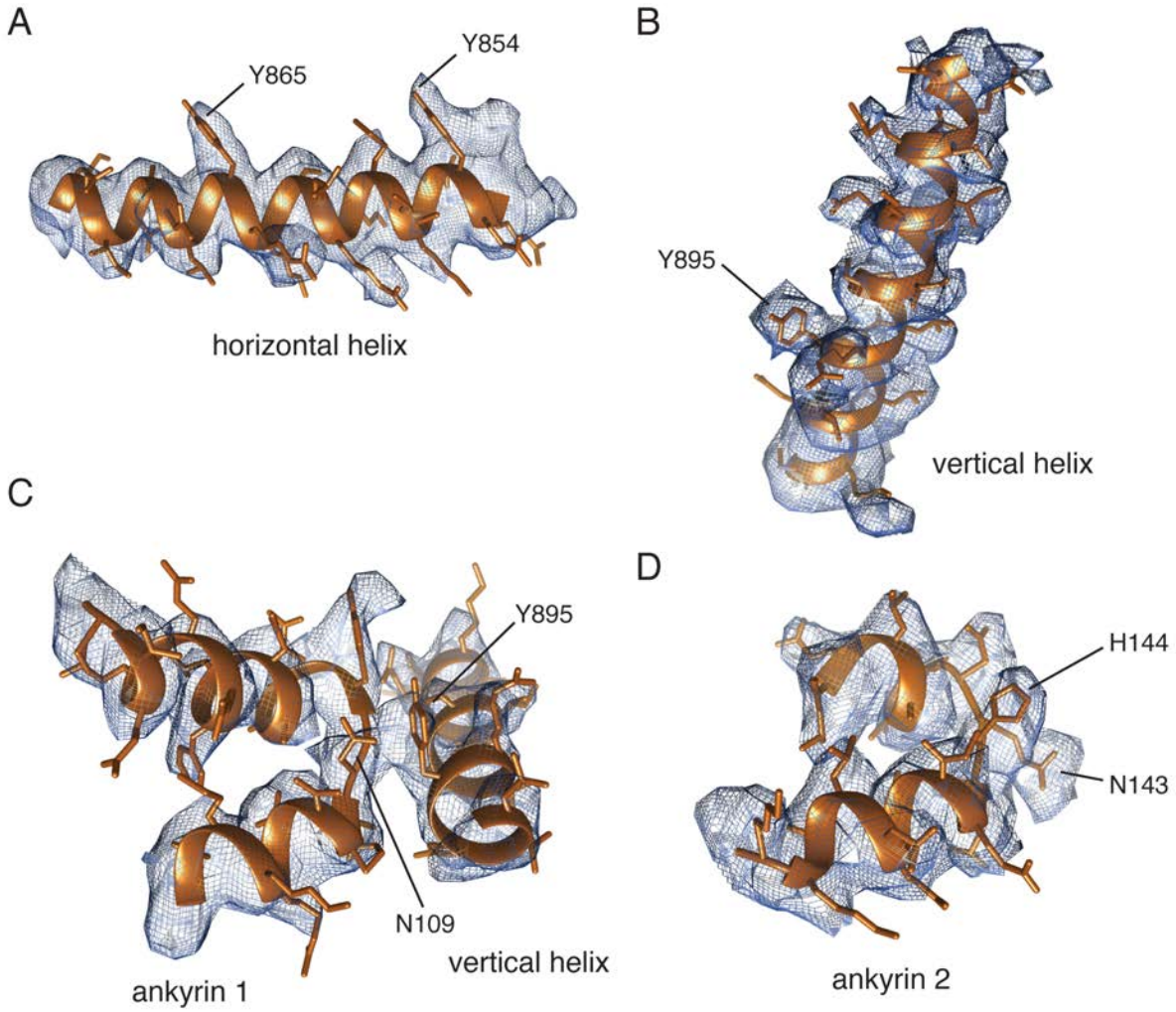

Figure 5-7. Local fit of the atomic model in TRPC6 electron density map.
A. The horizontal helix atomic model fit into the electron density map with side chains shown. **B.** The vertical helix atomic model fit into the electron density map with side chains shown. **C.** The AR1 and vertical helix atomic model fit into the electron density map with side chains shown. The contact between N109 in AR1 and 895 in VH is highlighted. **D.** The AR2 atomic model fit into the electron density map with side chains shown. N143 has additional density around the side chain that may be an additional object in the electron density map.

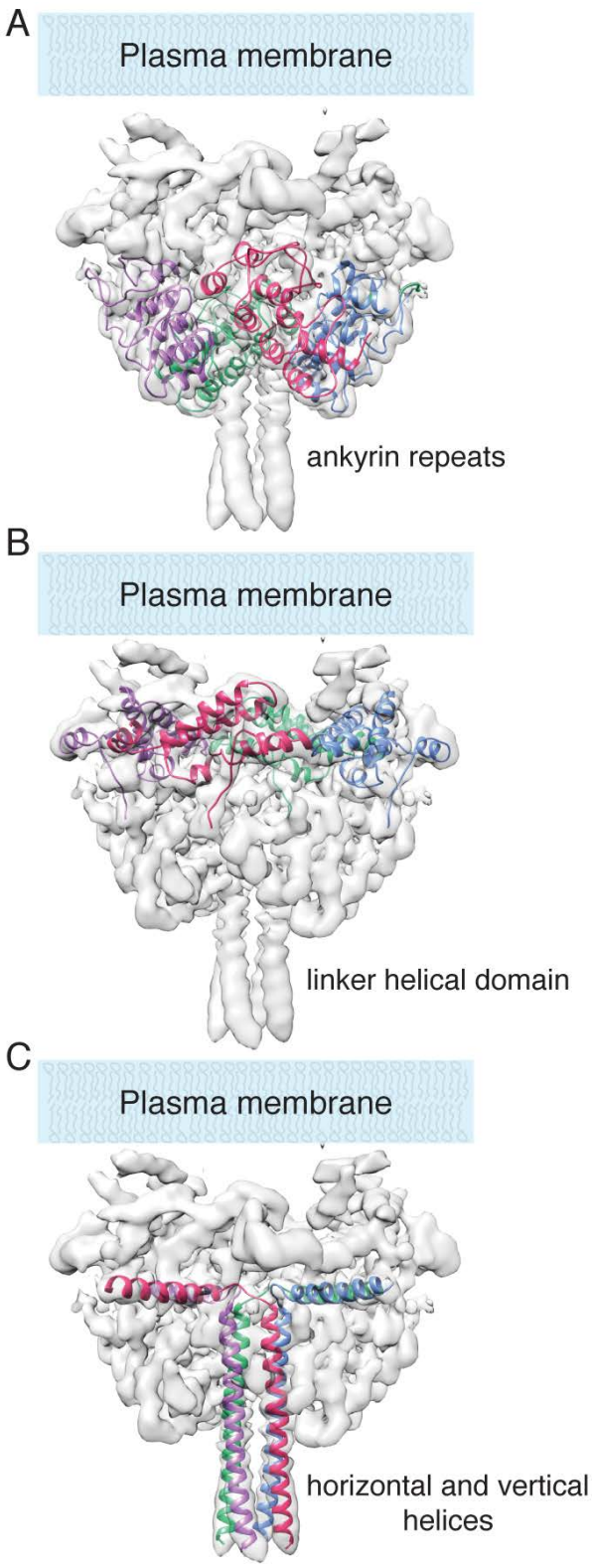

Figure 5-8. Organization of each domain in the cytoplasmic domain of TRPC6.
A. The atomic model of the ankyrin repeats forming the bottom of the dome of the cytoplasmic domain in the transparent EM density map. **B.** The atomic model of the linker helical domain forming the top of the dome of the cytoplasmic domain in the transparent EM density map. **C.** The atomic model of the C-terminal horizontal and vertical (coiled-coil) helices of the cytoplasmic domain in the transparent EM density map.

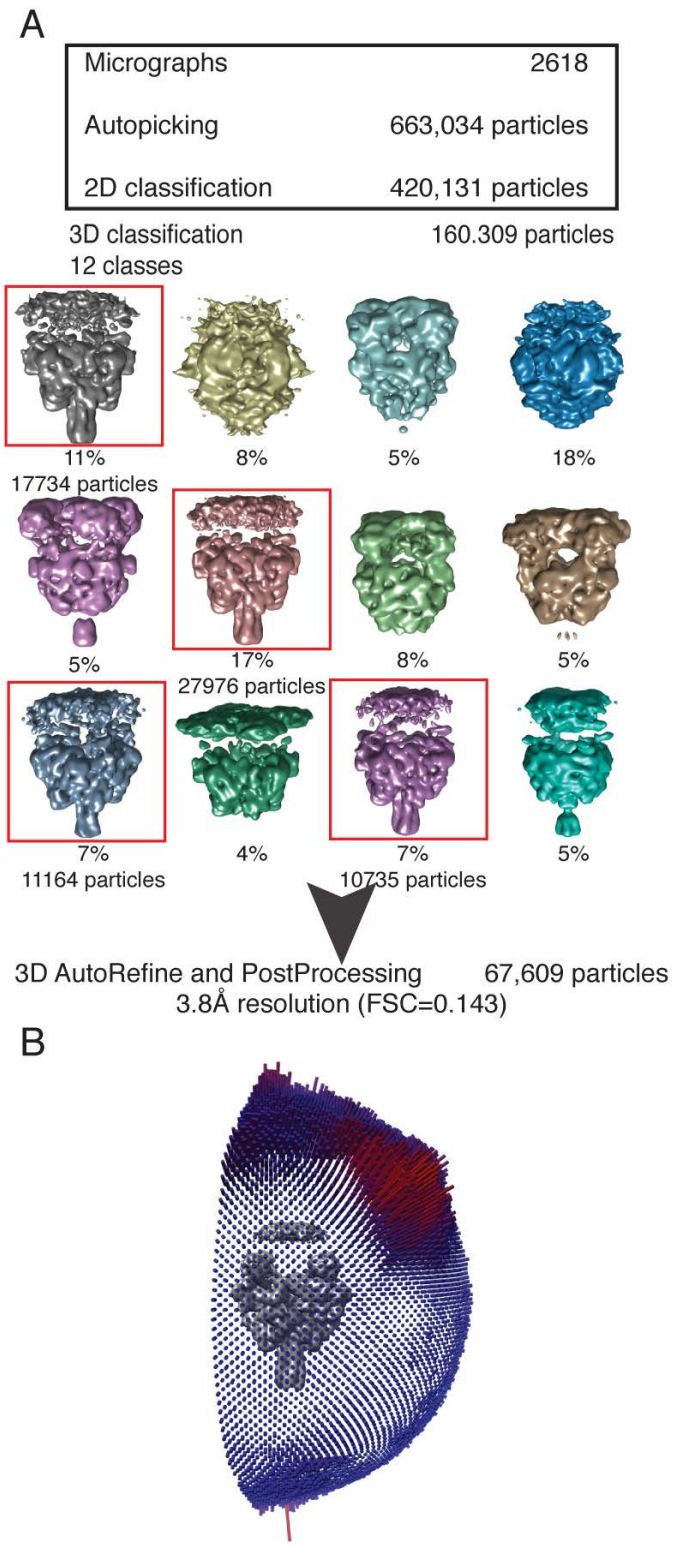

Figure 5-9. Titan Krios data for TRPC6.
A. Flowchart of image processing for the Titan Krios dataset, indicating the number of micrographs and particles in each step, culminating in a 3.8Å final structure. **B.** Angular distribution of the particles in the output of the final refinement of the structure.

the degree of twist found in TRPC6 coiled-coil is weaker when compared to the other family members. The global arrangement of the C-terminal α-helices of TRPC6 is reminiscent of the stretcher helices in the TRPM4, which merge at the center and transition to a coiled-coil[291]. However, the nearly horizontal arrangement of the α-helices forming an X-shape is a unique feature of TRPC6.

The inverted dome-like chamber at the cytoplasmic domain

Given the topology predicted from the primary structure and homology to other members of the TRP channels, the ion channel gate opens into the chamber formed inside the dome. The wall of the dome is made by two stacked layers, the ARs (**Figure 5-8A**) and the LHD. AR4 connects to LH1-6, which links the dome to the TMD (**Figure 5-8B**). LH1-6 interact with each other pairwise in an anti-parallel orientation, making contacts laterally along the helical axis (**Figure 5-6B**; arrow). They contribute significantly to the structure of the interface between the rim of the inverted dome and the membrane. AR1-4 make residue contacts with nearby structures, creating a physical continuity across different substructures along the wall of the dome. Specifically, towards the membrane they contact the LHD and the HHs, and towards the central four-fold symmetry axis they contact the VH (**Figure 5-11**).

The small openings of the dome at various locations would allow the escape of ions passing through the channel (**Figure 5-12**, yellow circle). Side chains that contain hydroxyl groups occupy the majority of the inner surface of the inverted dome-like chamber (**Figure 5-12B**) and its openings to the outside (**Figure 5-12C and D**). This arrangement would facilitate cations exiting from the chamber after entering the cytoplasm through the channel. The lower half of the dome's exterior exhibits an overall negative charge. On the other hand, a cluster of basic residues close to the transmembrane region is exposed, primarily stemming from the HH and the lower portion of the LHD (**Figure 5-12A, B,** and **D**).

The less rigid structural elements in the cytoplasmic domain

The resolution of the cryoEM density was locally lower in sub-regions that consist of loops, as well as the very C-terminus corresponding to the tip of the coiled-coil. The local resolution of the EM density map was calculated using ResMap[245] (**Figure 5-13**). Two long loops in the ankyrin repeats make long-range contacts with the C-terminal HH. The loop connecting AR1 and AR2 approaches the HH of the adjacent subunit from the bottom left. This loop is well defined in the density map, because tyrosine (Y) 130 at tip of the loop and Y231 in AR4's second α-helix of the adjacent subunit are engaged in direct contact (**Figure 5-11A** and **5-14C**). Similarly, the loop connecting AR3 and AR4 consisting of 36 residues is in close proximity with the HH, while adopting a unique fold (**Figure 5-11B**). The resolution of the second loop was ~5Å and thus only the alpha carbon backbone could be reliably modeled. However, when we place the actual residues into the map it was clear that the amino acids with larger side chains could easily make contact with the nearby structural elements, including the HH and LHD, located closer to the membrane. Overall, we were able to interpret the sub-regions of our EM density map that had lower resolution (~5Å) as loops, because the adjacent α-helices were well resolved.

The connection between the cytoplasmic domain and the TMD

The N-terminus of S1 and the C-terminus of the TRP box are geometrically close in the structures of other TRP channels[38,123,124,178,291,292]. In TRPC6, the HH follows the TRP box and LH6 precedes S1. It follows that LH6 and the N-terminus of the HH must be close in the tetrameric assembly. This is exactly what we find in our cytoplasmic domain structure. The existence of a large chamber in the cytoplasmic domain is predicted to occlude direct physical contact between the majority of the cytoplasmic domain and the ion channel gating machinery. The dynamics of the TMD must be transduced bi-directionally through the junction where the N-terminal tip of the HH and portions of the LHD co-localize. We suggest that, subtle conformational rearrangement in the cytoplasmic domain can potentially transduce to the TMD through this junction and *vice versa*.

Locations of disease-causing mutations

Many mutations in the cytoplasmic domain of TRPC6 have been found in patients with FSGS[149–151,153]. The geometrical information of residue contacts provided by our cryoEM structure and atomic model allows us to gain insights into how these mutations may function. We categorize the different

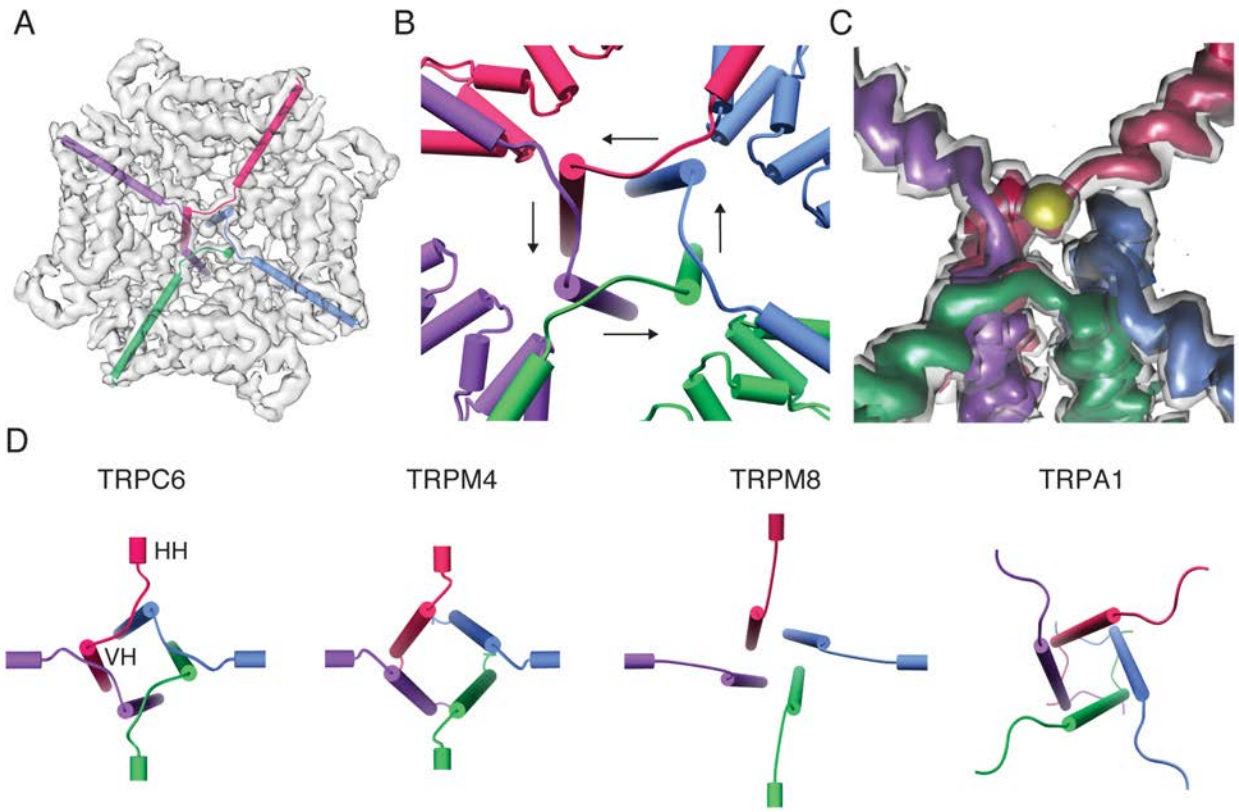

Figure 5-10. Unique arrangements of the C-terminal_-helices in TRPC6.
A and B. Top view of EM density map and cylinder representations of TRPC6 C-terminal segment domain swap. **B.** Arrows indicate the direction of the swap. **C.** EM density map of the domain swap visualized at two different map thresholds. The linker is clearly resolved in our map. Yellow sphere represents the unassigned density observed when the reconstruction was calculated from the Titan Krios dataset. **D.** Comparison of TRP channels HH and VH helices arranged in a coiled-coil structure PDB: 6BCL, 6BPQ, and 3J9P. Note that TRPA1 lacks the HH.

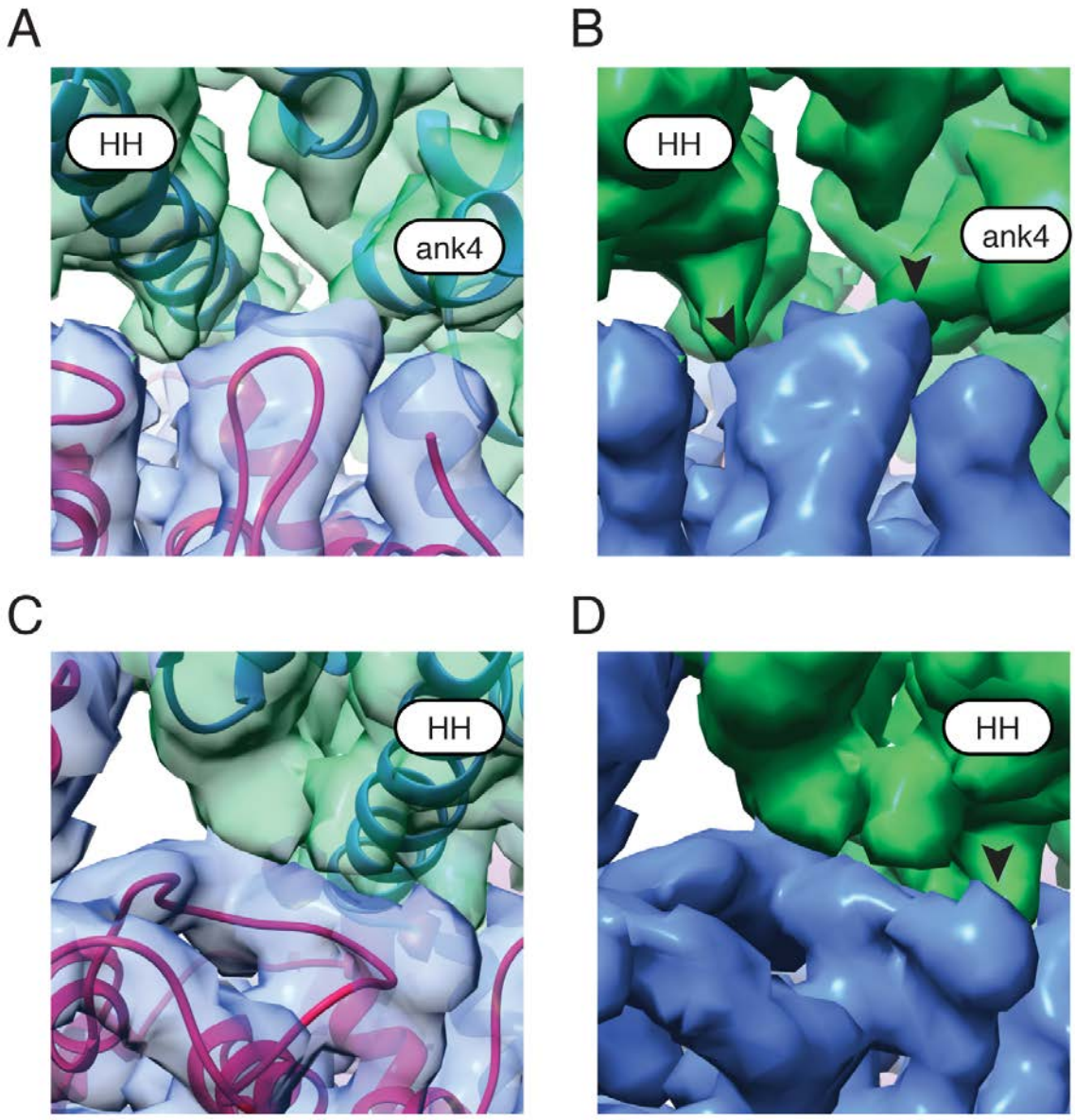

Figure 5-11. Interaction between the loops and horizontal helices.
A and B. Superposition of the EM density map and the ribbon diagram of the atomic model, highlighting the interaction between loop 1 (connecting AR1 and 2), HH, and AR4. **C and D.** Similar representations as above, showing the interface between loop 3 (connecting AR3 and 4) and HH. In B and D, the arrow indicates the merging point in the density map that corresponds to a residue contact.

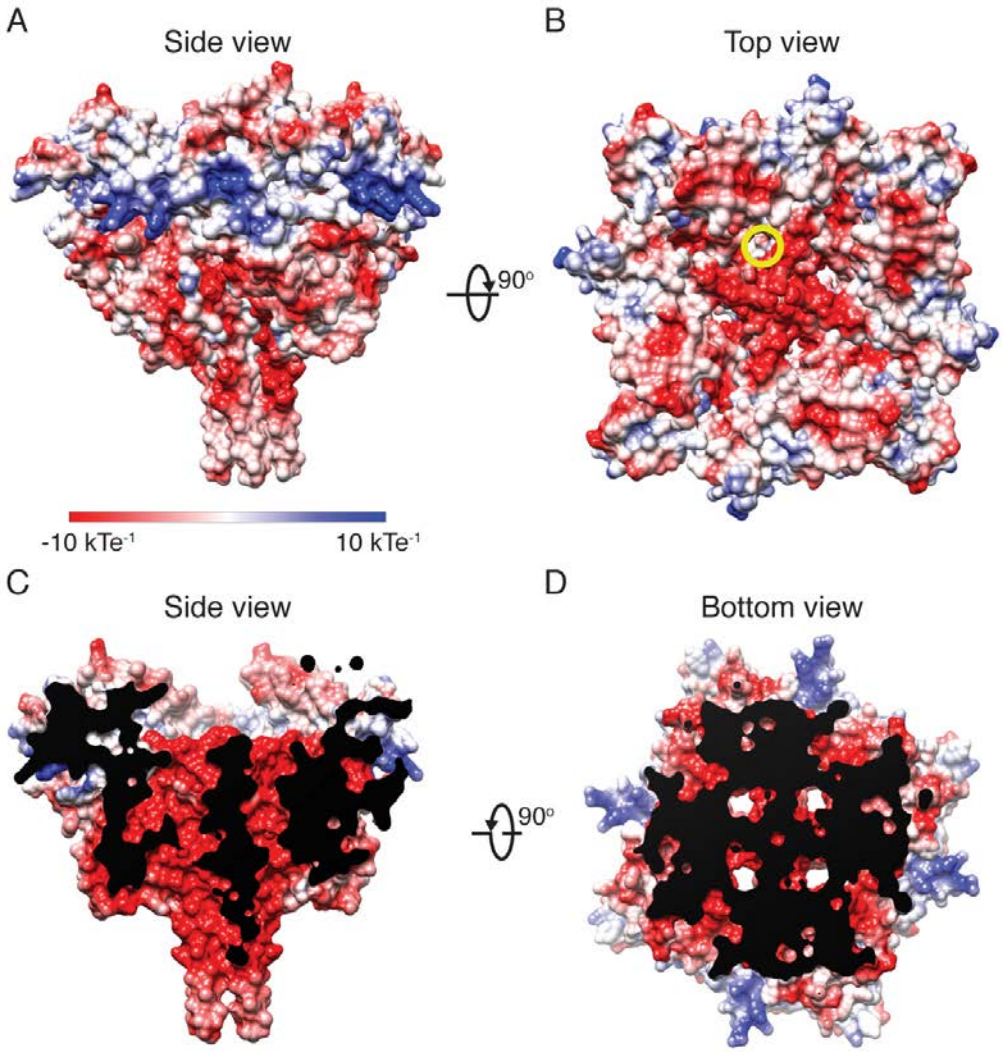

Figure 5-12. Electrostatic potential of TRPC6 cytoplasmic domain.
A. Side view of the cytoplasmic domain indicating an overall negative charge at the bottom of the domain and patches of positive charge at the intersections of the HH and the LHD. **B.** Top view indicating the overall negative charge of the inner chamber. The openings are difficult to see from this view, but are present (yellow circle). **C.** Cut-through view of the cytoplasmic domain showing an overall negative charge of the internal canal crossing from the cytoplasm to the inner chamber. **D.** Bottom view showing the openings between the inner chamber and the cytoplasm. Blue indicates positive and partial-positive regions; red indicates negative and partial-negative regions.

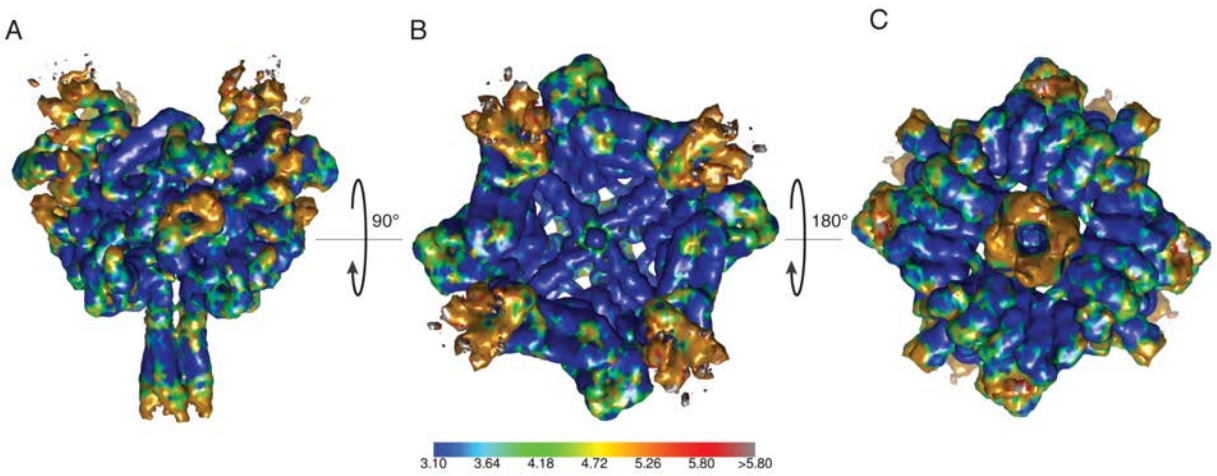

Figure 5-13. Local resolution of the TRPC6 EM density map.
A. Side **B.** Top **C.** Bottom views of the TRPC6 electron density map with local resolution values calculated from ResMap. The heat map represents the resolution scale.

mutations into three groups based on the substructures of TRPC6 that may be affected (**Figure 5-14A**). The first group of mutations is clustered at the buried interface between the ARs and the VHs (**Figure 5-14A** and **B**, red). Because they are inaccessible from the outside, we postulate that the effect of these mutations on ion channel function is mediated by influencing the internal motion between the AR and coiled-coil, rather than altering TRPC6's interaction with other effectors. These mutations surround a strong point of contact between AR1 and the VH between N109 and Y895 (**Figure 5-14B**, black).

The second group contains two mutations that are near or within the HHs (**Figure 5-14A**, green). Methionine (M)131 and its adjacent residues located in the loop connecting AR1 and AR2 reach out to the HH and AR4 of the adjacent subunit (**Figure 5-14C**, green and black). Hence, the M131T mutation is predicted to alter this inter-subunit interaction. An amber mutation, lysine (K)873X, is located in the HHs at the end nearest the coiled-coil. These two mutations are positioned in a way that could potentially influence the dynamics of the HHs. Because the HHs and VHs are directly attached, it is conceivable that mutations in the two groups influence a similar underlying mechanism of TRPC6 gating. The third group of mutations are scattered in various locations, which did not allow us to deduce specific insights (**Figure 5-14A**, magenta).

Discussion

The cytoplasmic domain of TRPC channels is a site for protein interaction with regulatory factors, such as CaM and IP_3R[136]. These protein interactions are known to modulate channel function. Determining the structure of the cytoplasmic domain of TRPC6 would be an effective first step towards revealing the mechanism by which these interactions modulate channel gating as well as trafficking. We report here the overall architecture of the cytoplasmic domain of TRPC6 at 3.8Å resolution. The domain forms a stable modular architecture in the absence of a structured TMD. Disease-causing mutations that produce changes in ion channel gating properties were mapped onto the structure, providing insight into their action.

The 94 residues at the N-terminus that were deleted in this study are unique to TRPC6 and absent in other members of the TRPC subfamily; TRPC6 is functional in the absence of these residues (**Figure 5-1A**). In the tetramer, they would add a significant mass (a total of ~40kDa) to the surface of the ankyrin repeat. This stretch has no predicted secondary structures, contains multiple prolines, and charged residues. If we assume that they do not form any secondary structure, the fragment may potentially have access to various surfaces of the cytoplasmic domain. Alternatively, this fragment may serve as an interface for interacting with other cytoplasmic proteins. More data is needed to address the role of this fragment.

Given that the mutations located at the distal portion of the dome influence channel gating[150,151,153], it is conceivable that yet unidentified conformational changes occur to the dome during the gating cycle. Because of the proximity of many mutations to interfaces between the N- and C-termini, they are likely to destabilize the cytoplasmic domain, which may cause the entire channel to become more unstable and permeable. In particular, we postulate that the C-terminal horizontal and vertical helices would be a dynamic module that undergoes rearrangement of residue contacts with the surrounding ankyrin repeats and their connecting loops, structures that form the wall of the inverted dome. Conformations of TRPC6 in different states would provide answers to these questions.

The cytoplasmic domain retained its structural integrity even when the TMDs were distorted. Therefore, the tetrameric assembly of the channel does not require the intact TMD. The stability of the coiled-coil has been reported before[293,294], but our data extend the previous finding by demonstrating that the combined global fold of the ankyrin repeats, together with the coiled-coil, form a stable modular unit. The connections between the TMD and the linker helical domain, that is positioned more proximal to the membrane relative to the ankyrin repeats, make extensive contacts with various elements of the dome, potentially functioning to bi-directionally transduce the effect of gating and subtle alteration of the residue contacts within the cytoplasmic domain.

An intriguing question arises about how the subunit assembly takes place and embeds the horizontal and vertical coiled-coil into the core of the tetramer, because these C-terminal elements of the polypeptide are synthesized last during translation by ribosomes in the rough ER. We speculate that the four ankyrin repeats are flexible during assembly and the incorporation of the C-terminus provides the final stability of the domain. An additional conformational rearrangement we postulate, assuming that a

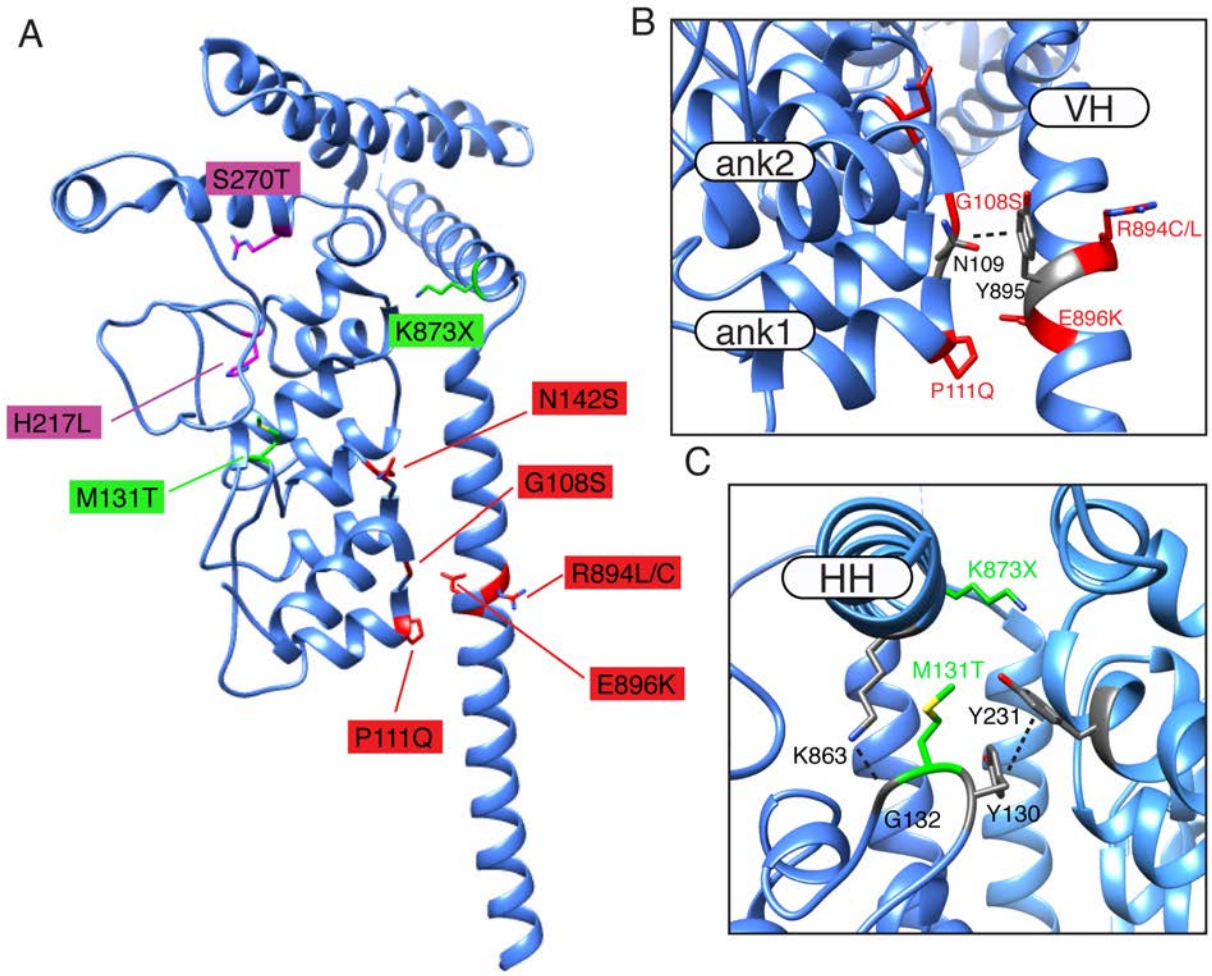

Figure 5-14. Location of FSGS mutations in the TRPC6 cytoplasmic domain.
A. One subunit of TRPC6 with mutations that have been identified in patients with FSGS mapped onto the 3D structure. Three different groups are labeled in red, green, and magenta (see text for details). **B.** Group 1 mutations are labeled in red and clustered around the intersection of the ankyrin repeats, mostly AR1, and the vertical helix. Asn-109 and Tyr-895 form a strong contact in this area and are highlighted in dark gray. **C.** Group 2 mutants are shown in green and clustered around the contact point of ankyrin repeats and the horizontal helix. Contacts between loop 1 and the HH and AR4 of the adjacent subunit, Gly-132 and Lys-863 and Tyr-130 and Tyr-231, respectively, are highlighted in dark gray.

state in which the ankyrin repeats detached from the coiled-coil exists, is the rotation of the coiled-coil that causes the crossover linkers, connecting the horizontal helix to the vertical helix, to unwind and adopt an arrangement seen in other members of the TRP channels.

Our structure lacks the TMD and to demonstrate the veracity of the structure of cytoplasmic domain in the context of the full-length ion channel architecture it would be essential to investigate the cryoEM structure of the TRPC6 with its TMD intact. We adjusted the detergent conditions to attempt and stabilize a physiological arrangement of the TMD. This showed a high degree of TMD homogeneity of protein seemingly embedded in a uniform detergent micelle in negative stain. When taken to cryoEM, none of these preparations were able to give ice conditions amenable to determining a high-resolution structure of full-length TRPC6. We predict that an optimal biochemical preparation preserving the structural integrity of the TMD is achievable, but it happens to be outside the experimental parameter space we had explored. Not only the types of detergents but also the lipid composition surrounding the ion channel may also influence the stability of the TMD. Reconstitution of the receptor in nanodiscs would be particularly preferred for future structural studies of the TRPC6 bound to drugs and modulators because of its stability.

Before structural biology guided drug design was a conceivable notion, the active ingredients of St. John's Wort (*Hypericum perforatum*, plant) were known to have anecdotal anti-depressant effects. The active ingredient was hyperforin, a bicyclic polyprenylated acylphloroglucinol derivative, that increases ion flux into cells via the TRPC6 channel[295]. Efforts have been made to develop synthetic small molecules that would specifically target TRPC6, with an end goal of treating FSGS or hypoxia-induced pulmonary vasoconstriction. Larixyl carbamate[296] and two other small molecules, GSK255B and GSK503A[297], have been identified as TRPC6-specific inhibitors. With a structural analysis pipeline of TRPC6 using cryoEM, it would become possible to reveal the effects of these drugs on the conformational states of the channel, providing mechanistic insights, and potential for future structure-based drug design for this subfamily of the TRP channels.

Experimental Procedures

Functional mTRPC6 with a 96 amino acid truncation at the N-terminus was expressed and purified from Sf9 cells using a baculovirus transfection protocol as detailed in *Materials and Methods*. Negative stain grids were prepared with purified TRPC6 protein, imaged on the TF20 in the Vanderbilt cryoEM Microscope Facility, and 2D class averages were generated using the SPIDER software package, see *Materials and Methods*. A random conical tilt data set was also collected on the TF20 microscope and analyzed using SPIDER (**Figure 5-4**). This generated an initial model (details in *Materials and Methods)* that was used to align cryoEM data sets that were collected on the Polara F30 microscope in the Vanderbilt cryoEM Microscope Facility and the FEI Titan Krios at Washington University in St. Louis in their Center for Cellular Imaging. Vitrification, imaging, and image processing conditions can be found in *Materials and Methods,* **Table 2-2**, **Table 2-3**, and **Table 2-4**. The cytoplasmic domain of TRPC6 was aligned by using a tight mask that excluded the disordered TMD when doing 3D classification. Particles from the best classes were pooled and subjected to 3D refinement, post-processing, and local resolution calculation in RELION 2.1 (**Figure 5-5** and **5-9**). After a full atom model of the cytoplasmic domain was built in Coot and Chimera (*see Materials and Methods*), this model was optimized using Phenix's real-space refinement run for two cycles with mid-range geometric restraints of 0.0075 and 0.75, while NCS was imposed. To conserve helix assignments, strict secondary structure restraints were included to ignore outliers. These refinement parameters were iterated four times with manual adjustment of the structure to correct for Ramachandran and rotamer outliers and bond angle deviations of more than 4σ. We performed a final round of refinement incorporating only morphing, global minimization, secondary structure restraints, and NCS. Validation of the final model was performed using MolProbity.

Data collection and processing	**TRPC6 Polara**	**TRPC6 Titan Krios**
Nominal magnification	31000x	89000x
Voltage (kV)	300	300
Electron exposure ($e^-/Å^2$)	100	46.8
Defocus range (μm)	2.0-5.0	1.2-3.0
Pixel size (Å)	1.247	1.41
Symmetry group	C4	C4
No. of micrographs	2,371	2,618
Total particle count (autopick)	550,467	663,034
Particles in 2D classification	426,706	420,131
Particles in final reconstruction	78,227	67,280
Map resolution (Å)	4.5	3.8
Refinement		
Map sharpening B factor ($Å^2$)		-126
Model resolution range (Å)		360.96-4.01
No. of residues (monomer)		316
No. of atoms (monomer)		2509
No. of bonds (monomer)		2545
B factors ($Å^2$) Mean		188.35-30.00 113.35
RMSD Bond lengths (Å) Bond angles (º)		 0.007 1.248
Validation MolProbity score Clashscore Rotamer outliers C-beta outliers		 1.85 (85^{th} percentile) 6.2 (92^{nd} percentile) 0.00% 0
Ramachandran plot Favored Allowed Disallowed		 91.35% 8.65% 0.00%

Table 5-1. Map and model statistics for mTRPC6 cytoplasmic domain.
Data collection parameters and statistics for processing for both Polara and Titan Krios electron density maps. Statistics for the atomic model of TRPC6 as determined by validation in MolProbity. RMSD, root mean square deviation.

CHAPTER VI: STRUCTURE-FUNCTION ANALYSIS OF HUMAN TRPC3

This section is a paper published in *The Journal of Biological Chemistry* as "Structure- function analyses of the ion channel TRPC3 reveal that its cytoplasmic domain allosterically modulates channel gating" Francisco Sierra-Valdez*, Caleigh M. Azumaya*, Luis O. Romero, Terunaga Nakagawa, and Julio F. Cordero-Morales.

Aims

The transient receptor potential ion channels support Ca^{2+} permeation in many organs, including the heart, brain, and kidney. Genetic mutations in TRPC3 are associated with neurodegenerative diseases, memory loss, and hypertension. To better understand the conformational changes that regulate TRPC3 function and may have a role in dysfunction, here we solved the cryo-EM structures for the full-length human TRPC3 and its CPD in the apo state at 5.8 and 4.0Å resolution, respectively. These structures revealed that the TRPC3 transmembrane domain resembles those of other TRP channels and that the CPD is a stable module involved in channel assembly and gating. We observed the presence of a C-terminal domain swap at the center of the CPD, where HHs transition into a coiled-coil bundle. Comparison of the two TRPC3 structures revealed that the HHs can reside in two distinct positions. Electrophysiological analyses disclosed that shortening the length of the C-terminal loop connecting the HH with the TRP helices increases TRPC3 activity and that elongating the length of the loop has the opposite effect. Our findings indicate that the C-terminal loop affects channel gating by altering the allosteric coupling between the cytoplasmic and transmembrane domains. We propose that molecules that target the HH may represent a promising strategy for controlling TRPC3-associated neurological disorders and hypertension.

Results and Discussion

Determination of the human TRPC3 structure

To determine the structure of TRPC3, we used the full-length human isoform b with an MBP tag at the N-terminus. This construct was expressed in Sf9 cells by infecting them with a recombinant baculovirus. Initially, TRPC3 was solubilized in digitonin and further purified using the synthetic digitonin GDN (the sample referred to as $TRPC3_{GDN}$ hereafter). In the final purification step, TRPC3 migrated as a stable and pure monodisperse species, as determined by size-exclusion chromatography, SDS-PAGE (**Figure 6-1A**), and negative stain EM (data not shown). 2D class averages of $TRPC3_{GDN}$ particles in vitreous ice revealed elements indicative of α-helices in the tetrameric channel (Figure 6-1B). We were able to calculate a 3D map by collecting a large dataset and using a subset of particles that produced class averages showing well-defined membrane spanning α-helices in the micelle (**Figure 6-2**). The final EM density map had an overall resolution of 5.8Å (**Figure 6-2C-D**). At this resolution, the secondary structures forming the TMD and the CPD are clearly resolved (**Figure 6-1C**). $TRPC3_{GDN}$ has a molecular mass of approximately 388 kDa with dimensions of 129 × 85Å. The TMD was surrounded by signals from the detergent micelle (**Figure 6-1C-D**), which disappeared when the map was viewed using a density threshold that optimally resolves the membrane spanning α-helices (**Figure 6-1C**). The channel pore opens into a large chamber inside the CPD located below the TMD (**Figure 6-1E** and **Figure 6-9C**). The ions that pass through the channel will enter this chamber and subsequently exit through openings between the linker helical domain and TMD or fenestrations between the ankyrin repeats (**Figure 6-1E**). Overall, $TRPC3_{GDN}$ displays a compact two-tiered architecture when compared to the TRPM4, a channel with similar fold,[127,128,291] 129 vs. >150Å, respectively.

The structure of the TRPC3 cytoplasmic domain

In a recent study, we solved the structure of the mTRPC6 channel CPD reconstituted in PMAL-C8 at 3.8Å resolution[120]. In those biochemical conditions, the TRPC6 TMD was flexible and appeared as a diffuse density in the cryo-EM class averages. On the other hand, the TRPC6 CPD was well-structured; and by masking out the TMD in the 3D classification using RELION[205,213], we were able to determine the

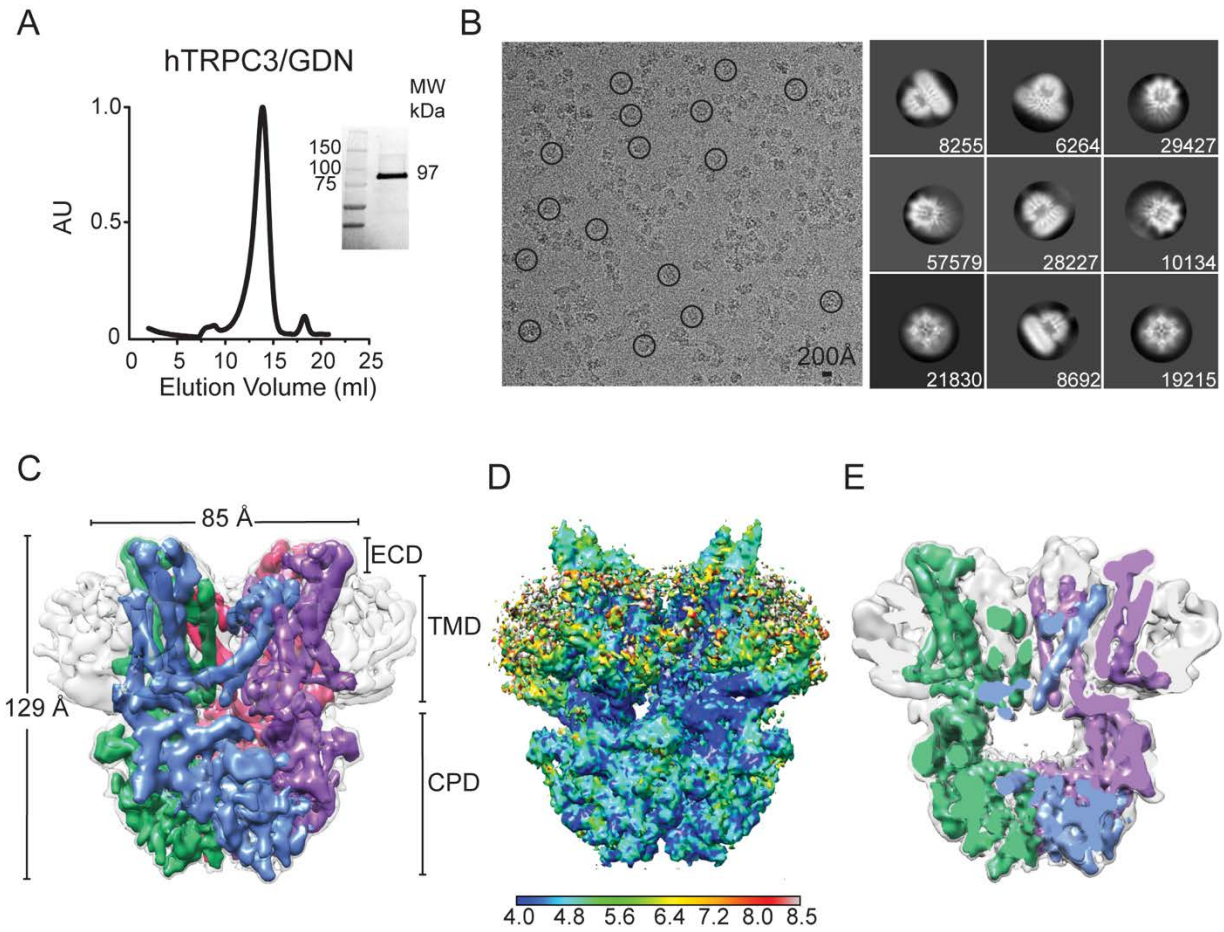

Figure 6-1. Cryo-EM structure of full-length human TRPC3 at 5.8Å.
A. Size-exclusion chromatography profile of digitonin-solubilized and GDN-purified TRPC3 from Sf9 cells. Inset, stain-free protein on SDS-PAGE gel corresponds to TRPC3 monomer (97 kDa). **B.** Left, micrograph after motion correction of TRPC3 in GDN micelles (TRPC3GDN), taken on an FEI Polara microscope. Note that particles are monodisperse and some are circled in black. Right, representative 2D class averages of TRPC3GDN. Particles were aligned and classified in RELION 2.1. The number of particles in each class is shown in the lower right corner of each box. **C.** Electron density map of TRPC3GDN tetrameric assembly. GDN micelle is denoted in light gray at a higher threshold than the four subunits, colored in blue, green, pink, and purple. **D.** Side view of TRPC3GDN with local resolution calculated in ResMap indicated by the heat map scale bar. High- to low-resolution runs are blue to red, from 4.0 to 8.0Å. **E.** Side view cross-section of the tetrameric TRPC3GDN highlighting the hollow inner chamber below the transmembrane domain. AU, arbitrary units; ECD, extracellular domain.

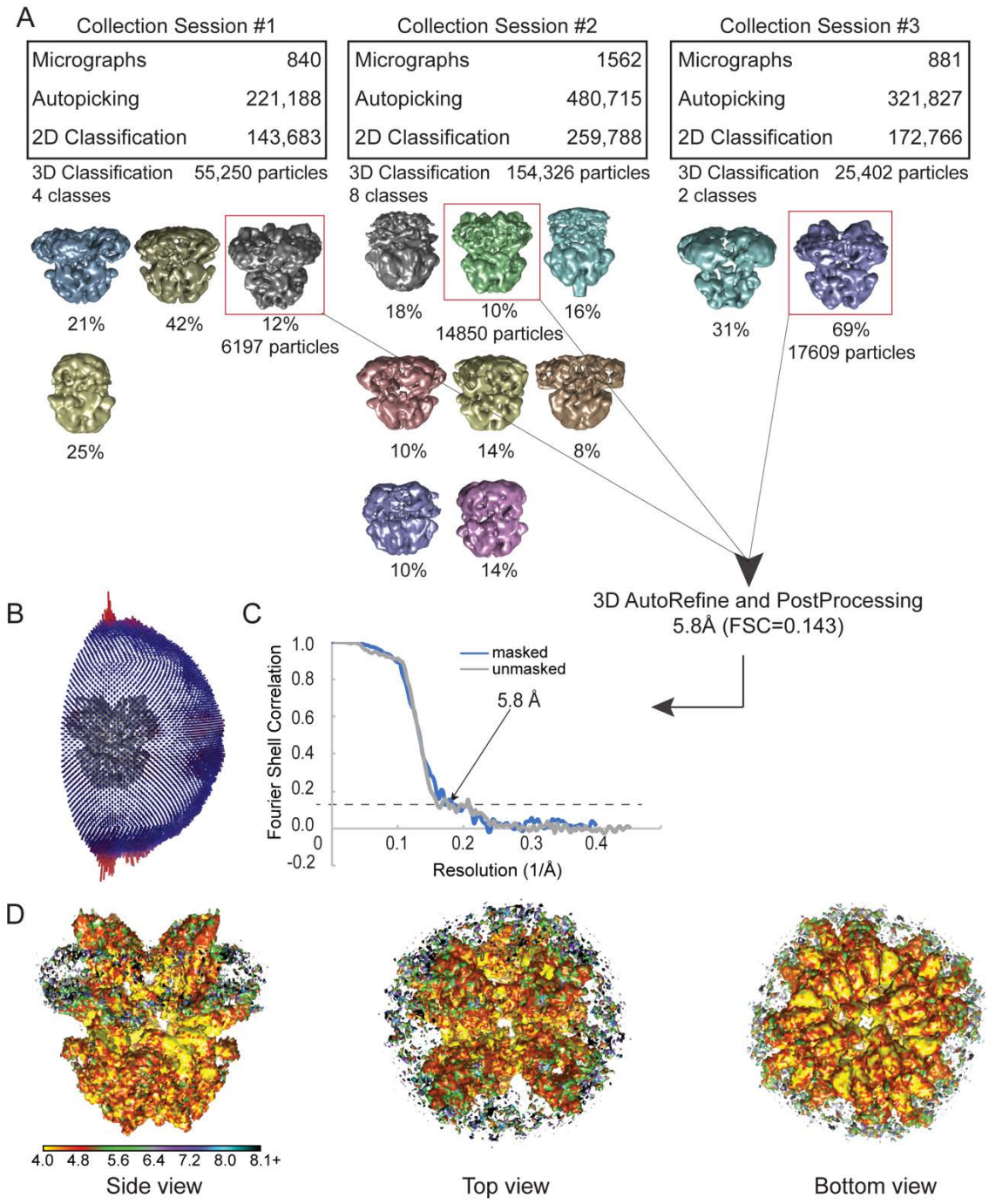

Figure 6-2. Flowchart for TRPC3$_{GDN}$ image processing pipeline.
A. Flowchart showing the number of micrographs, autopicked particles, and particles that went into 2D and 3D classification steps. All 3D class averages are shown with percentage of particles they contain underneath. Averages whose particles were used in 3D autorefine and post-processing are boxed in red. **B.** Angular distribution of views that went into the final reconstruction of TRPC3$_{GDN}$. **C.** Fourier shell correlation (FSC) curve for TRPC3$_{GDN}$ data taken on the Polara microscope showing a 5.8Å resolution cut-off at the gold standard value of 0.143. **D.** Side, top, and bottom views of TRPC3 with local resolution indicated in the heat map scale bar under the side view. High to low resolution runs yellow to black, with a scale from 4.0-8.0Å.

structure of the CPD. We followed the same approach in an attempt to increase the resolution of the TRPC3 CPD. In this preparation, full-length TRPC3 was solubilized in DDM, purified, and reconstituted into PMAL-C8 (referred to as $TRPC3_{PMAL}$ hereafter). $TRPC3_{PMAL}$ migrates as a stable and pure monodisperse species, as determined by size-exclusion chromatography and SDS-PAGE (**Figure 6-3A**). The particles of $TRPC3_{PMAL}$ were monodisperse in vitreous ice, and their 2D class averages displayed features corresponding to α-helices in the CPD (**Figure 6-3B**). The $TRPC3_{PMAL}$ TMD was flexible and diffuse in the cryo-EM class averages (**Figure 6-3B**, white arrows) when compared to $TRPC3_{GDN}$ (**Figure 6-1B**). We were able to calculate an EM density map of the $TRPC3_{PMAL}$ CPD at an average resolution of 4.0Å (**Figure 6-3C** and **Figure 6-4A-C**). The EM density map lacked any characteristic TMD α-helices (**Figure 6-3D**). As expected, the CPD displayed lower resolution at its junction to the flexible TMD (**Figure 6-4D**).

The cryo-EM density map is of sufficient quality to build an atomic model of the CPD *de novo* (**Figure 6-4D-E** and **Table 6-1**). The CPD model was built from residues Thr37 to Glu295 for the N-terminus and Thr773 to Leu819 for the C-terminus. Our model is in agreement with the predicted topology of TRPC3's primary structure (**Figure 6-5**) and allowed us to resolve individual polypeptides as well as large side chains (**Figure 6-6**) and resembles the CPD structure of the full-length channel obtained in nanodiscs[129]; hence, we consider our structure to be physiological relevant. The N- and C-terminal segments assemble into a stable tetramer, whose global architecture resembles a bowl (**Figure 6-3D-E**). The $TRPC3_{PMAL}$ CPD arrangement is comparable to the ones observed in TRPA1[123], TRPM4[127,128,291], and TRPM8[122] in which the N-terminal domain and the C-terminal coiled-coil engage in multiple interactions and contribute to the tetrameric assembly of the channel. Notably, the $TRPC3_{PMAL}$ CPD surface potential exhibits a striped distribution, as the negative charges in the upper and lower part of the bowl surround a patch of neutral and positive charges (**Figure 6-7**).

In the TRPC6 CPD, the lower half of the domain exhibits an overall negative charge and the upper half is mainly neutral and positive[120] (**Figure 6-7E**). These different surface potential distributions might be relevant for determining the specificity of interaction between the CPD and intracellular components. The inner surface of the $TRPC3_{PMAL}$ bowl displays a negative surface potential arising from the HHs (**Figure 6-7B**), similar to TRPC6 (**Figure 6-7F**). The CPD exhibits four openings, adjacent to the coiled-coil formed by four VHs, lined by negative charges (**Figure 6-7C-D**, arrows and yellow circles); hence, the CPD might have a direct impact on TRPC3 ionic currents.

Overall architecture of TRPC3

The $TRPC3_{GDN}$ electron density map was first interpreted by constructing a *de novo* polyalanine model (**Table 6-1**). Next, a "hybrid" full-length TRPC3 atomic model was generated by combining our polyalanine model (from residues 296-311 and 370-621) of the TMD with a full atom model of the CPD (Thr37 to Glu295 and Thr773 to Leu819) (**Figure 6-8** and **Table 6-1**). The overall architecture of the channel tetramer can be divided into two major sections: the TMD and the CPD. The N-terminus contains AR1-4 followed by the LHD composed of α-helices LH1-8 and the C-terminus consists of HHs and VHs connected by a short linker (**Figure 6-8F**, black arrow). The N-terminus connects to the S1 helix of the TMD through the pre-S1 elbow (**Figure 6-8B-C**). Loops (e.g., between AR3-AR4) and helices (e.g., LH9) that are shaded out in **Figure 6-8B** were not resolved in our structure but resolved elsewhere[121,129]. Notably, the C-terminal loop connecting the TRP and the HH helices is not resolved in any of the TRPC3 structures. Near the central axis, the ankyrin repeats make contact with the VHs (**Figure 6-6A**). The linker helical domains form a layer proximal to the plasma membrane (**Figure 6-9B**) and engage in extensive contact with the HHs (discussed below).

Similar to the other six-transmembrane segment cation channels, the S1-S4 domain is at the periphery of the TMD (**Figure 6-9D**), whereas the re-entrant loop with a pore helix links the S5 and S6 forming the pore (**Figure 6-8C**). At the central axis, the S6 helices adopt the shape of an inverted teepee reminiscent of the pore of potassium channels[118] (**Figure 6-9E**). The TMD polypeptide re-enters the cytoplasm via the TRP helix, which connects to a HH through an unresolved loop. The HHs penetrate the bowl from the side and converge at the center, forming a cross shape when viewed along the central axis (**Figure 6-8D-E** and **Figure 6-9F**). The VH forms a strong contact point with AR1 which we suggest is an anion-π interaction between Tyr-816 and Asn-51 (**Figure 6-10A**). This contact point is also seen in

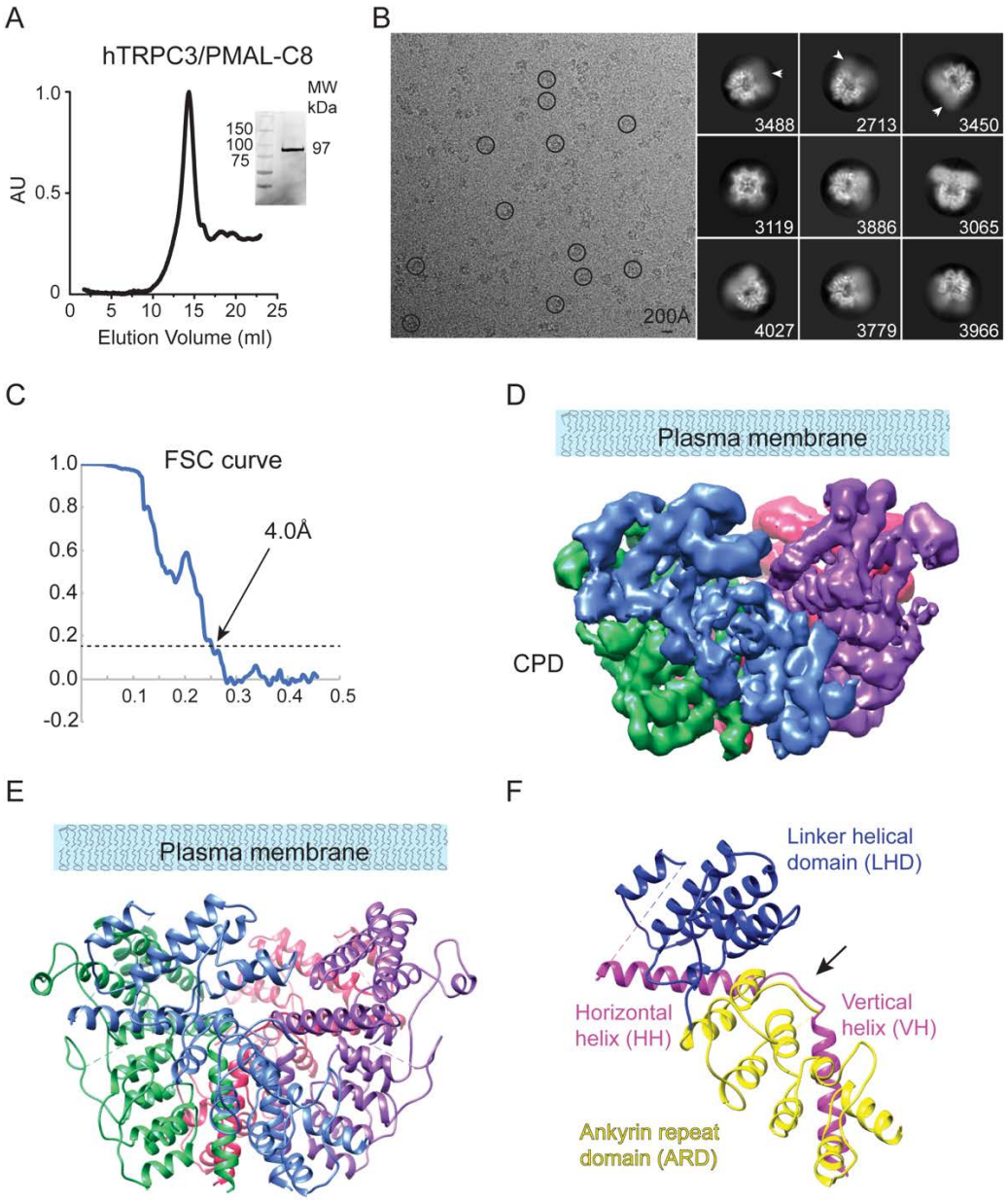

Figure 6-3. Cryo-EM structure of the TRPC3 CPD at 4.0Å.
A. Size-exclusion chromatography profile of PMAL-C8–stabilized TRPC3 protein. Inset, stain-free protein on the SDS-PAGE gel corresponds to the size of the purified channel monomers (97 kDa). B. Left, micrograph after motion correction of TRPC3 in PMAL-C8 (TRPC3PMAL), taken on a Titan Krios. Note that particles are monodisperse and some are circled in black. Right, representative 2D class averages of $TRPC3_{PMAL}$. Particles were aligned and classified in RELION 2.1, and the number of particles in each class is shown in the lower right corner of each box. Arrows indicate the diffuse density. C. FSC curve showing a 4.0-Å cutoff at the gold standard value of 0.143. D. Electron density map of TRPC3 CPD tetrameric assembly. E. Ribbon diagram of the atomic model generated from the EM density map shown in D. F. CPD ribbon diagram of a single $TRPC3_{PMAL}$ subunit. The subdomains are labeled as ARD (yellow), LHD (blue), and the C-terminal HH and VH (pink). The black arrow highlights the linker between the HH and VH. AU, arbitrary units.

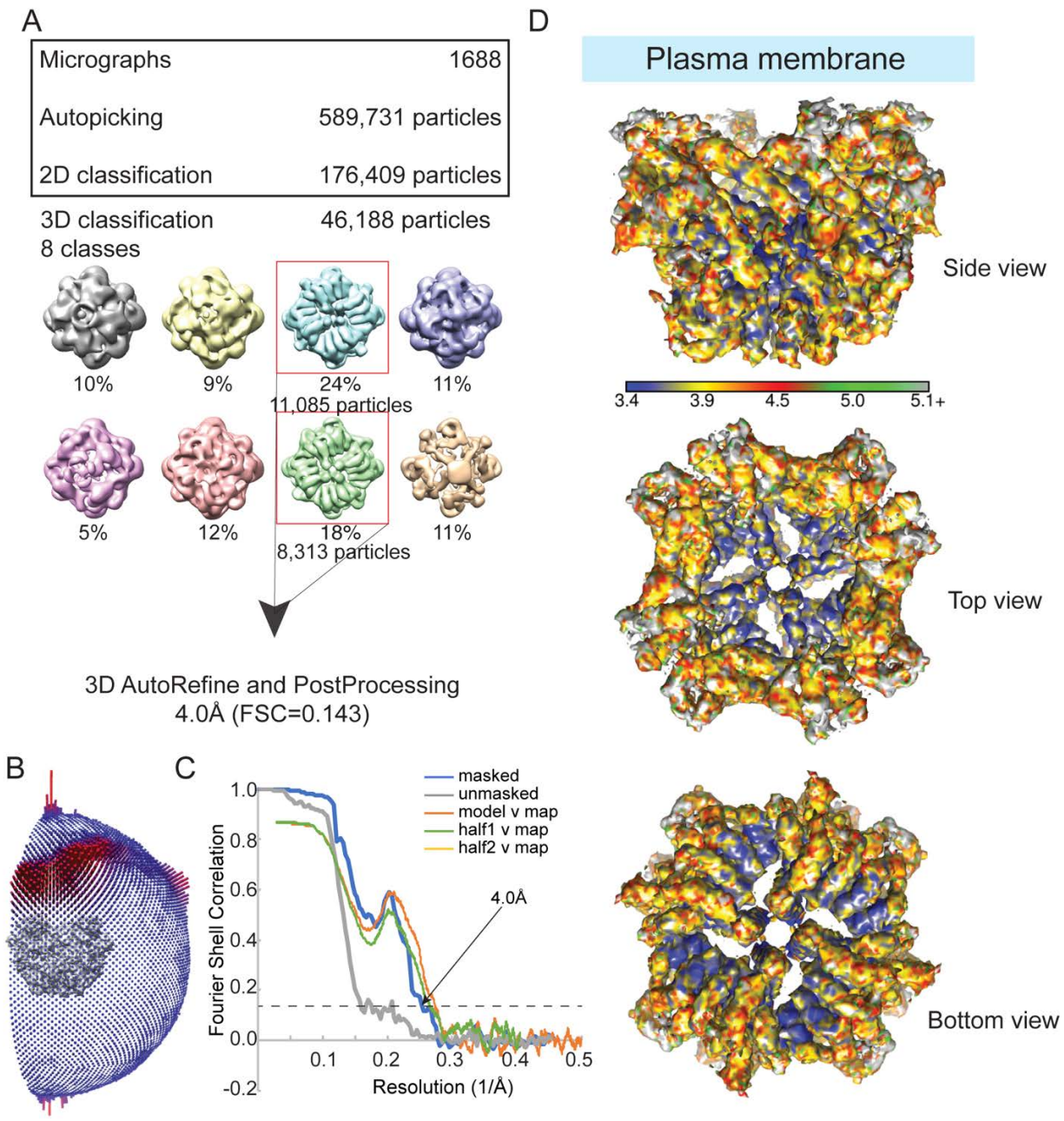

Figure 6-4. Flowchart for TRPC3$_{PMAL}$ image processing pipeline.
A. Flowchart showing the number of micrographs, autopicked particles, and particles that went into 2D and 3D classification steps. All 3D class averages are shown with percentage of particles they contain underneath. Averages whose particles were used in 3D autorefine and post-processing are boxed in red. **B.** Angular distribution of views that went into the final reconstruction of TRPC3$_{PMAL}$. **C.** Fourier shell correlation (FSC) curve for TRPC3$_{PMAL}$ data (blue) and TRPC3 model (orange) taken showing a 4.0Å resolution cut-off at the gold standard value of 0.143. **D.** Side, top, and bottom views of TRPC3$_{PMAL}$ with local resolution indicated in the heat map scale bar under the side view. High to low resolution runs blue to green, with a scale from 3.4-5.1Å.

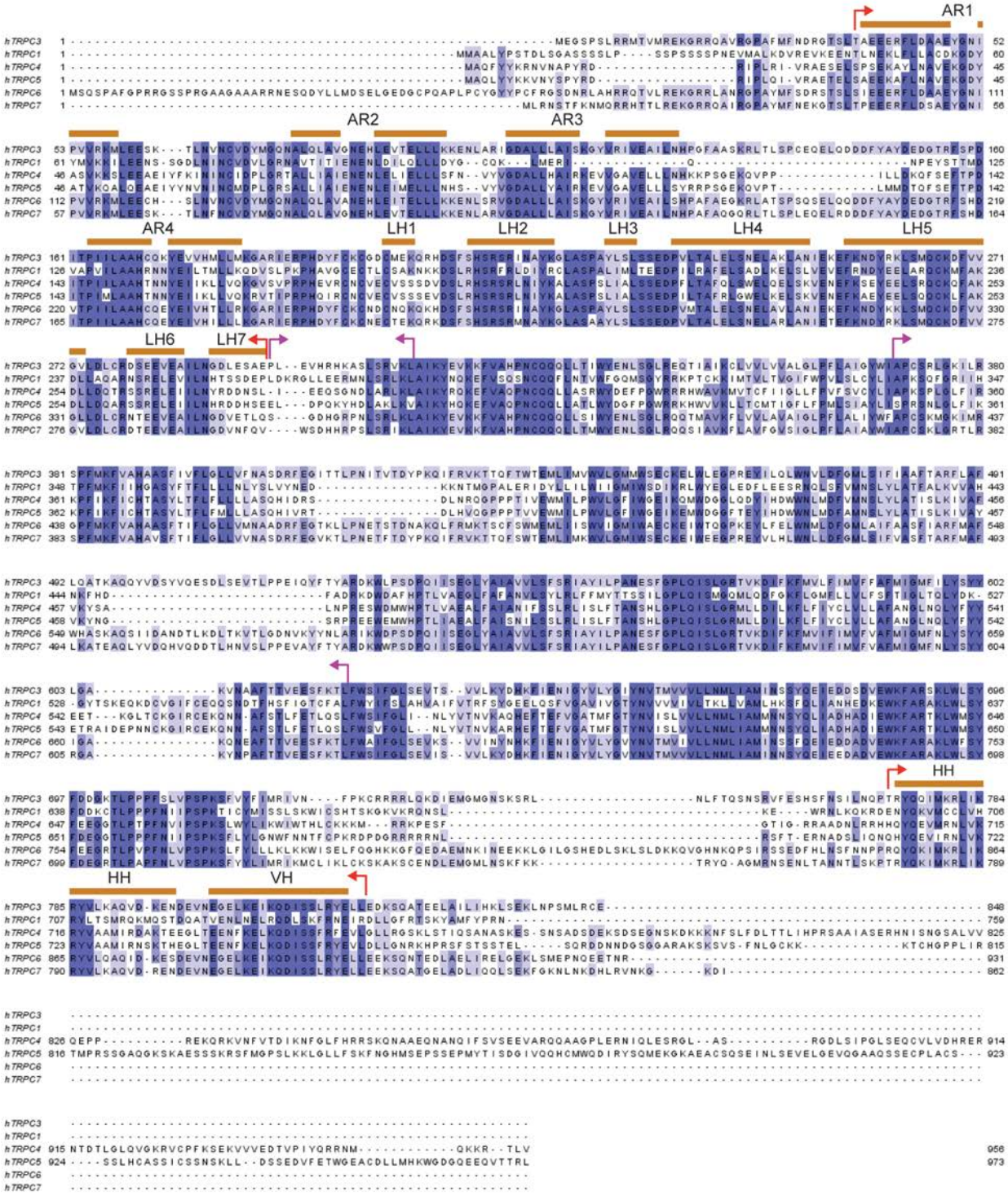

Figure 6-5. Sequence alignment of human TRPC channels.
The sequences for hTRPC1/3/4/5/6/7 were aligned using the Clustal Omega program and colored using percentage of identity score in Jalview v2 (Waterhouse et al., 2009). Secondary structure assignments are based on our human TRPC3 structure with α-helices indicated in orange. Red arrows indicate the CPD model built with side-chains, and magenta arrows indicate the polyalanine model built of the TMD.

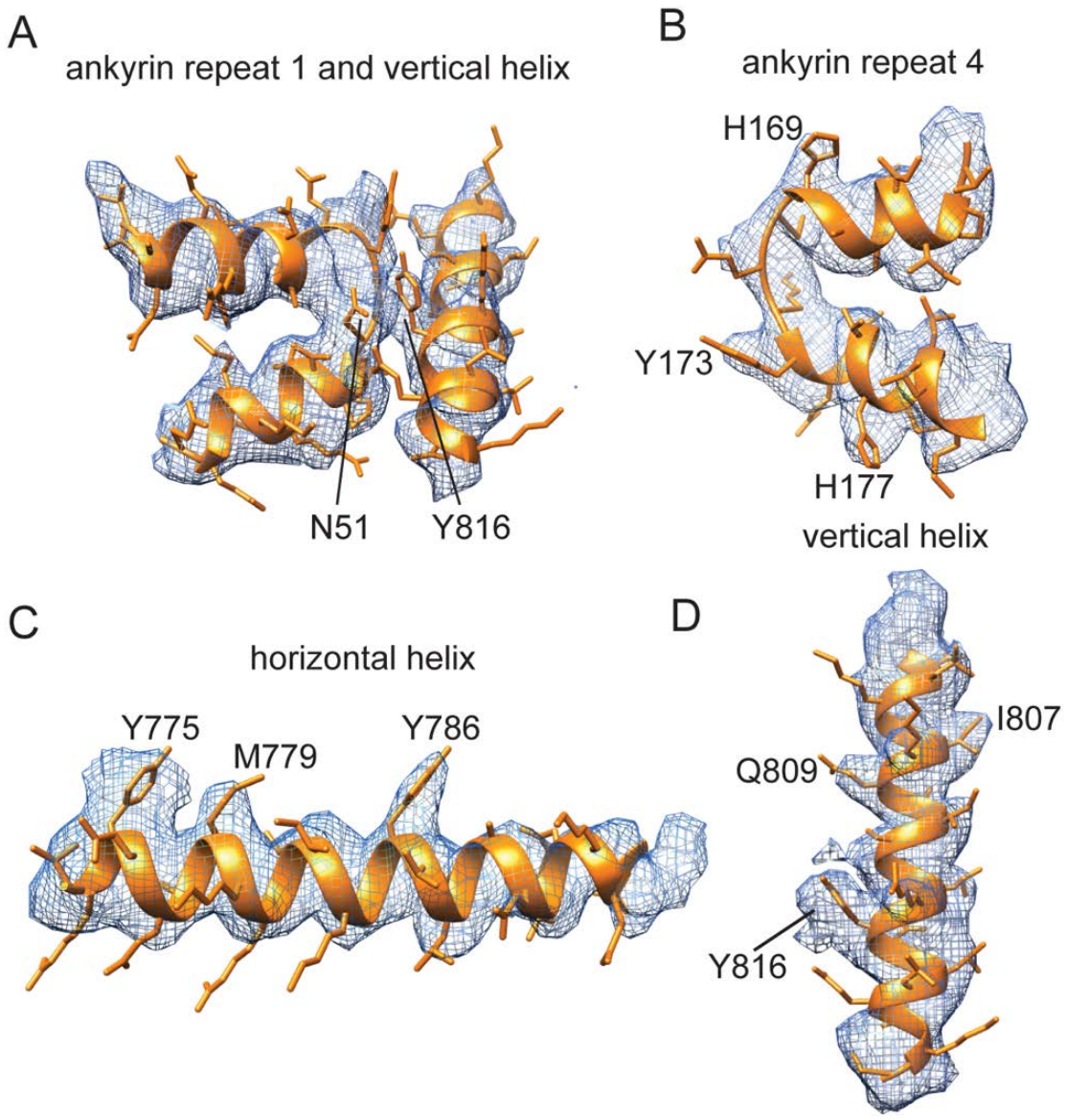

Figure 6-6. Representative regions for local fit of the atomic model of TRPC3$_{PMAL}$ cytoplasmic domain in the 4.0Å density map determined on the Titan Krios.
A. Ankyrin repeat 1 and part of the vertical helix, showing contact between N51 and Y816. **B.** Ankyrin repeat 4. **C.** C-terminal horizontal helix. **D.** C-terminal vertical helix.

TRPC6 between Tyr-895 and Asn-109[120]. On the periphery of the CPD, our structure also shows extensive intra-subunit interactions. Once such contact is formed between Tyr-72 in the first loop between AR1 and AR2 and His-177 in AR4 of the adjacent subunit (**Figure 6-10B**). Interactions in both the interior and exterior of the CPD are likely stabilizing and allow the CPD to exist as a stable module even when the TMD is heterogeneous, like in our structure solved in PMAL-8.

We also see interactions between two adjacent VHs. Most of the side chains in this region are small and not well resolved, but a point of contact can be seen in the density between Val-799 and Leu-804, which we speculate is a stabilizing hydrophobic interaction (**Figure 6-10C**). There are likely other points of interaction between the VH and HHs in this part of the protein, but our resolution is not high enough to describe additional interactions. Because the HH is coupled to the TRP helix, which is attached to S6 (channel gate), we suggest that changes in residue contacts on the HH could directly impact channel gating. Indeed, FSGS-causing mutations that affect channel gating are found in the HH and its associated structures[120]. Finally, at the central axis, the HH makes a 100° downward turn and transitions into the VH through a short linker (**Figure 6-8D-E** and **Figure 6-9F**). In the tetrameric assembly, the VHs form a coiled-coil domain. Notably, the structure of TRPC3 revealed a C-terminal domain swap in the center of the tetrameric assembly (**Figure 6-8E**). This arrangement is characterized by a counterclockwise crossover of linkers that connect the HHs and VHs. A similar domain swap is observed in TRPC6[120,129]. In contrast, this arrangement is absent in other members of the TRP subfamilies such as TRPM8, TRPA1, and TRPM4 (**Figure 6-8F**); hence, the C-terminal domain swap might be a unique fold of the TRPC subfamily.

Conformational diversity in the cytoplasmic domain

Two TRPC3 cryo-EM structures have been solved recently[121,129]. In Fan et al., TRPC3 was solved in digitonin whereas the structure in Tang et al. was solved in nanodiscs; hereafter, we will refer to each structure as $TRPC3_{digitonin}$ and $TRPC3_{nanodisc}$. The structural features of our $TRPC3_{GDN}$ model agree with the $TRPC3_{nanodisc}$ in the TMD as well as in the CPD (**Figure 6-10D**). On the other hand, we observed major differences in the CPD of $TRPC3_{GDN}$ (our structure) compared to $TRPC3_{digitonin}$. Particularly, we observed differences in the geometric arrangement of the HHs. In $TRPC3_{GDN}$, the angle formed between the HHs in opposite subunits is 172º (**Figure 6-11A**), whereas in $TRPC3_{digitonin}$ this angle is 153º (**Figure 6-11B**). The angles formed by TRP helices of opposite subunits are similar (~154º); hence, the TRP helix and the HH are maintained nearly parallel to each other in the $TRPC3_{digitonin}$ structure, whereas in our model they are not (**Figure 6-11A-C**, black dotted lines). Interestingly, the positions of the TRP helix and HH in $TRPC3_{digitonin}$ are similar to the ones observed in TRPC4[125]. We have captured a conformational state in which the HHs are nearly parallel to the membrane plane (**Figure 6-11C**, top); this putative conformation was also observed in the $TRPC3_{nanodisc}$ structure. Conformational changes in the HH could transduce to the ion channel gate (S6 segment); therefore, the loop connecting the TRP helix and the HH might play a critical role in channel gating.

Interestingly, our structure displays a counterclockwise rotation of AR1-3 when compared to those of $TRPC3_{digitonin}$ (**Figure 6-10E**). As a consequence, the ankyrin repeats are closer to each other and to the VH (**Figure 6-11D-E**, double headed arrows). These changes reduce the size of the lateral fenestrations between the ARDs and could decrease the movement of ions and small molecules in and out of the cytoplasmic cavity. It is also possible that these ARD displacements will expose distinct sites for interaction with intracellular components. Moreover, we observed that the inter-subunit interface of the coiled-coil domain is larger in our structure (14.7Å) than in $TRPC3_{digitonin}$ structure (7.8Å) (**Figure 6-11D-E**, dotted circles); likely due to the 4.5° difference between the VHs in both structures (**Figure 6-11C**, bottom). Unlike the structures of $TRPC3_{GDN}$ and $TRPC3_{nanodisc}$, the $TRPC3_{digitonin}$ does not display a C-terminal domain swap, resembling the TRPM4 organization (**Figure 6-11F**, bottom panel and **Figure 6-10F**). The cartoon shown in Fig 4G summarizes the major differences between $TRPC3_{GDN}$ and $TRPC3_{digitonin}$ highlighted with arrows.

The C-terminal loop fine-tunes channel function

Based on the TRPC3 structural comparisons, we hypothesize that upward and downward movements of the HH alter TRPC3 gating via the C-terminal loop connecting the TRP helix and HH. Indeed, a previous work reported that a rodent alternative splice variant (TRPC3c), in which 18% of the

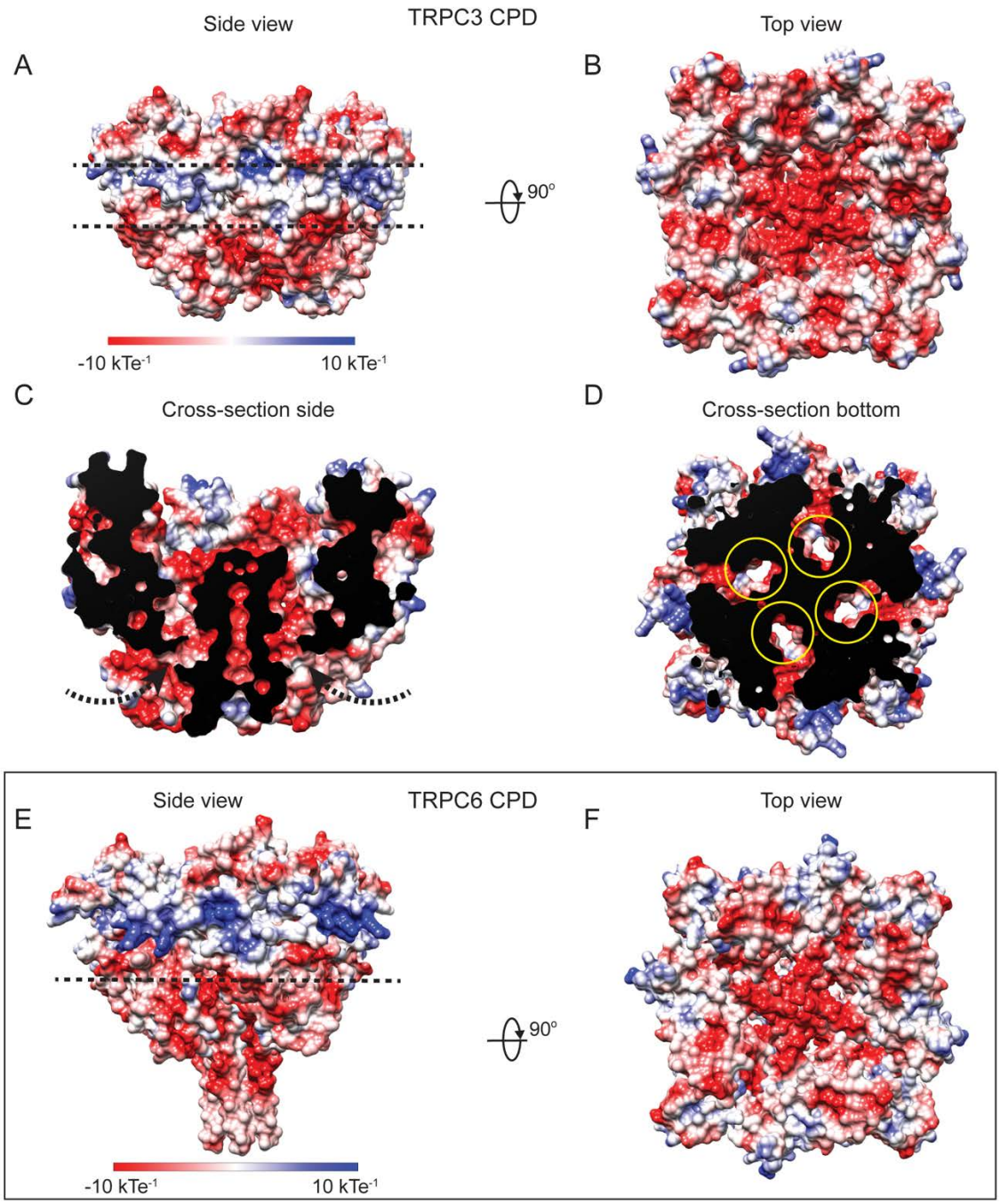

Figure 6-7. Electrostatic potential of TRPC3$_{PMAL}$ cytoplasmic domain.
A. Side view indicating the sandwich-like distribution of negative, neutral, and positive charges on the CPD surface. Dotted lines indicate a patch of neutral and positive charges. **B.** Top view indicating the overall negative charge of the inner chamber. **C.** Side view cross-section indicating the openings that provide access to the chamber interior (arrow). **D.** Top view cross-section showing the openings that connect the cytoplasm to the bowl interior and channel gate (yellow circles). **E.** Side view of the TRPC6 CPD indicating the dual distribution of negative and neutral, and positive charges on the CPD surface. Dotted line indicates the boundaries of the electrostatic potential. **F.** Top view indicating the overall negative charge of the TRPC6 inner chamber.

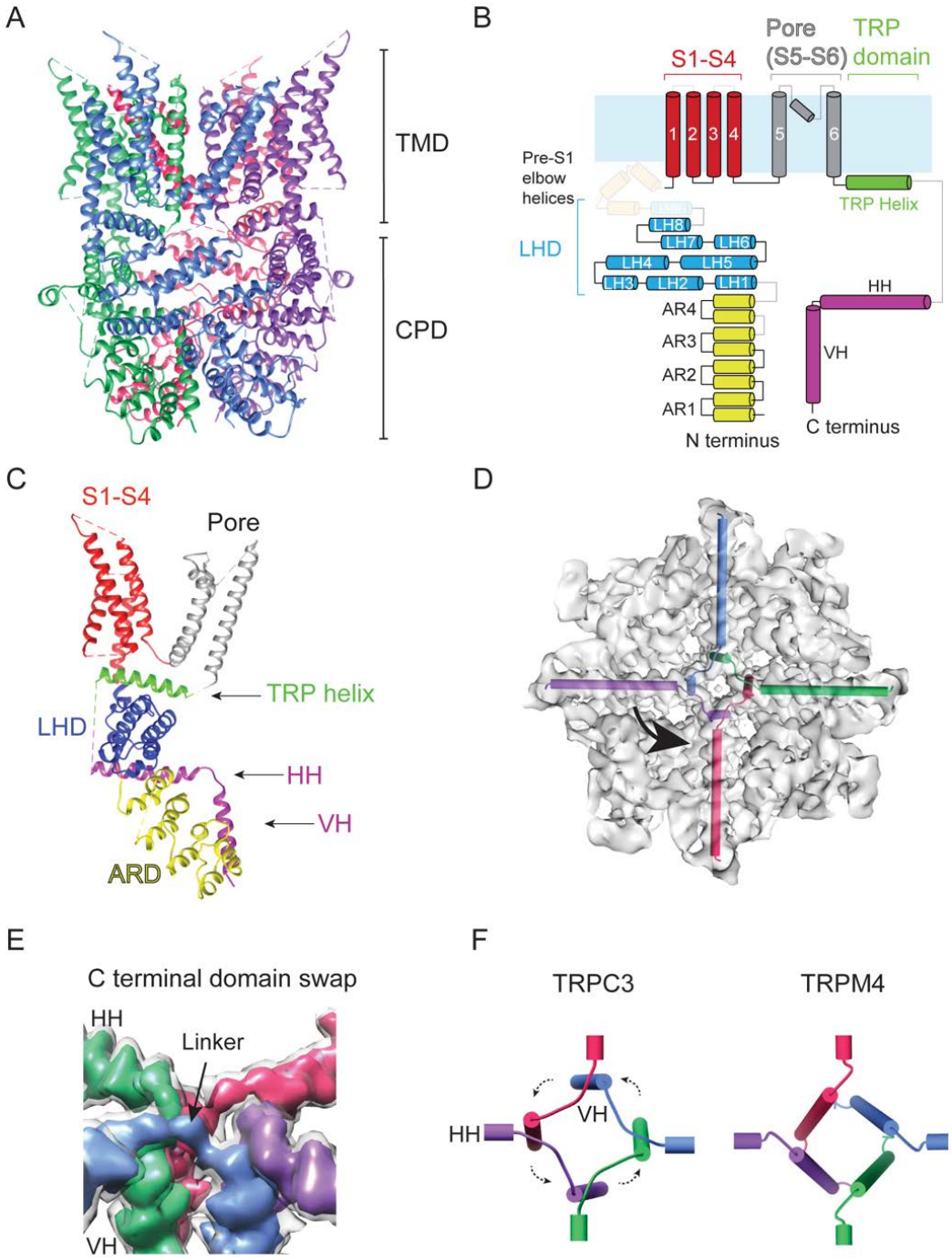

Figure 6-8. Detailed structural features of TRPC3.
A. Ribbon diagram of the TRPC3 model built from the EM density map shown in Figs. 1C and 2D with the four subunits in blue, green, pink, and purple. **B.** Cartoon representation of the secondary structure organization of a single TRPC3 subunit. ARD is in yellow, LHD is in blue, transmembrane helices are in red (S1–S4) and gray (S5, pore helix, and S6), the TRP domain helix is in green, and the C-terminal helices are in pink. Light blue represents the plasma membrane. Regions not resolved in the structure are shaded out. **C.** The ribbon diagram structure of a single TRPC3 subunit. The domains are color-coded in the same way as in B. **D.** Top view of TRPC3 with HHs and VHs represented by cylinders inside the electron density map, highlighting the C-terminal helices' domain swaps. **E.** Close-up look at the domain swap that occurs at the intersection of the HHs and VHs. The map is displayed at two threshold levels with the four-subunit map in light gray and four different subunits in colors showing the connection between the HHs and VHs. **F.** Cylindrical representation of the intersection of the four HHs and VHs of TRPC3 (left) and TRPM4 (right; PDB code 6BCL). Note the lack of domain swap in TRPM4.

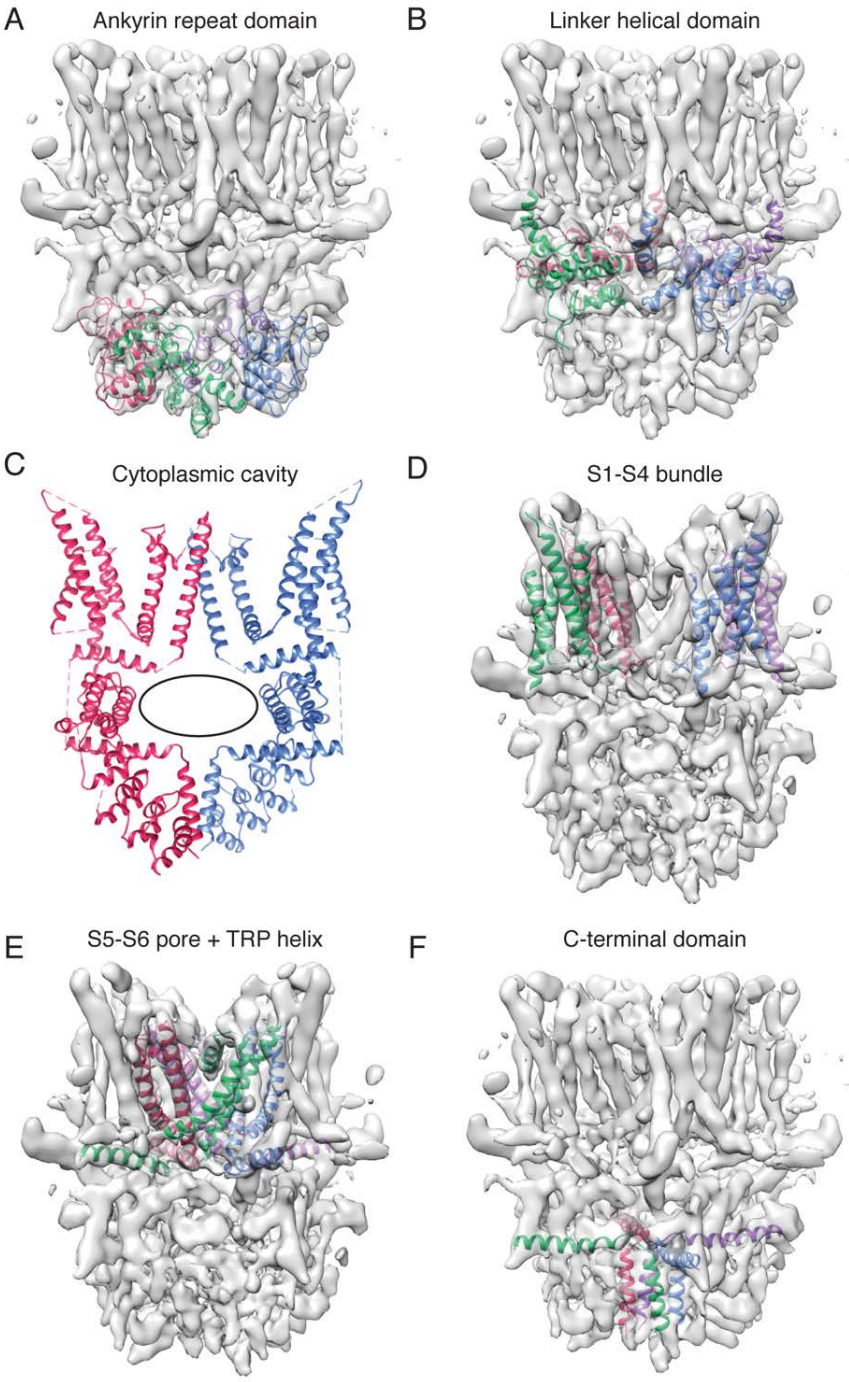

Figure 6-9. Layered organization of TRPC3.
A. Electron density map of $TRPC3_{GDN}$ is represented in transparent grey with only the ankyrin repeat domains of the four subunits shown and colored in blue, green, pink, and purple. These form the base of the inverted dome of the CPD. **B.** The linker helical domains of the four subunits are shown in the $TRPC3_{GDN}$ electron density map forming the top of the inverted dome of the CPD. **C.** Two, opposite subunits of TRPC3 are show in pink and blue to highlight the inner chamber (black oval) formed by the CPD that sits underneath the transmembrane helices. **D.** The S1-S4 transmembrane helix bundle of the four subunits shown and colored in blue, green, pink, and purple inside the $TRPC3_{GDN}$ electron density map. **E.** Electron density map of $TRPC3_{GDN}$ is represented in transparent grey with the S5-S6 pore helices, including the TRP helix, of the four subunits shown and colored in blue, green, pink, and purple. **F.** The C-terminal horizontal and vertical helices of the four subunits shown in the $TRPC3_{GDN}$ electron density map coming in from the sides of the dome and forming a coiled coil.

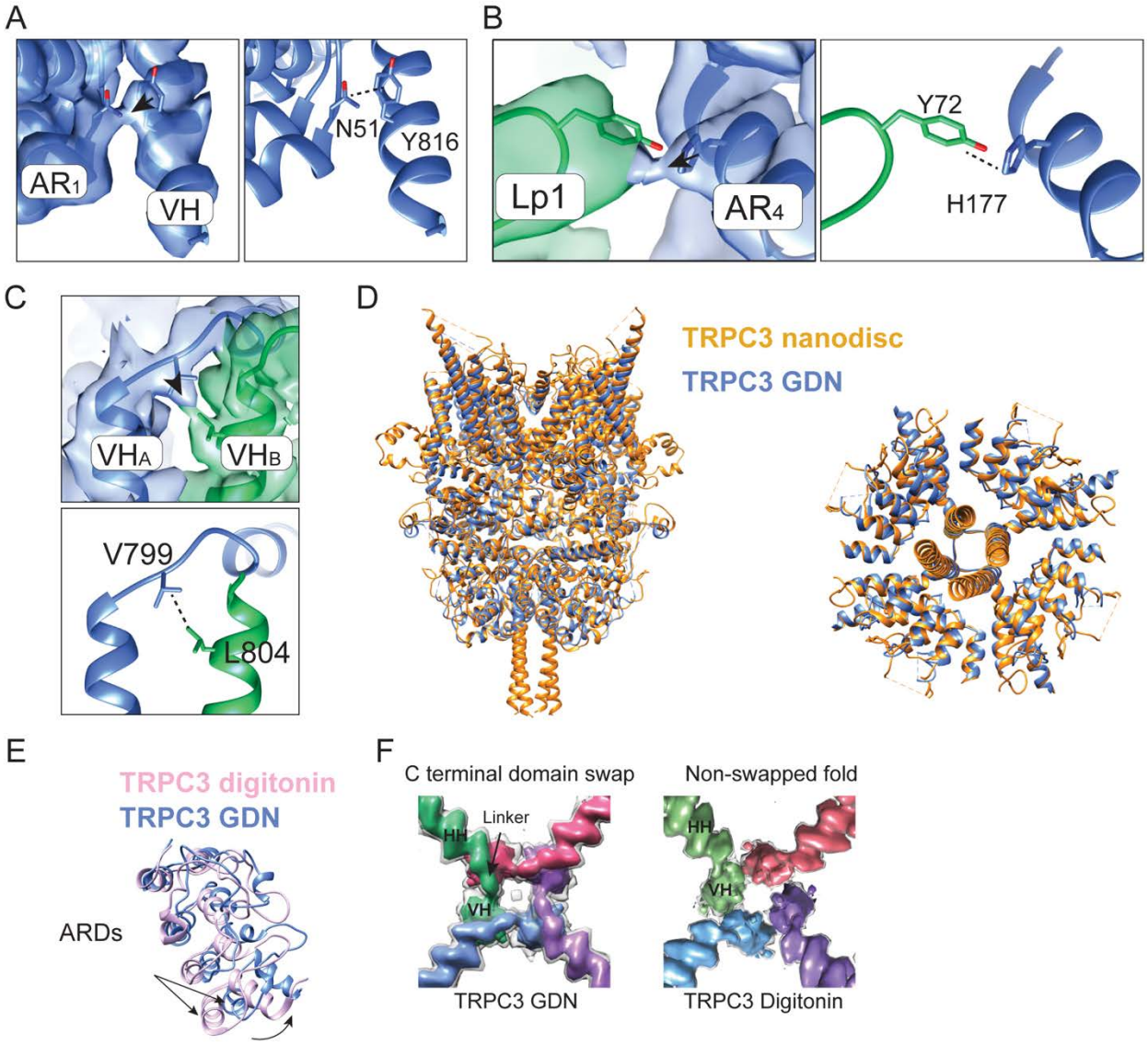

Figure 6-10. Cytoplasmic domain α-helix interactions.

A. Inter-subunit interactions between the VH and AR1. Map is presented at σ28 with sigma calculated as the map threshold divided by the RMS calculated in UCSF Chimera. **B.** Intra-subunit interactions between the loop between AR1 and AR2 (green) and the adjacent subunit's AR4 (blue). Maps are presented at σ19 and σ20. **C.** Intra-subunit interactions between adjacent VHs. Both maps are presented at σ17. **D.** Left: side view superposition of full length $TRPC3_{GDN}$ (blue) and $TRPC3_{nanodisc}$ (orange) and right: bottom view superposition of the CPD. **E.** Superposition of AR1-4 between the $TRPC3_{GDN}$ (blue) and $TRPC3_{digitonin}$ (pink) structures showing that AR1-3 are shifted counter-clockwise in $TRPC3_{GDN}$. Black arrows indicate the change in position between the ankyrin repeats. **F.** Electron density maps highlighting the intersection of the HHs and VHs of $TRPC3_{GDN}$ (domain swap) and $TRPC3_{digitonin}$ (no domain swap; EMD-7620). Individual subunits colored in blue, green, pink, and purple are displayed at a higher threshold than the tetramer in transparent grey.

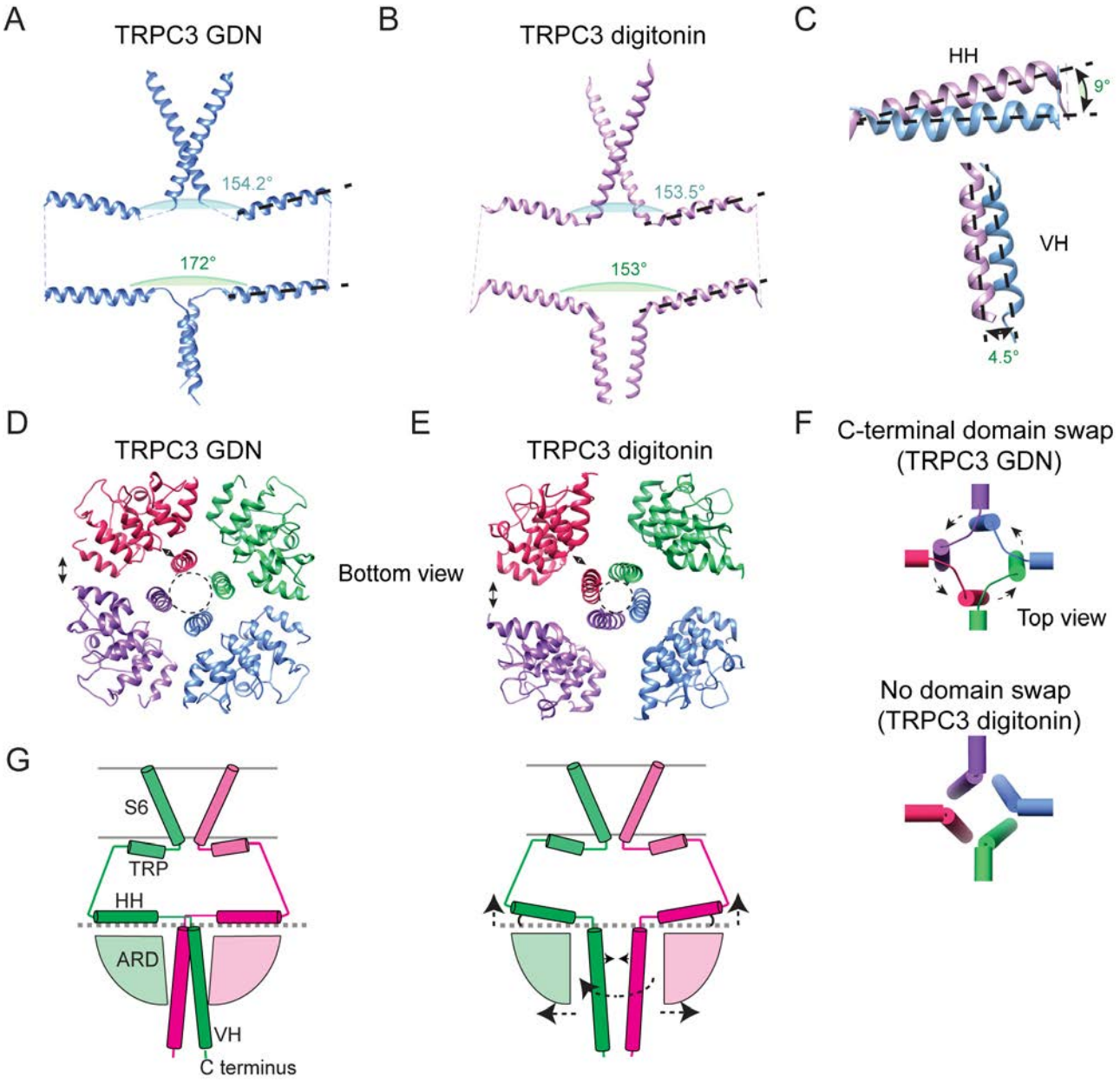

Figure 6-11. Structural diversity of the CPD.
Two opposite subunits of the $TRPC3_{GDN}$ **(A)** and the $TRPC3_{digitonin}$ (PDB: 6CUD) **(B)** structures showing S6 segments, TRP helices, HHs, and VHs. Angles between opposite TRP helices and HHs are indicated. **C.** Close-up look comparing the angles of the HH (top) and VH (bottom) of the $TRPC3_{GDN}$ and $TRPC3_{digitonin}$ structures. Bottom views of the $TRPC3_{GDN}$ **(D)** and $TRPC3_{digitonin}$ **(E)** structures. Note, that the ARDs in the $TRPC3_{GDN}$ structure are closer to each other at the periphery of the CPD and to the VHs at the central axis, indicated by the double-headed arrows. **F.** Organization of the HHs and VHs in $TRPC3_{GDN}$ (top) and $TRPC3_{digitonin}$ (bottom) structures. Note, that the domain swap is absent in the $TRPC3_{digitonin}$. **G.** Cartoon summarizing the differences observed in the CPDs of the TRPC3 structures.

C-terminal loop and the first three amino acid residues of the HH helix are absent, displays enhanced activity when compared to the longest isoform[298]. We engineered the equivalent splice variant into the human TRPC3 isoform b (Δ28TRPC3) and found an increase in channel activity in response to the specific agonist GSK-170 when compared to wild type, as determined using the ratio of current amplitudes produced by 0.2 and 1μM GSK-170 at holding potential +100mV (**Figure 6-12B**, **C**, and **G**). CaM inhibits TRPC3 function by binding to the CIRB domain (**Figure 6-13B**, black arrow)[299] and the Δ28TRPC3 lacks the N-terminal half of the CIRB (**Figure 6-12A**). Therefore, this construct would not allow us to determine that the change in channel function is solely due to the C-terminal loop. To this end, we generated a shorter construct lacking six amino acid residues (Δ6TRPC3) without disrupting the CIRB (**Figure 6-12**). We found that Δ6TRPC3 enhances TRPC3 activity similarly to Δ28TRPC3 (**Figure 6-12D** and **6-12G**). Importantly, we observed in most of our whole-cell recordings that background channel activities (i.e., currents without agonist) were higher in the Δ28 and Δ6 TRPC3 when compared to WT TRPC3 (**Figure 6-13A**).

Conversely, we observed a decrease in channel activity when elongating the C-terminal loop with the addition of four glycines (**Figure 6-12E** and **6-12G**). This result is supported when further decreasing TRPC3 activity by elongating the loop and increasing its flexibility with the addition of eight glycines (between Gly-743-Asn-744) and a neighbor single point mutation (M742G; **Figure 6-12F-G**). We also observed that linker-elongated construct M742G + 8G displays lower background currents when compared to WT and Δ28 TRPC3 (**Figure 6-13A**). Given these results – different deletion or insertion locations yield distinct background currents and channel activation – it is unlikely that we are altering the affinity of the mutant channels for GSK-170 but rather impairing the coupling between the C-terminal domain and the TMD. Our results support the idea that there is a correlation between the length of the linker and the magnitude of channel modulation, specifically shortening the C-terminal loop increases channel activity by creating a stronger coupling between the TRP helix and the HH. It is tempting to speculate that binding of the Ca^{2+}-CaM complex inhibits channel activity by restricting HH movement and decreasing allosteric coupling.

Discussion

Unlike the ionotropic glutamate receptors that transfer information on a millisecond time scale[300], the activation and desensitization of TRPC3-mediated currents are on the order of seconds, often requiring the upstream activation of metabotropic glutamate and muscarinic acetylcholine receptors[160,301]. Given the slower time course of action compared to the fast-excitatory synaptic transmission, TRPC3 likely modulates the sensitivity of neurons to fire action potentials[302]. Consistent with this idea, pharmacological inhibition of TRPC3 influences simple spike frequency in Purkinje neurons[303]. At the behavioral level, a TRPC3 gain-of-function mutation in the *moonwalker* mouse, T573A, results in cerebellar ataxia that facilitates backward ambulation[160]. Mechanistic information on TRPC3 channel gating – including how TRPC3 integrates multiple intracellular signals – is critical for understanding its biological roles. Our structural and functional analyses provide insights into the conformational changes that regulate channel function.

Our TRPC3 structures in PMAL-C8 and GDN indicate that the CPD is a stable domain that can maintain its tetrameric assembly even in the presence of a flexible TMD; our CPD and full-length TRPC3 structures resemble that of TRPC3 in nanodiscs (**Figure 6-10D**)[120,129]. The architecture of the CPD also provides insights into how subunits assembly occurs in TRPC3. The structure of the mature assembly shows that the HH and VH are buried within the ARD and provide stability and anchorage by securing the bowl-shaped CPD. Notably, domain swaps occur when the four HHs merge near the central axis-of-symmetry, characterized by a crossover of linkers that connect the HHs and VHs. This organization facilitates intra- and inter-subunit interactions between residues at the HHs and VHs; this assembly must confer cooperativity among the subunits and provide enhanced stability to this domain. Contacts between the ARD and VH (**Figure 6-6A**) are also conserved in TRPC6[120] and coincide with the locations of human mutations that cause FSGS[149–151,153]. Since these disease-causing mutations in TRPC6 affect channel gating without making direct contact with the pore domain, this interface is predicted as a site of allosteric modulation for the TRPC subfamily. Moreover, intracellular molecules that alter these interactions might impact channel gating.

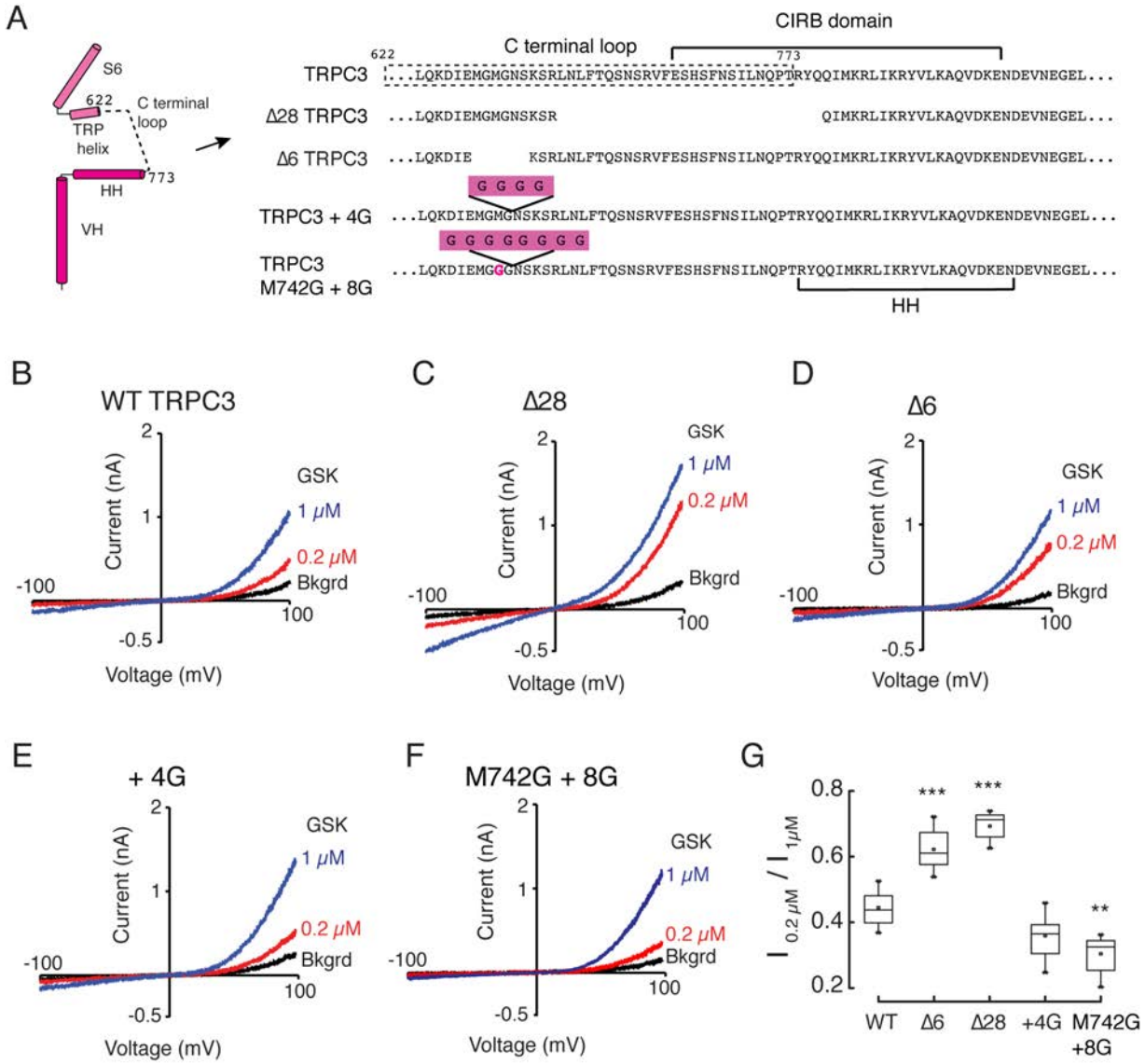

Figure 6-12. Functional characterization of TRPC3 C-terminal loop mutants.
A. Subunit diagram and amino acid sequence highlighting the changes made in the C-terminal loop of human TRPC3 to generate the deletion constructs Δ749–776 (Δ28TRPC3), Δ740–745 (Δ6TRPC3), and the two glycine insertion constructs TRPC3+4G and M742G+8G. Shown are representative whole-cell recording from HEK293 cells expressing TRPC3 **(B)**, Δ28TRPC3 **(C)**, Δ6TRPC3 **(D)**, TRPC3+4G **(E)**, and M742G+8G **(F)**. Currents were evoked by 0.2 (red) and 1 μM (blue) GSK-170 (GSK). G. Box-plot summary of the ratio between the current evoked by 0.2 μM and the maximal current at 1 μM GSK-170 at±100 mV. For each construct, we measured n=12 independent whole-cell recordings. Box plots show the mean, median, and the 75th to 25th percentiles. Statistics were calculated using a one-way analysis of variance and Bonferroni test. Error bars indicate the 1 and 99th percentiles, ** indicates $p<0.05$, and *** indicates $p<0.001$. Bkgrd, background.

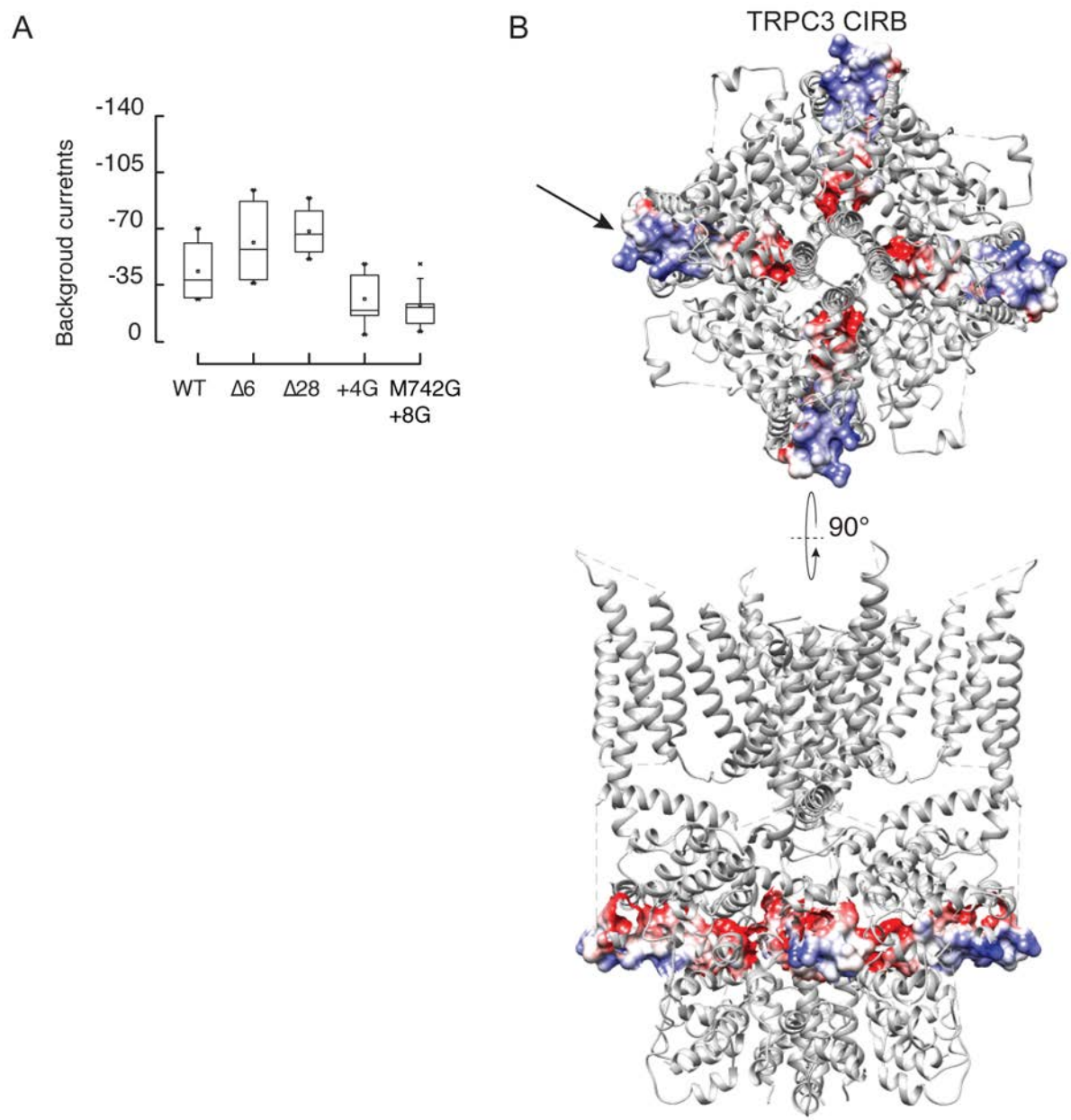

Figure 6-13. Effects of the C-terminal loop and CIRB domain on TRPC3 gating.
A. Background currents for the C-terminal loop mutants at -60 mV. **B.** Bottom and side view highlighting the CIRB domain and the electrostatic potential of this region.

We observed substantial differences in the VHs and ARDs organization when comparing the $TRPC3_{GDN}$ and $TRPC3_{digitonin}$ structures[120,121] (**Figure 6-11D-E** and **6-11G**). For instance, the intra-subunit distance between AR1 (Pro53) and the end of the VH (Leu819) are 10.1Å for $TRPC3_{GDN}$ and 14.3Å for the equivalent positions in $TRPC3_{digitonin}$. Likewise, the inter-subunit space between AR1 and AR4 are 18.4Å for $TRPC3_{GDN}$ and 22.2Å for $TRPC3_{digitonin}$. Although it is possible that these differences are due to sample preparation methods, we speculate that TRPC3 can interchange between these two states during gating. If this were the case, the CPD would undergo major conformational changes such that the HH and VH could switch or unwind from a domain-swapped arrangement ($TRPC3_{GDN}$ and $TRPC3_{nanodisc}$) to a non-swapped fold ($TRPC3_{digitonin}$) and back. The TRPC3 non-swapped fold architecture is also seen in other TRP channels such as TRPM4[127,128,291]. Future structure and function experiments are required to determine whether these conformational states occur during TRPC3 gating; it would be interesting to investigate whether TRPM4 can also adopt a domain-swapped arrangement.

TRPC3 is a sensor molecule that integrates a variety of intracellular signals, including bioactive lipids and Ca^{2+} gradients[170]. For instance, it was recently shown that a single mutation in the S6 segment behind the pore helix reduces the activation by DAG[304]. Phosphorylation after the TRP helix has been shown to negatively regulate channel function[305]. The Ca^{2+}-CaM complex inhibits channel activity; however, at low Ca^{2+} concentration the IP_3R binds the CIRB and enhances its function[165].

How does the cytoplasmic domain modulate channel function? We propose a model in which the HH can bend upward and downward (**Figure 6-14A-B**); this rigid-body motion would be transduced to the TRP helix via the connecting loop and in turn influence the channel gate at the S6 segment (**Figure 6-14**). Several lines of evidence, including our own, support this model. First, the TRPC3 structures in GDN and digitonin display different angles of the HH with respect to the membrane, suggesting that the HH can reside in these positions. Second, shortening of the C-terminal loop enhances channel activity, presumably by increasing coupling between the TRP helix and the HH (**Figure 6-14B**); hence, the C-terminal loop is a critical region for the allosteric coupling between the cytoplasmic and transmembrane domains. The C-terminal loop might also provide buffering capacity due to its intrinsic flexibility, consistent with the different degrees of bending occurring at the HHs, the decrease in activity when lengthening the loop with glycines (**Figure 6-14C**), and the lack of structural organization. Such buffering might be advantageous to prevent spurious modulation caused by fluctuations of the CPD. Third, binding of CaM to the HH inhibits channel opening[165], likely by restricting movement of the HH and decreasing allosteric coupling. It is possible that the mechanism whereby the CPD modulate channel function through the HH and the C-terminal loop is conserved, since it has been shown that calmodulin also regulates TRPA1[306], and TRPM4[307] function by binding to the corresponding CPD region. Further functional and structural experiments are needed to validate whether the upward movement of the HHs corresponds to a positive modulation of the TRPC3 gating cycle.

Experimental Procedures

Functional (verified by whole cell current clamp, see *Materials and Methods*) human TRPC3 was expressed in Sf9 cells and two separate samples were purified in GDN detergent and PMAL-8 amphipol as described in *Materials and Methods*. hTRPC3 in GDN in vitrified ice was prepared as detailed in *Materials and Methods* and **Table 2-2**. Data was collected on a K2 summit direct electron detector using the Polara F30 microscope in the Vanderbilt Cryo-Electron Microscopy Facility, see *Materials and Methods* and **Table 2-3**. hTRPC3 in PMAL-8 amphipol was prepared in vitrified ice as in *Materials and Methods* and **Table 2-2**. Micrographs were collected on a K2 summit direct electron detector using the FEI Titan Krios microscope at the Washington University in St. Louis Center for Cellular Imaging with imaging conditions in *Materials and Methods* and **Table 2-3**. Image processing in RELION 2.1 was carried out as described in *Materials and Methods* and **Table 2-4** with 2D class averages from TRPC6 in PMAL-8 used as initial templates for automatic picking for both data sets. Separate 3D classifications were run on the three data collection sessions for $TRPC3_{GDN}$. Particles from the best 3 of 14 classes were pooled and subjected to 3D refinement, post-processing, and local resolution calculation in RELION 2.1 (**Figure 6-2**). A heat map of local resolution was generated for both EM maps using ResMap. TRPC structures were built *de novo*, see *Materials and Methods.* For the $TRPC3_{GDN}$ hybrid model, refinement steps using these parameters were iterated seven times with manual adjustment of the structure to correct for Ramachandran and rotamer outliers and bond angle deviations of more than 4σ. We performed a round

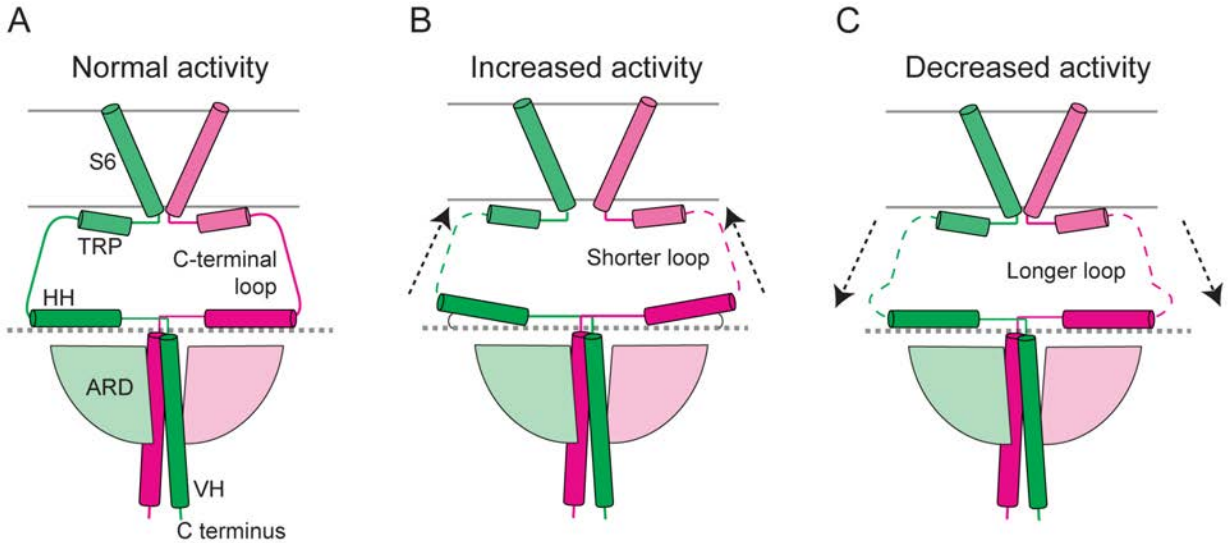

Figure 6-14. Model for the role of the C-terminal loop in TRPC3 channel function.
This diagram summarizes the electrophysiological data in which the C-terminal loop length modulates TRPC3 activity. **A.** schematic of the structure of TRPC3GDN. A shorter loop enhances coupling between the HH and the TMD and in turn increases activity **(B)**, whereas a longer loop has the opposite effect **(C)**.

of refinement that incorporated morphing, global minimization, secondary structure restraints, simulated annealing, and NCS, followed by a round with only morphing. A final two iterations of refinement with strict geometric restraints and manual adjustment in Coot were performed. To conserve helix assignments, secondary structure restraints were used throughout. For the $TRPC3_{PMAL}$ model, refinement steps using these parameters were iterated five times with manual adjustment of the structure to correct for Ramachandran and rotamer outliers and bond angle deviations of more than 4σ. We performed a round of refinement that incorporated morphing, global minimization, secondary structure restraints, simulated annealing, and NCS. A final four iterations of refinement with strict geometric restraints and manual adjustment in Coot were performed. Angles measurements and data deposits for data presented in this chapter are stated in *Materials and Methods.*

Data collection and processing	**$TRPC3_{GDN}$ Polara**			**$TRPC3_{PMAL}$ Titan Krios**
Nominal magnification	31000x			105000x
Voltage (kV)	300			300
Electron exposure ($e^-/Å^2$)	100			48.9
Defocus range (μm)	-2.0 - -5.0			-1.2 - -3.0
Pixel size (Å)	1.247			1.096
Symmetry group	C4			C4
No. of micrographs	3283			2032
Total particle count (particles in good 2D class averages)	1,023,730 (576,237)			464,991 (149,602)
Particles in final reconstruction	38,656			19,526
Map resolution (Å)	5.8			4.0
Map sharpening B factor ($Å^2$)	-179			-126
Refinement	**Alanine model**	**Hybrid model**		**Full atom model**
		Full model	**CPD only**	
Model resolution range (Å)	319.229-5.80	319.229-5.80	319.229-5.80	280.57-4.37
No. of residues (monomer)	490	490	215	288
No. of atoms (monomer)	2450	3222	1677	2293
No. of bonds (monomer)	2439	3237	2100	2322
B factors ($Å^2$)	375.04-41.50	436-01-79.20	324.38-79.20	191.00-67.19
Mean	201.00	219.69	207.38	130.77
RMSD				
Bond lengths (Å)	0.005	0.006	0.006	0.005
Bond angles (°)	0.942	1.142	1.274	1.137
Validation				
MolProbity score	1.67	1.83	2.02	1.70
Clashscore	4.35	6.92	8.96	4.18
Rotamer outliers	0.00%	0.00%	0.00%	0.00%
C-beta outliers	0	0	0	0
Ramachandran plot				
Favored	92.74%	93.11%	90.14%	91.49%
Allowed	7.26%	6.89%	9.96%	8.51%
Disallowed	0.00%	0.00%	0.00%	0.00%

Table 6-1. Map and model statistics for hTRPC3.
Microscope and image processing information for both $TRPC3_{PMAL}$ and $TRPC3_{GDN}$ data. Refinement statistics for the final models of the TRPC3 CPD and full-length TRPC3. Alanine model refers to the full-length polyalanine model of TRPC3. Hybrid model refers to the polyalanine model TMD with the full atom

model of the cytoplasmic domain with refinement in $TRPC3_{GDN}$. Validation and statistics were calculated using MolProbity. RMSD, root mean squared deviation.

CHAPTER VII: CRYO-EM STRUCTURE OF THE INOSITOL TRIPHOSPHATE RECEPTOR SHOWS BINDING OF SMALL MOLECULES, LIPIDS, AND PERMEANT IONS

This section is a paper currently being prepared for submission as "TBD" Caleigh M. Azumaya, Emily A. Linton, Terunaga Nakagawa, Erkan Karakas.

Aims

The type 3 IP_3R (IP_3R-3) regulates Ca^{2+} release from the ER. Revealing the precise mechanism of activation and inhibition of this ion channel will be critical to understand biological processes that are controlled by IP_3R-3, such as ER-mitochondria interaction, differentiation, and cancer. Here we report a cryo-EM structure of the IP_3R-3 at an overall resolution of 4Å, with local resolution reaching 2.7Å. To our surprise, the ligand-binding site was occupied by an unknown ligand. This is postulated to be EDTA, a competitive inhibitor of IP_3Rs, but ongoing analyses are being conducted to determine if the ligand is large than originally thought. Our structure also identified previously unresolved local structures, lipid binding sites, and ions in the ion permeation pathway. Collectively, the data we report provide new information on the architecture and interactions of IP_3Rs.

There are three different subtypes (1-3) of IP_3Rs, which share 60-70% identity in sequence, can form homo- or heterotetramers, exhibit different spatial expression profiles, and are involved in diverse signaling pathways. IP_3R-3s are predominantly expressed in rapidly proliferating cells and are involved in taste perception and hair growth[308–310]. Additionally, IP_3R-3 is the primary subunit involved in apoptotic Ca^{2+} flux from the ER to the mitochondria and its deregulation is implicated in diseases with deficiencies in cell fate decisions such as cancer and degenerative diseases[311–313]. For example, the expression of the IP_3R-3 is upregulated in several cancer types including glioblastoma, breast, gastric, and colorectal cancer[314–317]. Furthermore, many tumor suppressors and oncoproteins such as protein kinase B, protein phosphatase 2A, promyelocytic leukemia protein, phosphatase and tensin homolog (PTEN), and BRCA1-associated protein 1 tightly regulate the stability and activity of IP_3R-3s[312,318–320]. Moreover, inhibiting IP_3R-3 degradation in PTEN-regulated cancers was shown to be a valid therapeutic strategy[318].

Our structure identified previously unresolved local structures of the complex, ion binding sites in the ion permeation path, and location of lipid biding sites in the transmembrane domain. There is also an unknown density that we originally characterized as EDTA, but are considering may be a larger ligand carried over from purification or a site of autoinhibition. Collectively, our structural characterization of the hIP_3R-3 provides novel insight into the mechanistic function of IP_3Rs.

Results and Discussion

EDTA binds to hIP_3R-3 and competes against IP_3 binding

We expressed recombinant hIP_3R-3 using the insect cells/baculovirus expression system, purified detergent-solubilized protein in the absence of any known ligands, and solved its structure using cryo-EM to an average resolution of 4.0Å (**Figures 7-1**, **7-2**, **7-3**, **7-4**, **7-5A**). The majority of particles were grouped into only one 3D-class indicating high conformational homogeneity of the receptor (**Figure 7-2**). The local resolution of the cryo-EM map reached 2.7Å resolution at the core of the protein, allowing *de novo* modeling of the structure (**Figure 7-4**, **7-6**, and **Table 7-1**). We used high resolution crystal structures fit into the ligand binding core (LBC) (PDB IDs: 3JRR and 3UJ4) and modeled the rest of the structure manually[321,322]. The overall structure of the hIP_3R-3 expressed in Sf9 cells is consistent with the recently reported hIP_3R-3 expressed in HEK GnTI(-) cells, and very similar to the structure of rat IP_3R-1 purified from native tissues[223,231,323].

Close inspection of the cryo-EM density revealed a strong non-protein density at the IP_3 binding site despite our initial intention to obtain the structure in a ligand-free conformation (**Figure 7-5A-B**). Among the chemicals we used during protein purification, EDTA seemed the most likely candidate since it fits reasonably well into the density (**Figure 7-5B**). We reasoned if the density is of EDTA, EDTA would bind to the IP_3R-3 and compete against IP_3 binding. To test this hypothesis, we purified the LBC of hIP_3R-3 (residues 4-602) and performed isothermal titration calorimetry (ITC) experiments to measure the

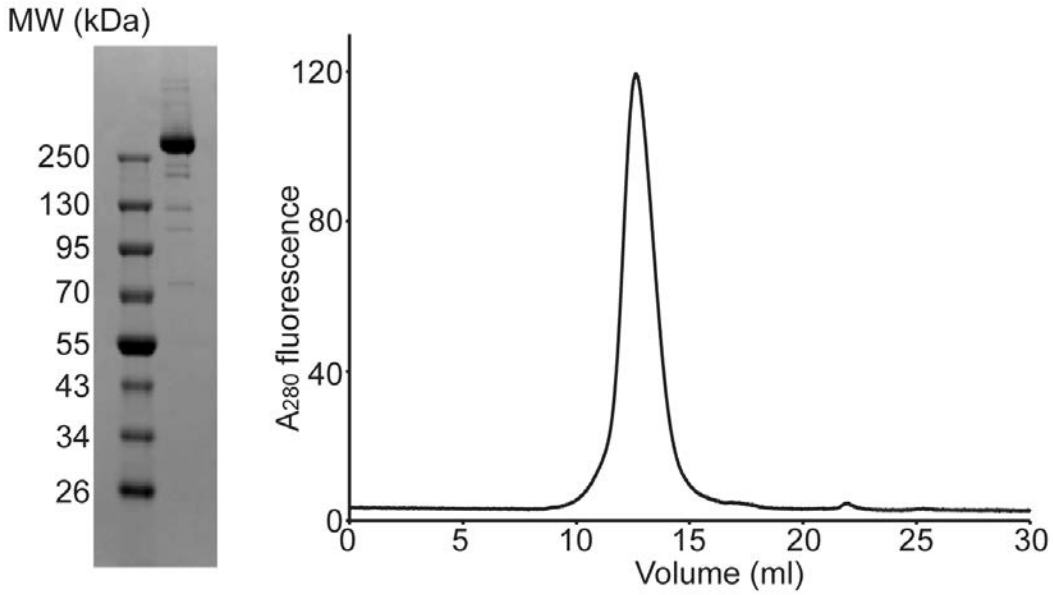

Figure 7-1. Purification of recombinant hIP$_3$R-3.
A. Purification of hIP$_3$R-3 proteins from insect cells using Strep-Tactin-XT Superflow resin followed by SEC. SDS-PAGE showing the final purified protein used in cryo-EM analysis. **B.** Size exclusion chromatogram of purified hIP$_3$R-3 proteins detected by intrinsic tryptophan fluorescence (280 nm excitation/330 nm emission).

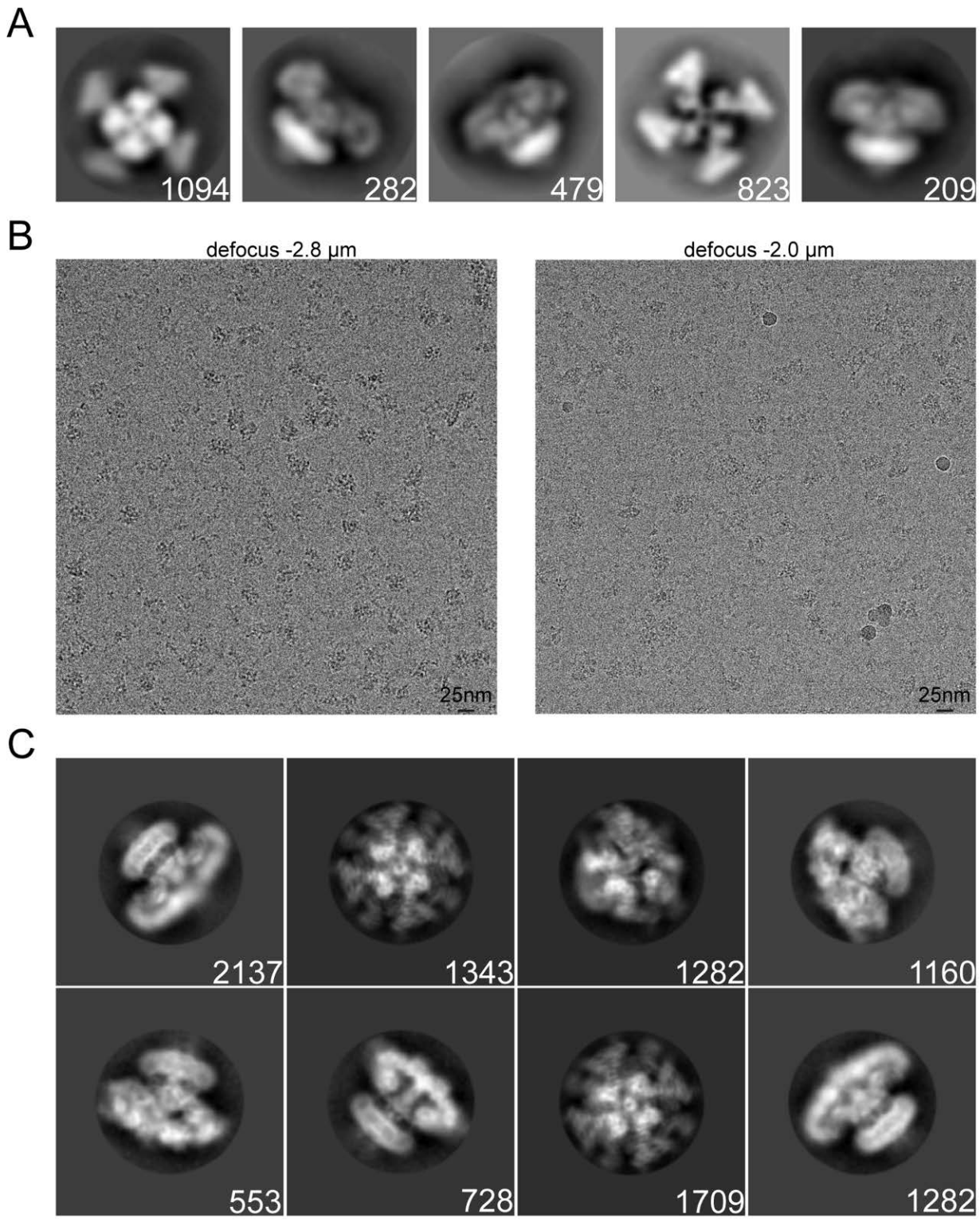

Figure 7-2. Raw data and 2D class averages for IP_3R-3.
A. Class averages from negative stain imaging of IP_3R-3 calculated in RELION. Number of particles in each class is indicated. **B.** Representative raw micrographs of the IP_3R-3 sample collected at 300kV on a Polara F30 microscope. **C.** Representative 2D class averages showing top, side, and orthogonal views of the IP_3R-3. Number of particles in each class is denoted in the bottom right corner.

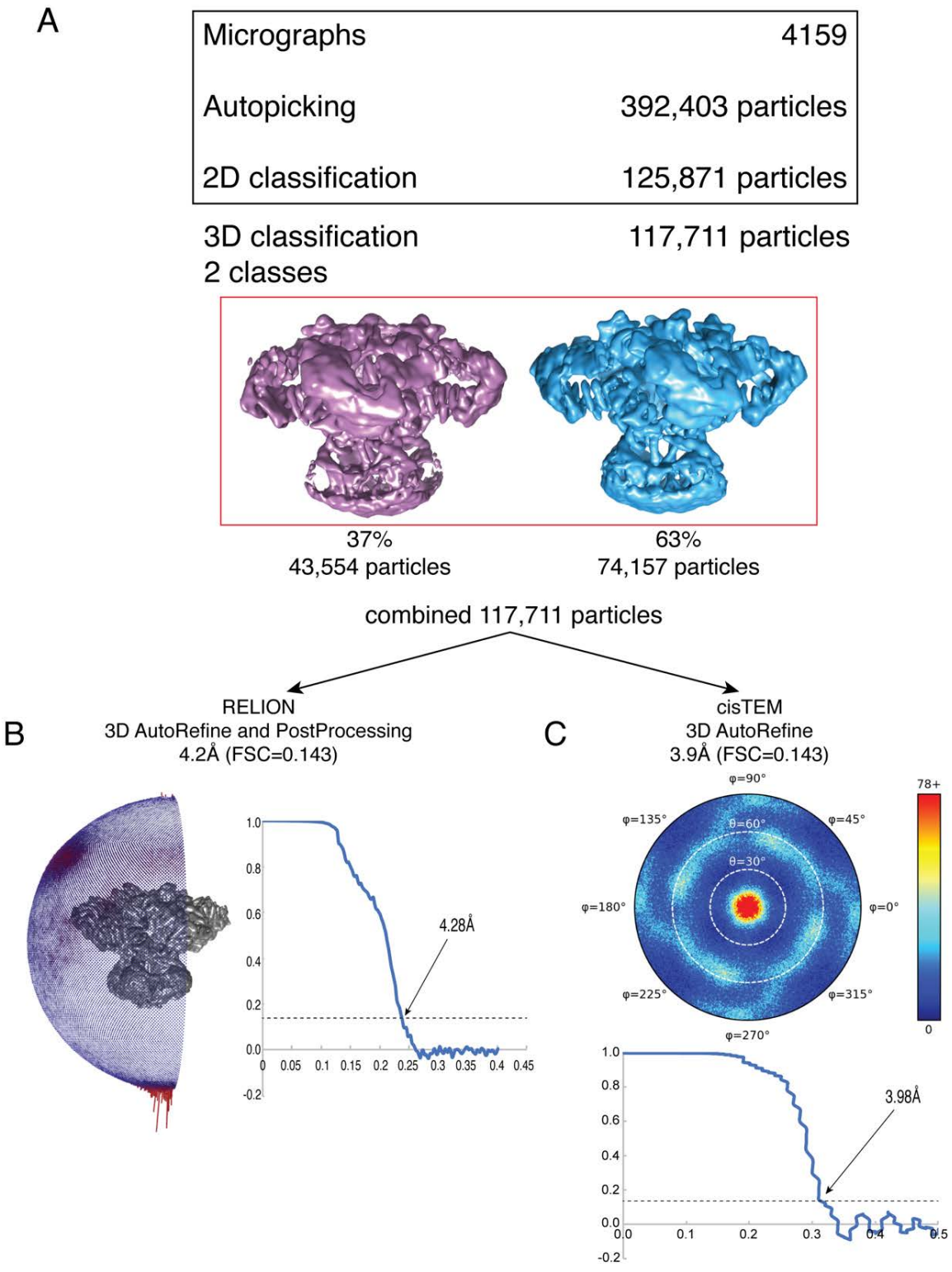

Figure 7-3. Flowchart of the image processing pipeline for RELION and cisTEM.
A. Flowchart showing the data collection, autopicking, 2D classification and sorting, and 3D classification statistics for the collected dataset. All of this image processing was done using RELION 2.1. **B.** Angular distribution (left) and FSC curve (right) for the final postprocessed map of IP_3R-3 bound to EDTA generated in RELION. **C.** Angular distribution (top) and FSC curve (bottom) for the final sharpened map for IP_3R-3 generated in cisTEM.

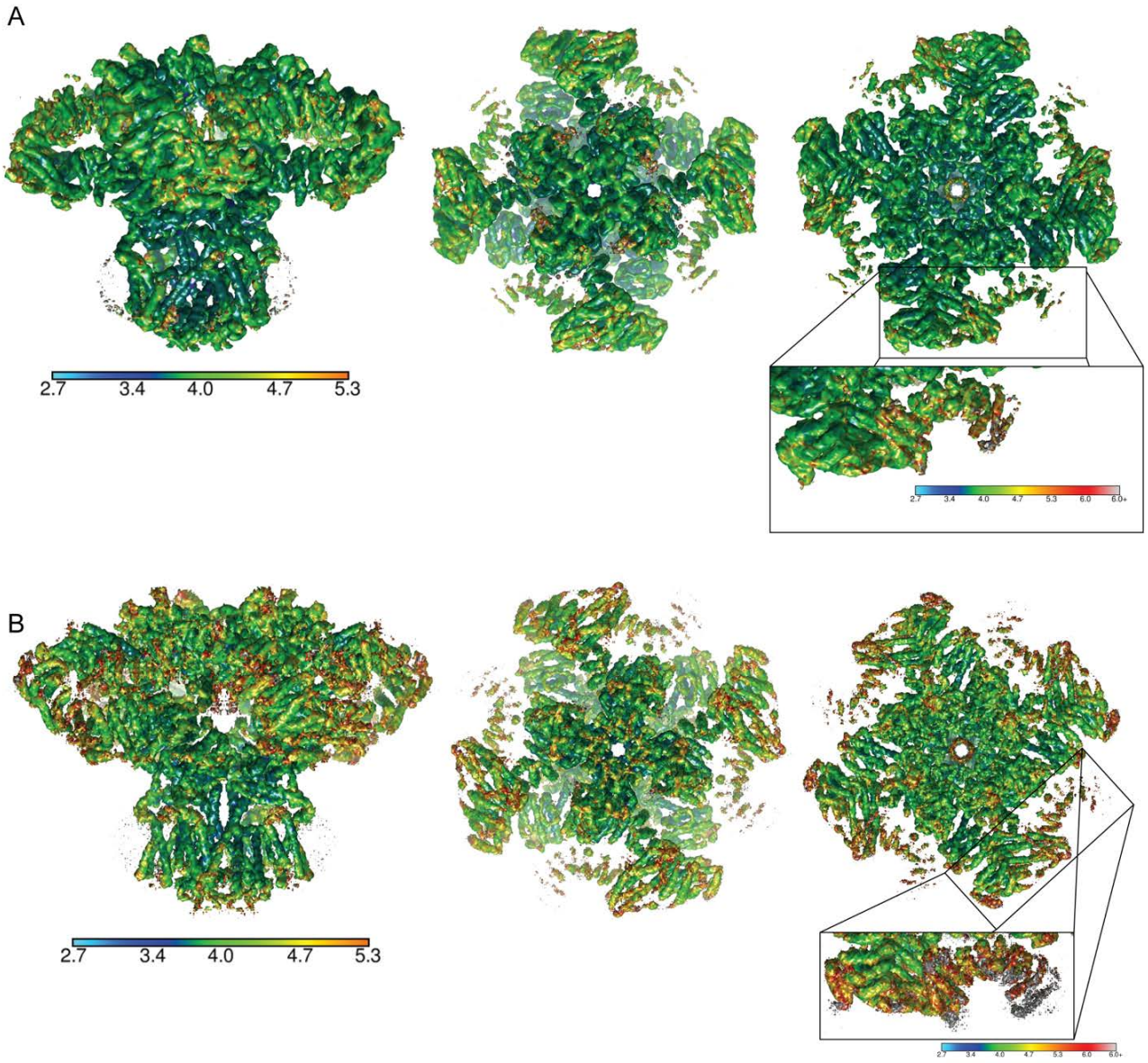

Figure 7-4. Local resolution of IP_3R-3 bound to EDTA.
A. Local resolution mapped onto final refined 3D reconstruction of IP_3R-3 generated in RELION. The average calculated resolution is 4.2Å and local resolution is mapped from 2.7Å – 6.0Å, cyan to red. The core of the protein and the TMD is the highest resolution part of the molecule, with most of the density falling in the 2.7-3.4Å range. **B.** Local resolution mapped onto the final refined structure determined using cisTEM. The average calculated resolution is 3.9Å. Again, the highest resolution parts of the molecule are around the core of the TMD and reach 2.7Å. Both local resolution heat maps were calculated using ResMap.

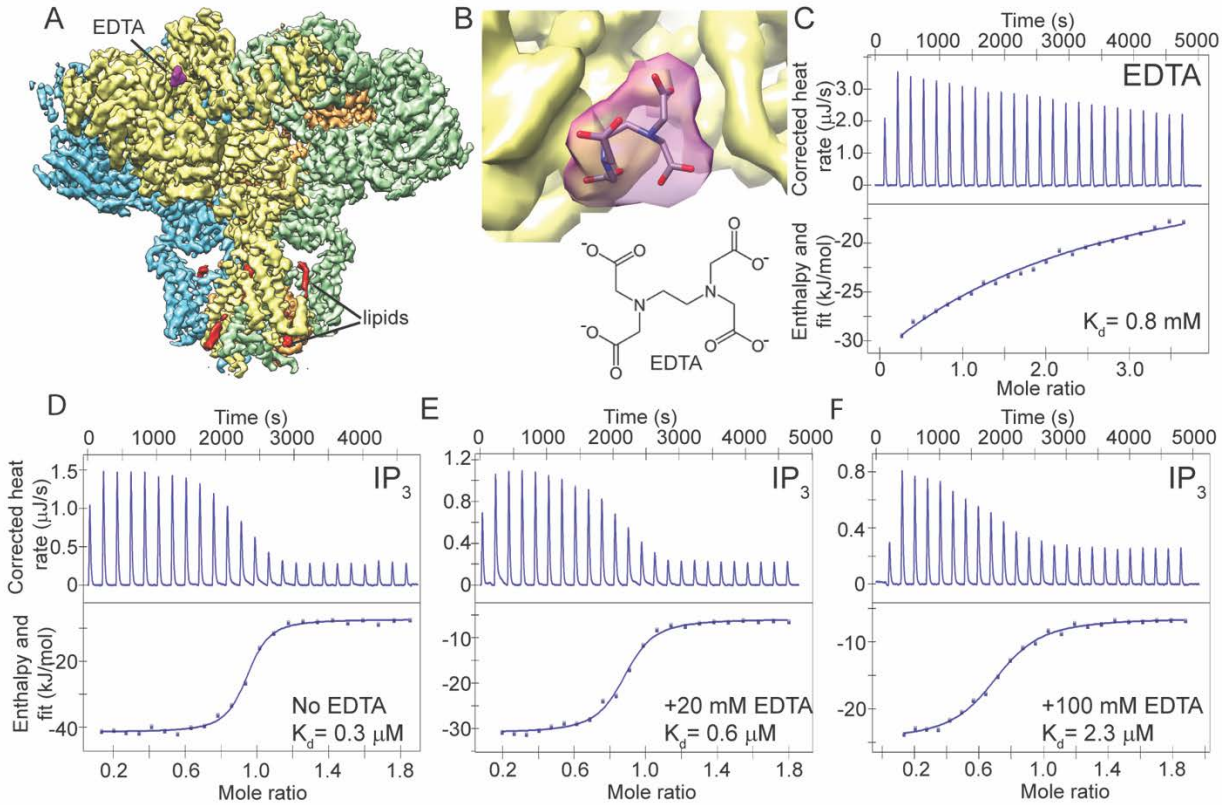

Figure 7-5. EDTA binds to h IP_3R-3 and competes against IP_3 binding.
A. Cryo-EM map of the hIP_3R-3 in EDTA-bound form. Each subunit is colored differently. Density for EDTA and lipids are shown in magenta and red, respectively. **B.** Close up view of EDTA binding site. Cryo-EM density for EDTA is countered at 4.5 σ level and shown transparent with the modeled EDTA molecule. Chemical structure of EDTA is shown below. **C.** Calorimetric titration of EDTA into hIP_3R-3 LBC (upper panel) and integrated heat as a function of the EDTA/protein molar ratio (lower panel). (D-F) Calorimetric titration of IP_3 into hIP_3R-3 LBC in the presence of 0 mM **(D)** 20 mM **(E)** and 100 mM **(F)** EDTA (upper panels) and integrated heat as a function of IP_3/protein ratio (lower panels). Calculated K_d values are shown for each panel.

thermodynamic properties of EDTA binding and its effect on IP_3 affinity. Our results indicate that EDTA binds to the hIP_3R-3 LBC with relatively low affinity (K_d= ~ 0.8 mM) (**Figure 7-5C**). To observe if EDTA would inhibit IP_3 binding, we performed ITC experiments using the isolated LBC dialyzed against buffers with different concentrations of EDTA (0-100 mM) (**Figure 7-5D-F**). The K_d for IP_3 binding to the hIP_3R-3 LBC was 307 nM in the absence of EDTA. This value is in agreement with previous studies performed using different methods (**Figure 7-5D**)[324,325]. Increasing EDTA concentrations in the sample buffer raised the K_d values for IP_3 gradually, reaching 2.7 μM in the presence of 100 mM EDTA (**Figure 7-5E-F** and **Figure 7-7**). Inhibition of IP_3Rs by metal chelators including BAPTA and EDTA was previously reported and shown to be result of direct binding to the LBC rather than metal chelating[326]. In the same study, BAPTA was shown to be more effective inhibitor than EDTA. In the line with this finding, we observed tighter binding of BAPTA (K_d=29 μM) to the LBC compared to the EDTA binding (**Figure 7-7**). We conclude that our structure may be in an EDTA-bound form, but increasing the threshold of map reveals the ligand in the IP_3 binding pocket may be larger than originally considered.

Structure of closed hIP_3R-3

Subunits that form the tetrameric ion channel can be divided into 3 regions; the large N-terminal cytoplasmic domain (CPD), the channel-forming TMD, and the C-terminal cytoplasmic domain (CTD) (**Figure 7-8**). CPD of each subunit resembles a tripod with a hinge-like central linker domain (CLD) (residues 790-1100 and 1587-1697) connected to 3 Armadillo solenoid domains (ARM1-3). The CLD is located at the outer perimeter of the tetrameric receptor. The N-terminal domain (ARM1) extends towards the central 4-fold symmetry axis and connects to 2 contiguous β-trefoil domains (β-TF1 and β-TF2), forming the IP_3 binding site. β-TF1 of one subunit interacts with the β-TF2 of the neighboring subunit forming a rim around the 4-fold symmetry axis. The second ARM domain (ARM2) bulges from the CLD oriented parallel to the membrane surface. It interacts with ARM1 of the neighboring subunit and forms the outer periphery of the receptor together with the CLD. The third ARM domain (ARM3) connects the cytoplasmic domains to a juxtamembrane domain (JD) positioned at the cytoplasmic face of the TMD. The JD is formed by assembly of two fragments separated by the TMD. A U-motif composed of a β-hairpin and a helix-turn-helix motif located at the C-terminal end of the ARM3 domain encapsulates a latch-like domain extending from the C-terminal end of the TMD. The JD is further stabilized by a H2C2 zinc finger domain formed by the residues Cys2538, Cys2541, His2558 and His2563.

Potential EDTA binding

If EDTA occupies the IP_3 binding site, between ARM1 and β-TF2, it is in close proximity to Arg503, Lys507, Arg510, Arg568 and Lys569, residues located in the ARM1 domain and involved in IP_3 binding. When the ARM1 domains of the EDTA-bound hIP_3R-3 and the IP_3-bound hIP_3R-3 LBC (PDB ID: 6DQN) are superimposed, EDTA overlays with the P1 group of IP_3 at the solvent exposed portion of the binding pocket. Unlike EDTA, P4 and P5 groups of IP_3 are positioned deeper at the binding pocket and form salt bridges with the basic residues located at both ARM1 and β-TF2 domains (**Figure 7-9A-B**). EDTA, on the other hand, only interacts with the residues in the ARM1 domain and does not form any close contact with residues in the β-TF2 domain, which moves towards the ARM1 domain upon IP_3 binding (**Figure 7-9A-B**). When compared to the apo-LBC (PDB ID:6DQJ), the LBC of the EDTA-bound hIP_3R-3 adopts a slightly more closed conformation (~1.5°) (**Figure 7-9C**). This slight movement does not seem to affect the overall arrangement of the CD of the IP_3R-3 as the whole CD can be superimposed with an rmsd value of 1.1Å over 1,728 aligned residues. However, an approximately 3° counter-clockwise rotation of the whole tetrameric CD relative to the TMD in the EDTA-bound hIP_3R-3 compared to the apo-hIP_3R-3 is observed when the TMDs of both structures are aligned (**Figure 7-9D**). Possible explanations for the structural differences are the effects of EDTA binding and differences in sample preparation. Whichever the case, the structural variation observed between different studies highlights the dynamic substructures in the intact receptor.

Transmembrane domain

The TMD has the overall architecture of voltage-gated ion channels with a central pore domain surrounded by voltage sensor like domains at the periphery. Unlike voltage-gated ion channels, we observe two additional helices (S1` and S1``) per subunit penetrating through the membrane from the

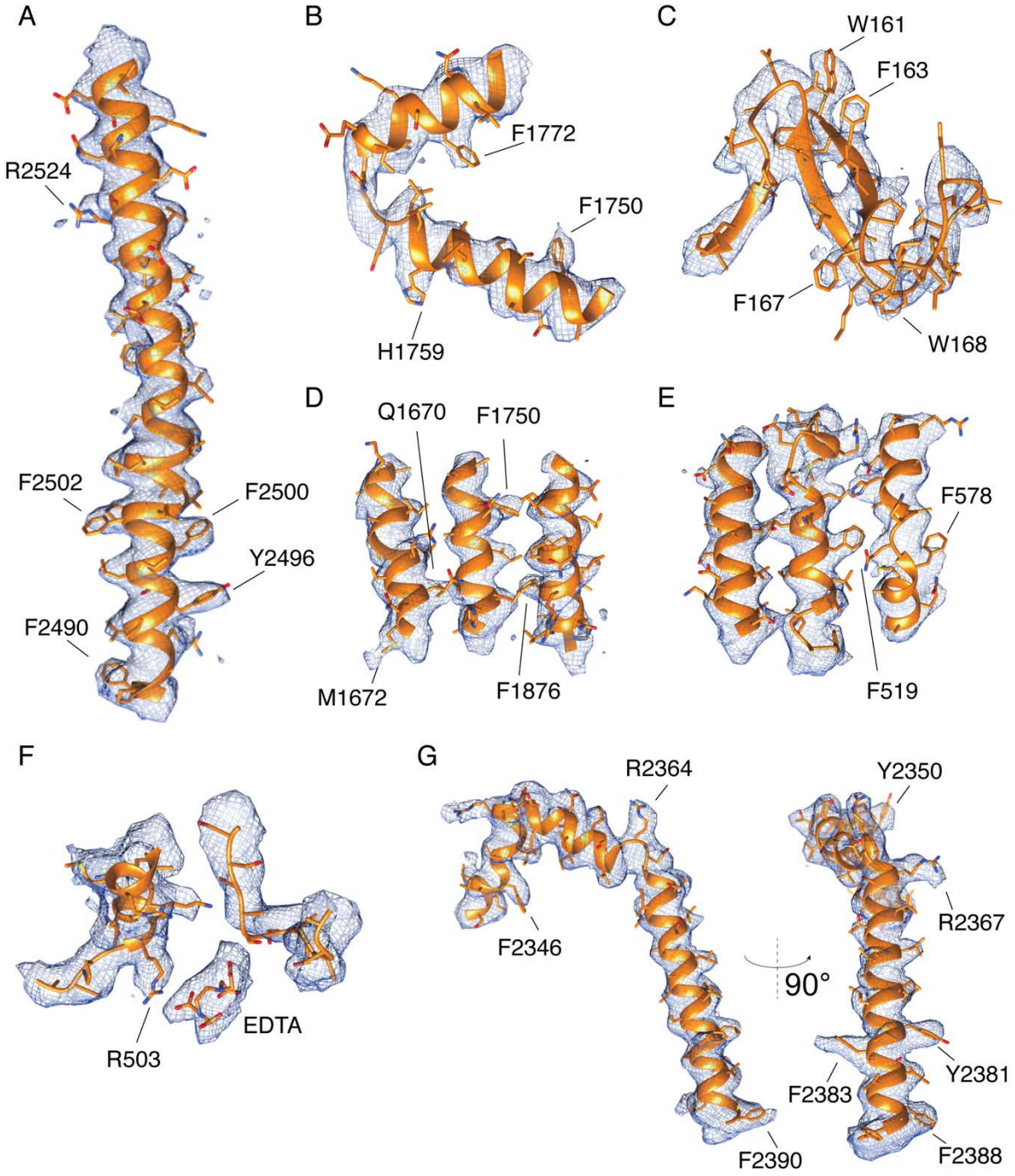

Figure 7-6. Local fit of IP_3R-3 atomic model into the electron density map.
A. Local fit of the S6 transmembrane helix. **B.** Local fit of helices in the ARM3 domain. **C.** Local fit of residues that form β-strands in the JD. **D.** Local fit of three adjacent helices in the central linker domain and ARM3. **E.** Local fit of three adjacent helices in the ARM1 domain. **F.** Local fit of EDTA, ARM1, and β-TF2 at the ligand binding site. **G.** Local fit of the peripheral S4, S4-5, and S5 helices in the TMD. Well-defined side chains that were used to guide building of the IP_3R-3 atomic model of are labeled in all panels.

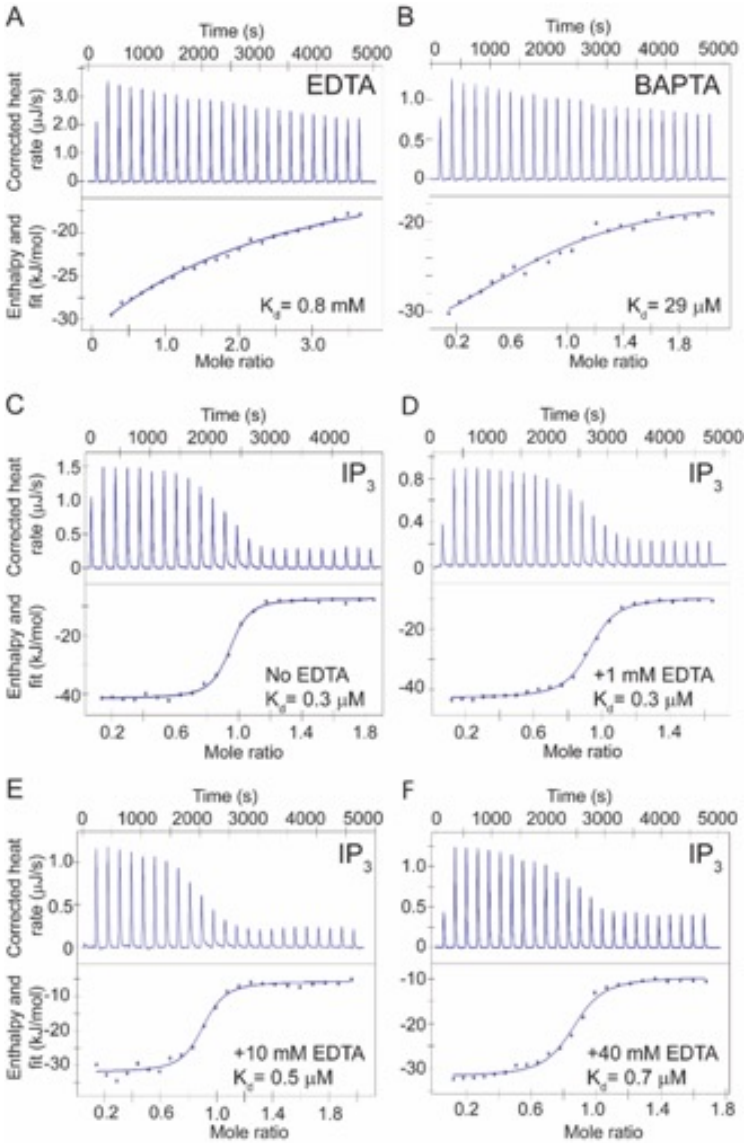

Figure 7-7. EDTA and BAPTA bind to the hIP$_3$R-3 LBC. Calorimetric titration of EDTA (A) and BAPTA (B) into hIP$_3$R-3 LBC (upper panel) and integrated heat as a function of the EDTA/protein molar ratio (lower panel). (C-F) Calorimetric titration of IP$_3$ into hIP$_3$R-3 LBC in the presence of 0 mM (C), 1 mM (D), 10 mM (E), and 40mM EDTA (upper panels) and integrated heat as a function of IP$_3$/protein ratio (lower panels). Calculated K_d values are shown for each panel.

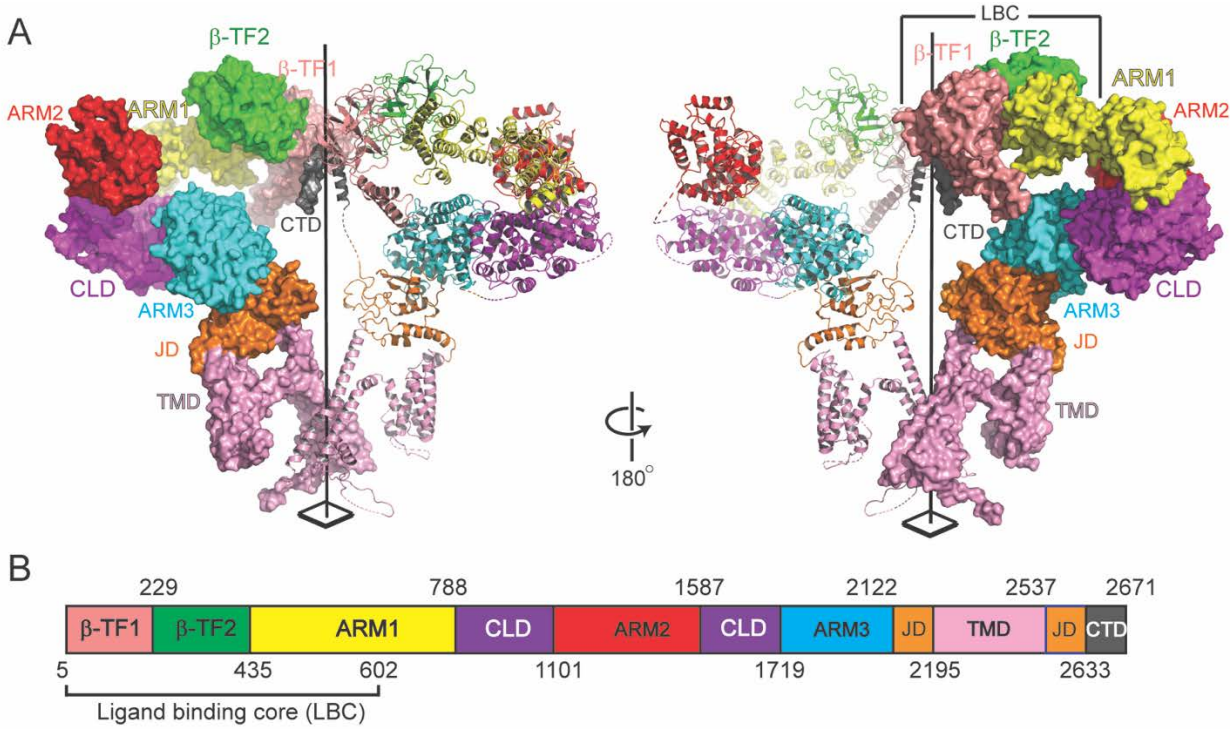

Figure 7-8. Domain architecture of human IP_3R-3. (A) Ribbon and surface representation of two subunits of the hIP_3R-3 colored by domains. Black rod indicates the four-fold symmetry axes. (B) Domain boundaries of hIP_3R-3 subunits. Domains are colored as in panel A.

luminal side (**Figure 7-10**). Density at the cytoplasmic sites of the helices is not well resolved. Therefore, it is not clear if these helices make a loop within the membrane or pass through completely. Based on the hydrophobicity plot and the number of the residues between the helices, these helices are likely to make complete pass with a short loop at the cytoplasmic side of the membrane. Similar densities were observed in recent cryo-EM studies of rat IP_3R-1 and hIP_3R-3s as well as rabbit RyR-1s[231,327]. Thus, these auxiliary TM helices seem to be a common feature of intracellular calcium release channels in general. Primary sequences of these two helices are the most diverse region within the TMD among 3 subtypes of IP_3Rs and could potentially be involved in subtype specific regulation and/or localization of the IP_3Rs.

Putative lipids at the TMD

Arrangement of non-protein EM densities that surround the TMD was different from other structures of IP_3R[223,231]. We found two strong, non-protein densities per subunit, which potentially derive from non-annular lipid molecules (**Figure 7-10**). Based on the density and the local chemical environment, we modeled a PE molecule into the density located in the cytoplasmic leaflet of the bilayer (**Figure 7-10A-B**). The density for one of the acyl chains was well defined and located in the vicinity of residues Tyr2322, Ile2349, Tyr2350 and Phe2356 of the S3, S4 and S4-5 helices. The second acyl chain is not in contact with any protein residues and highly flexible as its density is not well resolved. The polar head group of the PE is located at the cavity formed by the S3, S4 and S4-5 helices and the amine moiety of the PE forms a salt bridge with the side chain of Glu2353. The salt bridge is likely to be critical for the selectivity towards PE at this lipid binding site. There are also several positively charged residues in the vicinity of the phosphate group, but no salt bridge connection is observed. The second non-protein density is located at the interface of 3 subunits in the luminal leaflet of the bilayer (**Figure 7-10C-D**). The binding site is formed by S1 and S1` of one subunit together with the P helix and S6 helix of two neighboring subunits. This is potentially a lipid molecule; however, its identity cannot be determined with the current data. Of note, only the second density was present in the structure reported by another group highlighting that cryo-EM structures of the same membrane protein solved under different conditions reveal unique features of lipid-TMD interface[231].

Ion permeation pathway

The geometry of the ion permeation path of the channel formed was consistent with those of the known IP_3R architectures[223,231,323]. Specifically, from the cytoplasmic side, there is an upper vestibule, the narrowest constriction of the channel, and a lower vestibule followed by an architecture similar to the selectivity filter seen in potassium channels. In agreement with a closed channel conformation, the shortest pore diameter along the channel was 1.1Å where residue Phe2513 and Ile2522 are located (**Figure 7-11**). At the lower vestibule side of this constriction, there is a π-helix (residues 2501-2509) located at the middle of the S6 helix (**Figure 7-11**). Transition from π- to α-helix within this region is potentially coupled to gating as observed in TRPV6 channels where channel opening is accompanied by a local α-to-π-helical transition in S6[328]. The local resolution of the EM density surrounding the ion permeation pathway was 2.7-3.4Å (**Figure 7-6**), among the highest within our structure. Three strong spherical densities, that likely represent Na^+ ions, were found along the ion permeation pathway formed by S5, S6 helices and the P loop at the TMD. These densities were clearly visible in the density maps calculated using both RELION and cisTEM, but the signal was stronger in the maps calculated using RELION. We will refer to the locations occupied by the ions as sites 1-3. Spherical densities of the ion were identified above (site 1) and below (site 2) the narrowest constriction of the permeation path. Sites 2 is inside a lower vestibule formed between Asn2510 and Ile2505 along the S6 helix. Within this vestibule, four additional densities were found in a plane perpendicular to the ion permeation axis at the level of residue Ile2505. These densities are in close distance to the spherical density in site 2 (~6Å) and to the polar groups of the selectivity filter (~5Å), and thus we speculate that these are water molecules important for single file alignment of the ions permeating through the channel[329]. Site 3 was located at the bottom of the selectivity filter adjacent to residue Asp2478. We suggest that sites 1-3 are the locations where the permeating ions preferentially occupy in the closed state ion channel.

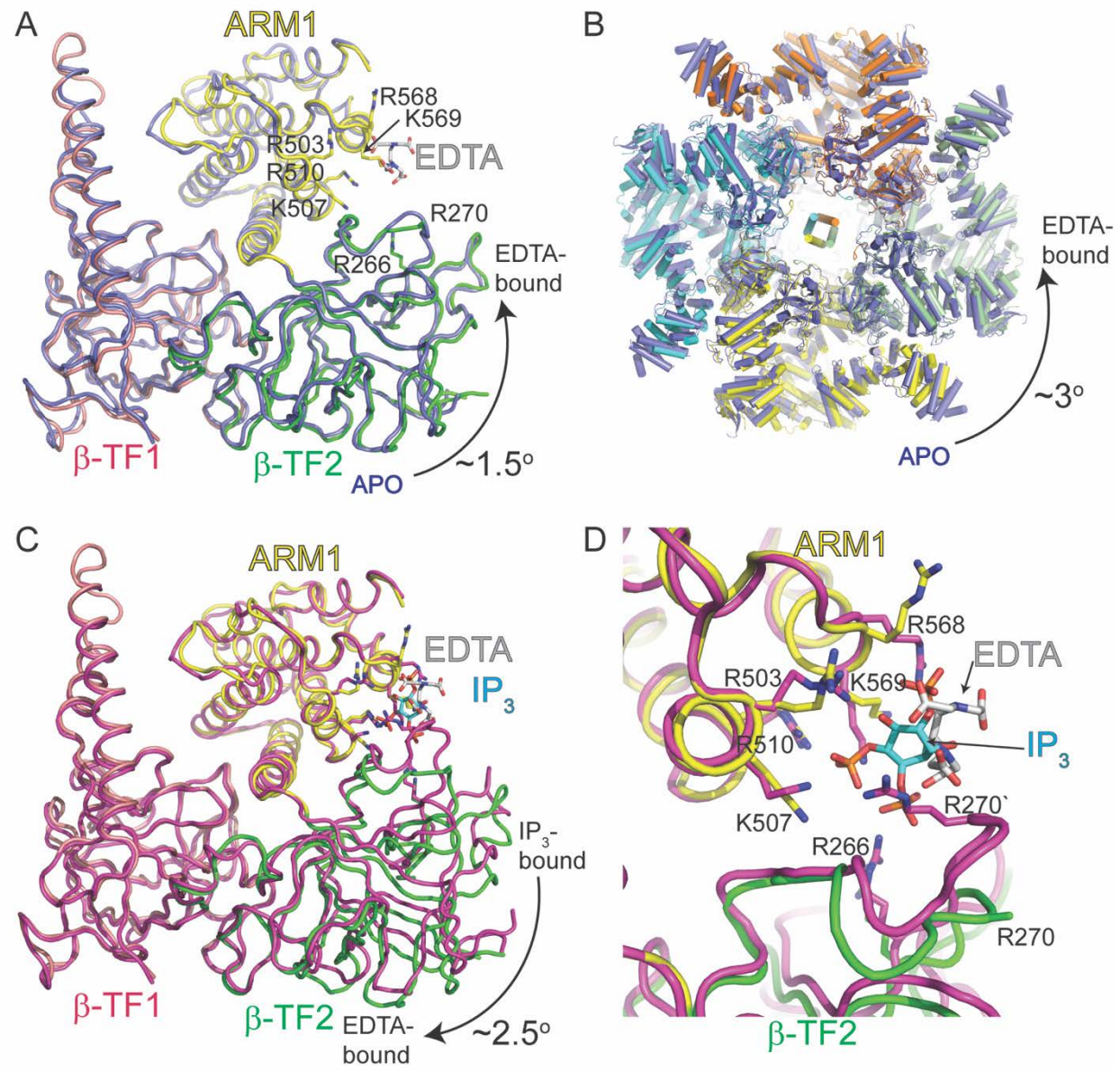

Figure 7-9. Structural comparison of EDTA-bound IP_3R-3 with apo and IP_3-bound hIP_3Rs. ARM1 domain of the EDTA-bound hIP_3R LBC are superposed onto ARM1 domains of IP_3-bound hIP_3R-3 (PDB ID: 6DQN, magenta) **(A)** and apo-hIP_3R-3 (PDB ID: 6DQJ, blue) **(B)**, and relative positioning of the β-TF1 and β-TF2 domains are compared. Domains of the EDTA-bound hIP_3R-3 is colored as in Fig. 7-8 **C.** Close-up view of the EDTA and IP_3 binding sites. Residues involved in ligand binding are shown as sticks. **D.** Comparison of the CDs of EDTA-bound and apo-hIP_3R-3 after superposing the TMDs.

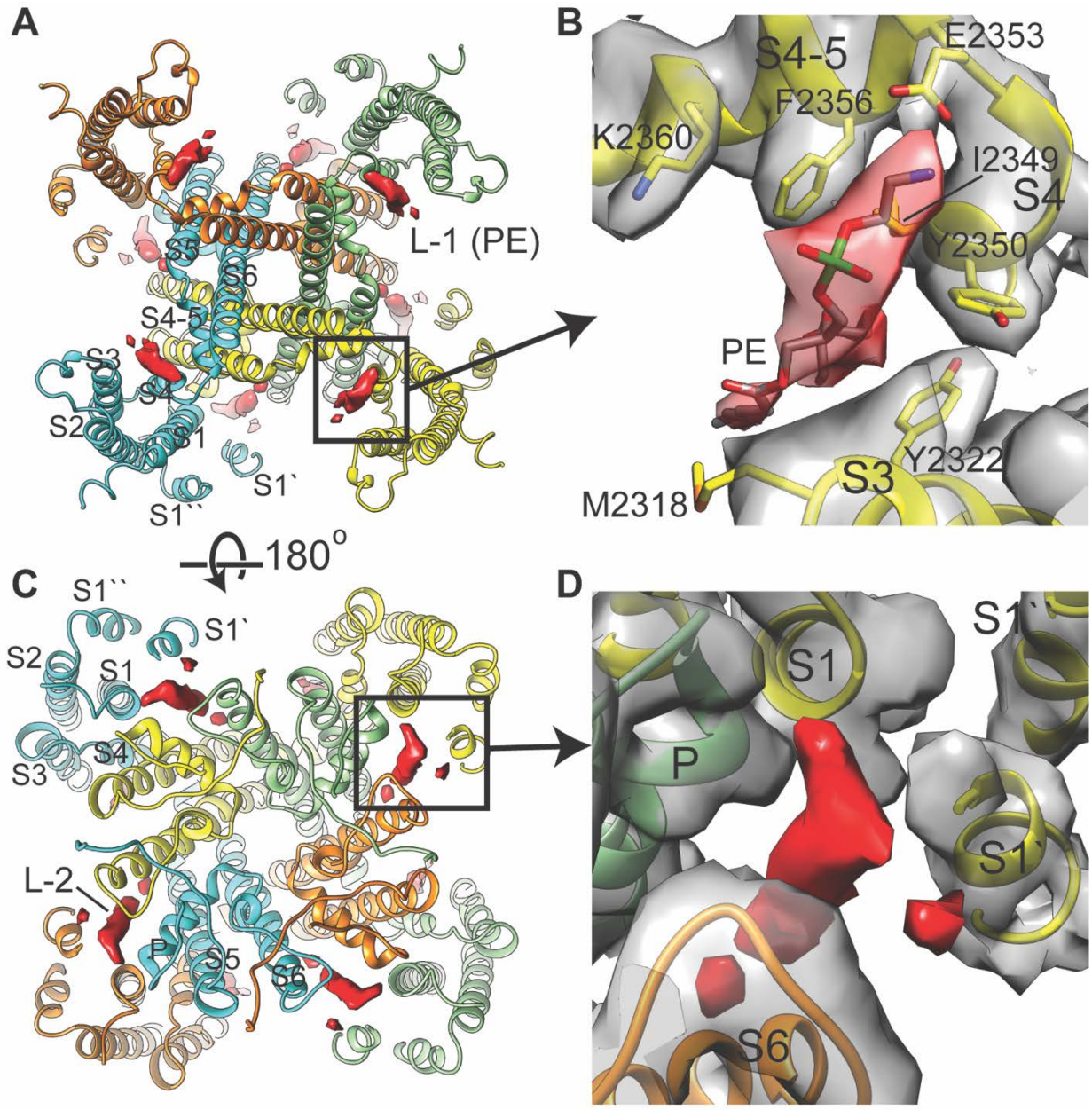

Figure 7-10. Structure of the TMD with the bound non-annular surface lipids.
Ribbon diagram of the hIP$_3$R-3 TMD viewed from the cytoplasm **(A)** and ER lumen **(C)** with non-protein cryo-EM density countered at 3 σ representing bound-lipid molecules. (B and D) The binding site for L-1 **(B)** and L-2 **(D)** viewed in the same orientation as in panels A and C, respectively. Cryo-EM density for the protein (grey) and the lipid (red) with the modeled PE molecule. Residues that are involved in L-1 binding are shown as sticks.

C-terminal cytoplasmic domain (CTD)

Unlike RyRs, the C-terminal ends of IP_3Rs extend through the central 4-fold axis and form a left-handed helical bundle at the core of the receptor[323]. In our structure, density for the CTD was less resolved compared to the rest of the receptor, but we were able to model a poly-alanine peptide that forms a left-handed coiled-coil domain (**Figure 7-12**). At the C-terminal side of these helices, there is additional density extending towards the β-TF2 domain of the adjacent subunit (**Figure 7-12**). Density for the residues that connect the coiled-coil domain to the JD and to the C-terminal interacting fragment were not visible indicating high flexibility of this region. A greater level of flexibility of the CTD was observed in the structures of hIP_3R-3 in apo, IP_3, and Ca^{2+}-bound conformations[231]. Therefore, it is unlikely that the conformational changes of the CTD can create enough tension to open the channel in IP_3R-3 as suggested for IP_3R-1[223,323]. We propose that the CTD is more important to maintain the overall tetrameric structure by compensating for the lack of additional domains present in ryanodine receptors.

Experimental Procedures

Human IP_3R-3 was purified from Sf9 cells in 0.005% LMNG and 0.005% GDN. Negative stain electron microscopy was performed to asses particle homogeneity. Particles were automatically picked using templates generated from 822 manually picked particles. 100 2D class averages were generated from 12,227 particles using 25 iterations of 2D classification and alignment in RELION. Cryo-EM grids were prepared as in *Materials and Methods* and **Table 2-2** and imaged on the Polara F30 in the Vanderbilt cryoEM Microscopy Facility using automation in SerialEM (see *Materials and Methods* and **Table 2-3***)*. Image processing in RELION 2.1 was carried out as described in *Materials and Methods* and **Table 2-4** with 2D class averages from 757 manually selected particles used as template. After multiple rounds of 2D classification to filter out good particles, a 3D classification into 2 classes with C4 symmetry was run with the EM density map of the IP_3R-1 (EMD-6369) scaled to match our pixel size and filtered to 60Å, as an initial model. Because both of these classes were similar in overall shape, all particles were subjected to 3D refinement, post-processing, and local resolution calculation in RELION 2.1 (**Figure 7-3**). Autorefinement was also conducted using cisTEM using the default settings with C4 symmetry. The map generated in RELION was filtered to 30Å and used as an initial model for this refinement. The final average resolution at the "gold-standard" 0.143 cutoff was 3.98Å. This map was then sharpened in cisTEM with a B-factor of -160 to facilitate model building. Half-maps were generated using the 3D-generate module in cisTEM and output to generate a map with local resolution parameters imposed in RELION. A heat map of local resolution was generated for both EM maps using ResMap.

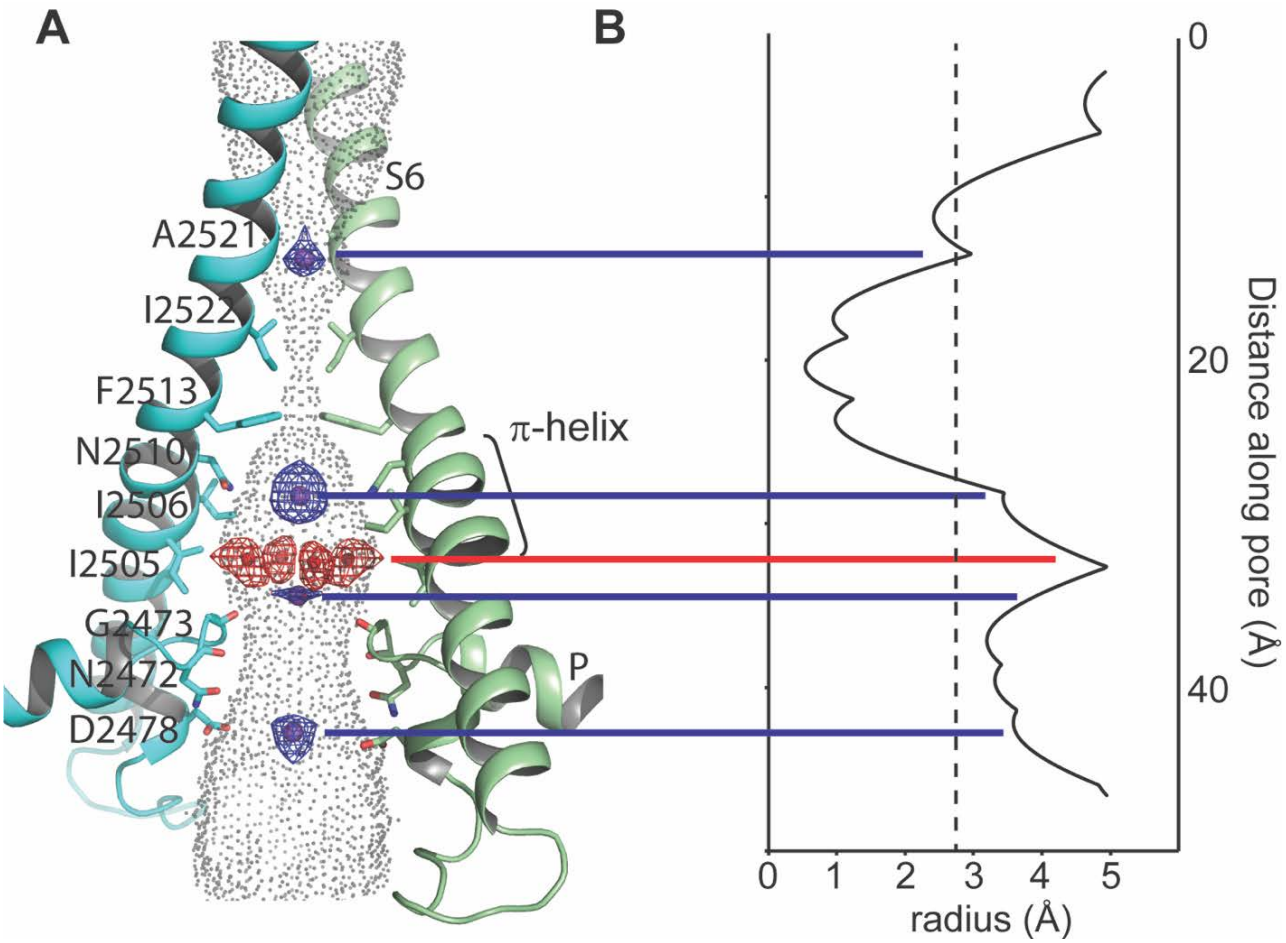

Figure 7-11. Ion permeation pathway with the cryo-EM density for putative sodium ions.
A. The pore profile generated by the HOLE program[330] are shown along with the S6 helix, P helix and P loop. Only two subunits are shown for clarity. Residues that line the ion permeation path are represented as sticks. The non-protein densities modeled as Na^+ (blue) and water (red) are countered at 3 σ and shown as mesh. B. A representation of pore radius along the permeation pathway. Positions of the ions and waters are indicated with lines. Dashed line indicates an approximate radius of a hydrated Na^+ ion[331].

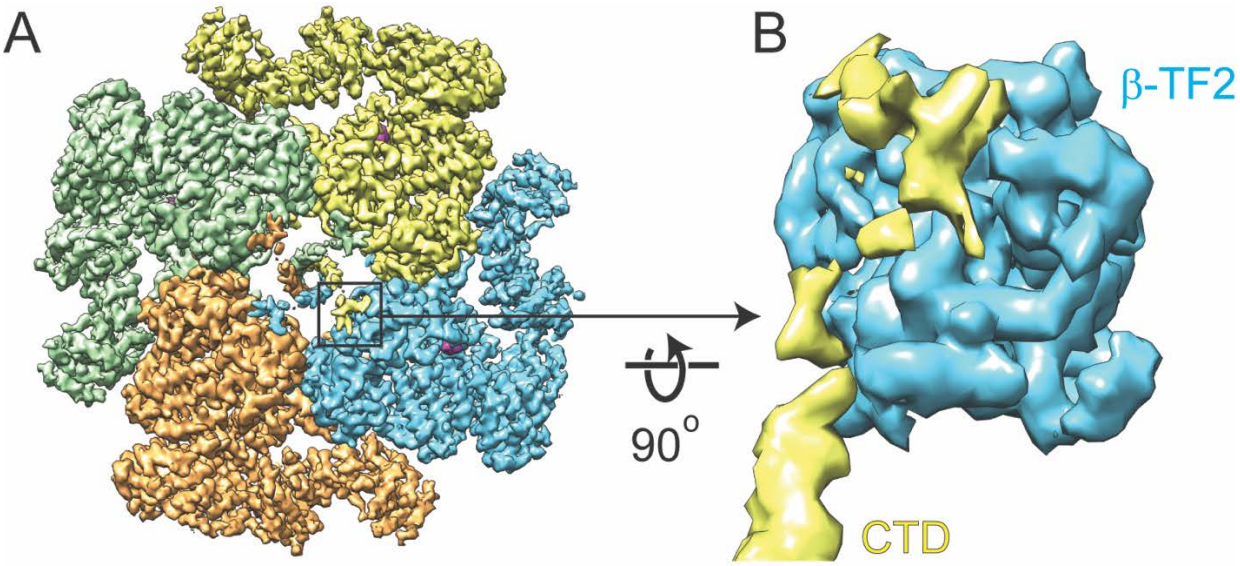

Figure 7-12. Coupling between the N- and C-terminal domains of hIP$_3$R-3.
A. Cryo-EM map of hIP$_3$R-3 viewed from cytoplasmic side. Density for each subunit is colored differently. **B.** Close-up view of the interaction site between the C-terminal end of one subunit with the β-TF2 domain of the neighboring subunit. Maps are countered at 2.9 σ.

Data collection and processing	
Microscope	FEI Polara TF30
Detector	Gatan K2 Summit
Nominal magnification	31,000 x
Voltage (kV)	300
Electron exposure ($e^-/Å^2$)	70
Defocus range (μm)	-1.4 to -3.5
Pixel size (Å)	1.247
Symmetry imposed	C4
Micrographs	4162
Initial particle images	125,871
Final particle images	117,711
Map resolution (Å)/FSC threshold	3.98/0.143
Map resolution range (Å)	2.7 - 8.0
Refinement	
resolution (Å)	4.0Å
B-factor used for map sharpening ($Å^2$)	-90
Model composition	
Non-hydrogen atoms	59,747
Protein residues	8,420
EDTA	4
PE	4
Zinc	4
Sodium	3
Water	4
Mean B factors ($Å^2$)	
Protein	139.8
EDTA	175.5
PE	154.3
Zinc	128.7
Sodium	75.6
Water	74.3
R.m.s. deviations	
Bond lengths (Å)	0.006
Bond angles (°)	0.924
Validation	
MolProbity score	1.75
Clashscore	4.13
Poor rotamers (%)	0.95
Ramachandran plot	
Favored (%)	90.0
Allowed (%)	9.9
Disallowed (%)	0.1

Table 7-1: Map and model statistic for hIP_3R-3.
Microscope and image processing information for the hIP_3R-3 bound to EDTA data collection and refinement statistics for the final model. All validation and statistics were calculated using MolProbity. RMSD, root mean squared deviation.

CHAPTER VIII: CONCLUSIONS AND FUTURE DIRECTIONS

AMPARs, auxiliary subunits and therapeutics

Movement in the AMPAR NTD has been shown to follow application of agonist. This has been observed in receptors purified from brain extract as well as recombinantly expressed proteins[19,86]. Some papers have reported that the NTDs do not separate and move toward the membrane. They postulate that this may be an artifact of negative stain, biochemical preparations, or is dampened by the presence of APs. Here we show that receptors that are reconstituted into lipids continue to show extreme flexibility when agonist is applied (**Figure 3-2**). This implies that this is not in fact a reconstitution artifact and likely represents a truly functional state of the receptor. CryoEM studies without negative stain present have also shown NTD rearrangement with agonist application in the past[18,19]. Using a controlled lipid environment, we also show that including brain lipids in the nanodiscs allows the receptors to enter a desensitized state more readily than embedding the receptor in POPC alone. By classifying the particles into three different conformations in negative stain EM, we were able to determine that there are a higher proportion of Type 3 receptors in the GluA2-brain lipid nanodisc sample when glutamate is applied. The proportion of this conformation is also slightly higher in the apo state. Since this class mostly disappears with application of the desensitization blocker CTZ, we postulate that this is representing a desensitized state of the receptor. A higher proportion of the receptors transitioning into this desensitized state in the presence of brain lipids may indicate that brain lipids lend unique functional flexibility to the AMPAR. This likely indicates that the stability of being reconstituted into a nanodisc and specific lipids in the polar brain extract allow the receptor to reach the largest range of conformations possible. Taking this preparation into cryo-EM to glean more information from high resolution data, we have found that while high-resolution raw data is obviously critical for successful reconstructions, high particle concentration and an abundance of particle views are also important. This will entail the use of techniques like GO coating to increase the number of particles in each micrograph[215] without having to concentrate our protein to a point of aggregation, as occurs often in our case with lipid nanodiscs. As we optimize the biochemical preparation of AMPAR reconstituted into nanodiscs, our GO grid preparation, and imaging conditions, we will continue to work toward a 3D reconstruction of the AMPAR in lipids.

Functionally, the AMPAR can be studied using a cell-based assay to screen for small molecule modulators that specifically affect AMPARs in complex with certain auxiliary subunits. A voltage sensing dye and intracellular calcium binding dye can be used in tandem to screen through HEK cells overexpressing the GluA2 subunit (RNA-edited or unedited) and an AP. The top hit from this screen was a PAM that was most potent on AMPAR-stg complexes. This finding in the cell-based assays was corroborated in fast ligand application outside-out patch recordings that indicated bath application of VU0627849 prevented the GluA2-stg complexes from maintaining a desensitized state. This was manifested by an observed increase in the steady-state current to nearly an activated level of current passage after 300 ms of glutamate application.

Future directions for the data presented in this thesis should combine both our high throughput screening results and preliminary structural work. Since the AMPAR has closed, open, and desensitized states, as well as existing in at least four different subconductance states that can be functionally identified in single-channel recordings, it follows that there must be considerable structural heterogeneity in the protein[332,333]. Heterogeneity has been identified in the highly mobile NTD dimers which can flex down to almost touch the membrane upon application of agonists with the receptor stabilized in both detergent and lipids. The LBDs also undergo large conformational rearrangements during channel activation, with the clamshell like D1 and D2 lobes closing around glutamate, and desensitization, with the D1 dimer interfaces rupturing to break their usual C2 symmetry and allow closure of the channel gate with glutamate still bound[12,19]. What has been less accessible for visualization until recently is the opening and closing of the AMPAR pore. Twomey et al. captured a mostly open state of the receptor in complex with stg, glutamate, and CTZ. This structure's gate is slightly small (~3Å) to allow passage of a fully hydrated sodium (2.9Å) and too small to accommodate a calcium (4.2Å) ion[331]. This may indicate that a receptor in detergent is not dynamic or stable enough to sample a fully open state. An additional advantage to reconstituting the AMPAR and other iGluRs into lipid nanodiscs would be the ability to study if there are any important protein-lipid interaction points in the TM region of the receptor. Are certain lipids that are enriched in neurons able to bind to the AMPAR and does this stabilize a more open state of the

receptor? Structural studies will certainly need to be coupled with functional analyses in the future to truly understand the complex gating mechanism of this receptor.

Another interesting avenue to explore will be to see if other AMPAR auxiliary subunits bind at a similar interface to the tetraspanins. The CNIH proteins contain two important binding surfaces that have been identified through mutational scanning, in the extracellular loop, exclusive to CNIH2 and CNIH3, and in the bottom half of the TM, in all four subunits[93]. It is intuitive to assume that these proteins form 3-helix bundles that slide into a binding site between the TM helices of the AMPAR like stg and GSG1L, but it is also possible that they bind in a more extended conformation since there is no structural information available for the individual proteins or any homologs. It seems as though CNIHs and TARPs are able to bind to GluA2 at the same time based off of the pharmacology of receptors that are expressed in the presence of both auxiliary subunits[334]. This begs the question; if they occupy overlapping binding sites or have exclusive binding interfaces? Extensive mutational analysis in Hawken et al, 2017 identified a surface on GluA2 that was integral for CNIH3 binding that coincides well with the binding surfaces seen in the cryoEM structures of AMPAR-tetraspanin complexes[335], but mutating these residues did not disrupt binding of stg to the same extent as CNIH3. This likely means the tetraspanins and CNIHs will have some overlap in their binding site, but different key stabilizing residues. It also follows that different auxiliary subunits should be able to displace one another. This could depend on the surrounding lipid environment, extracellular or intracellular conditions, particular conformations of the core tetramer, or any number of other variables. Again, nanodiscs and new small molecule modulators would allow us to control the lipid environment of the complex and potentially trap different states of the receptor. This would allow us to study whether inclusion of certain lipids or modulators increased the binding efficiency of CNIHs or other ASs to AMPARs.

In regards to our high throughput screening experiments, the most obvious question to ask is where does VU0627849 bind on the GluA2-stg complex? Leveraging the previously mentioned improvements in achievable resolution using cryoEM, it is now possible to visualize small molecules bound to proteins[180]. It is exciting to postulate that the binding site of VU0627849 is formed upon stg-binding to GluA2 and that the binding site is composed of residues from both proteins. This has not turned out to be the case in other pharmaceuticals. Stg could simply stabilize a conformation of the AMPAR that is more apt to bind VU0627849. Conversely, the binding site of LY3134081, a TARP γ-8 specific NAM, has been modeled and interrogated using point mutants to identify a pocket of the TARP that actually binds the compound without AMPAR subunits present[111]. Binding assays will need to be carried out for VU0627849 against stg alone to determine if this is also the case. The LY3134081 pocket is composed primarily of the extracellular extremes of TM3 and TM4, including Val-177 and Gly-210. When compared to the GluA2-stg structures, this is located near the binding interface with GluA2. VU0627849 is less bulky than LY3134081 and could fit into this pocket near the AMPAR-AS interface, but it could also act allosterically from a binding site further away from the interface. Determining if there are other binding pockets on ASs that allow for modulation of the AMPAR-AS complexes would open up drug targeting strategies even farther. Determining and verifying binding sites of VU0627849 and other AS-specific compounds will entail a combination of structural, biochemical, and biophysical techniques.

TRPC gating machinery

Using a combination of structural and functional techniques to interrogate the TRPC channel subfamily, we are able to postulate about the effect of their CPD on channel gating. Three different structures were recently published of TRPC3, including our reconstructions of the CPD and the full-length channel. As seen previously, cryoEM can be used to determine high-resolution structures of TRP channel family members. Bulky sidechains were visible in the CPDs of both our TRPC3 and TRPC6 structures so that *de novo* atomic models could be built and interpreted. This allowed us to map FSGS-causing mutations onto the TRPC6 structure and identify two hotspots on the protein that fall at the interface of the N- and C-terminal domains. Points of contact between the ARs and their loops with the HH and VH are surrounded by mutations that affect channel gating. A novel TRPC6 inhibitor that binds between the S3 and S4 of one subunit and the S5-S6 of the adjacent subunit was shown to inhibit three GOF mutations, P112Q, R895C, and E897K[129]. These mutations are all clustered at the interface of the AR1 and VH. While it was not reported whether this inhibitor was able to inhibit GOF mutations that fall elsewhere in the protein, if it was not, then it may indicate these individual mutational hotspots affect

gating through different allosteric pathways. The HHs' involvement in gating modulation was investigated through a combination of deletion and insertion mutations in the C-terminal loop. The length of the loop connecting the TRP helix and HH affects the level of channel conductance. These functional data, combined with the knowledge of different TRPC3 conformations that have been solved by cryoEM, insinuate that large rearrangements in the CPD could be snapshots of the channel's gating cycle. The flexing upwards of the HH and opening up of the ARDs to accommodate an unwinding of the domain swap at the center of the CPD could be linked to a transition between an open and close state of the receptor.

The information gleaned so far has introduced a variety of new questions that will need to be addressed in the future using more refined mutational analysis and biochemical/biophysical binding assays. The HHs can flex toward and away from the plane of the plasma membrane, which may predispose the CIRB binding site to either binding CaM or the IP_3R. Alternatively, Ca^{2+}/CaM binding may hinder the movement of the HH and explain CaM inhibition of multiple TRPC channels[137,141,298]. A structure of a TRPC channel and CaM or the IP_3R would give us more information into this modulation. The CIRB domain also sits close to the plasma membrane, raising the question of how the IP_3R is spatially accommodated. The relative orientation of the PM and ER needed to accommodate the binding of TRPC3/6 to IP_3Rs is indicated in cartoon form in **Figure 8-1**. The sequence conservation in the TRPC C-terminal helices is high, implying that the overall gating mechanism, if in fact tied to changing interactions of these helices with the ARs, may be conserved across the TRPC3/6/7. Additionally, the HH and VH are able to exist in a domain swapped and non-domain swapped conformation that implies a large opening of the ARs is available in the range of motion of the channel, as is observed in the Fan et. al. structure[121]. This expansion of the CPD would expose new binding surfaces and variable binding partners could push the channel toward a more open or closed state. Over 64 binding interactions have been identified for TRPC3 alone[163], implying that the CPD is likely a dynamic interaction site, that may be biased toward certain binding partners by being in a more open, non-domain swapped conformation or vice versa.

The potential of cryo-EM

Finally, we were able to reconstruct the IP_3R solubilized in LMNG and GDN detergent at an average resolution of 4.0Å using data collected on Vanderbilt's Polara F30 microscope equipped with a K2 Summit direct electron detector. In this structure, we were able to identify a small molecule in the IP_3 binding pocket acting, likely as an inhibitor since the receptor is clearly in a close state, as well as lipids and permeant ions in the TM region of the protein. We have hypothesized that the lipid present is PE because the negatively charged head group is bulky could coordinate the Glu-2353 sidechain. Since no lipids were added during purification, this lipid must be bound tightly to the protein and would have been extracted from the Sf9 cell membranes. PE has been shown to make up 38% of the lipids in Sf9 membranes and is, therefore, a very likely candidate[336,337]. We have also placed three sodium ions in the ion permeation pathway. This region of the protein was the highest resolution in local resolution calculations in ResMap[245] and many sidechains were visible because of the presence of multiple aromatic residues in this area. While ions should be placed cautiously when using C4 symmetry for alignment[174], we believe that because these densities are not noise because they remain strong at a threshold when noise outside the core protein density is no longer visible. Limited particle number did not allow for a high-resolution reconstruction using C1 symmetry, but aligning a larger data set with C1 symmetry or spiking in another type of ion, such as barium, to see if the density becomes stronger would be a good way to further confirm these ion assignments. In terms of future biological directions, the IP_3R has a variety of ligands and modulators including Ca^{2+}, ATP, IP_3, and more. The variety of conformations with different combinations and concentrations of these additives will be interesting and likely straightforward to study now that a purification, cryoEM data collection, and image processing pipeline has been established. Since purification schemes have been put forth for TRPC3 and IP_3R-3 that both rely on GDN for stabilization, it is not unreasonable to think that a complex of the two large membrane proteins could be formed and studied using cryo-EM. More broadly, the future developments and uses of cryoEM data, for

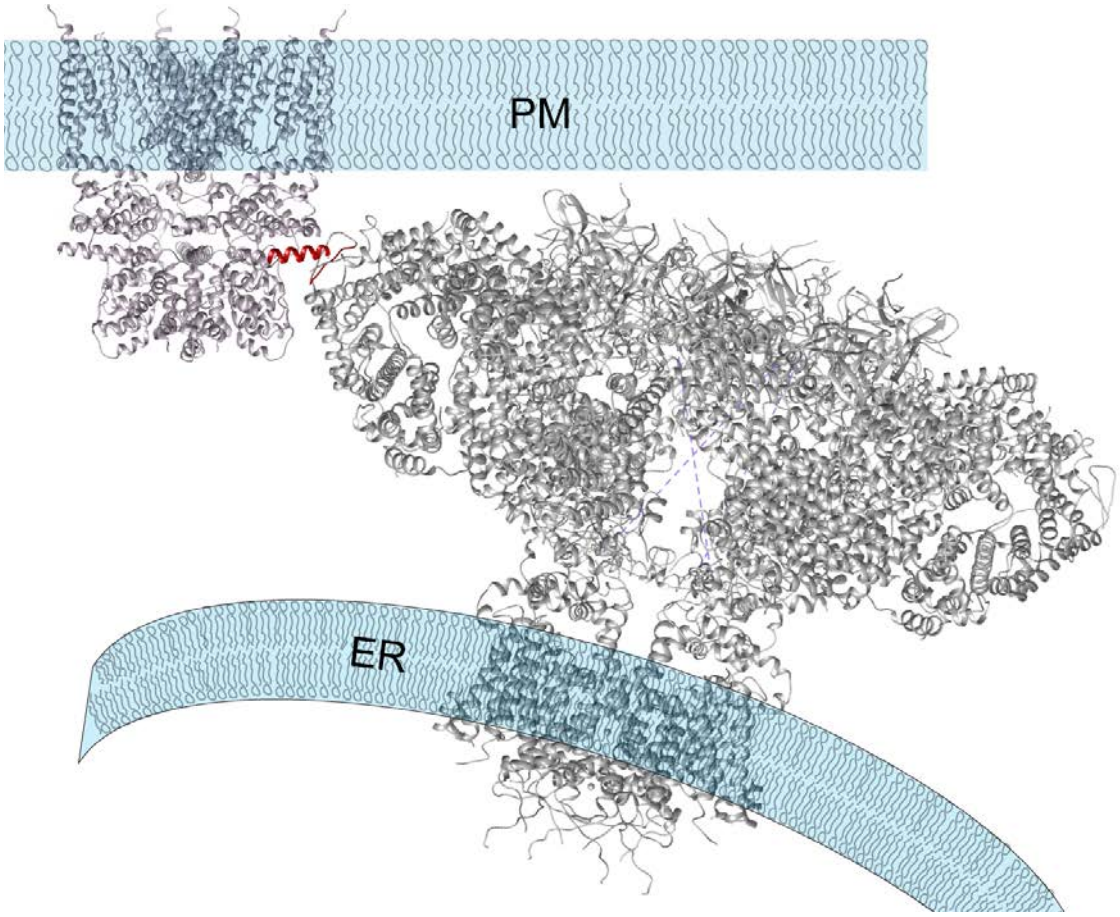

Figure 8-1. Cartoon representation of the interaction between IP_3R and TRPC3.
The sites of interaction for the two proteins have been highlighted in red. The IP_3R has a bulky cytoplasmic domain, but it's interaction interface with TRPC3 falls at the outside of the LBC and could easily wedge up next to the PM to contact the CIRB domain of TRPC3 as long as there was a certain amount of curvature in the ER membrane relative to the PM.

the moment, seem limitless. I will focus on two different EM techniques that I believe are interesting and touch on a just a few of many other future directions for single particle analysis (SPA) technique development.

Cryo-electron tomography (cryoET) is another imaging technique that is rapidly improving its potential resolution. CryoET began to be used in the late 1990's[338]. A sample is rotated by 1-2º at a time and a full "tilt series" from -70º to +70º is collected. This gives unique views of a single sample so that a 3D reconstruction can be calculated in reciprocal space, similar to single particle reconstruction, but with all of the views coming from a single specimen. This technique is often used on structures that are unique and do not occur in large numbers, like secretion system machinery. CryoET can be performed on thin samples of ~500 nm and resolve features up to a few nanometers in size. This allows small cells to be imaged so that complexes can be studied *in situ* with no purification necessary[339]. Secretion systems[340], flagella[341], and the nuclear pore complex[342–344] are some examples of complexes that are very large and not amenable to reconstitution *in vitro* that have been studied extensively using cryoET. Currently, the typical way to identify locations of specific proteins in a lower resolution cryoET structure is to generate KO cell lines and see which pieces of the complex are missing. This was used with great success to identify specific protein locations in the type IV pilus machinery[345]. Atomic resolution structures of individual components of large complexes such as the bacterial type IV pilus or the nuclear pore complex, can be rigid body fit into lower resolution structures of the entire complex solved by cryoET. This multi-disciplinary approach to studying large macromolecular complexes in their natural state is very promising as image collection and image processing pushes cryoET structures to even higher resolution. Being able to study complexes *in situ* also lends context to where these complexes are spatially inside the cell and a future direction for the field is to genetically encode electron dense tags so that individual proteins can be identified inside of a cell to perform visual proteomics. The use of phase plates has increased the signal in tomograms to allowed researchers to identify all 26S proteasomes present inside of an intact neuron[346]. Some hardware developments that are exciting in cryoET are the use of focused ion beam (FIB) milling and more advanced cryo-stages. FIB milling will allow researchers to ablate layers of cells or tissues that would normally be too thick for cryoET in a very controlled way[347]. This would allow all types of samples to be imaged and correlative light microscopy could be used to identify which plane of the cell would contain your item of interest[348]. More precise stages will allow samples to be rotated continuously while collecting images. This would allow more data to be collected faster. A large challenge will rest in how to best process this data in order to extract and align signals in the tomograms without distortion. The best application of cryoET will likely be to use it in combination with different structural techniques and light microscopy in order to combine high and low resolution structural information with dynamics that can be recorded in live cell light microscopy.

On the other end of the size spectrum, microcrystal electron diffraction (microED) is being used to determine structures of small proteins from microscopic 3D crystals. As mentioned in the introduction, analyzing 2D crystals of membrane proteins was able to determine structures to high-resolution using a TEM even before the advent of DEDs or improvements in image processing[7,187]. For microED, microscopic crystals are frozen on a grid and inserted into a TEM as with single particle samples, but MicroED is able to extract high resolution amplitude information from microscopic crystals because electrons interact with matter more strongly than X-rays and the de Broglie wavelength of electrons is shorter than X-rays using in crystallography. The signal amplitude is stronger from using the crystal's diffraction pattern and collecting images resolves the phase problem of crystallography. Images of the crystals can be resolved by focusing the electrons in the TEM, though integrating this information to determine phase is still being developed[349]. Low-resolution reconstructions of bovine liver catalase were generated in the 1970's[350], but the technique was improved greatly in 2013. Three microcrystals were imaged 90 times at 1º difference each time at a very low dose that recorded diffraction spots at 1.7Å resolution. These data were combined to reconstruct a 2.9Å structure of lysozyme[351]. A "continuous-rotation" rotation technique was then developed so that a single crystal can be used for data collection. This is similar to what is in the process of being developed for cryoET data collection. This continuous-rotation means that reciprocal space is sampled more, there is less dynamic scattering, which is when an electron diffracts multiple times inside the sample, and the crystal is moving in a similar way to traditional X-ray crystallography. This allows well-established X-ray crystallography data processing software can be used for map reconstructions[352]. While direct phasing techniques have been used so far

in microED, the ability for images to be collected directly would be an easy and accessible way to determine phasing information. This was the technique used in earlier 2D crystal work. How to determine accurate electron scattering factors will need to be improved before this type of phase information can be integrated with electron diffraction patterns. Recently, microED has been used to determine structures of small molecule crystals, indicating it could be an extremely fast way to determine structures of drugs or other substances[353]. CryoET is best applied when resolving structures of very large cellular machinery *in situ* and giving cellular context to these structures, but currently has a lower resolution limit than SPA and other structural techniques. On the other hand, microED is being developed to generate structures that are higher resolution than is easily achievable in SPA, but still necessitates the protein to form microcrystals. While microcrystals are usually more easily achievable than crystals suitable for crystallography, sample preparation will be a sizable hurdle to make this technique broadly applicable.

Briefly, SPA will likely be pushed forward by using different technical advancements in both sample preparation and data analysis. Fabs can be used as fiducial markers to allow for better alignment of small particles[354] or as a tool to alter preferred orientation in vitreous ice[355]. New equipment is being developed to improve cryoEM grid preparation. The Spotiton is one prototype and works by spraying nanoliter droplets of sample onto a self-wicking grid to form an ice layer of optimal thickness[217]. The sample is also sprayed onto the grid while it is the process of being plunged so that there is a less time for the protein to diffuse to the air-water interface before freezing. This is potentially a way to solve problems like proteins contacting the air-water interface and preferred orientation. Phase plates can also be used when imaging to increase contrast of small particles and allow improved image alignment[356]. On the processing side, improvements will need to be made in the rotational angle alignment for particles that are especially small[175]. Additionally, for heterogenous and flexible complexes there will likely be improvements in the classification steps of image processing software as multi-body refinement is improved. This allows different sections of the particles to be aligned separately as rigid bodies[357]. Machine learning algorithms that can either use unsupervised or supervised learning based on what is known about the particle previously can be utilized to pick particles from raw micrographs, like in the new crYOLO program[358], or classify in two or three dimensions. Some believe that all of these improvements could be best integrated into more people's science by centralizing the technology in large core facilities like x-ray crystallography[359]. This has begun with the funding and implementation of three national laboratories focused on increasing availability of the newest technology and training the next generation of EM specialists.

REFERENCES

1. Almén, M. S., Nordström, K. J. V., Fredriksson, R. & Schiöth, H. B. Mapping the human membrane proteome: A majority of the human membrane proteins can be classified according to function and evolutionary origin. *BMC Biol.* **7**, 50 (2009).
2. Arinaminpathy, Y., Khurana, E., Engelman, D. M. & Gerstein, M. B. Computational analysis of membrane proteins: the largest class of drug targets. *Drug Discov. Today* **14**, 1130–1135 (2009).
3. Terstappen, G. C. & Reggiani, A. In silico research in drug discovery. *Trends in Pharmacological Sciences* (2001). doi:10.1016/S0165-6147(00)01584-4
4. Rask-Andersen, M., Almén, M. S. & Schiöth, H. B. Trends in the exploitation of novel drug targets. *Nat. Rev. Drug Discov.* **10**, 579–590 (2011).
5. Eliezer, D., Kutluay, E., Bussell, R. & Browne, G. Conformational properties of α-synuclein in its free and lipid-associated states. *J. Mol. Biol.* **307**, 1061–1073 (2001).
6. Unwin, P. N. T. Three-dimensional model of purple membrane obtained by electron microscopy. *Nature* **269**, 118–122 (1977).
7. Gonen, T. *et al.* Lipid-protein interactions in double-layered two-dimensional AQP0 crystals. *Nature* (2005). doi:10.1038/nature04321
8. Pike, L. J., Han, X. & Gross, R. W. Epidermal growth factor receptors are localized to lipid rafts that contain a balance of inner and outer leaflet lipids: A shotgun lipidomics study. *J. Biol. Chem.* **280**, 26796–26804 (2005).
9. Bickel, P. E. *et al.* Flotillin and epidermal surface antigen define a new family of caveolae-associated integral membrane proteins. *J. Biol. Chem.* **272**, 13793–13802 (1997).
10. Kenworthy, A. K. *et al.* Dynamics of putative raft-associated proteins at the cell surface. *J. Cell Biol.* **165**, 735–746 (2004).
11. Milic, D. & Veprintsev, D. B. Large-scale production and protein engineering of G protein-coupled receptors for structural studies. *Frontiers in Pharmacology* (2015). doi:10.3389/fphar.2015.00066
12. Twomey, E. C., Yelshanskaya, M. V., Grassucci, R. A., Frank, J. & Sobolevsky, A. I. Structural Bases of Desensitization in AMPA Receptor-Auxiliary Subunit Complexes. *Neuron* **94**, 569–580.e5 (2017).
13. Twomey, E. C., Yelshanskaya, M. V., Vassilevski, A. A. & Sobolevsky, A. I. Mechanisms of Channel Block in Calcium-Permeable AMPA Receptors. *Neuron* **99**, 956–968.e4 (2018).
14. Chen, S. *et al.* Activation and Desensitization Mechanism of AMPA Receptor-TARP Complex by Cryo-EM. *Cell* (2017). doi:10.1016/j.cell.2017.07.045
15. Twomey, E. C., Yelshanskaya, M. V., Grassucci, R. A., Frank, J. & Sobolevsky, A. I. Elucidation of AMPA receptor-stargazin complexes by cryo-electron microscopy. *Science (80-.).* **353**, 83–86 (2016).
16. Twomey, E. C., Yelshanskaya, M. V., Grassucci, R. A., Frank, J. & Sobolevsky, A. I. Channel opening and gating mechanism in AMPA-subtype glutamate receptors. *Nature* **549**, 60–65 (2017).
17. Sobolevsky, A. I., Rosconi, M. P. & Gouaux, E. X-ray structure, symmetry and mechanism of an AMPA-subtype glutamate receptor. *Nature* **462**, 745–756 (2009).
18. Dürr, K. L. *et al.* Structure and dynamics of AMPA receptor GluA2 in resting, pre-open, and desensitized states. *Cell* **158**, 778–792 (2014).
19. Meyerson, J. R. *et al.* Structural mechanism of glutamate receptor activation and desensitization. *Nature* **514**, 328–334 (2014).
20. Schauder, D. M. *et al.* Glutamate receptor desensitization is mediated by changes in quaternary structure of the ligand binding domain. *Proc. Natl. Acad. Sci.* **110**, 5921–5926 (2013).
21. Yelshanskaya, M. V., Li, M. & Sobolevsky, A. I. Structure of an agonist-bound ionotropic glutamate receptor. *Science (80-.)*. (2014). doi:10.1126/science.1256508
22. Chen, L., Dürr, K. L. & Gouaux, E. X-ray structures of AMPA receptor-cone snail toxin complexes illuminate activation mechanism. *Science* **345**, 1021–1026 (2014).
23. Landau, E. M. & Rosenbusch, J. P. Lipidic cubic phases: A novel concept for the crystallization of membrane proteins. *Proc. Natl. Acad. Sci.* **93**, 14532–14535 (1996).
24. Suzuki, H. *et al.* Crystal structure of a claudin provides insight into the architecture of tight

junctions. *Science (80-.).* **344**, 304–307 (2014).
25. Nimigean, C. M. A radioactive uptake assay to measure ion transport across ion channel–containing liposomes. *Nat. Protoc.* (2006). doi:10.1038/nprot.2006.166
26. Tribet, C., Audebert, R. & Popot, J.-L. Amphipols: Polymers that keep membrane proteins soluble in aqueous solutions. *Proc. Natl. Acad. Sci.* (1996). doi:10.1073/pnas.93.26.15047
27. Popot, J.-L. *et al.* Amphipols From A to Z*. *Annu. Rev. Biophys.* **40**, 379–408 (2011).
28. Denisov, I. G., Grinkova, Y. V., Lazarides, A. A. & Sligar, S. G. Directed Self-Assembly of Monodisperse Phospholipid Bilayer Nanodiscs with Controlled Size. *J. Am. Chem. Soc.* **126**, 3477–3487 (2004).
29. Ritchie, T. K. *et al. Chapter 11 Reconstitution of Membrane Proteins in Phospholipid Bilayer Nanodiscs*. *Methods in Enzymology* **464**, (Elsevier Masson SAS, 2009).
30. Denisov, I. G. & Sligar, S. G. Nanodiscs for structural and functional studies of membrane proteins. *Nat. Struct. Mol. Biol.* **23**, 481–486 (2016).
31. Frauenfeld, J. *et al.* Cryo-EM structure of the ribosome-SecYE complex in the membrane environment. *Nat. Struct. Mol. Biol.* **18**, 614–621 (2011).
32. Cvetkov, T. L., Huynh, K. W., Cohen, M. R. & Moiseenkova-Bell, V. Y. Molecular architecture and subunit organization of TRPA1 ion channel revealed by electron microscopy. *J. Biol. Chem.* **286**, 38168–38176 (2011).
33. Frey, L., Lakomek, N. A., Riek, R. & Bibow, S. Micelles, Bicelles, and Nanodiscs: Comparing the Impact of Membrane Mimetics on Membrane Protein Backbone Dynamics. *Angew. Chemie - Int. Ed.* **56**, 380–383 (2017).
34. Saotome, K., Duong-Ly, K. C. & Howard, K. P. Influenza A M2 protein conformation depends on choice of model membrane. *Biopolymers* **104**, 405–411 (2015).
35. Ivanova, P. T. *et al.* Lipid Composition of the Viral Envelope of Three Strains of Influenza Virus - Not All Viruses Are Created Equal. *ACS Infect. Dis.* (2016). doi:10.1021/acsinfecdis.5b00040
36. Zhang, M., Huang, R., Im, S. C., Waskell, L. & Ramamoorthy, A. Effects of membrane mimetics on cytochrome P450-cytochrome b5 interactions characterized by NMR spectroscopy. *J. Biol. Chem.* **290**, 12705–12718 (2015).
37. Liu, K. C., Hughes, J. M. X., Hay, S. & Scrutton, N. S. Liver microsomal lipid enhances the activity and redox coupling of colocalized cytochrome P450 reductase-cytochrome P450 3A4 in nanodiscs. *FEBS J.* (2017). doi:10.1111/febs.14129
38. Liao, M., Cao, E., Julius, D. & Cheng, Y. Structure of the TRPV1 ion channel determined by electron cryo-microscopy. *Nature* **504**, 107–112 (2013).
39. Gao, Y., Cao, E., Julius, D. & Cheng, Y. TRPV1 structures in nanodiscs reveal mechanisms of ligand and lipid action. *Nature* **534**, 347–351 (2016).
40. Willegems, K. & Efremov, R. G. Influence of Lipid Mimetics on Gating of Ryanodine Receptor. *Structure* **26**, 1303–1313.e4 (2018).
41. Mathews, D. C., Henter, I. D. & Zarate, C. A. Targeting the Glutamatergic System to Treat Major Depressive Disorder. *Drugs* **72**, 1313–1333 (2012).
42. Alt, A., Nisenbaum, E. S., Bleakman, D. & Witkin, J. M. A role for AMPA receptors in mood disorders. *Biochemical Pharmacology* (2006). doi:10.1016/j.bcp.2005.12.022
43. Cirrito, J. R. *et al.* Synaptic activity regulates interstitial fluid amyloid-β levels in vivo. *Neuron* (2005). doi:10.1016/j.neuron.2005.10.028
44. Hsieh, H. *et al.* AMPAR Removal Underlies Aβ-Induced Synaptic Depression and Dendritic Spine Loss. *Neuron* (2006). doi:10.1016/j.neuron.2006.10.035
45. Hashimoto, K. Emerging role of glutamate in the pathophysiology of major depressive disorder. *Brain Research Reviews* (2009). doi:10.1016/j.brainresrev.2009.05.005
46. Hashimoto, K., Sawa, A. & Iyo, M. Increased Levels of Glutamate in Brains from Patients with Mood Disorders. *Biol. Psychiatry* (2007). doi:10.1016/j.biopsych.2007.03.017
47. O 'neill, M. J. & Witkin, J. M. AMPA Receptor Potentiators: Application for Depression and Parkinson's Disease. *Curr. Drug Targets* (2007). doi:10.2174/138945007780618517
48. Beneyto, M. & Meador-Woodruff, J. H. Lamina-specific abnormalities of AMPA receptor trafficking and signaling molecule transcripts in the prefrontal cortex in schizophrenia. *Synapse* (2006). doi:10.1002/syn.20329

49. Nelson, E. C. *et al.* Evidence of CNIH3 involvement in opioid dependence. *Mol. Psychiatry* **21**, 608–614 (2016).
50. Niciu, M. J., Kelmendi, B. & Sanacora, G. Overview of glutamatergic neurotransmission in the nervous system. *Pharmacology Biochemistry and Behavior* (2012). doi:10.1016/j.pbb.2011.08.008
51. Traynelis, S. F. *et al.* Glutamate Receptor Ion Channels: Structure, Regulation, and Function. *Pharmacol. Rev.* (2010). doi:10.1124/pr.109.002451
52. Shepherd, J. D. & Huganir, R. L. The Cell Biology of Synaptic Plasticity: AMPA Receptor Trafficking. *Annu. Rev. Cell Dev. Biol.* (2007). doi:10.1146/annurev.cellbio.23.090506.123516
53. Huganir, R. L. & Nicoll, R. A. AMPARs and synaptic plasticity: The last 25 years. *Neuron* (2013). doi:10.1016/j.neuron.2013.10.025
54. Martin, S. J., Grimwood, P. D. & Morris, R. G. M. Synaptic Plasticity and Memory: An Evaluation of the Hypothesis. *Annu. Rev. Neurosci.* (2000). doi:10.1146/annurev.neuro.23.1.649
55. Zamanillo, D. *et al.* Importance of AMPA receptors for hippocampal synaptic plasticity but not for spatial learning. *Science (80-.).* (1999). doi:10.1126/science.284.5421.1805
56. Sanderson, D. J. *et al.* Spatial working memory deficits in GluA1 AMPA receptor subunit knockout mice reflect impaired short-term habituation: Evidence for Wagner's dual-process memory model. *Neuropsychologia* (2010). doi:10.1016/j.neuropsychologia.2010.03.018
57. Meng, Y., Zhang, Y. & Jia, Z. Synaptic transmission and plasticity in the absence of AMPA glutamate receptor GluR2 and GluR3. *Neuron* (2003). doi:10.1016/S0896-6273(03)00368-4
58. Jia, Z. *et al.* Enhanced LTP in mice deficient in the AMPA receptor GluR2. *Neuron* (1996). doi:10.1016/S0896-6273(00)80225-1
59. Gerlai, R., Henderson, J. T., Roder, J. C. & Jia, Z. Multiple behavioral anomalies in GluR2 mutant mice exhibiting enhanced LTP. *Behav. Brain Res.* (1998). doi:10.1016/S0166-4328(98)00002-3
60. Bettler, B. *et al.* Cloning of a novel glutamate receptor subunit, GluR5: Expression in the nervous system during development. *Neuron* (1990). doi:10.1016/0896-6273(90)90213-Y
61. Moriyoshi, K. *et al.* Molecular cloning and characterization of the rat NMDA receptor. *Nature* (1991). doi:10.1038/354031a0
62. Wenthold, R., Petralia, R., Blahos J, I. & Niedzielski, A. Evidence for multiple AMPA receptor complexes in hippocampal CA1/CA2 neurons. *J. Neurosci.* (1996). doi:10.1523/JNEUROSCI.16-06-01982.1996
63. Sommer, B. *et al.* Flip and flop: A cell-specific functional switch in glutamate-operated channels of the CNS. *Science (80-.).* (1990). doi:10.1126/science.1699275
64. Rueter, S. M., Burns, C. M., Coode, S. A., Mookherjee, P. & Emesont, R. B. Glutamate receptor RNA editing in vitro by enzymatic conversion of adenosine to inosine. *Science (80-.).* (1995). doi:10.1126/science.7878468
65. Sommer, B., Köhler, M., Sprengel, R. & Seeburg, P. H. RNA editing in brain controls a determinant of ion flow in glutamate-gated channels. *Cell* **67**, 11–19 (1991).
66. Roche, K. W., O'Brien, R. J., Mammen, A. L., Bernhardt, J. & Huganir, R. L. Characterization of multiple phosphorylation sites on the AMPA receptor GluR1 subunit. *Neuron* (1996). doi:10.1016/S0896-6273(00)80144-0
67. Tomita, S. *et al.* Functional studies and distribution define a family of transmembrane AMPA receptor regulatory proteins. *J. Cell Biol.* **161**, 805–816 (2003).
68. Shanks, N. F. *et al.* Differences in AMPA and Kainate Receptor Interactomes Facilitate Identification of AMPA Receptor Auxiliary Subunit GSG1L. *Cell Rep.* **1**, 590–598 (2012).
69. Kato, A. S., Siuda, E. R., Nisenbaum, E. S. & Bredt, D. S. AMPA Receptor Subunit-Specific Regulation by a Distinct Family of Type II TARPs. *Neuron* **59**, 986–996 (2008).
70. Chen, L. *et al.* Stargazin regulates synaptic targeting of AMPA receptors by two distinct mechanisms. *Nature* (2000). doi:10.1038/35050030
71. Von Engelhardt, J. *et al.* CKAMP44: A brain-specific protein attenuating short-term synaptic plasticity in the dentate gyrus. *Science (80-.).* (2010). doi:10.1126/science.1184178
72. Kalashnikova, E. *et al.* SynDIG1: An Activity-Regulated, AMPA- Receptor-Interacting Transmembrane Protein that Regulates Excitatory Synapse Development. *Neuron* (2010).

doi:10.1016/j.neuron.2009.12.021
73. Zheng, Y., Mellem, J. E., Brockie, P. J., Madsen, D. M. & Maricq, A. V. SOL-1 is a CUB-domain protein required for GLR-1 glutamate receptor function in C. elegans. *Nature* (2004). doi:10.1038/nature02244
74. Schwenk, J. *et al.* Functional proteomics identify cornichon proteins as auxiliary subunits of AMPA receptors. *Science.* (2009). doi:10.1126/science.1167852
75. Klaassen, R. V. *et al.* Shisa6 traps AMPA receptors at postsynaptic sites and prevents their desensitization during synaptic activity. *Nat. Commun.* **7**, 1–12 (2016).
76. Schmitz, L. J. M. *et al.* The AMPA receptor-associated protein Shisa7 regulates hippocampal synaptic function and contextual memory. *Elife* (2017). doi:10.7554/eLife.24192
77. Herguedas, B. *et al.* Structure and organization of heteromeric AMPA-type glutamate receptors. *Science.* **352**, 1–16 (2016).
78. Karakas, E. & Furukawa, H. Crystal structure of a heterotetrameric NMDA receptor ion channel. *Science.* **344**, 992–997 (2014).
79. Zhu, S. *et al.* Mechanism of NMDA Receptor Inhibition and Activation. *Cell* **165**, 704–714 (2016).
80. Sumioka, A. Auxiliary subunits provide new insights into regulation of AMPA receptor trafficking. *J. Biochem.* **153**, 331–337 (2013).
81. Haering, S. C., Tapken, D., Pahl, S. & Hollmann, M. Auxiliary subunits: Shepherding AMPA receptors to the plasma membrane. *Membranes (Basel).* **4**, 469–490 (2014).
82. Jackson, A. C. & Nicoll, R. A. The Expanding Social Network of Ionotropic Glutamate Receptors: TARPs and Other Transmembrane Auxiliary Subunits. *Neuron* **70**, 178–199 (2011).
83. Nakagawa, T. The biochemistry, ultrastructure, and subunit assembly mechanism of AMPA receptors. *Mol. Neurobiol.* **42**, 161–184 (2010).
84. Schwenk, J. *et al.* High-Resolution Proteomics Unravel Architecture and Molecular Diversity of Native AMPA Receptor Complexes. *Neuron* **74**, 621–633 (2012).
85. Kang, M. G. *et al.* Proteomic analysis of α-amino-3-hydroxy-5-methyl-4-isoxazole propionate receptor complexes. *J. Biol. Chem.* (2012). doi:10.1074/jbc.M111.336644
86. Nakagawa, T., Cheng, Y., Ramm, E., Sheng, M. & Walz, T. Structure and different conformational states of native AMPA receptor complexes. *Nature* (2005). doi:10.1038/nature03328
87. Monyer, H. & von Engelhardt, J. Modulation of AMPA receptor function by auxiliary subunits. *e-Neuroforum* 39–48 (2015). doi:10.1007/s13295-015-0005-z
88. Letts, V. A. *et al.* The mouse stargazer gene encodes a neuronal Ca2+-channel γ subunit. *Nat. Genet.* (1998). doi:10.1038/1228
89. Lowenthal, M. S., Markey, S. P. & Dosemeci, A. Quantitative mass spectrometry measurements reveal stoichiometry of principal postsynaptic density proteins. *J. Proteome Res.* (2015). doi:10.1021/acs.jproteome.5b00109
90. Herring, B. E. *et al.* Cornichon Proteins Determine the Subunit Composition of Synaptic AMPA Receptors. *Neuron* **77**, 1083–1096 (2013).
91. Khodosevich, K. *et al.* Coexpressed Auxiliary Subunits Exhibit Distinct Modulatory Profiles on AMPA Receptor Function. *Neuron* **83**, 601–615 (2014).
92. Lein, E. S. *et al.* Genome-wide atlas of gene expression in the adult mouse brain. *Nature* (2007). doi:10.1038/nature05453
93. Shanks, N. F. *et al.* Molecular Dissection of the Interaction between the AMPA Receptor and Cornichon Homolog-3. *J. Neurosci.* **34**, 12104–12120 (2014).
94. Sauvageau, E. *et al.* CNIH4 interacts with newly synthesized GPCR and controls their export from the endoplasmic reticulum. *Traffic* **15**, 383–400 (2014).
95. Rogers, S. W. *et al.* Autoantibodies to glutamate receptor GluR3 in Rasmussen's encephalitis. *Science (80-.).* (1994). doi:10.1126/science.8036512
96. Akamatsu, M., Yamashita, T., Hirose, N., Teramoto, S. & Kwak, S. The AMPA receptor antagonist perampanel robustly rescues amyotrophic lateral sclerosis (ALS) pathology in sporadic ALS model mice. *Sci. Rep.* (2016). doi:10.1038/srep28649
97. Balannik, V., Menniti, F. S., Paternain, A. V., Lerma, J. & Stern-Bach, Y. Molecular mechanism of AMPA receptor noncompetitive antagonism. *Neuron* **48**, 279–288 (2005).

98. Yelshanskaya, M. V. *et al.* Structural Bases of Noncompetitive Inhibition of AMPA-Subtype Ionotropic Glutamate Receptors by Antiepileptic Drugs. *Neuron* **91**, 1305–1315 (2016).
99. Nagarajan, N., Quast, C., Boxall, A. R., Shahid, M. & Rosenmund, C. Mechanism and impact of allosteric AMPA receptor modulation by the Ampakine™ CX546. *Neuropharmacology* **41**, 650–663 (2001).
100. Miu, P. *et al.* Novel AMPA receptor potentiators LY392098 and LY404187: Effects on recombinant human AMPA receptors in vitro. *Neuropharmacology* **40**, 976–983 (2001).
101. Yamada, K. A. & Tang, C. M. Benzothiadiazides inhibit rapid glutamate receptor desensitization and enhance glutamatergic synaptic currents. *J. Neurosci.* (1993). doi:10.1523/jneurosci.5745-03.2004
102. Patneau, D. K., Vyklicky, L. & Mayer, M. L. Hippocampal neurons exhibit cyclothiazide-sensitive rapidly desensitizing responses to kainate. *J. Neurosci.* (1993).
103. Zwart, R. *et al.* Perampanel, an Antagonist of -Amino-3-Hydroxy-5-Methyl-4-Isoxazolepropionic Acid Receptors, for the Treatment of Epilepsy: Studies in Human Epileptic Brain and Nonepileptic Brain and in Rodent Models. *J. Pharmacol. Exp. Ther.* (2014). doi:10.1124/jpet.114.212779
104. Rogawski, M. A. Revisiting AMPA receptors as an antiepileptic drug target. *Epilepsy Curr.* **11**, 56–63 (2011).
105. French, J. A. *et al.* Adjunctive perampanel for refractory partial-onset seizures: Randomized phase III study 304. *Neurology* (2012). doi:10.1212/WNL.0b013e3182635735
106. Chappell, A. S. *et al.* AMPA potentiator treatment of cognitive deficits in Alzheimer disease. *Neurology* (2007). doi:10.1212/01.wnl.0000260240.46070.7c
107. Ren, J., Ding, X., Funk, G. D. & Greer, J. J. Ampakine CX717 protects against fentanyl-induced respiratory depression and lethal apnea in rats. *Anesthesiology* (2009). doi:10.1097/ALN.0b013e31819faa2a
108. Maher, M. P. *et al.* Discovery and Characterization of AMPA Receptor Modulators Selective for TARP- 8. *J. Pharmacol. Exp. Ther.* **357**, 394–414 (2016).
109. Gardinier, K. M. *et al.* Discovery of the First α-Amino-3-hydroxy-5-methyl-4-isoxazolepropionic Acid (AMPA) Receptor Antagonist Dependent upon Transmembrane AMPA Receptor Regulatory Protein (TARP) γ-8. *J. Med. Chem.* **59**, 4753–4768 (2016).
110. Kato, A. S. *et al.* Forebrain-selective AMPA-receptor antagonism guided by TARPλ 3-8 as an antiepileptic mechanism. *Nat. Med.* **22**, 1496–1501 (2016).
111. Lee, M. R. *et al.* Structural Determinants of the γ-8 TARP Dependent AMPA Receptor Antagonist. *ACS Chem. Neurosci.* **8**, 2631–2647 (2017).
112. Inoue, R. *et al.* Transient receptor potential channels in cardiovascular function and disease. *Circulation Research* (2006). doi:10.1161/01.RES.0000233356.10630.8a
113. Ramsey, I. S., Delling, M. & Clapham, D. E. An introdution to TRP channels. *Annu. Rev. Physiol.* (2006). doi:10.1146/annurev.physiol.68.040204.100431
114. Nilius, B. & Owsianik, G. Transient receptor potential channelopathies. *Pflugers Archiv European Journal of Physiology* (2010). doi:10.1007/s00424-010-0788-2
115. Madej, M. G. & Ziegler, C. M. Dawning of a new era in TRP channel structural biology by cryo-electron microscopy. *Pflugers Arch. Eur. J. Physiol.* **470**, 213–225 (2018).
116. Nilius, B., Voets, T., August, J. P. & Peters, J. TRP channels in disease. *Sci. STKE* **2005**, re8 (2005).
117. Doyle, D. A. *et al.* The structure of the potassium channel: Molecular basis of K+conduction and selectivity. *Science (80-.).* (1998). doi:10.1126/science.280.5360.69
118. Long, S. B., Campbell, E. B. & MacKinnon, R. Crystal structure of a mammalian voltage-dependent Shaker family K + channel. *Science (80-.).* (2005). doi:10.1126/science.1116269
119. Autzen, H. E. *et al.* Structure of the human TRPM4 ion channel in a lipid nanodisc. *Science (80-.).* **359**, 228–232 (2018).
120. Azumaya, C. M., Sierra-Valdez, F., Cordero-Morales, J. F. & Nakagawa, T. Cryo-EM structure of the cytoplasmic domain of murine transient receptor potential cation channel subfamily C member 6 (TRPC6). *J. Biol. Chem.* **293**, 10381–10391 (2018).
121. Fan, C., Choi, W., Sun, W., Du, J. & Lu, W. Structure of the human lipid-gated cation channel

TRPC3. *Elife* (2018). doi:10.7554/eLife.36852
122. Yin, Y. *et al.* Structure of the cold- And menthol-sensing ion channel TRPM8. *Science (80-.).* **359**, 237–241 (2018).
123. Paulsen, C. E., Armache, J. P., Gao, Y., Cheng, Y. & Julius, D. Structure of the TRPA1 ion channel suggests regulatory mechanisms. *Nature* **520**, 511–517 (2015).
124. Jin, P. *et al.* Electron cryo-microscopy structure of the mechanotransduction channel NOMPC. *Nature* (2017). doi:10.1038/nature22981
125. Vinayagam, D. *et al.* Electron cryo-microscopy structure of the canonical TRPC4 ion channel. *Elife* (2018). doi:10.7554/eLife.36615.001
126. Zubcevic, L. *et al.* Cryo-electron microscopy structure of the TRPV2 ion channel. *Nat. Struct. Mol. Biol.* (2016). doi:10.1038/nsmb.3159
127. Winkler, P. A., Huang, Y., Sun, W., Du, J. & Lü, W. Electron cryo-microscopy structure of a human TRPM4 channel. *Nature* (2017). doi:10.1038/nature24674
128. Guo, J. *et al.* Structures of the calcium-activated, non-selective cation channel TRPM4. *Nature* (2017). doi:10.1038/nature24997
129. Tang, Q. *et al.* Structure of the receptor-activated human TRPC6 and TRPC3 ion channels. *Cell Res.* **28**, 746–755 (2018).
130. Maruyama, Y. *et al.* Three-dimensional reconstruction using transmission electron microscopy reveals a swollen, bell-shaped structure of transient receptor potential melastatin type 2 cation channel. *J. Biol. Chem.* (2007). doi:10.1074/jbc.M705694200
131. Mio, K. *et al.* The TRPC3 Channel Has a Large Internal Chamber Surrounded by Signal Sensing Antennas. *J. Mol. Biol.* (2007). doi:10.1016/j.jmb.2006.12.043
132. Moiseenkova-Bell, V. Y., Stanciu, L. A., Serysheva, I. I., Tobe, B. J. & Wensel, T. G. Structure of TRPV1 channel revealed by electron cryomicroscopy. *Proc. Natl. Acad. Sci.* (2008). doi:10.1073/pnas.0711835105
133. Shigematsu, H., Sokabe, T., Danev, R., Tominaga, M. & Nagayama, K. A 3.5-nm structure of rat TRPV4 cation channel revealed by zernike phase-contrast cryoelectron microscopy. *J. Biol. Chem.* (2010). doi:10.1074/jbc.M109.090712
134. Hofmann, T. *et al.* Direct activation of human TRPC6 and TRPC3 channels by diacylglycerol. *Nature* **397**, 259–263 (1999).
135. Estacion, M. *et al.* Activation of human TRPC6 channels by receptor stimulation. *J. Biol. Chem.* (2004). doi:10.1074/jbc.M402320200
136. Dietrich, A. & Gudermann, T. TRPC6. *Handb. Exp. Pharmacol.* (2007). doi:10.1007/978-3-540-34891-7_7
137. Kwon, Y., Hofmann, T. & Montell, C. Integration of Phosphoinositide- and Calmodulin-Mediated Regulation of TRPC6. *Mol. Cell* **25**, 491–503 (2007).
138. Zhu, M. X. Multiple roles of calmodulin and other Ca2+-binding proteins in the functional regulation of TRP channels. *Pflugers Arch. Eur. J. Physiol.* **451**, 105–115 (2005).
139. Minke, B. TRP channels and Ca2+signaling. *Cell Calcium* (2006). doi:10.1016/j.ceca.2006.05.002
140. Wedel, B. J., Vazquez, G., McKay, R. R., Bird, G. S. J. & Putney, J. W. A calmodulin/inositol 1,4,5-trisphosphate (IP3) receptor-binding region targets TRPC3 to the plasma membrane in a calmodulin/IP3receptor-independent process. *J. Biol. Chem.* **278**, 25758–25765 (2003).
141. Shi, J. *et al.* Multiple regulation by calcium of murine homologues of transient receptor potential proteins TRPC6 and TRPC7 expressed in HEK293 cells. *J. Physiol.* **561**, 415–432 (2004).
142. Hofmann, T., Schaefer, M., Schultz, G. & Gudermann, T. Subunit composition of mammalian transient receptor potential channels in living cells. *Proc. Natl. Acad. Sci.* (2002). doi:10.1073/pnas.102596199
143. Bröker-Lai, J. *et al.* Heteromeric channels formed by TRPC1, TRPC4 and TRPC5 define hippocampal synaptic transmission and working memory. *EMBO J.* **36**, e201696369 (2017).
144. Álvarez-Miguel, I., Cidad, P., Pérez-García, M. T. & López-López, J. R. Differences in TRPC3 and TRPC6 channels assembly in mesenteric vascular smooth muscle cells in essential hypertension. *J. Physiol.* (2017). doi:10.1113/JP273327
145. Sierra-Valdez, F., Azumaya, C. M., Romero, L. O., Nakagawa, T. & Cordero-Morales, J. F.

Structure–function analyses of the ion channel TRPC3 reveal that its cytoplasmic domain allosterically modulates channel gating. *J. Biol. Chem.* (2018). doi:10.1074/jbc.RA118.005066
146. Spassova, M. A., Hewavitharana, T., Xu, W., Soboloff, J. & Gill, D. L. A common mechanism underlies stretch activation and receptor activation of TRPC6 channels. *Proc. Natl. Acad. Sci.* **103**, 16586–16591 (2006).
147. Xu, P., Xu, J., Li, Z. & Yang, Z. Expression of TRPC6 in Renal Cortex and Hippocampus of Mouse during Postnatal Development. *PLoS One* **7**, e38503 (2012).
148. Zhou, J. *et al.* Critical role of TRPC6 channels in the formation of excitatory synapses. *Nat. Neurosci.* **11**, 741–743 (2008).
149. Santín, S. *et al.* TRPC6 mutational analysis in a large cohort of patients with focal segmental glomerulosclerosis. *Nephrol. Dial. Transplant.* (2009). doi:10.1093/ndt/gfp229
150. Heeringa, S. F. *et al.* A novel TRPC6 mutation that causes childhood FSGS. *PLoS One* (2009). doi:10.1371/journal.pone.0007771
151. Reiser, J. *et al.* TRPC6 is a glomerular slit diaphragm-associated channel required for normal renal function. *Nat. Genet.* (2005). doi:10.1038/ng1592
152. Mottl, A. K., Lu, M., Fine, C. A. & Weck, K. E. A novel TRPC6 mutation in a family with podocytopathy and clinical variability. *BMC Nephrol.* (2013). doi:10.1186/1471-2369-14-104
153. Winn, M. P. *et al.* Medicine: A mutation in the TRPC6 cation channel causes familial focal segmental glomerulosclerosis. *Science.* **308**, 1801–1804 (2005).
154. Winn, M. P. Unexpected Role of TRPC6 Channel in Familial Nephrotic Syndrome: Does It Have Clinical Implications? *J. Am. Soc. Nephrol.* **17**, 378–387 (2006).
155. Kestilä, M. *et al.* Positionally cloned gene for a novel glomerular protein - Nephrin - Is mutated in congenital nephrotic syndrome. *Mol. Cell* (1998). doi:10.1016/S1097-2765(00)80057-X
156. Kaplan, J. M. *et al.* Mutations in ACTN4, encoding α-actinin-4, cause familial focal segmental glomerulosclerosis. *Nat. Genet.* (2000). doi:10.1038/73456
157. Sekerkova, G. *et al.* Early Onset of Ataxia in Moonwalker Mice Is Accompanied by Complete Ablation of Type II Unipolar Brush Cells and Purkinje Cell Dysfunction. *J. Neurosci.* (2013). doi:10.1523/JNEUROSCI.2294-13.2013
158. Hartmann, J. *et al.* TRPC3 Channels Are Required for Synaptic Transmission and Motor Coordination. *Neuron* **59**, 392–398 (2008).
159. Hartmann, J., Henning, H. A. & Konnerth, A. mGluR1/TRPC3-mediated synaptic transmission and calcium signaling in mammalian central neurons. *Cold Spring Harb. Perspect. Biol.* **3**, 1–16 (2011).
160. Becker, E. B. E. *et al.* A point mutation in TRPC3 causes abnormal Purkinje cell development and cerebellar ataxia in moonwalker mice. *Proc. Natl. Acad. Sci.* **106**, 6706–6711 (2009).
161. Fogel, B. L., Hanson, S. M. & Becker, E. B. E. Do mutations in the murine ataxia gene TRPC3 cause cerebellar ataxia in humans? *Movement Disorders* (2015). doi:10.1002/mds.26096
162. Neuner, S. M. *et al.* TRPC3 channels critically regulate hippocampal excitability and contextual fear memory. *Behav. Brain Res.* (2015). doi:10.1016/j.bbr.2014.12.018
163. Lockwich, T. *et al.* Analysis of TRPC3-Lnteracting proteins by tandem mass spectrometry. *J. Proteome Res.* **7**, 979–989 (2008).
164. Zhang, Z. *et al.* Activation of Trp3 by inositol 1,4,5-trisphosphate receptors through displacement of inhibitory calmodulin from a common binding domain. *Proc. Natl. Acad. Sci. U. S. A.* (2001). doi:10.1073/pnas.051632698
165. Zhang, Z. *et al.* Activation of Trp3 by inositol 1,4,5-trisphosphate receptors through displacement of inhibitory calmodulin from a common binding domain. *Proc. Natl. Acad. Sci. U. S. A.* **98**, 3168–3173 (2001).
166. Yuan, J. P. *et al.* Homer binds TRPC family channels and is required for gating of TRPC1 by IP3receptors. *Cell* **114**, 777–789 (2003).
167. Kim, M. S. *et al.* Deletion of TRPC3 in Mice Reduces Store-Operated Ca^{2+}Influx and the Severity of Acute Pancreatitis. *Gastroenterology* **137**, 1509–1517 (2009).
168. Kim, M. S. *et al.* Genetic and pharmacologic inhibition of the Ca^{2+}influx channel TRPC3 protects secretory epithelia from Ca2+-dependent toxicity. *Gastroenterology* (2011). doi:10.1053/j.gastro.2011.02.052

169. Di, A. & Malik, A. B. TRP channels and the control of vascular function. *Current Opinion in Pharmacology* (2010). doi:10.1016/j.coph.2009.11.010
170. Eder, P., Poteser, M. & Groschner, K. TRPC3: A multifunctional, pore-forming signalling molecule. *Handb. Exp. Pharmacol.* (2007). doi:10.1007/978-3-540-34891-7_4
171. Xi, Q. *et al.* IP3 constricts cerebral arteries via IP3 receptor-mediated TRPC3 channel activation and independently of sarcoplasmic reticulum Ca^{2+} release. *Circ. Res.* (2008). doi:10.1161/CIRCRESAHA.108.173948
172. Schleifer, H. *et al.* Novel pyrazole compounds for pharmacological discrimination between receptor-operated and store-operated Ca^{2+} entry pathways. *Br. J. Pharmacol.* (2012). doi:10.1111/j.1476-5381.2012.02126.x
173. Kiyonaka, S. *et al.* Selective and direct inhibition of TRPC3 channels underlies biological activities of a pyrazole compound. *Proc. Natl. Acad. Sci.* (2009). doi:10.1073/pnas.0808793106
174. Cheng, Y. Membrane protein structural biology in the era of single particle cryo-EM. *Curr. Opin. Struct. Biol.* **52**, 58–63 (2018).
175. Subramaniam, S., Earl, L. A., Falconieri, V., Milne, J. L. & Egelman, E. H. Resolution advances in cryo-EM enable application to drug discovery. *Curr. Opin. Struct. Biol.* **41**, 194–202 (2016).
176. Efremov, R. G., Leitner, A., Aebersold, R. & Raunser, S. Architecture and conformational switch mechanism of the ryanodine receptor. *Nature* (2015). doi:10.1038/nature13916
177. Gogol, E. P. *et al.* Three dimensional structure of the anthrax toxin translocon-lethal factor complex by cryo-electron microscopy. *Protein Sci.* (2013). doi:10.1002/pro.2241
178. Shen, P. S. *et al.* The Structure of the Polycystic Kidney Disease Channel PKD2 in Lipid Nanodiscs. *Cell* (2016). doi:10.1016/j.cell.2016.09.048
179. Merk, A. *et al.* Breaking Cryo-EM Resolution Barriers to Facilitate Drug Discovery. *Cell* **165**, 1698–1707 (2016).
180. Wong, W. *et al.* Cryo-EM structure of the Plasmodium falciparum 80S ribosome bound to the anti-protozoan drug emetine. *Elife* (2014). doi:10.7554/eLife.03080
181. Cao, E., Liao, M., Cheng, Y. & Julius, D. TRPV1 structures in distinct conformations reveal activation mechanisms. *Nature* (2013). doi:10.1038/nature12823
182. Campbell, M. G., Veesler, D., Cheng, A., Potter, C. S. & Carragher, B. 2.8Å resolution reconstruction of the thermoplasma acidophilum 20 s proteasome using cryo-electron microscopy. *Elife* (2015). doi:10.7554/eLife.06380
183. Binshtein, E. & Ohi, M. D. Cryo-electron microscopy and the amazing race to atomic resolution. *Biochemistry* **54**, 3133–3141 (2015).
184. Taylor, K. A. & Glaeser, R. M. Retrospective on the early development of cryoelectron microscopy of macromolecules and a prospective on opportunities for the future. *J. Struct. Biol.* (2008). doi:10.1016/j.jsb.2008.06.004
185. DE ROSIER, D. J. & KLUG, A. Reconstruction of Three Dimensional Structures from Electron Micrographs. *Nature* **217**, 130–134 (1968).
186. Taylor, K. A. & Glaeser, R. M. Electron diffraction of frozen, hydrated protein crystals. *Science (80-.).* (1974). doi:10.1080/00207599308246920
187. Unwin, P. N. T. & Henderson, R. Molecular structure determination by electron microscopy of unstained crystalline specimens. *J. Mol. Biol.* (1975). doi:10.1016/0022-2836(75)90212-0
188. Schultz, P. Cryo-electron microscopy of vitrified specimens. *Q. Rev. Biophys.* (1988). doi:10.1017/S0033583500004297
189. Dubochet, J., Booy, F. P., Freeman, R., Jones, A. V & Walter, C. A. Low Temperature Electron Microscopy. *Annu. Rev. Biophys. Bioeng.* **10**, 133–149 (1981).
190. Frank, J., Penczek, P., Grassucci, R. & Srivastava, S. Three-dimensional reconstruction of the 70S Escherichia coli ribosome in ice: The distribution of ribosomal RNA. *J. Cell Biol.* (1991). doi:10.1083/jcb.115.3.597
191. Christensen, A. K. Frozen thin sections of fresh tissue for electron microscopy, with a description of pancreas and liver. *J. Cell Biol.* **51**, 772–804 (1971).
192. Taylor, K. A. Structure determination of frozen, hydrated, crystalline biological specimens. *J. Microsc.* **112**, 115–125 (1978).
193. Adrian, M., Dubochet, J., Lepault, J. & McDowall, A. W. Cryo-electron microscopy of viruses.

Nature (1984). doi:10.1038/308032a0
194. Liu, Z. *et al.* Determination of the ribosome structure to a resolution of 2.5Å by single-particle cryo-EM. *Protein Sci.* **26**, 82–92 (2017).
195. McMullan, G. *et al.* Experimental observation of the improvement in MTF from backthinning a CMOS direct electron detector. *Ultramicroscopy* (2009). doi:10.1016/j.ultramic.2009.05.005
196. McMullan, G., Faruqi, A. R. & Henderson, R. *Direct Electron Detectors*. *Methods in Enzymology* **579**, (Elsevier Inc., 2016).
197. Bammes, B. E., Rochat, R. H., Jakana, J., Chen, D. H. & Chiu, W. Direct electron detection yields cryo-EM reconstructions at resolutions beyond 3/4 Nyquist frequency. *J. Struct. Biol.* (2012). doi:10.1016/j.jsb.2012.01.008
198. McMullan, G., Faruqi, A. R., Clare, D. & Henderson, R. Comparison of optimal performance at 300keV of three direct electron detectors for use in low dose electron microscopy. *Ultramicroscopy* (2014). doi:10.1016/j.ultramic.2014.08.002
199. Brink, J., Sherman, M. B., Berriman, J. & Chiu, W. Evaluation of charging on macromolecules in electron cryomicroscopy. *Ultramicroscopy* **72**, 41–52 (1998).
200. Glaeser, R. M. & Taylor, K. A. Radiation damage relative to transmission electron microscopy of biological specimens at low temperature: a review. *J. Microsc.* **112**, 127–138 (1978).
201. Brilot, A. F. *et al.* Beam-Induced Motion of Vitrified Specimen on Holey Carbon Film. *J Struct Biol* **177**, 630–637 (2012).
202. Campbell, M. G. *et al.* Movies of ice-embedded particles enhance resolution in electron cryo-microscopy. *Structure* **20**, 1823–1828 (2012).
203. Li, X. *et al.* Electron counting and beam-induced motion correction enable near-atomic-resolution single-particle cryo-EM. *Nat. Methods* **10**, 584–590 (2013).
204. Zheng, S. Q. *et al.* MotionCor2: Anisotropic correction of beam-induced motion for improved cryo-electron microscopy. *Nature Methods* (2017). doi:10.1038/nmeth.4193
205. Scheres, S. H. W. RELION: Implementation of a Bayesian approach to cryo-EM structure determination. *J. Struct. Biol.* (2012). doi:10.1016/j.jsb.2012.09.006
206. Grant, T., Rohou, A. & Grigorieff, N. CisTEM, user-friendly software for single-particle image processing. *Elife* (2018). doi:10.7554/eLife.35383
207. Punjani, A., Rubinstein, J. L., Fleet, D. J. & Brubaker, M. A. CryoSPARC: Algorithms for rapid unsupervised cryo-EM structure determination. *Nat. Methods* **14**, 290–296 (2017).
208. Fernández, I. S. *et al.* Molecular architecture of a eukaryotic translational initiation complex. *Science (80-.).* **342**, (2013).
209. Fernández, I. S., Bai, X. C., Murshudov, G., Scheres, S. H. W. & Ramakrishnan, V. Initiation of translation by cricket paralysis virus IRES requires its translocation in the ribosome. *Cell* (2014). doi:10.1016/j.cell.2014.04.015
210. Sigworth, F. J. A maximum-likelihood approach to single-particle image refinement. *J. Struct. Biol.* **122**, 328–339 (1998).
211. Scheres, S. H. W. Maximum-likelihood methods in cryo-EM. PartII: application to experimantal data. *Methods Enzym.* **6879**, 295–320 (2010).
212. Mastronarde, D. N. SerialEM: A Program for Automated Tilt Series Acquisition on Tecnai Microscopes Using Prediction of Specimen Position. *Microsc. Microanal.* (2003). doi:doi:null
213. Kimanius, D., Forsberg, B. O., Scheres, S. H. W. & Lindahl, E. Accelerated cryo-EM structure determination with parallelisation using GPUs in RELION-2. *Elife* (2016). doi:10.7554/eLife.18722
214. Feng, X. *et al.* A Fast and Effective Microfluidic Spraying-Plunging Method for High-Resolution Single-Particle Cryo-EM. *Structure* **25**, 663–670.e3 (2017).
215. Palovcak, E. *et al.* A simple and robust procedure for preparing graphene-oxide cryo-EM grids. *J. Struct. Biol.* **204**, 80–84 (2018).
216. Wei, H. *et al.* Self-Blotting Nanowire Grids for Cryo-EM Sample Preparation. *Microsc. Microanal.* (2017). doi:10.1017/S1431927617004901
217. Jain, T., Sheehan, P., Crum, J., Carragher, B. & Potter, C. S. Spotiton: A prototype for an integrated inkjet dispense and vitrification system for cryo-TEM. *J. Struct. Biol.* (2012). doi:10.1016/j.jsb.2012.04.020

218. Foskett, J. K., White, C., Cheung, K.-H. & Mak, D.-O. D. Inositol Trisphosphate Receptor Ca^{2+} Release Channels. *Physiol. Rev.* (2007). doi:10.1152/physrev.00035.2006
219. Berridge, M. J. The Inositol Trisphosphate/Calcium Signaling Pathway in Health and Disease. *Physiol. Rev.* **96**, 1261–1296 (2016).
220. Parys, J. B. & De Smedt, H. Inositol 1,4,5-trisphosphate and its receptors. *Adv. Exp. Med. Biol.* (2012). doi:10.1007/978-94-007-2888-2_11
221. Mikoshiba, K. Role of IP3receptor signaling in cell functions and diseases. *Adv. Biol. Regul.* **57**, 217–227 (2015).
222. da Fonseca, P. C. A., Morris, S. A., Nerou, E. P., Taylor, C. W. & Morris, E. P. Domain organization of the type 1 inositol 1,4,5-trisphosphate receptor as revealed by single-particle analysis. *Proc. Natl. Acad. Sci.* (2003). doi:10.1073/pnas.0536251100
223. Fan, G. *et al.* No Title. (2018).
224. Fan, G. *et al.* Gating machinery of InsP3R channels revealed by electron cryomicroscopy. *Nature* **527**, 336–341 (2015).
225. Hamada, K., Terauchi, A. & Mikoshiba, K. Three-dimensional Rearrangements within Inositol 1,4,5-Trisphosphate Receptor by Calcium. *J. Biol. Chem.* (2003). doi:10.1074/jbc.M309743200
226. Jiang, Q. X., Thrower, E. C., Chester, D. W., Ehrlich, B. E. & Sigworth, F. J. Three-dimensional structure of the type 1 inositol 1,4,5-trisphosphate receptor at 24Å resolution. *EMBO J.* (2002). doi:10.1093/emboj/cdf380
227. Nakade, S., Rhee, S. K., Hamanaka, H. & Mikoshiba, K. Cyclic AMP-dependent phosphorylation of an immunoaffinity-purified homotetrameric inositol 1,4,5-trisphosphate receptor (type I) increases Ca2+ flux in reconstituted lipid vesicles. *J. Biol. Chem.* (1994).
228. Sato, C. *et al.* Inositol 1,4,5-trisphosphate Receptor Contains Multiple Cavities and L-shaped Ligand-binding Domains. *J. Mol. Biol.* (2004). doi:10.1016/j.jmb.2003.11.024
229. Serysheva, I. I. *et al.* Structure of the type 1 inositol 1,4,5-trisphosphate receptor revealed by electron cryomicroscopy. *J. Biol. Chem.* (2003). doi:10.1074/jbc.C300148200
230. Supattapone, S., Worley, P. F., Baraban, J. M. & Snyder, S. H. Solubilization, purification, and characterization of an inositol trisphosphate receptor. *J. Biol. Chem.* (1988).
231. Paknejad, N. & Hite, R. K. Erratum to: Structural basis for the regulation of inositol trisphosphate receptors by Ca2+ and IP3 (Nature Structural & Molecular Biology, (2018), 25, 8, (660-668), 10.1038/s41594-018-0089-6). *Nat. Struct. Mol. Biol.* **25**, 902 (2018).
232. Farina, A. N. *et al.* Separation of Domain Contacts Is Required for Heterotetrameric Assembly of Functional NMDA Receptors. *J. Neurosci.* (2011). doi:10.1523/JNEUROSCI.6041-10.2011
233. Levy, J. M., Chen, X., Reese, T. S. & Nicoll, R. A. Synaptic Consolidation Normalizes AMPAR Quantal Size following MAGUK Loss. *Neuron* **87**, 534–548 (2015).
234. Dietrich, A. *et al.* N-Linked Protein Glycosylation Is a Major Determinant for Basal TRPC3 and TRPC6 Channel Activity. *J. Biol. Chem.* (2003). doi:10.1074/jbc.M302983200
235. Strausberg RL, Fingold EA, Grouse LH, Derge JG, Klausner RD, Collins FS, Wagner L, Shenmen CM, Schuler GD, Altschul SF, Zeeberg B, Buetow KH, Schaefer CF, Bhat NK, Hopkins RF, Jordan H, Moore T, Max SI, Wang J, Hsieh F, Diatchenko L, Marusina K, Farmer, M. M. M. G. C. P. T. Generation and initial analysis of more than 15,000 full-length human and mouse cDNA sequences. **99**, (2002).
236. Fitzgerald, D. J. *et al.* Protein complex expression by using multigene baculoviral vectors. *Nat. Methods* (2006). doi:10.1038/nmeth983
237. Di Virgilio, F., Steinberg, T. H. & Silverstein, S. C. Inhibition of Fura-2 sequestration and secretion with organic anion transport blockers. *Cell Calcium* (1990). doi:10.1016/0143-4160(90)90059-4
238. Ohi, M., Li, Y., Cheng, Y. & Walz, T. Negative staining and image classification - Powerful tools in modern electron microscopy. *Biol. Proced. Online* **6**, 23–34 (2004).
239. Shaikh, T. R. *et al.* Spider image processing for single-particle reconstruction of biological macromolecules from electron micrographs. *Nat. Protoc.* (2008). doi:10.1038/nprot.2008.156
240. Mindell, J. A. & Grigorieff, N. Accurate determination of local defocus and specimen tilt in electron microscopy. *J. Struct. Biol.* (2003). doi:10.1016/S1047-8477(03)00069-8
241. Tang, G. *et al.* EMAN2: An extensible image processing suite for electron microscopy. *J. Struct.*

Biol. (2007). doi:10.1016/j.jsb.2006.05.009
242. Zhang, K. Gctf: Real-time CTF determination and correction. *J. Struct. Biol.* (2016). doi:10.1016/j.jsb.2015.11.003
243. Biyani, N. *et al.* Focus: The interface between data collection and data processing in cryo-EM. *J. Struct. Biol.* (2017). doi:10.1016/j.jsb.2017.03.007
244. Rosenthal, P. B. & Henderson, R. Optimal determination of particle orientation, absolute hand, and contrast loss in single-particle electron cryomicroscopy. *J. Mol. Biol.* **333**, 721–745 (2003).
245. Kucukelbir, A., Sigworth, F. J. & Tagare, H. D. Quantifying the local resolution of cryo-EM density maps. *Nat. Methods* (2014). doi:10.1038/nmeth.2727
246. Emsley, P. & Cowtan, K. Coot: Model-building tools for molecular graphics. *Acta Crystallogr. Sect. D Biol. Crystallogr.* (2004). doi:10.1107/S0907444904019158
247. Pettersen, E. F. *et al.* UCSF Chimera - A visualization system for exploratory research and analysis. *J. Comput. Chem.* (2004). doi:10.1002/jcc.20084
248. Afonine, P. V *et al.* Real---space refinement in. (2018).
249. Afonine, P. V. *et al.* Towards automated crystallographic structure refinement with phenix.refine. *Acta Crystallogr. Sect. D Biol. Crystallogr.* (2012). doi:10.1107/S0907444912001308
250. Chen, V. B. *et al.* MolProbity: All-atom structure validation for macromolecular crystallography. *Acta Crystallogr. Sect. D Biol. Crystallogr.* (2010). doi:10.1107/S0907444909042073
251. Shanks, N. F., Maruo, T., Farina, A. N., Ellisman, M. H. & Nakagawa, T. Contribution of the Global Subunit Structure and Stargazin on the Maturation of AMPA Receptors. *J. Neurosci.* **30**, 2728–2740 (2010).
252. Rosenmund, C., Stern-Bach, Y. & Stevens, C. F. The tetrameric structure of a glutamate receptor channel. *Science.* (1998). doi:10.1126/science.280.5369.1596
253. Smith, T. C. & Howe, J. R. Concentration-dependent substrate behavior of native AMPA receptors. *Nat. Neurosci.* (2000). doi:10.1038/79931
254. Suzuki, Y. *et al.* Visualization of structural changes accompanying activation of N-methyl-D-aspartate (NMDA) receptors using fast-scan atomic force microscopy imaging. *J. Biol. Chem.* (2013). doi:10.1074/jbc.M112.422311
255. Taylor, J. N., Li, C. B., Cooper, D. R., Landes, C. F. & Komatsuzaki, T. Error-based extraction of states and energy landscapes from experimental single-molecule time-series. *Sci. Rep.* (2015). doi:10.1038/srep09174
256. MacLean, D. M., Ramaswamy, S. S., Du, M., Howe, J. R. & Jayaraman, V. Stargazin promotes closure of the AMPA receptor ligand-binding domain. *J. Gen. Physiol.* (2014). doi:10.1177/1473325015622530
257. Choi, U. B. *et al.* Modulating the intrinsic disorder in the cytoplasmic domain alters the biological activity of the N-methyl-D-aspartatesensitive glutamate receptor. *J. Biol. Chem.* (2013). doi:10.1074/jbc.M113.477810
258. Schmidt-Krey, I. & Rubinstein, J. L. Electron cryomicroscopy of membrane proteins: Specimen preparation for two-dimensional crystals and single particles. *Micron* (2011). doi:10.1016/j.micron.2010.07.004
259. Nakagawa, T., Cheng, Y., Sheng, M. & Walz, T. Three-dimensional structure of an AMPA receptor without associated stargazin/TARP proteins. in *Biological Chemistry* (2006). doi:10.1515/BC.2006.024
260. Barrett, P. J. *et al.* The amyloid precursor protein has a flexible transmembrane domain and binds cholesterol. *Science (80-.).* (2012). doi:10.1126/science.1219988
261. McCoy, J. G. *et al.* A KcsA/MloK1 chimeric ion channel has lipid-dependent ligand-binding energetics. *J. Biol. Chem.* (2014). doi:10.1074/jbc.M113.543389
262. Hering, H., Lin, C.-C. & Sheng, M. Lipid Rafts in the Maintenance of Synapses , Dendritic Spines , and Surface AMPA Receptor Stability. *J. Neurosci.* (2003). doi:23/8/3262 [pii]
263. Korinek, M. *et al.* Cholesterol modulates open probability and desensitization of NMDA receptors. *J. Physiol.* (2015). doi:10.1113/jphysiol.2014.288209
264. Sumioka, A., Yan, D. & Tomita, S. TARP Phosphorylation Regulates Synaptic AMPA Receptors through Lipid Bilayers. *Neuron* (2010). doi:10.1016/j.neuron.2010.04.035
265. Ogden, K. K. & Traynelis, S. F. Contribution of the M1 Transmembrane Helix and Pre-M1 Region

to Positive Allosteric Modulation and Gating of N-Methyl-D-Aspartate Receptors. *Mol. Pharmacol.* (2013). doi:10.1124/mol.113.085209
266. Derkach, V. A., Oh, M. C., Guire, E. S. & Soderling, T. R. Regulatory mechanisms of AMPA receptors in synaptic plasticity. *Nature Reviews Neuroscience* (2007). doi:10.1038/nrn2055
267. Hayashi, T., Rumbaugh, G. & Huganir, R. L. Differential regulation of AMPA receptor subunit trafficking by palmitoylation of two distinct sites. *Neuron* (2005). doi:10.1016/j.neuron.2005.06.035
268. Cais, O. *et al.* Mapping the interaction sites between AMPA receptors and TARPs reveals a role for the receptor N-terminal domain in channel gating. *Cell Rep.* (2014). doi:10.1016/j.celrep.2014.09.029
269. Yelshanskaya, M. V., Saotome, K., Singh, A. K. & Sobolevsky, A. I. Probing Intersubunit Interfaces in AMPA-subtype Ionotropic Glutamate Receptors. *Sci. Rep.* (2016). doi:10.1038/srep19082
270. Matsuda, S., Kamiya, Y. & Yuzaki, M. Roles of the N-terminal domain on the function and quaternary structure of the ionotropic glutamate receptor. *J. Biol. Chem.* (2005). doi:10.1074/jbc.M410513200
271. Lee, S. H., Liu, L., Wang, Y. T. & Sheng, M. Clathrin adaptor AP2 and NSF interact with overlapping sites of GluR2 and play distinct roles in AMPA receptor trafficking and hippocampal LTD. *Neuron* (2002). doi:10.1016/S0896-6273(02)01024-3
272. Xia, J., Zhang, X., Staudinger, J. & Huganir, R. L. Clustering of AMPA receptors by the synaptic PD domain-containing protein PICK1. *Neuron* (1999). doi:10.1016/S0896-6273(00)80689-3
273. Leonard, A. S., Davare, M. A., Horne, M. C., Garner, C. C. & Hell, J. W. SAP97 is associated with the α-amino-3-hydroxy-5-methylisoxazole-4-propionic acid receptor GluR1 subunit. *J. Biol. Chem.* (1998). doi:10.1074/jbc.273.31.19518
274. Dong, H. *et al.* GRIP: A synaptic PDZ domain-containing protein that interacts with AMPA receptors. *Nature* (1997). doi:10.1038/386279a0
275. Srivastava, S. *et al.* Novel anchorage of GluR2/3 to the postsynaptic density by the AMPA receptor-binding protein ABP. *Neuron* (1998). doi:10.1016/S0896-6273(00)80568-1
276. Osten, P. *et al.* The AMPA receptor GluR2 C terminus can mediate a reversible, ATP- dependent interaction with NSF and α- and β-SNAPs. *Neuron* (1998). doi:10.1016/S0896-6273(00)80518-8
277. Nishimune, A. *et al.* NSF binding to GluR2 regulates synaptic transmission. *Neuron* (1998). doi:10.1016/S0896-6273(00)80517-6
278. Song, I. *et al.* Interaction of the N-ethylmaleimide-sensitive factor with AMPA receptors. *Neuron* (1998). doi:10.1016/S0896-6273(00)80548-6
279. Chen, X. *et al.* Organization of the core structure of the postsynaptic density. *Proc. Natl. Acad. Sci.* (2008). doi:10.1073/pnas.0800897105
280. MacGillavry, H. D., Song, Y., Raghavachari, S. & Blanpied, T. A. Nanoscale scaffolding domains within the postsynaptic density concentrate synaptic ampa receptors. *Neuron* (2013). doi:10.1016/j.neuron.2013.03.009
281. McGee, T. P., Bats, C., Farrant, M. & Cull-Candy, S. G. Auxiliary Subunit GSG1L Acts to Suppress Calcium-Permeable AMPA Receptor Function. *J. Neurosci.* **35**, 16171–16179 (2015).
282. Gu, X. *et al.* GSG1L suppresses AMPA receptor-mediated synaptic transmission and uniquely modulates AMPA receptor kinetics in hippocampal neurons. *Nat. Commun.* **7**, 1–18 (2016).
283. Burnashev, N., Monyer, H., Seeburg, P. H. & Sakmann, B. Divalent ion permeability of AMPA receptor channels is dominated by the edited form of a single subunit. *Neuron* (1992). doi:10.1016/0896-6273(92)90120-3
284. Swanson, G. T., Kamboj, S. K. & Cull-Candy, S. G. Single-channel properties of recombinant AMPA receptors depend on RNA editing, splice variation, and subunit composition. *J. Neurosci.* (1997). doi:20026333
285. Zhang, J. H., Chung, T. D. Y. & Oldenburg, K. R. A simple statistical parameter for use in evaluation and validation of high throughput screening assays. *J. Biomol. Screen.* **4**, 67–73 (1999).
286. Montgomery, K. E., Kessler, M. & Arai, A. C. Modulation of Agonist Binding to AMPA Receptors by Differential Effects across Brain Regions and GluA1 – 4 / Transmembrane AMPA Receptor

Regulatory Protein. **331**, 965–974 (2009).
287. Tomita, S., Sekiguchi, M., Wada, K., Nicoll, R. a & Bredt, D. S. Stargazin controls the pharmacology of AMPA receptor potentiators. *Proc.Natl.Acad.Sci.U.S.A* **103**, 10064–10067 (2006).
288. Semenov, A., Möykkynen, T., Coleman, S. K., Korpi, E. R. & Keinänen, K. Autoinactivation of the Stargazin-AMPA Receptor Complex: Subunit-Dependency and Independence from Physical Dissociation. *PLoS One* **7**, (2012).
289. Morimoto-Tomita, M. *et al.* Autoinactivation of Neuronal AMPA Receptors via Glutamate-Regulated TARP Interaction. *Neuron* (2009). doi:10.1016/j.neuron.2008.11.009
290. Kato, A. S. & Witkin, J. M. Auxiliary subunits of AMPA receptors: The discovery of a forebrain-selective antagonist, LY3130481/CERC-611. *Biochem. Pharmacol.* **147**, 191–200 (2018).
291. Autzen, H. E. *et al.* Structure of the human TRPM4 ion channel in a lipid nanodisc. *Science (80-.).* (2018). doi:10.1126/science.aar4510
292. Hirschi, M. *et al.* Cryo-electron microscopy structure of the lysosomal calcium-permeable channel TRPML3. *Nature* (2017). doi:10.1038/nature24055
293. Fujiwara, Y. & Minor, D. L. X-ray Crystal Structure of a TRPM Assembly Domain Reveals an Antiparallel Four-stranded Coiled-coil. *J. Mol. Biol.* (2008). doi:10.1016/j.jmb.2008.08.059
294. Tsuruda, P. R., Julius, D. & Minor, D. L. Coiled Coils Direct Assembly of a Cold-Activated TRP Channel. *Neuron* (2006). doi:10.1016/j.neuron.2006.06.023
295. Leuner, K. *et al.* Hyperforin—a key constituent of St. John's wort specifically activates TRPC6 channels. *FASEB J.* (2007). doi:10.1096/fj.07-8110com
296. Urban, N. *et al.* Pharmacological inhibition of focal segmental glomerulosclerosis-related, gain of function mutants of TRPC6 channels by semi-synthetic derivatives of larixol. *Br. J. Pharmacol.* (2017). doi:10.1111/bph.13977
297. Seo, K. *et al.* Combined TRPC3 and TRPC6 blockade by selective small-molecule or genetic deletion inhibits pathological cardiac hypertrophy. *Proc. Natl. Acad. Sci.* (2014). doi:10.1073/pnas.1308963111
298. Kim, Y. *et al.* Alternative Splicing of the TRPC3 Ion Channel Calmodulin/IP3 Receptor-Binding Domain in the Hindbrain Enhances Cation Flux. *J. Neurosci.* (2012). doi:10.1523/JNEUROSCI.6446-11.2012
299. Tang, J. *et al.* Identification of Common Binding Sites for Calmodulin and Inositol 1,4,5-Trisphosphate Receptors on the Carboxyl Termini of Trp Channels. *J. Biol. Chem.* (2001). doi:10.1074/jbc.M102316200
300. Greger, I. H., Watson, J. F. & Cull-Candy, S. G. Structural and Functional Architecture of AMPA-Type Glutamate Receptors and Their Auxiliary Proteins. *Neuron* **94**, 713–730 (2017).
301. Berg, A. P., Sen, N. & Bayliss, D. A. TrpC3/C7 and Slo2.1 Are Molecular Targets for Metabotropic Glutamate Receptor Signaling in Rat Striatal Cholinergic Interneurons. *J. Neurosci.* (2007). doi:10.1523/JNEUROSCI.0551-07.2007
302. Zhou, F.-W., Matta, S. G. & Zhou, F.-M. Constitutively Active TRPC3 Channels Regulate Basal Ganglia Output Neurons. *J. Neurosci.* (2008). doi:10.1523/JNEUROSCI.3978-07.2008
303. Zhou, H. *et al.* Cerebellar modules operate at different frequencies. *Elife* (2014). doi:10.7554/eLife.02536
304. Lichtenegger, M. *et al.* An optically controlled probe identifies lipid-gating fenestrations within the TRPC3 channel article. *Nat. Chem. Biol.* (2018). doi:10.1038/s41589-018-0015-6
305. Trebak, M. *et al.* Negative regulation of TRPC3 channels by protein kinase C-mediated phosphorylation of serine 712. *Mol. Pharmacol.* (2005). doi:10.1007/s00572-016-0692-5
306. Hasan, R., Leeson-Payne, A. T. S., Jaggar, J. H. & Zhang, X. Calmodulin is responsible for Ca^{2+}-dependent regulation of TRPA1 Channels. *Sci. Rep.* **7**, 45098 (2017).
307. Nilius, B. *et al.* Regulation of the Ca^{2+} sensitivity of the nonselective cation channel TRPM4. *J. Biol. Chem.* (2005). doi:10.1074/jbc.M411089200
308. Hisatsune, C. *et al.* Abnormal taste perception in mice lacking the type 3 inositol 1,4,5-trisphosphate receptor. *J. Biol. Chem.* (2007). doi:10.1074/jbc.M705641200
309. Miura, H. *et al.* Expression of gustducin overlaps with that of type III IP_3 receptor in taste buds of the rat soft palate. *Chem. Senses* (2007). doi:10.1093/chemse/bjm036

310. Sato-Miyaoka, M. *et al.* Regulation of hair shedding by the type 3 IP 3 receptor. *J. Invest. Dermatol.* (2012). doi:10.1038/jid.2012.141
311. Hayashi, T. & Su, T. P. Sigma-1 Receptor Chaperones at the ER- Mitochondrion Interface Regulate Ca^{2+} Signaling and Cell Survival. *Cell* (2007). doi:10.1016/j.cell.2007.08.036
312. Kuchay, S. *et al.* PTEN counteracts FBXL2 to promote IP_3R3- and Ca^{2+} -mediated apoptosis limiting tumour growth. *Nature* (2017). doi:10.1038/nature22965
313. Gomes, D. A. *et al.* The type III inositol 1,4,5-trisphosphate receptor preferentially transmits apoptotic Ca^{2+} signals into mitochondria. *J. Biol. Chem.* (2005). doi:10.1074/jbc.M506623200
314. Kang, S. S. *et al.* Caffeine-mediated inhibition of calcium release channel inositol 1,4,5-trisphosphate receptor subtype 3 blocks glioblastoma invasion and extends survival. *Cancer Res.* (2010). doi:10.1158/0008-5472.CAN-09-2886
315. Mound, A. *et al.* Downregulation of type 3 inositol (1,4,5)-trisphosphate receptor decreases breast cancer cell migration through an oscillatory Ca^{2+} signal. *Oncotarget* (2017). doi:10.18632/oncotarget.20327
316. Sakakura, C. *et al.* Possible Involvement of Inositol 1,4,5-Trisphosphate Receptor Type 3 (IP3R3) in the Peritoneal Dissemination of Gastric Cancers. *Anticancer Res.* (2003).
317. Shibao, K. *et al.* The type III inositol 1,4,5-trisphosphate receptor is associated with aggressiveness of colorectal carcinoma. *Cell Calcium* (2010). doi:10.1016/j.ceca.2010.09.005
318. Bononi, A. *et al.* BAP1 regulates IP3R3-mediated Ca^{2+} flux to mitochondria suppressing cell transformation. *Nature* (2017). doi:10.1038/nature22798
319. Giorgi, C. *et al.* PML regulates apoptosis at endoplasmic reticulum by modulating calcium release. *Science.* (2010). doi:10.1126/science.1189157
320. Szado, T. *et al.* Phosphorylation of inositol 1,4,5-trisphosphate receptors by protein kinase B/Akt inhibits Ca^{2+} release and apoptosis. *Proc. Natl. Acad. Sci. U. S. A.* (2008). doi:10.1073/pnas.0711324105
321. Chan, J. *et al.* Structural studies of inositol 1,4,5-trisphosphate receptor: Coupling ligand binding to channel gating. *J. Biol. Chem.* (2010). doi:10.1074/jbc.M110.140160
322. Seo, M. D. *et al.* Structural and functional conservation of key domains in InsP 3 and ryanodine receptors. *Nature* (2012). doi:10.1038/nature10751
323. Fan, G. *et al.* Gating machinery of InsP3R channels revealed by electron cryomicroscopy. *Nature* (2015). doi:10.1038/nature15249
324. Iwai, M. *et al.* Molecular cloning of mouse type 2 and type 3 inositol 1,4,5-trisphosphate receptors and identification of a novel type 2 receptor splice variant. *J. Biol. Chem.* (2005). doi:10.1074/jbc.M413824200
325. Iwai, M., Michikawa, T., Bosanac, I., Ikura, M. & Mikoshiba, K. Molecular basis of the isoform-specific ligand-binding affinity of inositol 1,4,5-trisphosphate receptors. *J. Biol. Chem.* (2007). doi:10.1074/jbc.M609833200
326. Richardson, A. & Taylor, C. W. Effects of Ca2+ chelators on purified inositol 1,4,5-trisphosphate (InsP3) receptors and InsP3-stimulated Ca2+ mobilization. *J. Biol. Chem.* (1993).
327. des Georges, A. *et al.* Structural Basis for Gating and Activation of RyR1. *Cell* (2016). doi:10.1016/j.cell.2016.08.075
328. McGoldrick, L. L. *et al.* Opening of the human epithelial calcium channel TRPV6. *Nature* (2018). doi:10.1038/nature25182
329. Zhou, Y., Morais-Cabral, J. H., Kaufman, A. & Mackinnon, R. Chemistry of ion coordination and hydration revealed by a K^+channel-Fab complex at 2.0Å resolution. *Nature* (2001). doi:10.1038/35102009
330. Smart, O. S., Neduvelil, J. G., Wang, X., Wallace, B. A. & Sansom, M. S. P. HOLE: A program for the analysis of the pore dimensions of ion channel structural models. *J. Mol. Graph.* (1996). doi:10.1016/S0263-7855(97)00009-X
331. Marcus, Y. Ionic radii in aqueous solutions. *J. Solution Chem.* (1983). doi:10.1007/BF00646201
332. Mayer, M. L. The Challenge of Interpreting Glutamate-Receptor Ion-Channel Structures. *Biophys. J.* **113**, 2143–2151 (2017).
333. Mayer, M. L. Structural biology of glutamate receptor ion channel complexes. *Curr. Opin. Struct. Biol.* **41**, 119–127 (2016).

334. Shi, Y. *et al.* Functional comparison of the effects of TARPs and cornichons on AMPA receptor trafficking and gating. *Proc. Natl. Acad. Sci.* **107**, 16315–16319 (2010).
335. Hawken, N. M., Zaika, E. I. & Nakagawa, T. Engineering defined membrane-embedded elements of AMPA receptor induces opposing gating modulation by cornichon 3 and stargazin. *J. Physiol.* **595**, 6517–6539 (2017).
336. Dawaliby, R. *et al.* Phosphatidylethanolamine is a key regulator of membrane fluidity in eukaryotic cells. *J. Biol. Chem.* (2016). doi:10.1074/jbc.M115.706523
337. Marheineke, K., Grünewald, S., Christie, W. & Reilländer, H. Lipid composition of Spodoptera frugiperda (Sf9) and Trichoplusia ni (Tn) insect cells used for baculovirus infection. *Fed. Eur. Biochem. Soc. Lett.* (1998). doi:10.1016/S0014-5793(98)01523-3
338. Koster, A. J. *et al.* Perspectives of molecular and cellular electron tomography. in *Journal of Structural Biology* (1997). doi:10.1006/jsbi.1997.3933
339. Oikonomou, C. M. & Jensen, G. J. Cellular Electron Cryotomography: Toward Structural Biology In Situ. *Annu. Rev. Biochem.* **86**, 873–896 (2017).
340. Basler, M., Pilhofer, M., Henderson, G. P., Jensen, G. J. & Mekalanos, J. J. Type VI secretion requires a dynamic contractile phage tail-like structure. *Nature* (2012). doi:10.1038/nature10846
341. Lin, J., Okada, K., Raytchev, M., Smith, M. C. & Nicastro, D. Structural mechanism of the dynein power stroke. *Nat. Cell Biol.* (2014). doi:10.1038/ncb2939
342. Kosinski, J. *et al.* Molecular architecture of the inner ring scaffold of the human nuclear pore complex. *Science.* (2016). doi:10.1126/science.aaf0643
343. Bui, K. H. *et al.* Integrated structural analysis of the human nuclear pore complex scaffold. *Cell* (2013). doi:10.1016/j.cell.2013.10.055
344. Lin, D. H. *et al.* Architecture of the symmetric core of the nuclear pore. *Science.* (2016). doi:10.1126/science.aaf1015
345. Chang, Y. W. *et al.* Architecture of the type IVa pilus machine. *Science.* (2016). doi:10.1126/science.aad2001
346. Asano, S. *et al.* A molecular census of 26S proteasomes in intact neurons. *Science.* (2015). doi:10.1126/science.1261197
347. Marko, M., Hsieh, C., Moberlychan, W., Mannella, C. A. & Frank, J. Focused ion beam milling of vitreous water: Prospects for an alternative to cryo-ultramicrotomy of frozen-hydrated biological samples. *J. Microsc.* (2006). doi:10.1111/j.1365-2818.2006.01567.x
348. Arnold, J. *et al.* Site-Specific Cryo-focused Ion Beam Sample Preparation Guided by 3D Correlative Microscopy. *Biophys. J.* (2016). doi:10.1016/j.bpj.2015.10.053
349. Nannenga, B. L. & Gonen, T. MicroED opens a new era for biological structure determination. *Curr. Opin. Struct. Biol.* **40**, 128–135 (2016).
350. Dorset, D. L. & Parsons, D. F. Electron diffraction from single, fully-hydrated, ox-liver catalase microcrystals. *Acta Crystallogr. Sect. A* (1975). doi:10.1107/S0567739475000423
351. Nederlof, I., Li, Y. W., Van Heel, M. & Abrahams, J. P. Imaging protein three-dimensional nanocrystals with cryo-EM. *Acta Crystallogr. Sect. D Biol. Crystallogr.* (2013). doi:10.1107/S0907444913002734
352. Nannenga, B. L., Shi, D., Leslie, A. G. W. & Gonen, T. High-resolution structure determination by continuous-rotation data collection in MicroEDED. *Nat. Methods* (2014). doi:10.1038/nmeth.3043
353. Jones, C. G. *et al.* The CryoEM Method MicroED as a Powerful Tool for Small Molecule Structure Determination. *ACS Cent. Sci.* (2018). doi:10.1021/acscentsci.8b00760
354. Wu, S. *et al.* Fabs enable single particle cryoEM studies of small proteins. *Structure* (2012). doi:10.1016/j.str.2012.02.017
355. Dang, S. *et al.* Cryo-EM structures of the TMEM16A calciumactivated chloride channel. *Nature* (2017). doi:10.1038/nature25024
356. Danev, R. & Baumeister, W. Expanding the boundaries of cryo-EM with phase plates. *Current Opinion in Structural Biology* (2017). doi:10.1016/j.sbi.2017.06.006
357. Nakane, T., Kimanius, D., Lindahl, E. & Scheres, S. H. W. Characterisation of molecular motions in cryo-EM single-particle data by multi-body refinement in RELION. *Elife* (2018). doi:10.7554/eLife.36861
358. Wagner, T. *et al.* SPHIRE-crYOLO: A fast and well-centering automated particle picker for cryo-

EM. *bioRxiv* (2018). doi:10.1101/356584
359. Stuart, D. I., Subramaniam, S. & Abrescia, N. G. A. The democratization of cryo-EM. *Nat. Methods* **13**, 607–608 (2016).

APPENDICES

Appendix 1-1: TEV protease purification

1. Transform TEV-S219V plasmid in BL21(DE3)CodonPlus-RIL strain and plate on LB, 100mg/L AMP+ 34 mg/L CHLOR
2. Make starter culture of TEV in 50 mL and shake O/N at 37deg in LB, AMP + CHLOR
3. Inoculate 2L TB with AMP and CHLOR with 50 mL starter culture at 37deg until OD_{600} 1.5
4. Induce with 1mM IPTG overnight at 25deg and 225 rpm (~18hrs)
5. Pellet 3500rpm, 10-15min, resuspend in PBS, pellet 3500rpm, 10-15min

---

6. Wash MonoS column extensively with high salt buffer (20 mM phosphate pH 7.0, 1 M NaCl, 10% glycerol)
7. Equilibrate MonoS column with 20 mM phosphate pH 7.0, 20 mM NaCl, 10% glycerol
8. Lyse ~15 mL cells in 75 mL buffer – 40 mM phosphate pH8, 400 mM NaCl, 20 mM imidazole, 5 mM BMe -- sonicate at power=4 and duty cycle=50% with large tip in beaker on ice – take breaks to let tip cool – total "on" time should add to 2.5 min
9. Pellet at 50k rpm, 1hr - ultracentrifuge
10. Apply to 3 mL Ni-NTA beads
11. Wash with resuspension buffer 15 CV
12. Wash with wash buffer 8 CV (resuspension buffer with 40 mM imidazole)
13. Elute with 7 CV (9 mL) elution buffer – 10 mM phosphate pH 7.0, 40 mM NaCl, 400 mM imidazole, 10% glycerol
14. Bradford to see where TEV is (usually E2 and maybe E3)
15. Run SDS-PAGE gel to see where TEV is concentrated
16. Dilute slowly 2-fold with 20 mM phosphate pH 7.0, 20 mM NaCl, 10% glycerol
17. Inject 5 mL at a time of the diluted solution onto the S column (as many times as necessary to load all protein)
18. Run elution onto MonoS column with 20 CV @ 1 mL/min (or slower if pressure is too high) linear gradient to 20 mM phosphate pH 7.0, 1 M NaCl, 10% glycerol with a 5 mL loop
19. Run SDS-PAGE gels with fractions 16-39 to locate protein (came out ~fraction 25-29)
20. Pool fractions and add 80% glycerol to 50% final concentration(1:1.3) and freeze in 1mL aliquots in LN2 (store in -80)

Appendix 1-2: MSP purification and cleavage

1. Transform MSP into BL21 Rosetta cells - plate 10 uL on LB, 50 mg/L KAN
2. Grow O/N culture in LB, KAN+CAM
3. Inoculate 2L TB,KAN+CAM (grow to 0.8 OD_{600} 37deg, 225rpm) (2 hr induction 1mM IPTG, 37deg, 225rpm)

---

4. Resuspend the cells in 60 mL 100 mM sodium phosphate 7.6, 1 mM PMSF
5. Sonicate 3 times for 1 min (50% duty cycle - 1 min on/1 min rest)
6. Add 1% Triton - 10 mL (20% stock)
7. Sonicate 2-3 times for 1 min (50% duty cycle - 1 min on/1 min rest)
8. Check cells under scope
9. Centrifuge 20000 rpm - Ti 45 - for 45 min, 4 deg

---

10. Regenerate column - 9 mL resin
11. Run 45 mL of 10 mM EDTA over column to strip
12. Wash with 90 mL water
13. Add 4.5 mL 100 mM NiSO4 and let sink into beads
14. Wash with 90 mL water
15. Wash with 90 mL phosphate buffer

---

16. Add supernatant to column
17. Wash column with 225 mL 40 mM Tris/HCl, 0.3 M NaCl, 1% Triton, pH 8.0

18. Wash column with 130 mL 40 mM Tris/HCl, 0.3 M NaCl, 50 mM sodium cholate, pH 8.0, 20 mM imidazole
19. Wash column with 125 mL 40 mM Tris/HCl, 0.3 M NaCl, 50 mM imidazole, pH 8.0
20. Elute protein with 40 mM Tris/HCl, 0.3 M NaCl, 0.5 M imidazole - collect 6 x 6, 12, 9, 9, 9, 9 mL fractions
21. Quick by eye Bradford assay for most concentrated fractions (verify protein conc. isn't > 8-10 mg/mL)
22. Hydrate dialysis membrane in 10 mM EDTA
23. Dialyze most concentrated fractions against 20 mM Tris/HCL, 0.1 M NaCl pH 7.4 - 3x 2L (~3hr each)
24. Bradford for protein concentration
25. (hopefully ~8 mg/mL)
26. Cleave with TEV protease (-80 stock) 1:3 molar ratio with MSP, diluted 2.5x in 20 mM sodium phosphate buffer pH 7.0, 50 mM NaCl, 1 mM DTT (8-12hrs)

---

27. Dialyze to remove DTT (20 mM Tris 7.4, 100 mM NaCl) -- 2x 4L (~3hr each)
28. Add imidazole to 40 mM
29. Bind with 5 mL Ni beads - 1 hr, 4deg, nutating
30. Collect FT (should have MSP without TEV) and add 0.01% DDM
31. Dialyze to remove any Ni^{2+} leak (20 mM Tris 7.4, 100 mM NaCl, 0.01% DDM, 0.25 mM EDTA) -- 2x 4L (~2hr each)
32. Concentrate to ~3-4 mg/mL (large 10k MWCO)
33. Bradford to confirm protein concentration, run SDS PAGE
34. Aliquot and freeze in 3mg tubes (~1mL)

Appendix 1-3: GluA2 lipid nanodisc protocol

1. **~4:30pm:** Prep buffers and beads
    a. 50 mL cells
    b. 400 mL Base Buffer - 20 mM HEPES 7.4, 150 mM NaCl, 33 mM NBQX
    c. 40 mL DDM Buffer – 2.5% DDM, 20 mM HEPES 7.4, 150 mM NaCl, 1% POPC
    d. 5 ml anagrade DDM buffer – 1% DDM, 20 mM HEPES 7.4, 150 mM NaCl, 0.4% POPC
2. Prepare beads (3 mL of FLAG M2 agarose beads).
    a. Wash the beads 3x 1.5CV using (0.1% DDM, 20 mM HEPES pH7.4, 150 NaCl, 30 uM NBQX, 0.04%POPC))

3. 5pm Resusupend 50 mL pellet in 310 mL Base + 400 uL each PI and add 40mL (0.25% DDM) and stir in cold room for 2.5 hr
4. 7:30pm Spin solubilized cells 3500 rpm, 10 min and balance supernatant in Ti45 tubes
5. 8pm Spin for 1 hr at 45k rpm in Ti45 rotor - *tubes balanced within 0.01 g*
6. 9:30pm Take out supernatant from HS spin and put in plastic beaker to gravity flow over FLAG column

7. Run supernatant (~400mL) over column for ~9 hours
8. **~8am:** Wash column of 3mL FLAG beads with 3CV of wash buffer (0.1% DDM, 20mM HEPES pH7.4, 150mM NaCl, 30 mM NBQX), one column volume at a time.
9. Elute protein with (0.2µg/ml 3xFLAG peptide, 0.1% DDM, 20 mM HEPES pH7.4, 150 NaCl, 30 mM NBQX). EL1=1.5ml, EL2 = 4.5ml, EL3 = 3ml.
    a. *let elution 2 sit on the beads capped for 30 min-1 hour before running it through*
10. Soak 100 kD concentrater in 0.1% DDM buffer for 30 min
11. Concentrate elutions 2/3 (~7mL) in 100 kD MWCO to ~700 uL
12. Add concentrated FLAG elution (500-700 µL), POPC:brain lipid (250µL) MSP (3 mg (1mL)) and let sit for 45 min on ice, then add biobeads (1.5 g)
    a. *negative control = (500 µL buffer under concentrator + uL lipid + 900 µL 0.1% DDM buffer + 1.5 g biobeads*

13. Parafilm the tubes and reconstitute in cold room on ice – 48-72hr on ice – add 1g biobeads after 24 hr
14. Equilibrate Superose 6 column with 60 mL GF buffer - (20 mM HEPES 7.4, 150 mM NaCl, 0.2 um filtered and sonicated for 40 min)

---

15. **2-3days later:** Run PD-10 column for the reconstituted nanodiscs
    a. Wash with 25 mL GF buffer
    b. Add 2.5 mL nanodiscs - *BTV with GF buffer by washing biobeads quickly*
    c. Add 3.5 mL buffer and save this elution fraction
16. Concentrate to ~700 µL in 100 kD MWCO
17. Ultracentrifuge concentrated sample - 15 min, 50krpm
18. Run Superose 6 GF – 0.5 mL/min
19. Make NS grids for fractions 14-17 and check on Morgagni
20. Concentrate as needed
    a. *try to make concentration unnecessary*
21. Make cryogrid – check vitrobot notebook
22. Check on Polara
23. Make more cryogrids in best condition
24. Run FLAGpur. gel and gel on concentrated sample – save ~10-15 µL

Appendix 2-1: SPIDER instructions

1. Convert to 8-tiff
    a. ImageJ & - Process, Batch, Convert -> input folder, output folder, 8-bit tiff, bilinear, 0.5=scale
2. Convert tif to pic files
    a. emacs tif2spiV2.sc & -> first, last, file_base, ext (*use and identifying ext like .glu*)
    b. ./tif2spiV2.sc > XXX.log &
3. Pick particles
    a. web *ext* & - Command -> Markers -> Open pic_file = name, doc file = crd_000X
        i. Option -> Cursor
        ii. Left click center of particle (to pick)
        iii. Center click -> Shift image (to move)
        iv. Center click -> Stop + Command -> Clear (to exit)
4. Pick noise
    a. web *ext* & - Command -> Image (pic_file)
        i. Edit -> Window Last File -> Interactive (drag box from top left to bottom right in area with no particles)
        ii. Enter window file name = nse_000X
        iii. Command -> Shift (if you need to move)
5. Prepare for removing bad particles
    a. mkdir: crd-files; pic-files; nse-files; cut
    b. cd cut/ and then fetchpi -> 4
    c. mkdir (under cut/) crd-files
    d. cp prepared_crds.sc to crd-files/ (original crd-files folder)
6. Prepare crd-files
    a. (in original crd-files) emacs prepare_crds.sc & -> first, last, ext
    b. ./prepare_crds.sc > XXX.log &
7. Window particles
    a. (in cut) emacs window_s.sc & -> ext, first, last, box size (100) radius (40)
    b. Create links
        i. ln -s ../pic-files pic-files
        ii. ln -s ../nse-files nse-files
        iii. ls -l (to confirm that links were created)
    c. ./window_s.sc > XXX.log &

8. Remove bad particles
    a. web *ext* & - Commands -> Clear
    b. Commands -> Categorize -> seq. montage
        i. win/000X/win_ooox.ext (double click), ACCEPT -> output = bad_000X, starting # = 1, categories = 3
        ii. left click bad particles (font set to 24, bold so you can see)
        iii. right click (to stop)
    c. fetchpi 5
    d. (in cut) emacs cull_s.sc & -> est, first, last, box size (100)
    e. ./cut_s.sc > XXX.log &
9. Alignment
    a. mkdir align (in main folder)
    b. fetchpi 6
    c. emacs mra.sc & -> # of particles (determine from tail -100 ../cut/cull.log), box size, radius, groups (100), ext
    d. (in align) ./mra.sc > XXX.log1 &
10. wc sel* > XXX.txt (this will give you a list of the number of particles in each class

Appendix 2-2: Random conical tilt instructions

1. Align F20, insert RCT sample, and find the square you want to image
2. Wobble to find eucentric height
3. Target the hole at 0° and focus on tilt angle (longest part of oval)
4. Tilt 50°, move stage to center of target, burn focus spot to orient
5. Take a row of tilted images (defocus -1.8)
6. Untilt stage and move back across row taking untilted images (defocus -1.5)
7. Move one row, check 0° targeting, tilt 50° and repeat 4-7 until finished
8. Note numbering and which are tilt pairs (easiest is X_001 (0°) = X_002 (50° of X_001)
9. Convert dm3 -> tif files
    a. SPIDER section (1)
10. fetchpi 3
    a. emacs tp_raw2mrc2spiV3.sc & -> first, last, file base, ext, new first
    b. ./ tp_raw2mrc2spiV3.sc
11. web ext &
    a. Commands -> Tilted particles
    b. Open -> untilt = left, tilt = right, docfile = 1
    c. Menu -> Shift (to line up images)
    d. Pick left particle, pick right particle (pick 4-6 particles very carefully)
    e. Manu -> Determine tilt and axes
        i. Save angles in doc file
        ii. Key number = particle pair 3
12. wc dcu* -> particle # = first column
13. Pick noise for untilted
    a. Same as SPIDER section (4)
14. fetchpi 8
    a. mkdir nse-files, cut, crd-files, pic-files
    b. mv dc* crd-files/
    c. mv pic_* pic-files/
    d. mv README cut/
    e. mv b02template_p.wnd cut/
    f. mv window_p.sc cut/
    g. mv prepared_crds.sc crd-files/
    h. prepare and window crd-files in the same way as SPIDER sections (6 and 7)
15. Remove bad particle
    a. Same as SPIDER section (8) except badu_000X = untilted and badt_000X = tilted

16. fetchpi 7
    a. (inside cut) emacs cull_p.sc & -> ext, image #
    b. ./cull_p.sc > XXX.log &
17. Alignment same as SPIDER section (9)
18. wc sel*.ext | sort -nr (get # of particles)
19. (in top directory) mkdir backprojection
    a. (in backprojection) fetchpi 9
    b. cp transXXX.ext
    c. cp cull_p.log
    d. ln -s ../cut/crd-files/ crd-files
    e. emacs prep.sc & -> ext, #micrograph, trans_file, select_doc (selXXX.ext = class you want to use)
    f. ./prep.sc > XXX.log &
    g. emacs back_project.sc & -> radius, nomir_selXXX (selection doc), ext
    h. ./back_project.sc > XXX.log
20. Convert spider volume to mrc
    a. e2proc3d.py selXXX_volXXX.ext output.mrc
    b. e2proc3d.py –clip=(boxsize) output.mrc output2.mrc
    c. e2proc3d.py –scale=(F20px/Polarapx) output2.mrc output3.mrc

Appendix 2-3: RELION scripts and instructions

Re-centering script (Terunaga Nakagawa)
batch_shift.py*

```
#!/usr/bin/python

import sys
import os
import subprocess
import shlex

################################################################################
################
### !!!!!!You must have shift_particles.sc in the cwd!!!!!!
### Usage: script shift_table path_to_particle_star output_root conf combined_star
###
###       shift_table - text file with [Class, shiftX, shiftY, particles, Conf, Comments].
###                     First line contains the name of each column.
###       path_to_particle_star - [relative path + file root] to the relion selection files
###                               (they must be named with same suffix, such as 'sel_class_XXX')
###       output_root - file root name of individual shifted particle.star file
###       conf - conformation class (any word with no space is fine)
###       combined_star - output of the combined shifted particle.star file
###
###       Example: ./batch_shift.py recentered_particles.txt sel_class_ shifted_ c combined.star
################################################################################
################
#######
#######  Author Teru Nakagawa Jan23, 2017
#######  Notes: command argument for subprocess.call() cannot be an alias
#######  Bug fix: 12.21.2017, Teru, L40; input_for_star_combine = ' " '
#######
################################################################################
################
f1=open(sys.argv[1],'r')
```

```
current_dir = os.getcwd()
relative_dir_pre = sys.argv[2]
output_root = sys.argv[3]
conf = sys.argv[4]
combined_star_file = sys.argv[5]

p=subprocess.Popen(shlex.split("which relion_star_combine"), stdout=subprocess.PIPE)
relion_star_combine_path = p.communicate()[0][:-1]

Colunm_names=f1.readline() ##reads the first line

input_for_star_combine = ' " '
total =0
each_line = 'text'
while(each_line != 0):
    each_line=f1.readline()
    try:
        each_line.split()[0]
    except IndexError:
        break
    print each_line
    Class = each_line.split()[0]
    shiftX = each_line.split()[1]
    shiftY = each_line.split()[2]
    particle_counts = each_line.split()[3]
    category = each_line.split()[4]
    if (category != conf):
        print "Class ", Class, " excluded. Category is not ", conf
        continue
    star_file = os.path.join(current_dir, relative_dir_pre+str(Class), 'particles.star')
    if (os.path.isfile(star_file) == False):
        print star_file, " does not exist!"
        continue
    shifted_star_file = os.path.join(current_dir, relative_dir_pre+str(Class), output_root + 'particles.star')
    args = 'shift_particles.sc' + ' ' + shifted_star_file + ' ' + star_file + ' ' + str(shiftX) + ' ' + str(shiftY)
    print args, '\n'
    p2 = subprocess.Popen(shlex.split(args))
    p2.wait()
    print shifted_star_file, " created", '\n'
    input_for_star_combine += (shifted_star_file+ ' ')
    total += int(particle_counts)
f1.close()

input_for_star_combine += '" '
print input_for_star_combine, '\n'

p_combine = subprocess.Popen([relion_star_combine_path, "--i", input_for_star_combine, "--o",
combined_star_file])

p_combine.wait()

print "total paticles are = ", total
```

shift_particles.sc*

```
#!/bin/tcsh

##### Script to write new micrograph autopick files after cleaning n 2D/3D#####

if ("$1" == "") then
  echo "Usage: EM_newautopick.sh output.star allparticles_data.star pixel-ofset-X pixel-ofset-Y"
  echo "Example: EM_newautopick.sh output.star particles_from_2D.star 20 10"
  exit
endif

if ("$2" == "") then
  echo "Usage: EM_newautopick.sh output.star allparticles_data.star pixel-ofset-X pixel-ofset-Y"
  echo "Example: EM_newautopick.sh output.star particles_from_2D.star 20 10"
  exit
endif

if ("$3" == "") then
  echo "Usage: EM_newautopick.sh output.star allparticles_data.star pixel-ofset-X pixel-ofset-Y"
  echo "Example: EM_newautopick.sh output.star particles_from_2D.star 20 10"
  exit
else
  set difX=$3
endif

if ("$4" == "") then
  echo "Usage: EM_newautopick.sh output.star allparticles_data.star pixel-ofset-X pixel-ofset-Y"
  echo "Example: EM_newautopick.sh output.star particles_from_2D.star 20 10"
  exit
else
  set difY=$4
endif

#Variables
set outfile=$1
set datastar=$2
set mic=`grep _rlnMicrographName $datastar | awk -F"#" '{print $2}' `
set coordX=`grep _rlnCoordinateX $datastar | awk -F"#" '{print $2}' `
set coordY=`grep _rlnCoordinateY $datastar | awk -F"#" '{print $2}' `
set oriX=`grep _rlnOriginX $datastar | awk -F"#" '{print $2}'`
set oriY=`grep _rlnOriginY $datastar | awk -F"#" '{print $2}' `
set psi=`grep "_rlnAnglePsi " $datastar | awk -F"#" '{print $2}' `
set numberOFfield=`grep _rln $datastar | wc -l`

#TEST FOR PARTICLE RECENTERING
#offsetX+((displacementX*-cos)-(displacementY*sin) --> component X from moving the particle in X + component X from moving the particle in Y
#offsetY+((displacementX*sin)-(displacementY*cos)--> component Y from moving the particle in X + component Y from moving the particle in Y
#I am not sure about the sign of the movements... trial and error with test particle...

awk 'NF<3{print}' $datastar | sed ':a;/^[ \n]*$/{$d;N;ba}' | grep -v '_rlnOriginX\|_rlnOriginY' | tr ' ' '@' | tr '\n' '?' | awk '{print $1"_rlnOriginX@?_rlnOriginY@"}' | tr '?' '\n' | tr '@' ' ' > header.tmp
```

```
awk -v oX=$oriX -v oY=$oriY 'NF>3{$oX=$oY="";print}' $datastar > data.tmp

grep mrc $datastar | awk -v oX=$oriX -v oY=$oriY -v psi=$psi -v difX=$difX -v difY=$difY '{print
((($oX+(((difX)*(-cos(($psi)*(3.141592/180))))-
((difY)*(sin(($psi)*(3.141592/180)))))),(($oY+(((difX)*(sin(($psi)*(3.141592/180))))-
((difY)*(cos(($psi)*(3.141592/180)))))))}' > offsets.tmp

paste data.tmp offsets.tmp > all.tmp
cat header.tmp all.tmp > $outfile

rm -f *.tmp
```

CPU submission script (Terunaga Nakagawa)
relion_accre_template_V3os7.slurm

```
#!/bin/bash

# submit script with: sbatch filename
# (number of mpi tasks)*(threads) = (node)*(cores)
# This script template is for Relion V2

#SBATCH --ntasks=XXXmpinodesXXX          # number of mpi tasks
###SBATCH --nodes=XXXnodesXXX             # number of nodes (need not specify at ACCRE. Let the Slurm do its job.)
#SBATCH --ntasks-per-node=2              # mpi tasks per nodes (ACCRE nodes are dual quad or dual hex)
###SBATCH --cpus-per-task=XXXthreadsXXX  # CPU per mpi task (take advantages of multicore CPU)
###SBATCH --threads-per-core=XXXthreadsXXX  # threads per CPU (take advantages of multicore CPU) use quad(4) or hex(6)
###SBATCH --cores-per-socket=XXXdedicatedXXX
#SBATCH --mem-per-cpu=20G                # memory per CPU core
#SBATCH --time=XXXextra1XXX              # wall time hour:min:sec
###SBATCH --exclusive                   # Want the node exlusively
#SBATCH -J XXXnameXXX                    # Job name
#SBATCH --output=XXXoutfileXXX
#SBATCH --error=XXXerrfileXXX
#SBATCH --mail-user=caleigh.m.azumaya@vanderbilt.edu   # email address
#SBATCH --mail-type=ALL

echo "Starting at `date`"
echo "Job name: $SLURM_JOB_NAME JobID: $SLURM_JOB_ID"
echo "Running on hosts: $SLURM_NODELIST"
echo "Running on $SLURM_NNODES nodes."
echo "Running on $SLURM_NPROCS processors."
echo "Current working directory is `pwd`"

#setpkgs -a openmpi_1.8.4       #OpenMPI version needs to match with relion2 is compiled with (check the relion sch script env info)
#setpkgs -a cuda7.5             #CUDA environment
#setpkgs -a relion_1.4

#setpkgs -a gcc_compiler_4.9.3
#setpkgs -a openmpi_1.10.2_roce
#setpkgs -a cuda7.5
#setpkgs -a relion_2.0.3
```

```
#source #a shell script for Relion2 environment

set -v
mpirun -n XXXmpinodesXXX XXXcommandXXX
set +v

echo "Program finished with exit code $? at: `date`"
```

GPU submission scripts (Terunaga Nakagawa)
relion_accre_GPU_Pascal.slurm

```
#!/bin/bash

# submit script with: sbatch filename
# (number of mpi tasks)*(threads) = (node)*(cores)
# This script template is for Relion V2

#SBATCH --account=csb_gpu          #To submit to the GPU (Titan-X) at ACCRE
#SBATCH --partition=pascal
#SBATCH --gres=gpu:4

#SBATCH --ntasks=XXXmpinodesXXX          # number of mpi tasks
#SBATCH --nodes=XXXextra2XXX             # number of nodes (need not specify at ACCRE. Let the Slurm do its job.)
##SBATCH --ntasks-per-node=4             # mpi tasks per nodes (ACCRE nodes are dual quad or dual hex)
##SBATCH --cpus-per-task=         # CPU per mpi task (take advantages of multicore CPU)
###SBATCH --threads-per-core=XXXthreadsXXX  # threads per CPU (take advantages of multicore CPU) use quad(4) or hex(6)
#SBATCH --mem=120G                # memory
#SBATCH --time=XXXextra1XXX              # wall time hour:min:sec
#SBATCH --exclusive                # Want the node exlusively
#SBATCH -J XXXnameXXX                  # Job name
#SBATCH --output=XXXoutfileXXX
#SBATCH --error=XXXerrfileXXX
#SBATCH --mail-user=caleigh.m.azumaya@vanderbilt.edu   # email address
#SBATCH --mail-type=ALL

###setpkgs -a gcc_compiler_4.9.3
###setpkgs -a openmpi_1.10.2_roce
###setpkgs -a cuda7.5
###setpkgs -a relion_2.0.3

echo "Starting at `date`"
echo "Job name: $SLURM_JOB_NAME JobID: $SLURM_JOB_ID"
echo "Running on hosts: $SLURM_NODELIST"
echo "Running on $SLURM_NNODES nodes."
echo "Running on $SLURM_NPROCS processors."
echo "Current working directory is `pwd`"

set -v
srun --mpi=pmi2 -n XXXmpinodesXXX XXXcommandXXX
set +v
```

```
echo "Program finished with exit code $? at: `date`"
```

relion_accre_GPU_V203.slurm

```
#!/bin/bash

# submit script with: sbatch filename
# (number of mpi tasks)*(threads) = (node)*(cores)
# This script template is for Relion V2

#SBATCH --account=csb_gpu         #To submit to the GPU (Titan-X) at ACCRE
#SBATCH --partition=maxwell
#SBATCH --gres=gpu:4

#SBATCH --ntasks=XXXmpinodesXXX          # number of mpi tasks
#SBATCH --nodes=XXXextra2XXX              # number of nodes (need not specify at ACCRE. Let the Slurm do its job.)
##SBATCH --ntasks-per-node=5             # mpi tasks per nodes (ACCRE nodes are dual quad or dual hex)
##SBATCH --cpus-per-task=         # CPU per mpi task (take advantages of multicore CPU)
###SBATCH --threads-per-core=XXXthreadsXXX  # threads per CPU (take advantages of multicore CPU) use quad(4) or hex(6)
#SBATCH --mem=120G                # memory
#SBATCH --time=XXXextra1XXX               # wall time hour:min:sec
#SBATCH --exclusive                # Want the node exlusively
#SBATCH -J XXXnameXXX                  # Job name
#SBATCH --output=XXXoutfileXXX
#SBATCH --error=XXXerrfileXXX
#SBATCH --mail-user=caleigh.m.azumaya@vanderbilt.edu   # email address
#SBATCH --mail-type=ALL

###setpkgs -a gcc_compiler_4.9.3
###setpkgs -a openmpi_1.10.2_roce
###setpkgs -a cuda7.5
###setpkgs -a relion_2.0.3

echo "Starting at `date`"
echo "Job name: $SLURM_JOB_NAME JobID: $SLURM_JOB_ID"
echo "Running on hosts: $SLURM_NODELIST"
echo "Running on $SLURM_NNODES nodes."
echo "Running on $SLURM_NPROCS processors."
echo "Current working directory is `pwd`"

set -v
```

RELION settings

****settings that are particularly variable or important are indicated, obviously change input, references, etc. for each job**

CTF estimation settings to adjust

- Cs: Polara = 2.2, Krios (WashU) = 0.001
- Amplitude contrast: cryo = 0.07, NS = 0.14
- Pixel size: Polara (31kX) = 1.247, Krios (81kX) = 1.41, Krios (109kX) = 0.96

Manualpick settings to adjust

- Particle diameter: A2 = 256, TRPC = 180, IP3R = 280
- Scale for micrographs: 0.2

- Sigma contrast: cryo = 3, NS = 0 or 1
- Lowpass filter: cryo = 20, NS = 5 or 10
- Scale for CTF image = 0.5

Autopick settings to pay attention to

- References
  - Lowpass filter references: 20
  - Mask: same as manualpick “particle diameter”
  - In-plane angular sampling: 5
  - References have inverted contrast: cryo = yes, NS = no
  - Are References CTF corrected: cryo = yes, NS = no
- Autopicking
  - Picking threshold: determine on a subset of images that samples from a range of defocus values (generally, cryo = ~0.2, NS = ~0.5)
  - Minimum interparticle distance: ~0.6x of particle diameter
  - Maximum stddev noise: determine on a subset of images that samples from a range of defocus values (generally, cryo = ~1.05, NS = ~1.1)
- Running
  - Number of MPI procs: 1
  - Queue submit command: sbatch
  - Time: varies (~1000 images = ~2hr)
  - Number of ACCRE GPU Nodes: 1
  - Standard submission script: relion_accre_GPU_Pascal.slurm OR relion_accre_GPU_V203.slurm (see above)
  - Minimum dedicated cores per node: 1

Extraction settings to adjust

- Extract
  - Particle box size: TRPC – 256, A2 and IP3R = 324
  - Invert contrast: cryo – yes, NS – no
  - Rescale particles: YES for initial cleanup classification (64px), possibly two rounds at 64px or a round at 64 and a round at 128

2D classification settings to pay attention to

- Optimization
  - Number of classes: varies (~1000/class, not over 200)
  - Use fast subsets: No – doesn’t work well for A2
  - Limit resolution: start with 8-10 in initial cleanups, drop to 4-6 as you select good particles
- Sampling
  - Perform image alignment: yes (unless doing a reclassification and you want to see if the particles recentered correctly
  - Offset search range: 5 (if particles are binned or have recentered), 10 (if initial pick and aligning at full size, like for manual classes)
  - Offset search step: 1 (if above is 5), 2 (if above is 10)
- Compute
  - Number of pooled particles: 3-12 (depending on number of particles)
- Running
  - Number of MPI procs: 50-200 (depending on # of particles and binning)
  - Number of threads: 6
  - Queue submit command: sbatch
  - Time: varies greatly (can be up to 3 days, try not to underestimate)
  - Standard submission script: relion_accre_template_V3os7.slurm

3D classification settings to pay attention to

- Reference
  - Symmetry: good to run in C1 as well as the symmetry your particle has
- Optimization

    - Number of classes: run at least 3 different
    - Regularization parameter: 4 recommended (can go up to 10 to test)
    - Number of iterations: 40 is usually good
    - Limit resolution E-step to: 5-6 for initial, can drop once cleaned some
- Running
    - Number of MPI procs: 5
    - Number of threads: 4
    - Queue submit command: sbatch
    - Time: varies (usually at least a day and a half)
    - Number of ACCRE GPU Nodes: 1
    - Standard submission script: relion_accre_GPU_Pascal.slurm
    - Minimum dedicated cores per node: 1

Mask create settings to adjust

- Lowpass filter map: 10
- Initial binarization threshold: determined in Chimera how much you want to encompass in the map
- Extend binary map this many pixels: 3-7 (make multiple to test for best resolution in refinement or postprocess)
- Add a soft-edge of this many pixels: 3-7 (make multiple to test for best resolution in refinement or postprocess)

3D refinement settings to adjust

- Running
    - Number of MPI procs: 5
    - Number of threads: 4
    - Queue submit command: sbatch
    - Time: varies (usually at least a day and a half)
    - Number of ACCRE GPU Nodes: 1
    - Standard submission script: relion_accre_GPU_Pascal.slurm
    - Minimum dedicated cores per node: 1

Postprocessing settings to adjust

- MTF of the detector: /home/nakagat1/accre_tnlab/TRPC6/MTF_K2_300keV.star

Local resolution settings to adjust

- User-provided B-factor: taken from the postprocessing run.out file (line: + apply b-factor of: XXX)

Appendix 2-4: cisTEM instructions and parameters

cisTEM settings

1) New project
2) Assets – Refine Pkgs,
    a. make .mrcs file with relion_stack_create –I particles.star –o XXX.mrcs
    b. Import: Relion: particle stack (XXX.mrcs) and star file (particles.star)
3) Assets – 3D Volumes
    a. Import: reference
    b. Import: mask

3D refinement settings to adjust

- Auto refine
    - Used defaults in IP3R paper except outer mask radius: 280

Postprocessing settings to adjust

- Sharpen
    - Input and mask imported from refinement and from RELION respectively
    - Flatten from Res: 7-9 was good
    - Resolution cut-off: 2.76 (highest res from Gctf, slightly above Nyquist)
    - Pre-Cut-Off B-Factor: -90 is default, increased to -130 and -160
    - Suggest to save many different maps and inspect them in chimera/coot

Export half maps for local resolution

- Generate 3D
    - Outer/inner radius: 280/0
    - Score to weight constant: tried 2-5, went with default of 2
    - Autocrop images: no
    - Also save half-maps: yes
    - Overwrite statistics: no
    -

Appendix 2-5: Modeling notes

Coot

- Install the EM plug-ins so that you can use jiggle fit – v important
- You're going to need a mouse with 3 buttons
    - Middle roller – changes threshold of map
    - Middle click – move around
    - Left click – rotate
    - Right click and move – zoom in/out
- Main tools you will use
    - Draw – Go to Atom
    - Draw – Display Manager
    - Edit – Map Parameters – Map radius
    - Edit – Map color
    - Edit – Skeleton parameters – Skeletonization Level (can lead Ca baton building)
    - Calculate – Other modeling tools – Place helix here (first navigate to the middle of your helix that you think you see, then you need to pick whether the helix or reverse helix fits best.
    - Calculate – Other modeling tools – Ca Zone -> Mainchain (select first and last carbons that you need to build a chain between)
    - Calculate – Other modeling tools – Ca Baton Mode (build along the density (you choose the next Ca placement, it will predict based on the density the ways it could go)
    - Calculate – Mutate residue range (add in a long stretch of correct sequence after building alanine model)
    - Calculate – Model/Fit/Refine – Simple mutate (change single amino acid to something else)
    - Calculate – Renumber residues
    - Calculate – Change chain IDs
    - Calculate – Fit loop – Fit loop by Rama search
    - Calculate – Model/Fit/Refine – Real space refine zone
    - Calculate – Model/Fit/Regine – Rotamers
    - Validate – Ramachandran Plot
    - Validate – Density fit analysis
    - Validate – Rotamer analysis
- You can pull the mainchain around and it will snap to the density, you have to pull it really far sometimes
- Usually I will place all of the helices into one subunit and then join them together
    - Place helices and then start from the N-terminus and find an anchor point with a large amino acid. Build from there in the helix and see if the amino acids would make sense. Do this for two helices and then figure out how many amino acids are likely to be in the loop region
    - To build in the loops, number your helices in the way that there is the correct number of amino acids in the loop and then change the chain IDs on the helices so that they are both the same. Go to the fit loop tool and then click on the last amino acid of the first helix and the first amino acid of the second helix and it should try and auto fit the correct number of amino acids into this area. Only use this if the loop is pretty well defined

- If the loop density is not well resolved, build from the last amino acid of the first helix with either the Ca Baton mode and then join the two helices and the loop you're building by changing the chain IDs to the same thing
- You will likely need to re-number and mutate the chain a variety of times in order to build the whole subunit
- Make tetramer in Chimera and then do a four separate chain jiggle fit
- Adjust individual phi and psi angles to nudge certain amino acids from Ramachandran acceptable to Ramachandran favored, real space refine will minimize the clashscore but usually won't minimize the Ramachandran outliers

Phenix

- Make an ncs file (this one is for C4 symmetry)
  - emacs ncs.eff &
  - pdb_interpretation {
    ncs_group
    reference = chain A
    selection = chain B
    selection = chain C
    selection = chain D
    }
- Run from the command line: phenix.real_space_refine *map*.mrc resolution=X.X *model*.pdb target_bonds_rmsd=0.005-0.01 (use smaller number if lower resolution) target_angles_rmsd=0.5-1.0 (use smaller number if lower resolution *ncs.eff* secondary_structure.enabled=True max_reasonable_bond_distance=100
  - Try a few different target_angles_rmsd and target_bonds_rmsd to see how far restraints can be relaxed
  - Note: it looks like the secondary structure restraints command may have been updated, though this one still works
- Molprobity – validation (load in a map and a PDB file and run it) this is now outdated, there is a new "Validation" tab that runs in the same way but gives more output statistics (no MolProbity score though)

PDB submission

1) Create deposition ID
2) Upload files
   a. FSC curve (it is an excel (.xml) file of the X and Y values
   b. Half maps (from the refinement)
   c. Map (postprocessing, masked but not sharpened, make sure it's flipped if it needs to be)
   d. Mask (that you used for final map)
   e. Image (.jpg image of the final map saved from chimera)
   f. Need to include pixel size and a recommended threshold for all of the maps
3) Then you have to fill out all of the informational fields
   a. Contact information
   b. Funding information and
   c. Release status – usually going to be HPUB (hold for publication) also probably best to hold back the name of the submission
   d. Title of entry, keywords, authors
   e. Citation information – probably not done before you submit the structure, can be sent in later
   f. Sequence, source of the protein (what species is the DNA from and what did you express it in)
   g. Specimen state (particle), buffer (pH required, contents, optional), cryogen (ethane), optional things are: blotting conditions, grid type, glow discharge

h. Microscope, illumination, imaging mode, electron source, voltage, optional things are: software, defocus, C2, Cs, magnification, energy filter
i. Detector, electron dose, optional things are: mode, width, height, number of movie frames, exposure time, number of images (optional)
j. Ctf correction process, technique used to generate initial model, angle assignment, number of particles at each step (initial pick, 2D, final), final resolution and FSC cutoff, symmetry
k. Modelling software, refinement software, B-factor used (all optional)
l. Assembly details (tetrameric ion channel), does this include all change (yes), can you generate this assembly without applying matrices (yes?)
m. Validation report is generated at the end of the submission that you have to check over

Chimera

1) Make tetramer after building one subunit in coot
    a. Open map and open .pdb file that you've made in coot of the single subunit
    b. Command line - sym group C4 axis z center #0 coordinateSystem #0
    c. Structure editing – change chain IDs – need to rename chains to A, B, C, D (will all be named A at this point)
    d. Save new PDB file that has all four chains – go back into coot and jiggle fit them into the map
2) Generally
    a. Want to go to Viewing – Side View (to see if your particle is at an angle that you want it to be, and to zoom), and go to Rotation (independent if you have multiple maps open then will spiral around their own central axes, front center if only one is open will be good)
3) Commands used for ribbon diagram figures
    a. Command line – background solid white
    b. Command line - delete #model:chain-chain.residue-residue (delete certain amino acids) i.e. delete #2:a-d.1002-1209
    c. Structure comparison – Matchmaker (aligning different models based on similarity)
    d. Depiction – pipes and planks (easier for measuring angles between helices)
    e. Structure analysis – Axes/Planes/Centroids (also good way to measuring angles between helices) – select two of the axes and it will tell you the angle between them
    f. Surface binding analyses – Coulombic surface coloring
    g. Sequence – (how to select a subset of residues most easily)
    h. Action – Atoms/Bonds – show – Color – by heteroatom (when you have a certain set of AA selected (usually from sequence) that you want to show them in stick form and to see their oxygens and nitrogens
4) Map figures
    a. Volume data – Volume viewer – set to step size 1 – change color, A is transparency
    b. Volume data – Color zone – select the part of the pdb file that you want to color around (change the ribbon color to the color that you want) and then set radius to 2-2 – click "Color" – click "Split Map" – change the threshold of the new map to step size 1, save .mrc file in the Volume viewer console
    c. Volume data – Volume eraser – change the radius of the eraser – use control middle as the move command – "Erase" when you're on top of the part of the map that you want to delete – make sure to view this from a few angles to make sure you're in the right place in X,Y, Z – save this as a new volume in the volume viewer console
    d. For opening the local resolution maps
        i. Open the chimera.cmd in Text Edit and delete everything that is below OPTIONAL
        ii. Save and open the .cmd file
        iii. Utilities – Color Key – make the colors labeled like in the .cmd file (open in Text Edit to see it)

iv. Place the color key in the screen to save in a .jpg – click and drag to the size that you want it to be. It will re-do this placement until you exit out of the Color Key menu, then it is permanently there